Edinburgh Wave Power Project

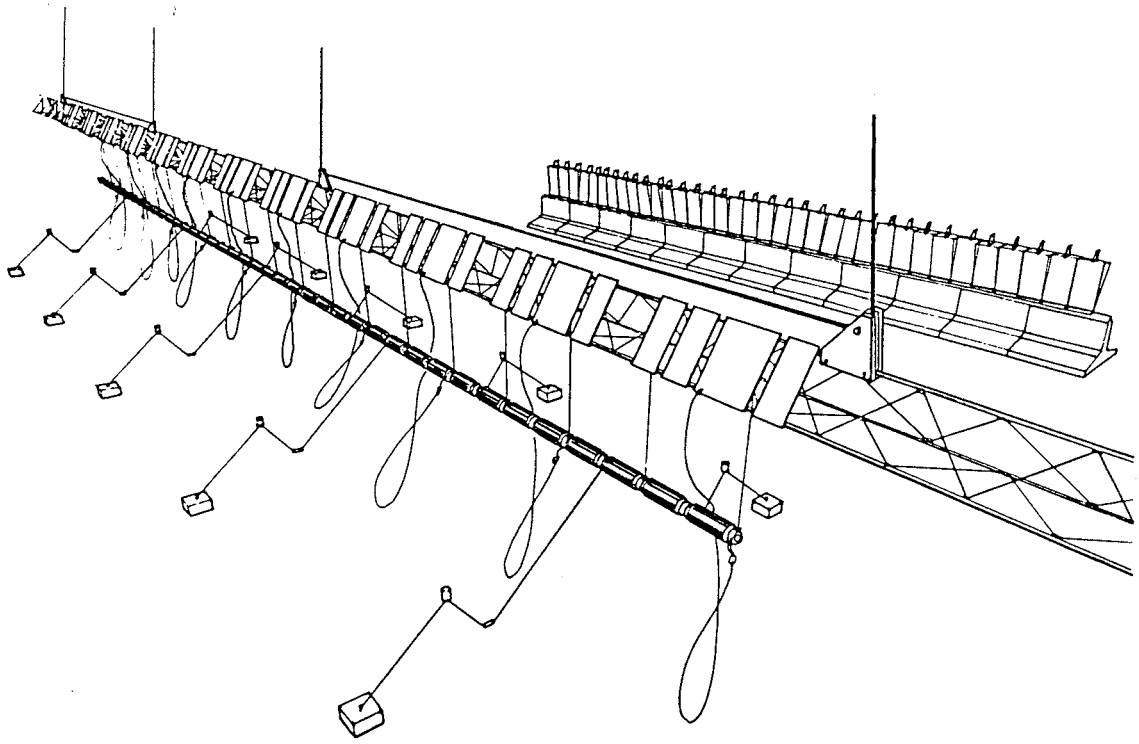

Bending Moments in Long Spines

1984

BENDING MOMENTS IN LONG SPINES

A report to the Wave Energy Steering Committee

covering work supported by the United Kingdom Department of Energy

EDINBURGH UNIVERSITY WAVE POWER PROJECT
University of Edinburgh
Mayfield Road
Edinburgh 9
031 667 1081 ext 3276

C O N T E N T S

1.A INTRODUCTION

While it is unusual to test tank-models with controlled, variable elasticity there are several reasons why we believe that it is important to exert the large effort required.

1. The convenient model-building materials are much too stiff to represent the proper behaviour of concrete and steel at full scale.

2. We believe that, although the close-packed, crest-spanning terminator configuration is the best possible arrangement for a wave-energy device, it is not economic to resist bending moments greater than those which would occur at the power limit. This means that non-destructive yielding to bigger waves must be achieved. This will not only save money on the spine structure but will also produce dramatic reductions in mooring forces.

3. Work in the narrow tank had shown that the correct control of a duck mounting could produce large improvements in duck performance, doubling the efficiency in waves twenty-five duck diameters in length. We had also discovered that the best values of mounting stiffness were low, less than those that would be provided by post-tensioned concrete at full scale, and that the mounting movement could itself be a useful power-generating mechanism. Furthermore the *hardware* needed to provide non-destructive yielding needed very little modification to provide intelligent control and the extra generating capability. We realised that the *software* requirements would be formidable - well beyond our present knowledge. But we were confident that the existence of a controlled model would, as so often before, stimulate theoretical work. Furthermore we were quite certain that the progress of computer technology between now and the date of the return of energy shortage would be so enormous that *any* level of control sophistication could be safely assumed to be available at virtually zero cost. On many occasions it has seemed that this view was not shared by the civil and marine engineers who assess our progress.

(1.A cont)

The work reported in this volume covers the measurements of bending moments and joint angles as a function of sea conditions, model lengths and stiffness, for circular spine sections without ducks. Other volumes will contain the observations of shear, axial, torsion and mooring forces, for spines with various appendages.

We found that it was necessary to put a very great deal of effort into the presentation of the data if the essential truth was to be revealed. The graphs in this report are about one twentieth of those plotted during the analysis of the results. They are largely the work of Mr. J.R.M. Taylor.

In parallel with the experimental programme sponsored by the Department of Energy was a computer simulation study which formed the doctoral thesis of Ian Bryden, supported by the SERC. Copies of this thesis have been sent to the Energy Technology Support Unit at Harwell and the UK Department of Energy. I would like to draw the attention of WESC to the close correspondence of theoretical simulation and experimental tests even for the most bizarre model behaviour.

The Wave Energy Steering Committee will not be surprised to read that the problem of plant availability has been given a great deal of attention. Several papers on the subject have been submitted to WESC through Harwell. I would like to emphasise the importance which we attach to the questions raised in these papers.

S. H. Salter
August 1984

1.B MAIN CONCLUSIONS

1. There seems to be no obvious relationship between length and bending moment for long compliant spines. Length squared and length cubed rules do not apply.

2. Bending moments are nearly independent of energy period over the central part of the useful energy-generating spectrum and fall for the very shortest periods.

3. Heave bending moments are proportional to the first power of wave amplitude.

4. Surge bending moments rise with wave amplitude to the power 0.8.

5. Surge bending moments are nearly always about twice heave moments. For engineering purposes it is safe to assume that there is a 90° phase shift between heave and surge moments. We can reduce the quantity of steel used for resisting heave loading.

6. Bending moments rise rather gently with stiffness. A logarithm relationship fits our test range. Reducing stiffness makes the effects of period change even smaller.

7. Changing the stiffness in one direction produces little effect on the bending moments in the other. We cannot run away from surge moments by yielding in heave.

8. Seas with a mean approach direction of 90° to the length of the spine produce a bending moment pattern which oscillates about a mean level in the central regions and which is raised at points approximately a wave-length in from each end.

9. Seas which approach the spine from an oblique direction produce smaller moments at the up-wave end and much larger ones at the down-wave end.

(1.B cont)

10. The down-wave enhancement factor in monochromatic waves can be as high as twenty five so that obliquity is by far the most powerful variable. As it is a relatively narrow effect (changing over one or two degrees) we must do some careful experiments to decide whether or not the use of 75-tooth comb spectra is sound.

11. We believe that enhancement happens when the velocity of a flexural wave along the length of the spine is close to the velocity of an intersecting wave crest. As flexural propagation velocity is a function of spine rigidity the effects can be controlled by the use of intelligent joints and perhaps even turned to advantage for power generation.

12. Changes to the mooring pattern, including the removal of a large fraction of the moorings, do not significantly change bending moment. We can afford to lose a lot of moorings and need not repair them immediately.

13. The maximum joint angle in the steepest, largest, credible wave is only just over 4° so that the 12° design allowance is generous. The result is unaffected by any attempt to stiffen or loosen the joint.

14. Broken joints reduce their own bending moment and raise the moments at adjacent joints.

2. DESCRIPTION OF THE MODEL

Fig 2.1 shows the general arrangement of the model, its moorings and the wireless mast which carries the multiple control boards. At the back of the drawing can be seen some of the eighty wavemakers.

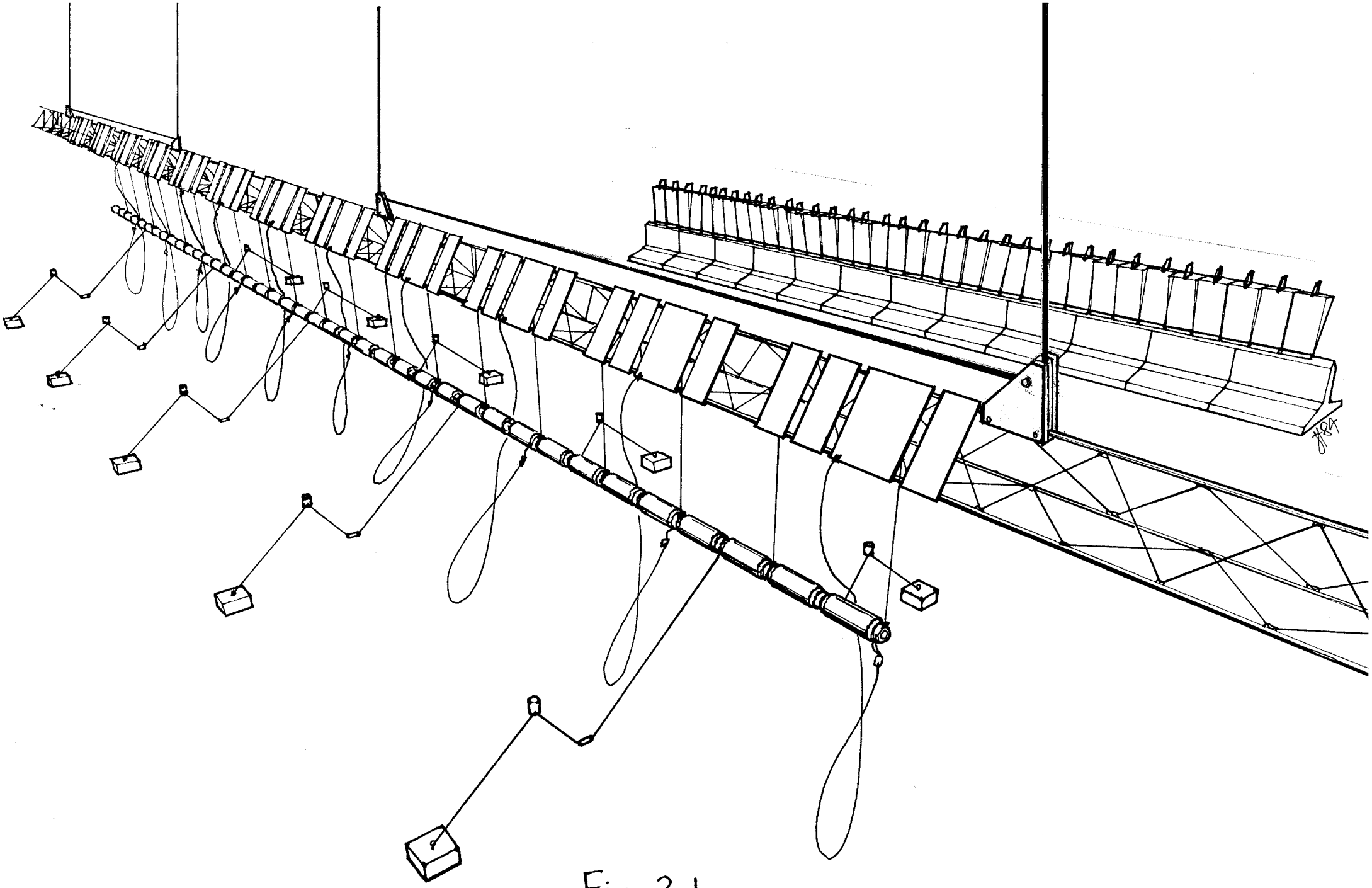

Fig 2.1

Fig 2.2 shows more detail of the spine sections and gives leading dimensions, weights and calibrations.

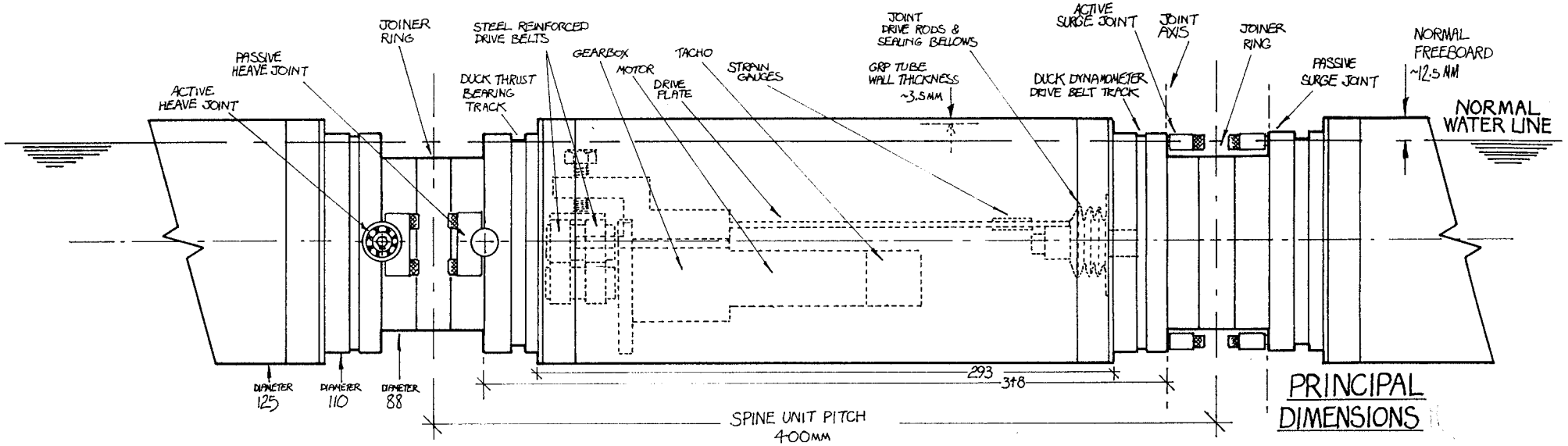

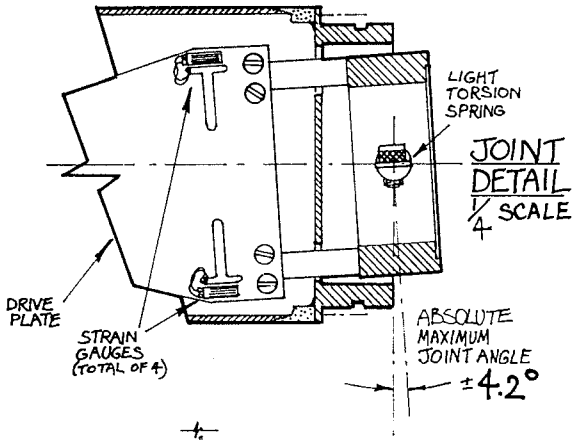

WEIGHT, SPINE UNIT + JOINER RING 3.830kg ≡ 9.57 kg/M
VOLUME, " " " " 4.0 LITRE ≡ 10 LITRE/M
FREEBOARD 12.5MM ≡ 10% OF DIAMETER
BUOYANCY SURPLUS 2.0N ≡ 5N/M
ABSOLUTE MAXIMUM JOINT ANGLE 4.2° ≡ 0.073 RAD
MAXIMUM JOINT BENDING MOMENT 60NM
GEAR RATIO, MOTOR SHAFT/JOINT 565:1
TORSION SPRING AT ACTIVE JOINT ~15NM/RAD
G.R.P. TUBE STIFFNESS $>10^4$NM/RAD @ 10NM TORQUE

LOOP GAIN STRAIN GAUGES
STATUS 9 : 0
STATUS 10 : 2.7 = 8.5 dB
OLD STATUS 12 : 2.7 = 28.5 dB
NEW STATUS 12 : 8.3 = 18 dB AFTER OCTOBER '83

CALIBRATIONS
TORQUE/BENDING MOMENT 10NM/V
TORQUE COMMAND 10NM/V
VELOCITY 0.1 RAD/SEC/V
MOTOR CURRENT 1AMP/V
LEAKS -10V E' DRY'

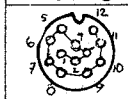

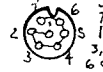

SPINE UNIT PHYSICAL DETAILS FIG: 2.2

jf 83

SHOWING SEA GOING CONFIGURATION WITH ELECTRICAL & AIR CONNECTIONS (JOINTS OPENED UP)

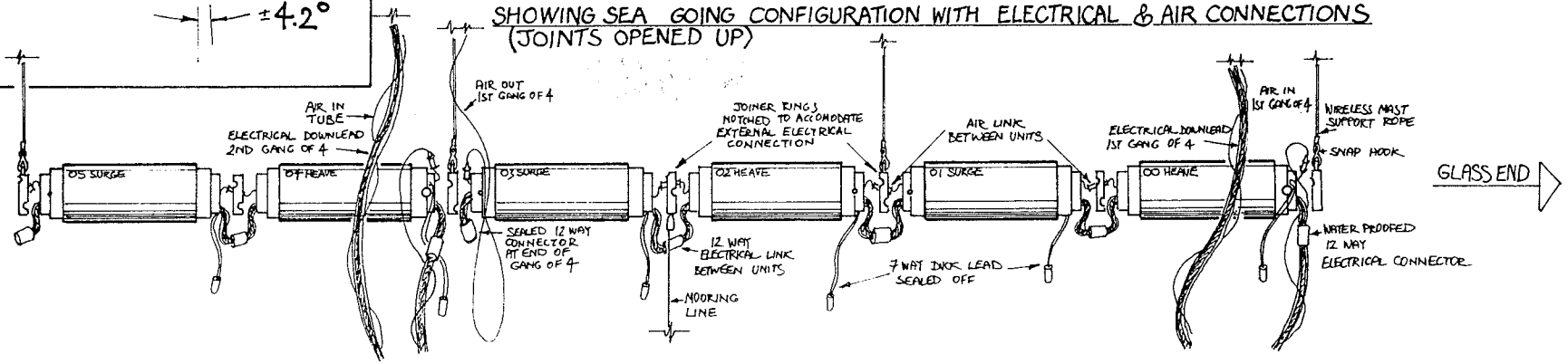

Fig 2.3 shows the mooring arrangements used for these experiments. The system is symmetrical fore and aft. It is an adaptation of the system developed for full scale ducks and based on force measurements in the narrow tank (ref e).

It is designed to provide a restoring force by changing the direction of a rode rather than the magnitude of its tension. In many ways it performs too well with rms tension variations less than 0.5% of the mean value. Other configurations have also been tested.

The cost of the full-scale sinker weights is high but they can very conveniently make use of the scrap obtained when round gyros discs are made from rectangular steel sheet.

Model anchors are placed 2 metres up- and down-wave of the mean spine centre-line. We have two types of anchor block. The passive ones are plastic lunch boxes filled with scrap steel and cement. Force-sensing ones use a steel base-plate with a square-bar cantilever fitted with vertical and horizontal strain gauges.

The experiments in section 4.M show the effects of making a major change to the mooring system.

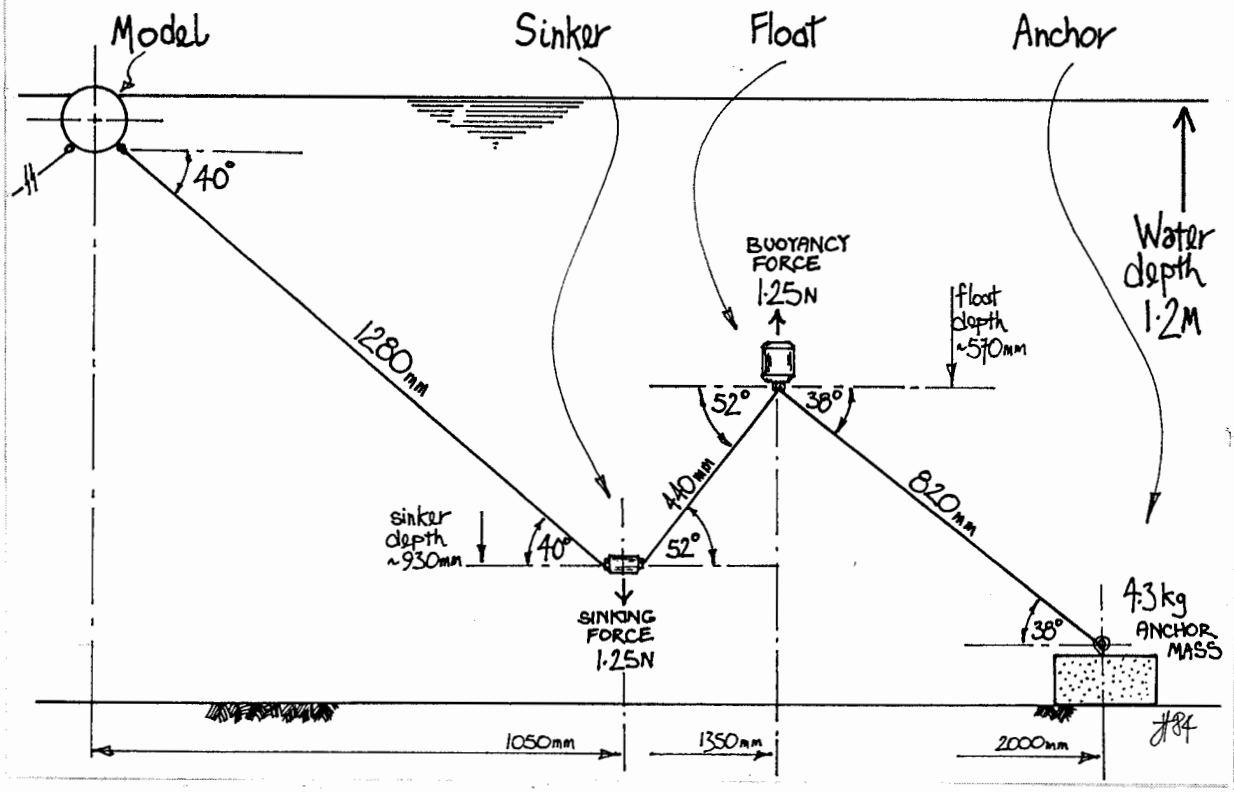

MOORING SYSTEM. Forces and Dimensions (nominal values)

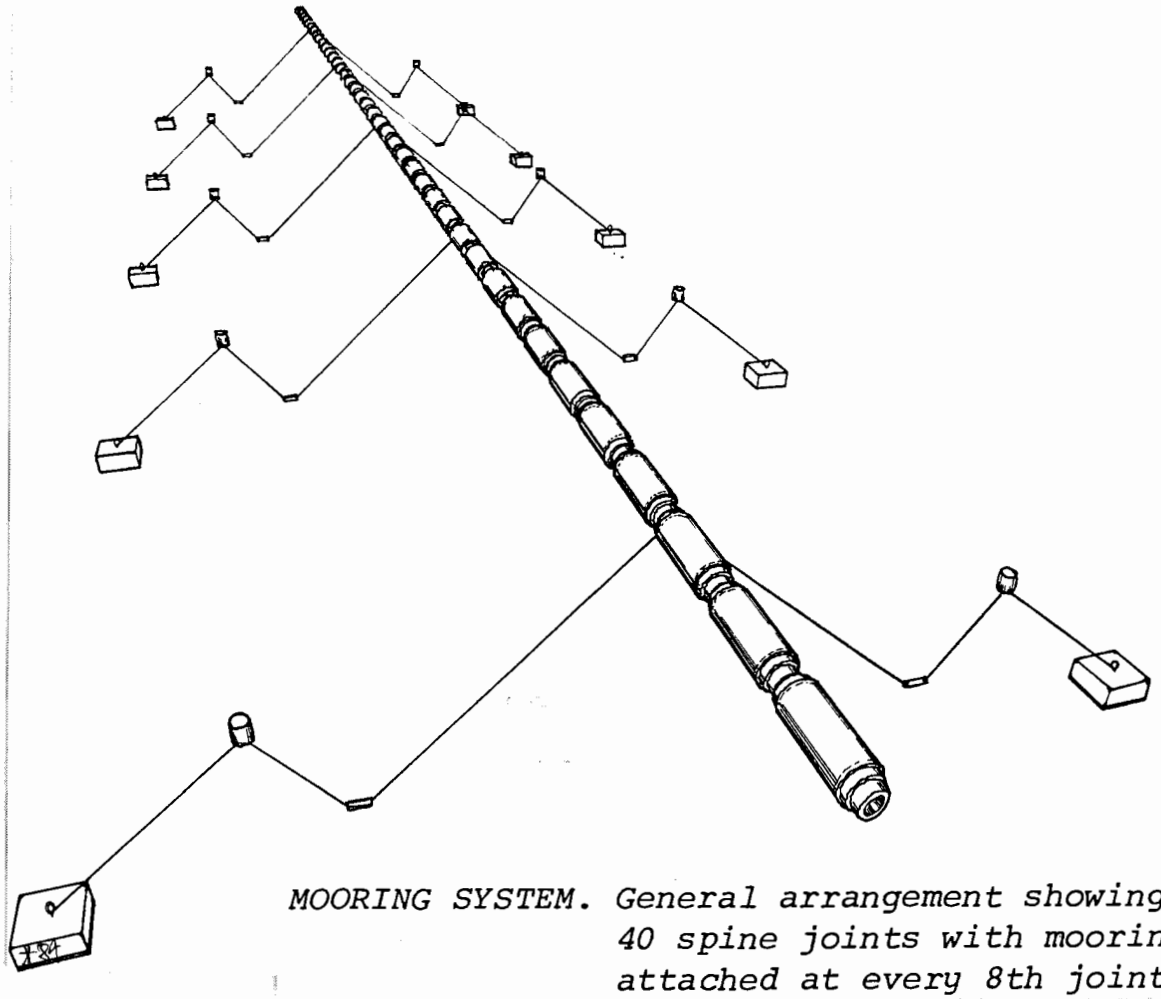

MOORING SYSTEM. General arrangement showing 40 spine joints with mooring attached at every 8th joint.

FIG 2.3

Photograph 2.4 shows a spine section with its outer skin removed.

The spines are connected to one another by finger clamps which can be tightened by radial screws. These can be seen protruding from the inner ring at the near end of the spine. Between the fingers is a flat beryllium-copper strip which acts as a low-rate torsion spring to centralise the AC-coupled stiffness control.

Inside the bulkhead we can see the triangular plate torque-arm with two of the four strain-gauges which sense fluid loading. Note the T-shaped slots which concentrate strain under the gauges.

The far end of the triangular plate can be moved through an angle of ±4.2° by a pair of steel-reinforced polyurethane toothed belts. These run on pulleys with tension-adjusting eccentrics.

The low-inertia motor and its 18:1 gear box can just be seen behind the torque arm. The length of the torque arm contributes the final stage of the step-down gearing which has an overall ratio of 565:1 from motor shaft to joint angle.

The low-inertia motors are fitted with tacho-generators. We use integrated velocity to indicate position.

Although rotation is constrained by carbon steel ball-bearings exposed to the water, the addition of a corrosion inhibitor known as 'Cimplus' has prevented problems and the original joint bearings are still in use.

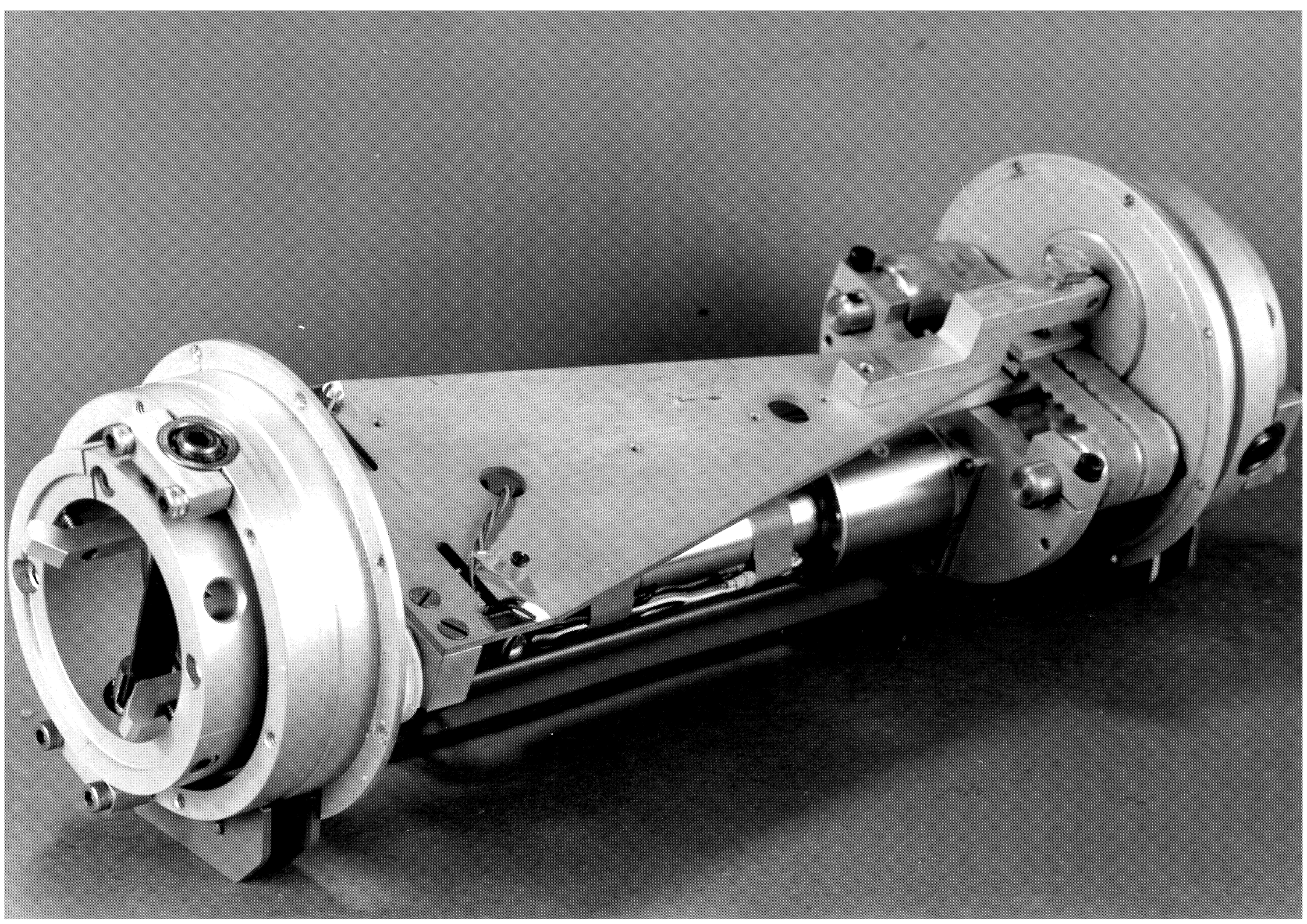

Photograph 2.5 shows a spine section with electronic control board. Signals from the strain-gauge bridge are conditioned and sent to a control computer which decides the correct command signal to be sent to the servo-motor. This moves the joint via belts and torque arm. The tank operator can control both stiffness and damping at each joint. We can also send a series of command signals to induce eel-like swimming motions in the model.

We had to fit a 16 channel bi-directional multiplexer to measure and control the spine joint and the duck which will be mounted on it. Each spine section contains two servo amplifiers. Their power transistors can be seen to the left of the board and are in excellent thermal contact with the water. One amplifier will be used for duck control.

In front of the spine is a collection of its machined parts. The entire assembly is enclosed in a centrifugally cast G.R.P. tube with light alloy end rings. We found that G.R.P. shows some long term porosity and that after a few years the bond between epoxy resin and freshly anodised light alloy is degraded. We are replacing the outer tubes with light alloy. Cimplus does not get through G.R.P. and there was quite serious corrosion on the pulley bearings *inside* the spine. These were all replaced and arrangements were made to pass a slow current of dry air through the model.

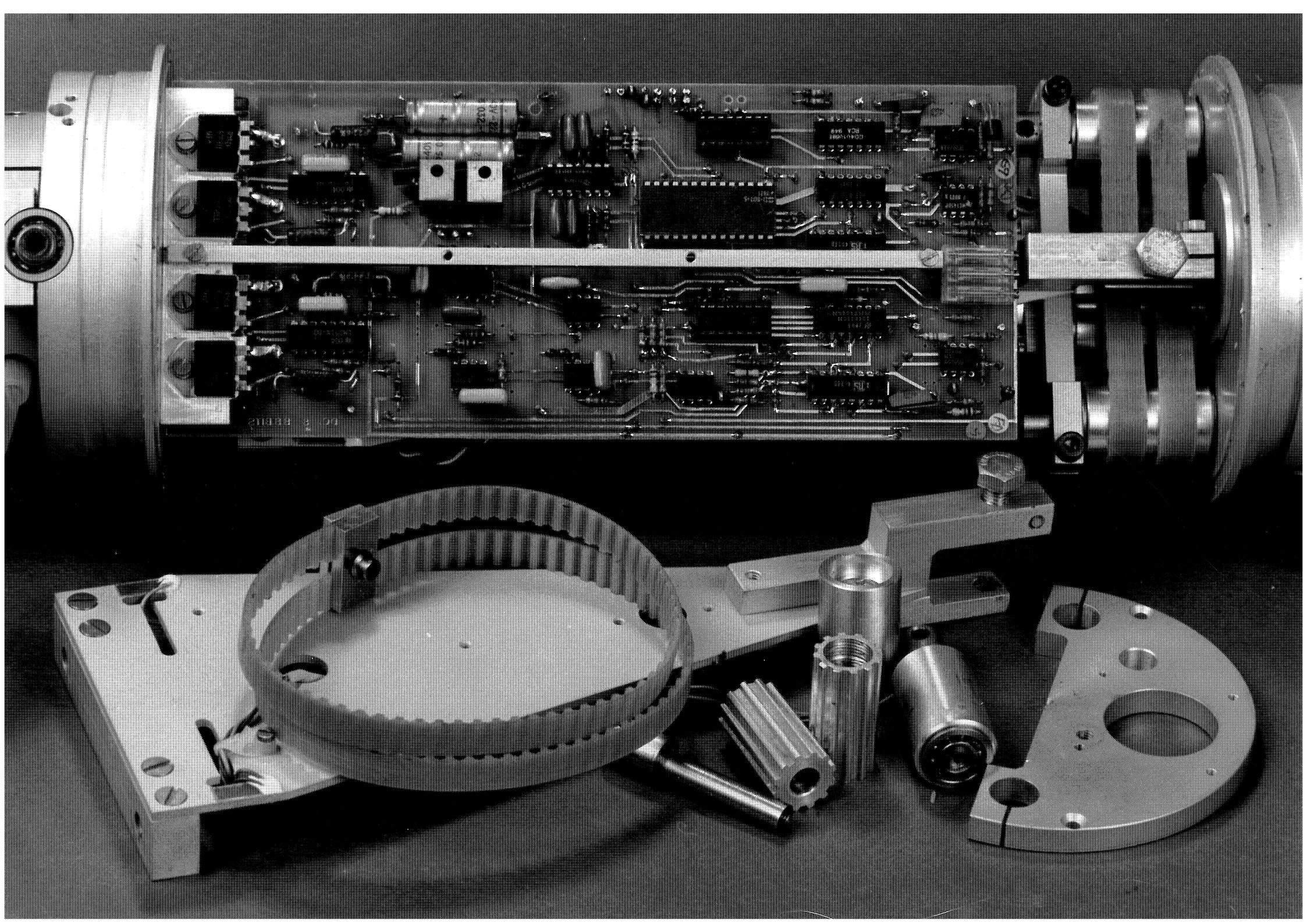

Figure 2.6 shows a circuit diagram of the spine electronics. This diagram divides roughly into three sections:

Section 1: (ICs 1 to 3) shows the conditioning and pre-amplification for the strain gauge bridge and the tacho-generator. At the right-hand end can be seen the resistive divider that drives the "BLOT" leak detector. It normally sits at -10V, but water in the module will change it to about -3V.

Section 2: (IC 10 down to IC 9) shows the multiplex section. There are 3 lines multiplexed out, labelled ZERO, BB (backbone or spine) and DUCK. (The line marked (DUCK) is connected to the local duck.) The Harris H1-507 chip handles most of the switching and an H1-201 the rest. Clocking is managed by a "token passing" system. Clock pulses are fed to either "CK1" or "CK2" (it doesn't matter which) and the spine counts eight of them, sending out spine and duck data appropriately. At this point IC 9 closes a switch between "CK1" and "CK2", allowing the clock pulses to go on to the next spine in line. This system allows all spines to be electronically identical.

IC8 is a 4-bit counter that sets the "STATUS" of the spine. It programmes the gain of IC15 and thus the overall spine force-feedback loop gain.

Section 3: IC11 down. This circuitry comprises a sample and hold (ICs 11 and 14) which handles the local duck multiplex, and op-amps 16, 17 and 15, which optimise the frequency responses of the duck and spine feedback loops. The bottom row, ICs 18 and 19, shows the two power amplifiers needed to drive the duck and spine motors. These amplifiers are based on the LM391 IC which is designed for hi-fi work but, when combined with a pair of Darlington transistors, makes a very compact servo unit.

"BBBITS" BACKBONE ELECTRONICS
5-5-80 DCJ

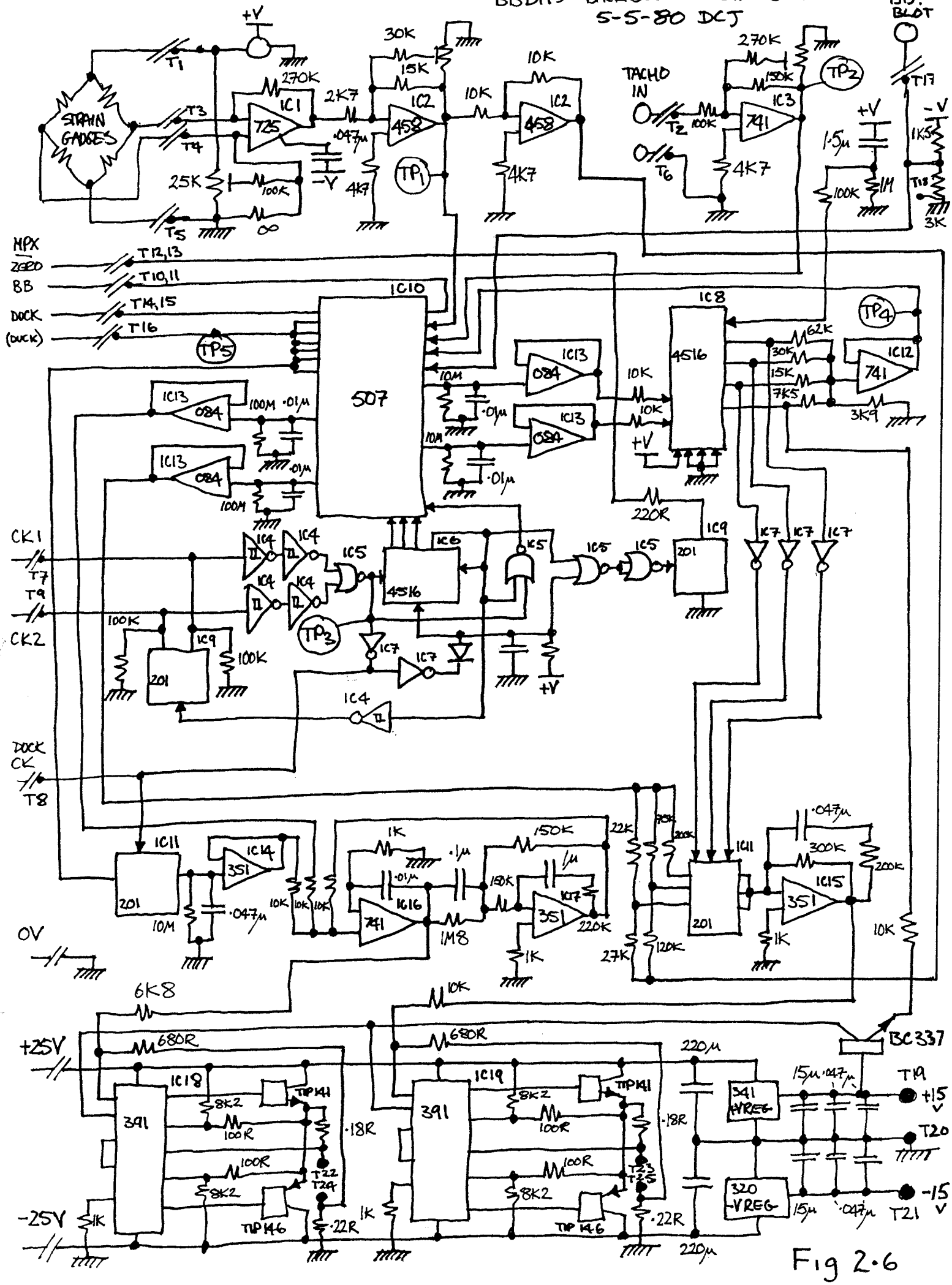

Fig 2·6

Photograph 2.7 shows David Jeffrey and a pile of spine sections prior to launching.

Each is connected to its neighbours with a waterproofed multiway plug carrying power and signals. Two units in front of the pile have their ducks fitted.

At the top right of the photograph we can see a few of the circuit boards which select data channels for control and measurement. The boards are mounted on a triangular-section wireless mast which spans the entire width of the tank and is used to launch and recover models.

Photograph 2.8 shows Chris Retzler checking the clamping of a joining ring.

The model is hanging up by nylon ropes from its wireless mast. When this is pulled back over the work platforms which cover our beaches we can get convenient access to both mechanical and electronic bits.

Launching the model and connecting all the moorings takes one person less than 3 minutes.

Photograph 2.9 shows the spine model in the tank. Joint deflection can be clearly seen. Grid lines on the tank floor are at 5 metre intervals. The joint pitch is 0.4 metres.

The wireless mast has been moved beachward to allow a clearer view. For testing it would be placed so as to minimise the drag of lifting ropes and umbilical cables. Initial tests of candidate cables in the narrow tank showed that this drag was about 5% of the mooring force.

A line of mooring floats can be seen to the right of the model. We found that these could be replaced by others one third of the displacement.

The three heavy bars on the front of the wireless mast distribute power to the model. Each group of four spines is protected by separate fuses and over-voltage crow bars. One spine caught fire but the damage was contained.

All the multiplex control boards are mounted on the beachward side of the wireless mast. Their Terry-clip attachments can be seen.

Fig 2.10 shows a block diagram of the data collection and model control system.

We found that the combination of distributed multiplex boards, differential signal-pairs and insulation-displacing ribbon-cable connectors has produced excellent reliability. The settling time of the 30 metre length of the wireless mast data-collection system is about 12 microsecond with a noise level of 1.5 millivolts. We ran into a problem with a residual dielectric 'remnance' which required the signal wires to be 'cleaned-out' by the subtraction of a small charge which depended on the previous measurement.

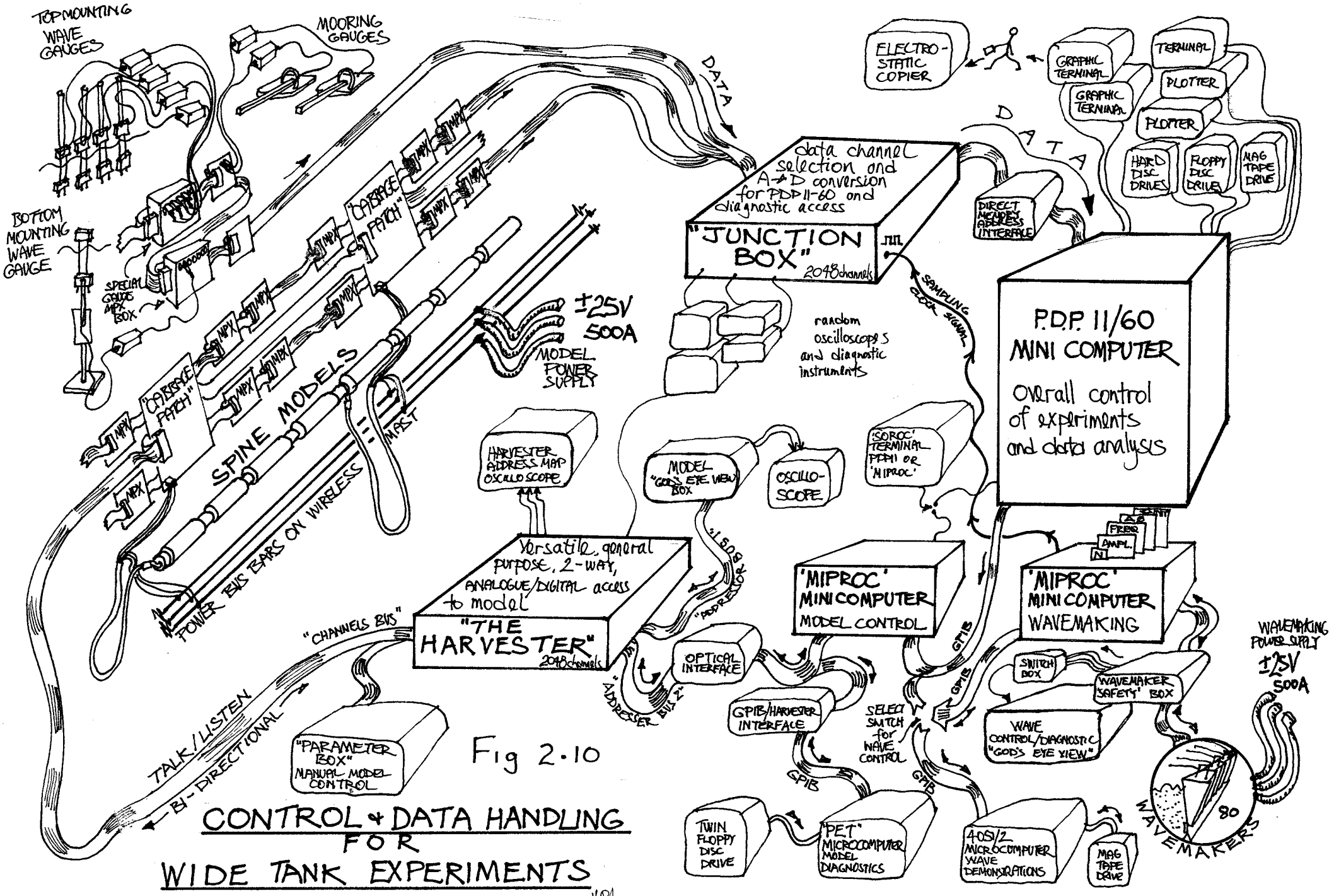

Fig 2.10

CONTROL + DATA HANDLING FOR WIDE TANK EXPERIMENTS

jf84

3.A POX-PLOTS

Introduction

We find visual representations of the sea states very useful both as a check that we are getting the sea that we want and as an aid to understanding test results. We found that the most useful representation is the 'pox-plot'. An example is shown below. Each individual pox-plot identifies, with a dot or cross, the period and angle of the component wavefronts making up a sea state. The number of wavefronts is limited to 75 by the current wavemaker-controlling computer. Angle is shown as the horizontal variable, usually scaled between -70 and +70 degrees, with period increasing from 0 to 2.0 seconds vertically. A separate diagram on each page of pox-plots shows the scaling in use.

Information about wave height is not displayed graphically, but as a single value of Hrms (in centimetres) below and to the left of each plot. This is the mean of several measurements made at different times during the course of the experiments. We use a row of sixteen conductivity-corrected wave gauges placed 2 metres in front of the wavemakers.

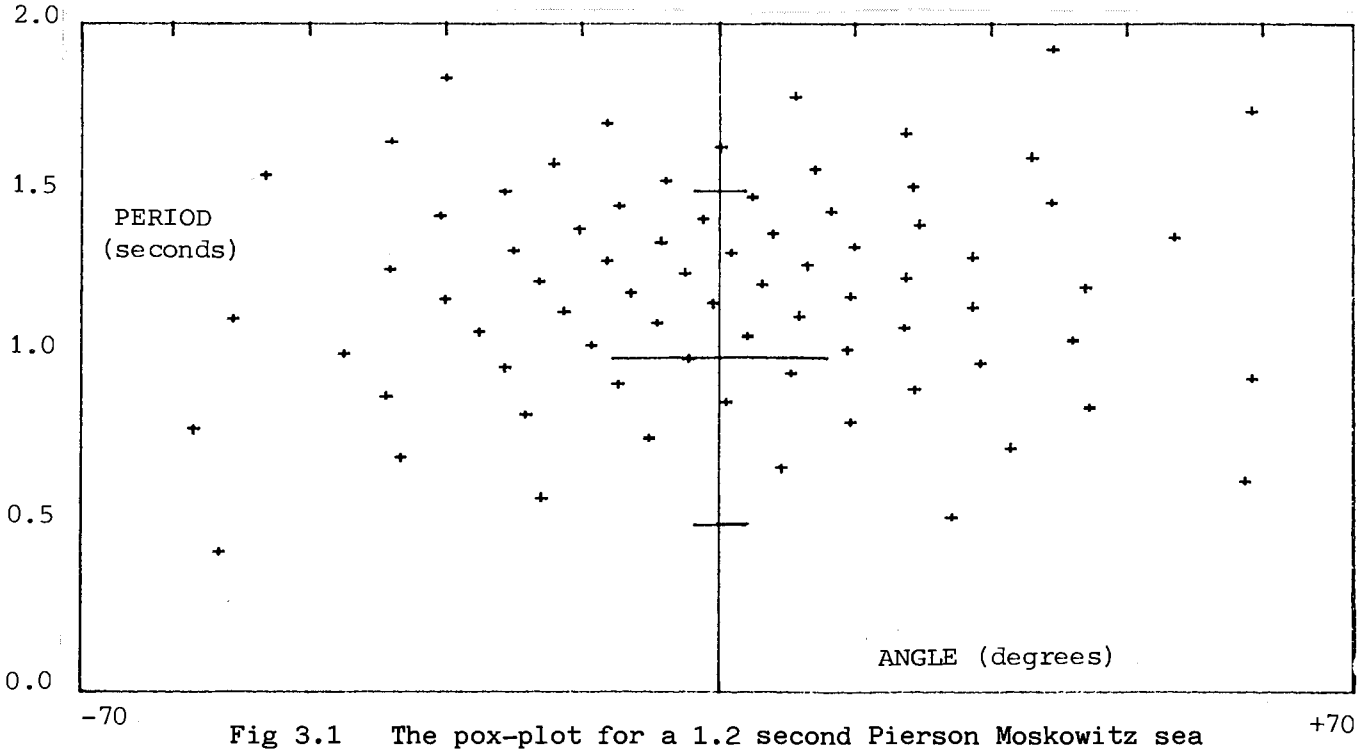

Fig 3.1 The pox-plot for a 1.2 second Pierson Moskowitz sea with a Mitsuyasu spread.

(3.A cont)

In this section we include diagrams of every sea used in the experiments. The pox-plots are produced by reading back tank data files normally sent to the wave-making computer, and then performing a 'reverse tank transfer function' to convert back to amplitudes, periods and angles. On more than one occasion this process has uncovered faults in our tank software.

We lay out pox-plots in 2-dimensional arrays to match test results given in other sections. Where appropriate, rows and columns of the array are assigned particular values of a sea constant such as energy period or Hrms, which varies vertically or horizontally. The names of these variables are then printed with a large set of cross-arrows at the top left of the page. In the case of the South Uist spectra the Institute of Oceanographic Science reference number is placed at the bottom right of each plot.

The lack of height information about individual wavefronts is not a drawback with single-component monochromatic seas, or with our standard Pierson-Moskowitz spectra, which comprise equal amplitude 'teeth', each representing a wavefront of identical energy.[1] The South Uist seas, however, are made up by combining up to 3 separate 'sub-seas' (see section 6.G), each of which has its own fixed tooth size, so dots may represent wavefronts of slightly differing heights.

1 In fact at low frequencies the heights of wavefronts are adjusted slightly to maintain constant energy in finite tank-depth (see section 6.B).

(3.A cont)

Sea Set: PM 'm' 'Scatter Diagram Explorer' Graph 3.2

This is a basic set of Pierson-Moskowitz spectra with energy period and Hrms varying independently. We use a modification of the standard PM spectrum as described in our 4th year report, (see ref b, page 6.9).

The directional spread is based on the Mitsuyasu formula discussed in ref b, page 6.10.

We limited the spectral frequencies to the range 0.5 to 3.0 Hz, corresponding to periods of 0.33 to 2.0 seconds. The noticeable similarity between the patterns of dots shows that the same random number seed was used throughout to initiate the choice of angles.

For a standard Pierson-Moskowitz spectrum the theoretical value of Hrms is related to energy period by:

$$\text{Hrms (cm)} = 1.361\ Te^2$$

Wavemaking geometry sets limits on the range of wavefront frequencies and angles (section 6.D), so the realisable Hrms is reduced. The amount of this reduction clearly depends on the energy period and the directional spread of each spectrum. The seas here all have Mitsuyasu spread with mean direction of zero degrees, so the reduction in Hrms due to angular limits is low and virtually constant at 1.5%. The tank frequency limits have varying effects. Hrms is reduced by only 0.5% at an energy period of 1 second, but this increases to a maximum of 3% at 1.4 seconds. The combined effect is to reduce the realisable Hrms values from 2% to 4.5%.

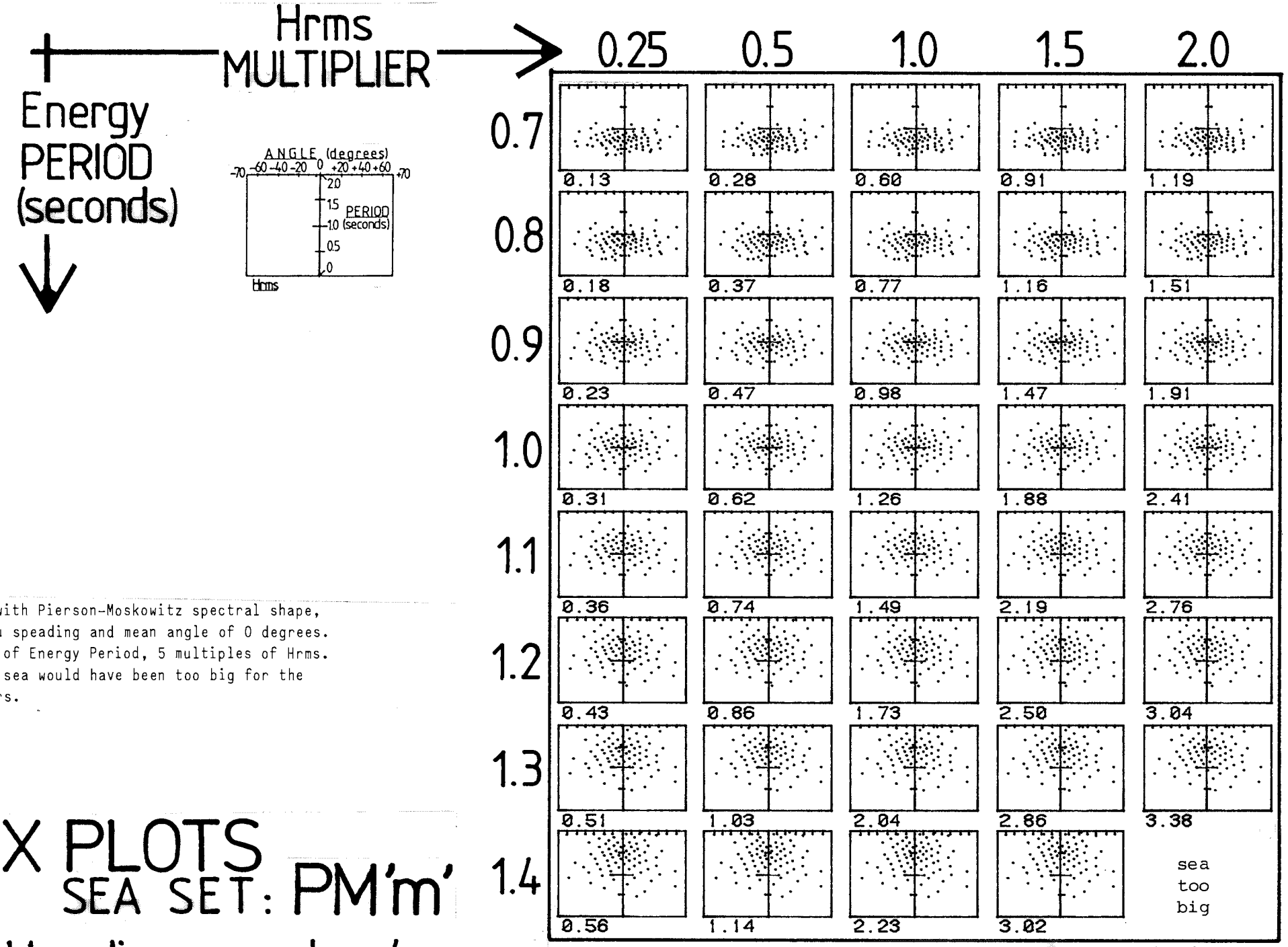

39 seas with Pierson-Moskowitz spectral shape, Mitsuyasu speading and mean angle of 0 degrees. 9 values of Energy Period, 5 multiples of Hrms. The 40th sea would have been too big for the wavemakers.

POX PLOTS
SEA SET: PM'm'
'scatter diagram explorer'

"[300,325] PMmnM. TNK"

GRAPH 3.2

(3.A cont)

However our measured Hrms values are up to 10% lower than these corrected theoretical values. The most likely cause is the reduction that we make in wavemaker drive command signals as wavefront angle increases. This is part of the wide tank 'transfer function'. We multiply by the square root of the cosine of the wavefront angle. A quick test confirms that this is too severe a correction for angles greater than about 40°, so that wavefronts near the sides of the plots are being over-attenuated.

All test results in this report use actual measured values so that deviations from our initial tank transfer function do not affect conclusions. We hope to produce an improved multi-parameter transfer function for further reports.

Graph 3.3 shows the Hrms and Te test points superimposed on a South Uist scatter diagram. Lines of constant power density have been added.

These seas were used for the scatter diagram exploring experiments in section 4.A. The 1.0 second sea with nominal Hrms of 1.36 cm was used for the stiffness variation experiments in section 4.B.

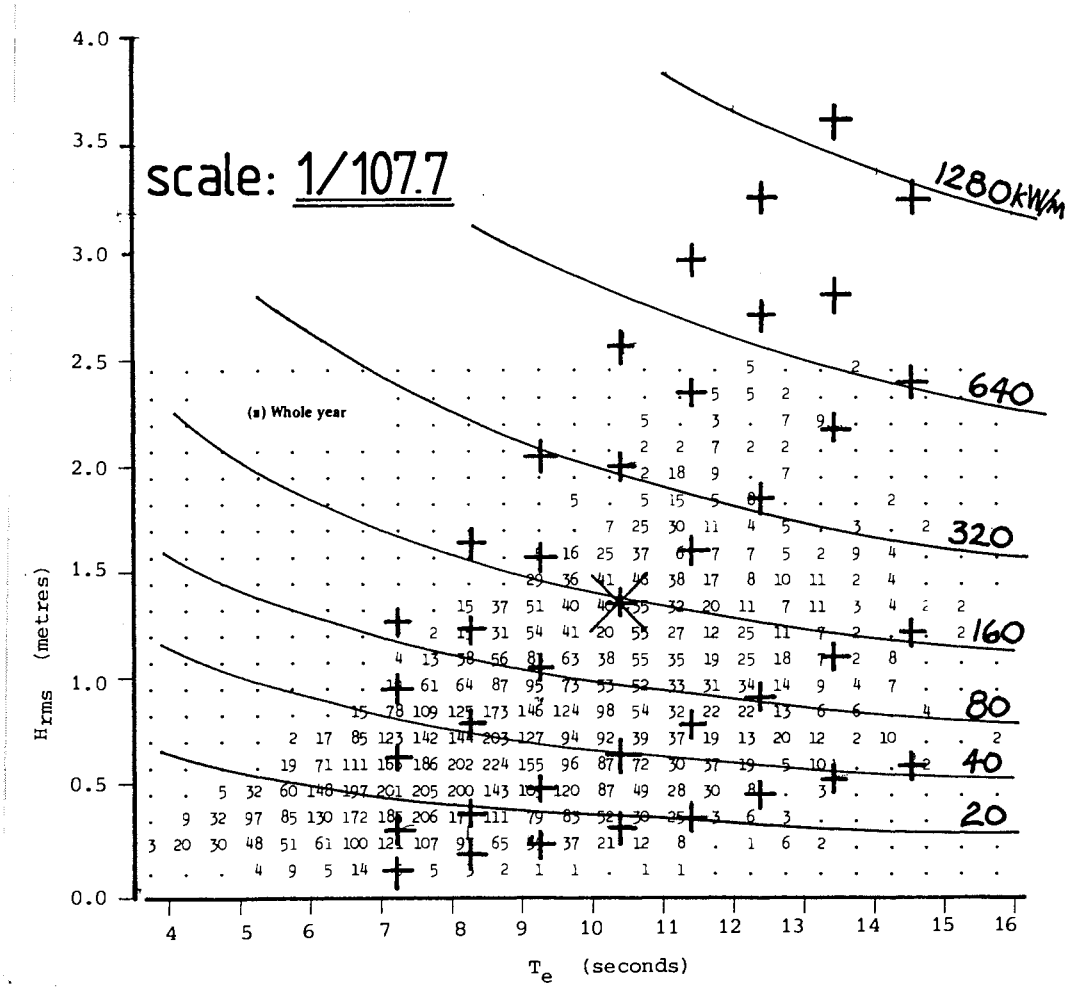

GRAPH 3.3 Whole Year South Uist scatter diagram, with 'Scatter Diagram Explorer' sea-set superimposed. scale:1/107.7

(3.A cont)

Sea Set PM 'a' Graph 3.4

These are standard Pierson-Moscowitz seas with Mitsuyasu spreading.

We wanted to investigate the effect of angled seas, and to check tank angular symmetry. The wavefront angles are biased positively and negatively.

Energy period varies vertically with a higher maximum value than in the previous set.

The expected Hrms losses due to frequency clipping range from 0.4% at an energy period of 1.0 seconds, to 9.3% at 1.6 seconds. The expected losses due to angular clipping average about 1.3% for the 0° offset seas, and about 7% for the 40° seas. The combined effects range from a total expected Hrms loss of 2% at 1 second and 0°, to 15% at 1.6 seconds and 40°.

Measured Hrms values are lower than these expectations by an average of 7%, the errors being worst at 1.4 and 1.6 seconds, and at 40° offset.

These seas were used for the experiments of section 4.C.

POX PLOTS
SEA SET: PM'a'

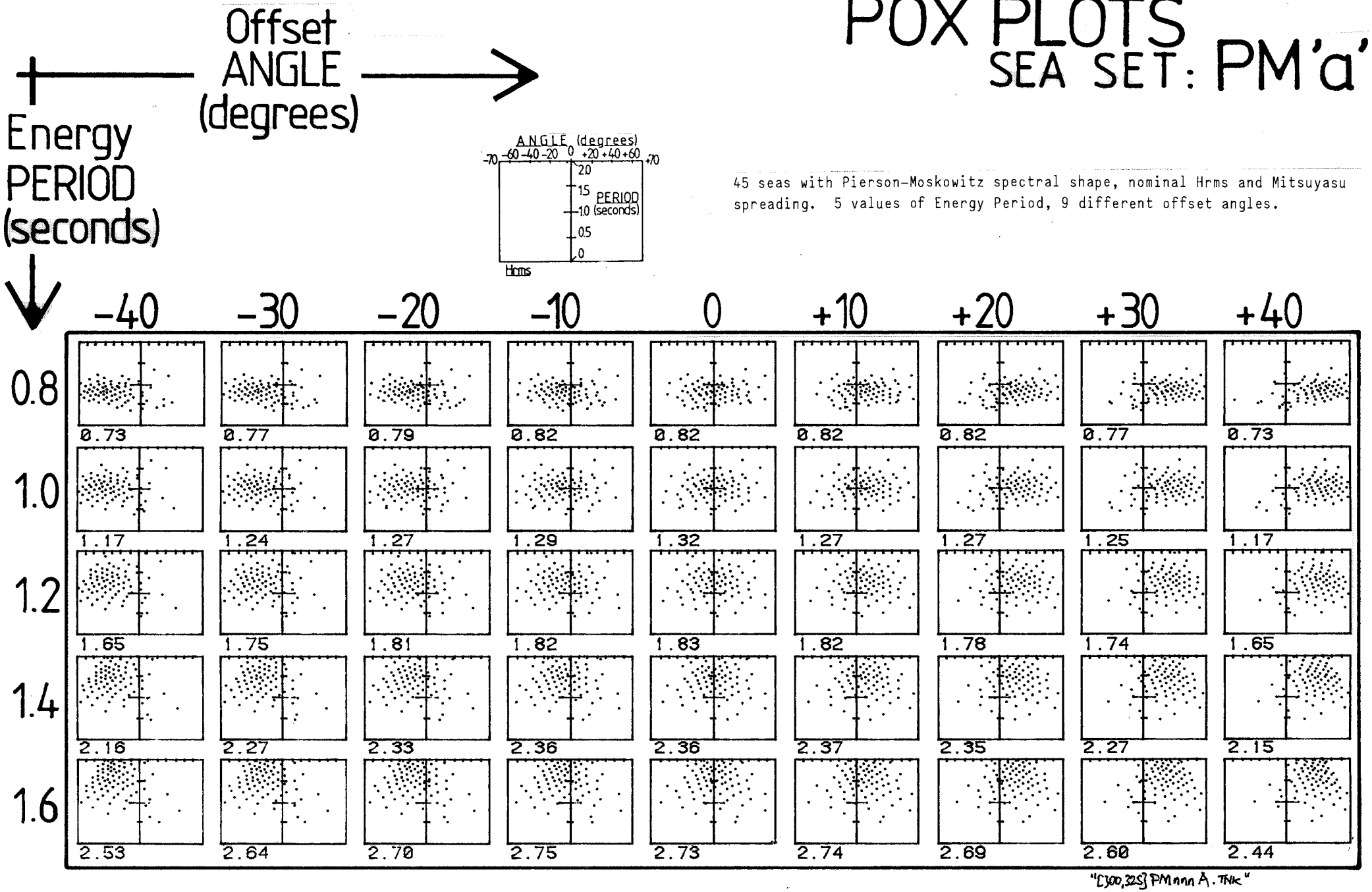

45 seas with Pierson-Moskowitz spectral shape, nominal Hrms and Mitsuyasu spreading. 5 values of Energy Period, 9 different offset angles.

"[300,325]PMnnnA.TNK"

GRAPH 3.4

(3.A cont)

Sea Set CO 'a' Graph 3.5

These are Pierson-Moskowitz spectra again, but spreading is according to the $\cos^s$ model. We varied **s** from 2 to 10,000. (This is deemed to be within a few percent of infinity!) Offset angle is also varied again but this time only in a positive sense, away from the glass.

Nominal Hrms for a 1 second Pierson-Moskowitz sea is 1.36 cm. The expected loss due to frequency clipping is constant throughout this set, at 0.4%. Angular clipping is most severe for the widely spread seas and for those with large angular offsets. Even at 0° offset, Hrms will be reduced by 8% for a spread exponent of 2 and at 50° offset this increases to 16%.

For the first time, many of the seas in this set have measured Hrms values greater than expected, and in many cases greater than the nominal value. For instance, Hrms for the bottom left sea is 10% higher and the effect is clearly related to angular spread and mean angle.

In the 'infinity' row some of the upper wavefronts are seen breaking away from the line. This is the result of an insufficiently subtle shallow-water correction. The symptoms are hard to see in the actual tank sea, even to a well-briefed observer.

Occasional wavefronts seen wandering well away from the herd, near the bottom right of the plots, are symptoms of the 'tank limits' problem discussed in section 6.D, and are illustrated more clearly in the additional set of pox-plots in section 3.B.

These seas were used for the experiments described in section 4.D.

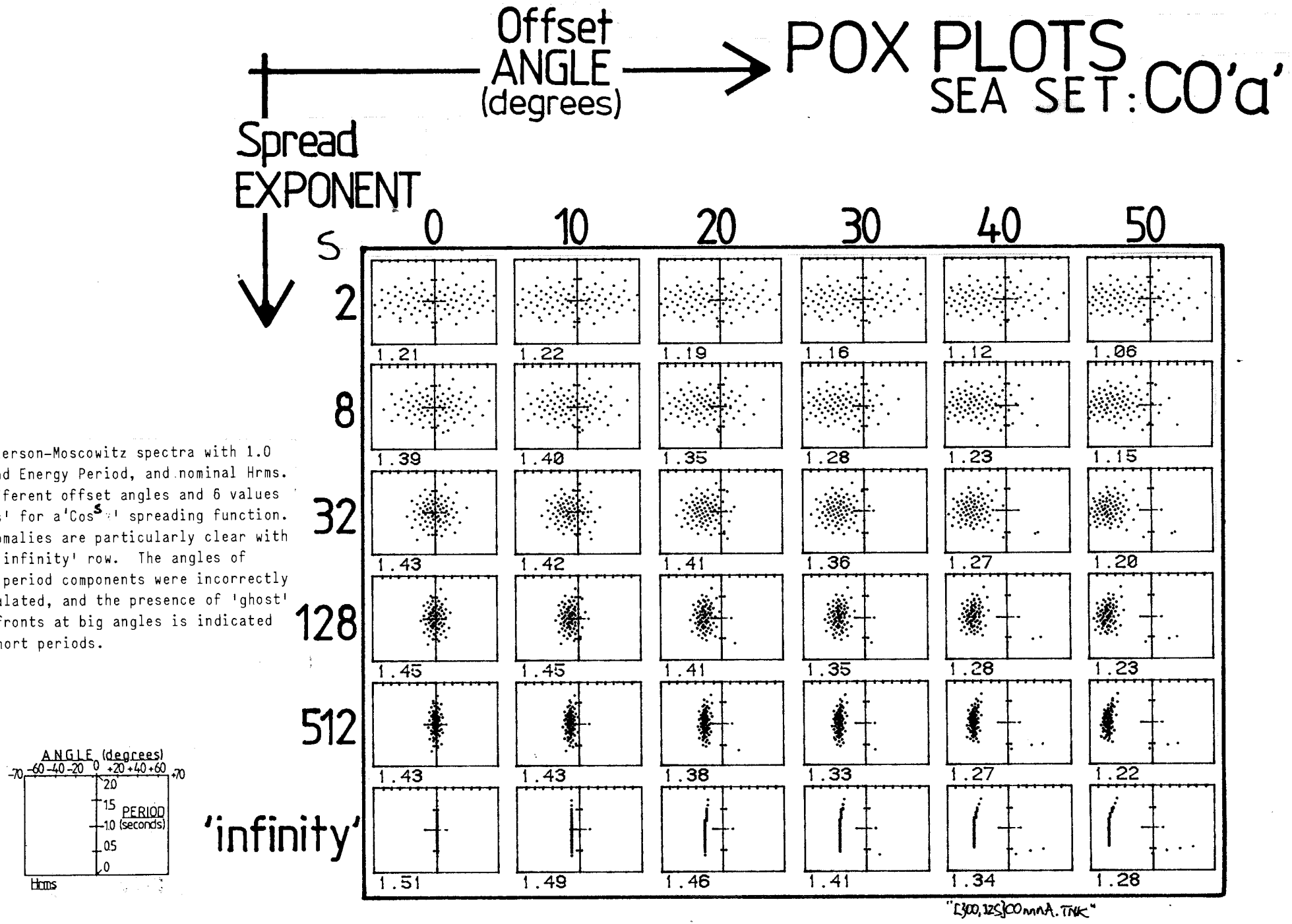

36 Pierson-Moscowitz spectra with 1.0 second Energy Period, and nominal Hrms. 6 different offset angles and 6 values of 's' for a 'Cos^s' spreading function. 2 anomalies are particularly clear with the 'infinity' row. The angles of long period components were incorrectly calculated, and the presence of 'ghost' wavefronts at big angles is indicated at short periods.

GRAPH 3.5

(3.A cont)

Sea Sets: South Uist 'su' 'a', 'b', 'c' & 'd' Graphs 3.6 - 3.9

The South Uist seas make much more interesting pox-plots. Our tank implementation of the Institute of Oceanographic Science (IOS) data is described in section 6.H.

An additional image on each page depicts our tank and model in their working relationships to the compass.

Components in the right half of each plot represent wavefronts approaching from the south of the mean direction, and those to the left approach from north of the mean direction.

The separate wind, swell and old wind components are often clearly visible. Swell is usually in the upper part of the plot and tightly bunched in spread. The width of spread indicates the size and distance of the originating weather. Wind sea is usually at lower frequencies near the bottom of the plots, and well spread. The effect of the spectral width parameter in compressing the frequency range of wavefronts is also often clear.

Sea number 223A (graph 3.6) has only a single component from a well-defined and small swell source. Sea 371A (graph 3.6) has a wide swell source to the north and its 'wind' and 'old wind' components are not superimposed on the pox-plot.

Measured Hrms values for a scale of 107.7 are given in centimetres at the bottom left of each plot. They generally increase with sea number.

Although 13 of the 46 spectra are not very accurately represented by the 'a' version (graph 3.6) we used them for most of our experiments. There are enough variations in this one group to test out any bending moment theories and model deployment is very much easier when parallel to the wavemakers.

the 46 SPECTRA 'a' set

IOS data adjusted for 100m water depth and rescaled at 1/108

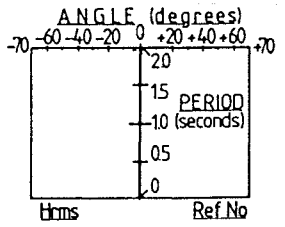

POX PLOTS SEA SET: SU 'a'

The '46 spectra', based on buoy data off the coast of South Uist, with directions synthesised from wind records. The 46 are selected to be representative of all seasons, but their weightings are not equal. For the 'a' set, the normal to the wavemaker axis represents a compass bearing of 260 degrees with the model parallel to the wavemakers. 13 of the 46 spectra are poorly represented by the 'a' version, and the 'b' or 'c' version is a closer match.

Nominal Westerly seas

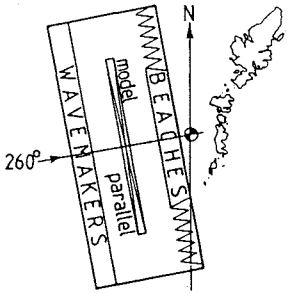

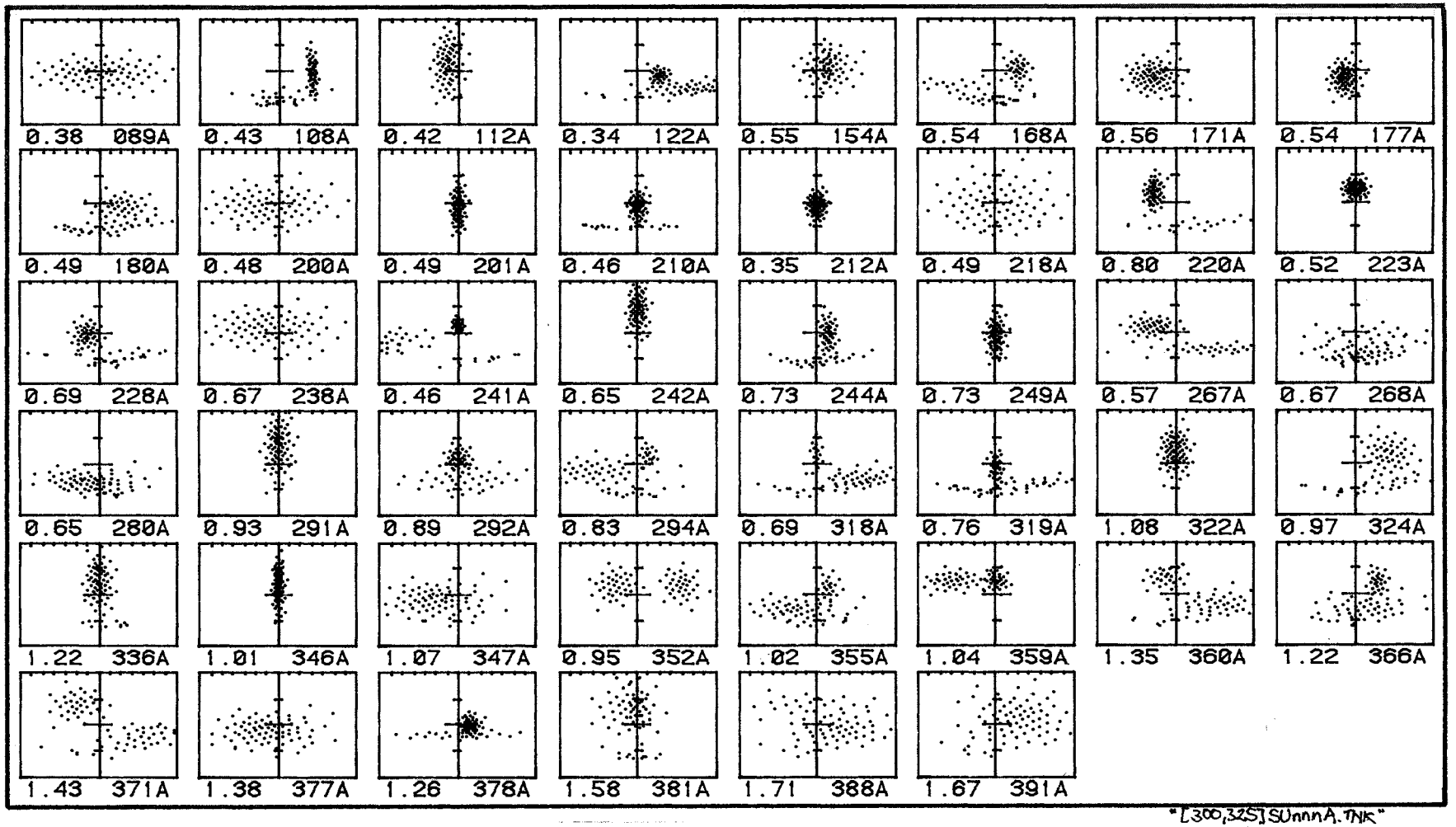

"[300,325]SUnnnA.TNK"

GRAPH 3.6

(3.A cont)

The 'b' set (graph 3.7) provide improved versions of those seas which have strong southerly components. The model is rotated clockwise 40 degrees and the tank mean heading shifts to 220°. It is interesting to compare the 'a' and 'b' version of the same sea. The swell components clearly shift left and the number of wavefronts allocated to them are reduced, as the new orientation allows wind sea components to be realised within the wavemaker angular range.

The 'c' set (graph 3.8) provide improved versions of those seas which have strong northerly components. The mean wave direction represents a compass bearing of 310 degrees. Swell now moves to the right compared with the 'a' set.

It is not very convenient to yaw the model clockwise for the 'b' set and then anti-clockwise for the 'c' set. In practice we use the 'd' set to implement a mirror image of the 'c' set. The model need only be yawed another 10° clockwise from the position for the 'b' set. The Hebrides look strange that way round, but it makes little difference to our bending moment tests.

The South Uist seas were used for the experiments described in sections 4.E to 4.H, and 4.L to 4.M.

POX PLOTS
SEA SET: SU 'b'

the 46 SPECTRA 'b' set

IOS data adjusted for 100m water depth and rescaled at 1/108

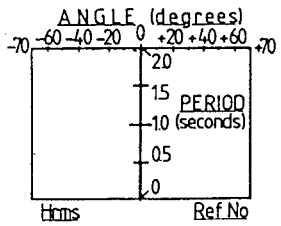

9 of the 46 spectra which are porly represented by the 'a' set. For these, the normal to the wavemaker axis represents a compass bearing of 220 degrees when the model is set at an angle of 40 degrees to the wavemaker.

Southerly seas

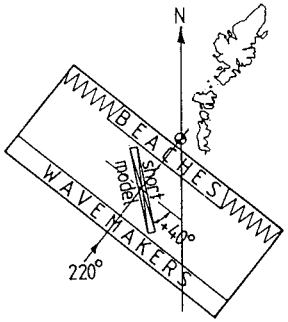

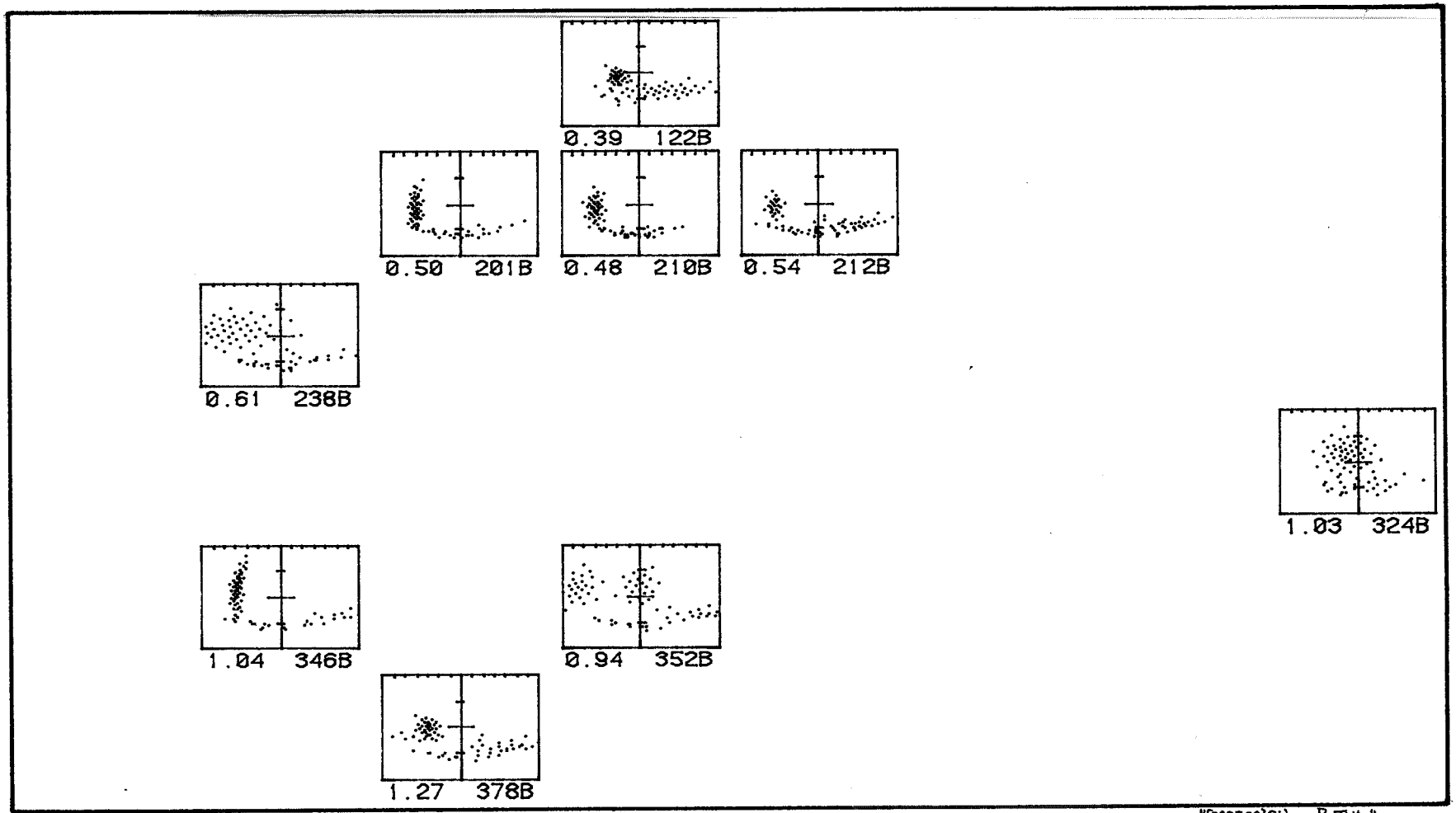

"[300,325]SUnnn B.TNC"

GRAPH 3.7

the 46 SPECTRA 'c' set

IOS data adjusted for 100m water depth and rescaled at 1/108

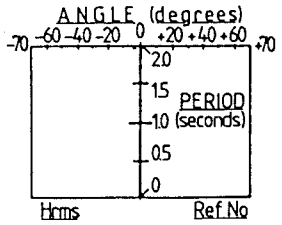

POX PLOTS SEA SET: SU 'c'

4 of the 46 spectra which are inadequately represented by the 'a' set. For these the normal to the wavemaker axis represents a compass bearing of 310 degrees when the model is set at an angle of -50 degrees to the wavemakers. Even so, a considerable proportion of the spectral energy is lost.

Northerly seas

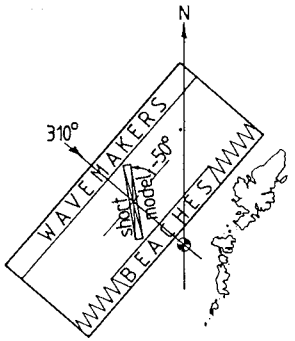

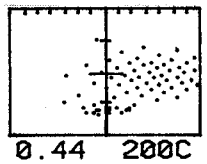

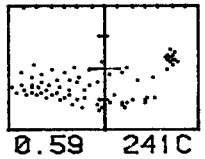

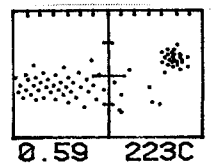

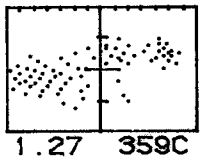

"[300,325]SUnnnC.TNK"

GRAPH 3.8

the 46 SPECTRA 'd' set

IOS data adjusted for 100m water depth and rescaled at 1/108

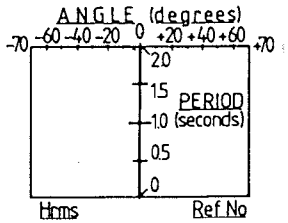

POX PLOTS SEA SET: SU 'd'

The mirror image of the 'c' set. The polarity of all wave angles is inverted, so that the model can be used at an angle of +50 degrees to the wavemakers.

mirrored Northerly seas

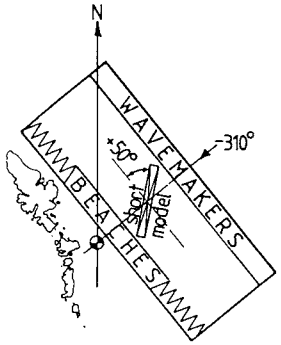

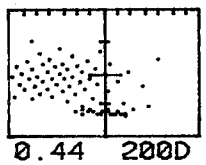

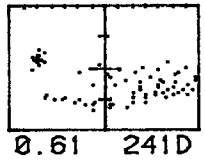

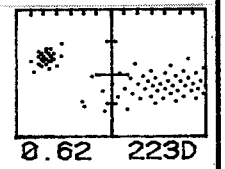

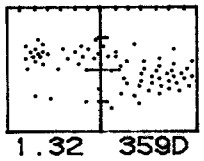

"[300,325] SU nan D. TMK"

GRAPH 3.9

(3.A cont)

Sea Sets: MO 'a', 'b' & 'c' Graphs 3.10 - 3.12

Regular seas do not make very interesting pox-plots.

We increased the angular limit of the tank to 80° for these waves. The nominal Hrms is 1.414cm for the 'a' set, and 1.0cm for the 'b' and 'c' sets.

In all 3 sets, the vertical variable is energy period with a range of 0.8 to 1.6 seconds in 5 steps.

'a' set: (graph 3.10)

The nominal crest angle varies from -10° to -80°. At long periods and extreme angles (bottom right corner) the actual angles produced in the tank are visibly lower than their nominal values. This was the first indication of a faulty shallow water correction in our sea-generating software. The effect is also clearly visible in Graph 3.5.

These seas were used for the experiments in section 4.I.

'b' set: (graph 3.11)

The crest length is varied from 2 to 12 metres in 2 metre steps.

These seas were used for the experiments in section 4.J.

'c' set: (graph 3.12)

In addition to angle and crest length we discovered that it was useful to describe wavefronts in terms of the velocity of movement of the crest along the spine. The crest velocity is varied from 2 to 8 metres per second.

These seas were used for the experiments in section 4.K and 4.L.

40 monochromatic seas giving known crest angles at various periods, with nominal Hrms of 1.414cm. The angular limits of the wavemakers were increased to 80 degrees from the normal value of 70 degrees. The fall off in measured Hrms values at large angles shows incorrect amplitude compensation in the tank transfer function.

POX PLOTS
SEA SET: MO'a'
(monochromatic)

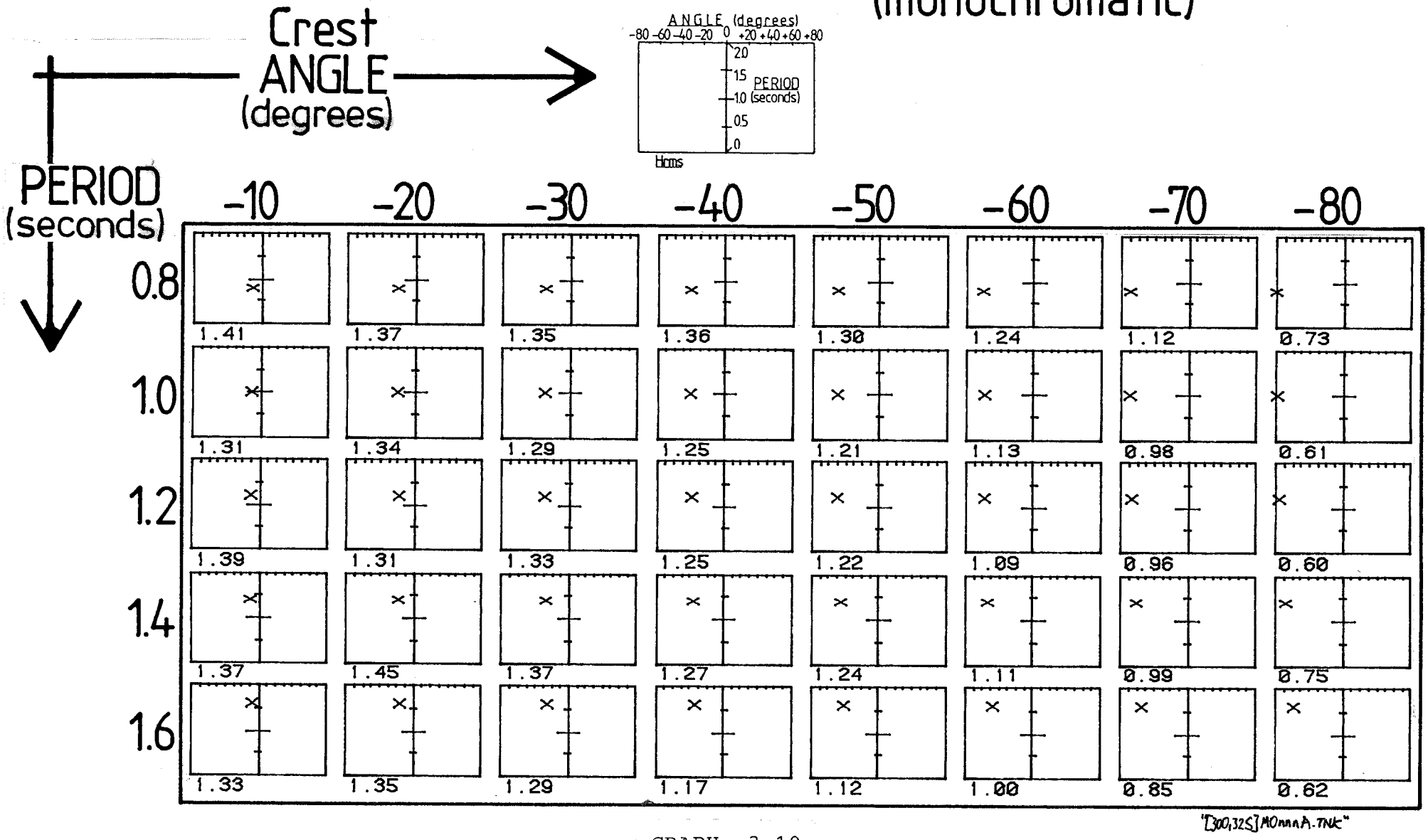

"[300,325]MOnnA.TNK"

GRAPH 3.10

37 monochromatic seas giving known crest lengths at various periods, with nominal Hrms of 1.0cm. The wavemaking angular limits were increased to 80 degrees, but 3 seas were still unrealisable at 2 metres. Hrms for the 4 metre sea at 1.2 seconds was inadvertently doubled. The fall off in measured Hrms values at large angles shows incorrect amplitude compensation in the tank transfer function.

POX PLOTS
SEA SET: MO"b"
(monochromatic)

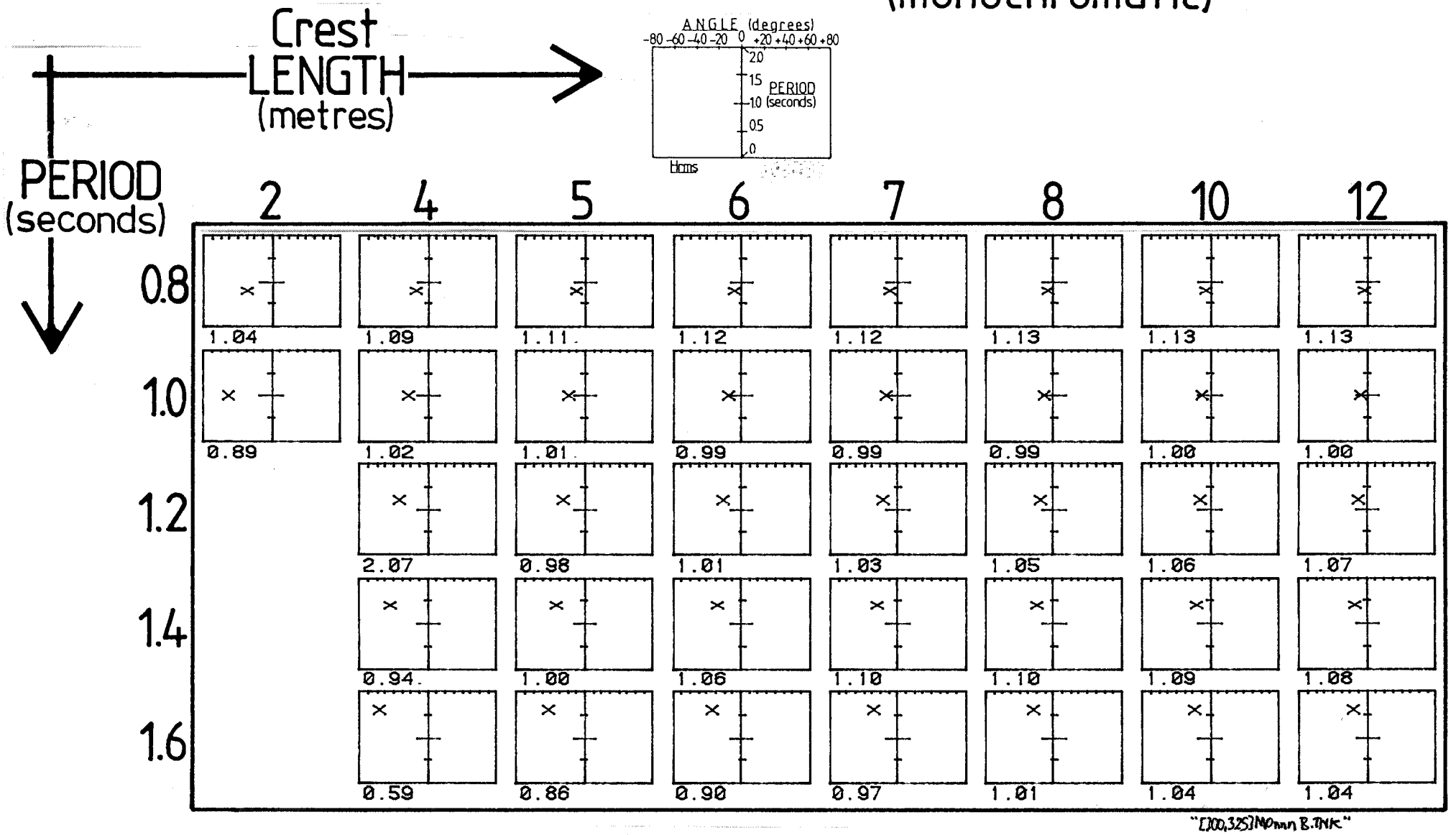

"[100,325]MOmm B.TNK"

GRAPH 3.11

33 monochromatic seas giving known crest velocities at various periods, with nominal Hrms of 1 cm. The wavemaking angular limits were increased to 80 degrees, but 2 seas were still unrealisable at 2 metres/sec. The fall off in measured Hrms values at large angles shows incorrect amplitude compensation in the tank transfer function.

POX PLOTS
SEA SET: MO'c'
(monochromatic)

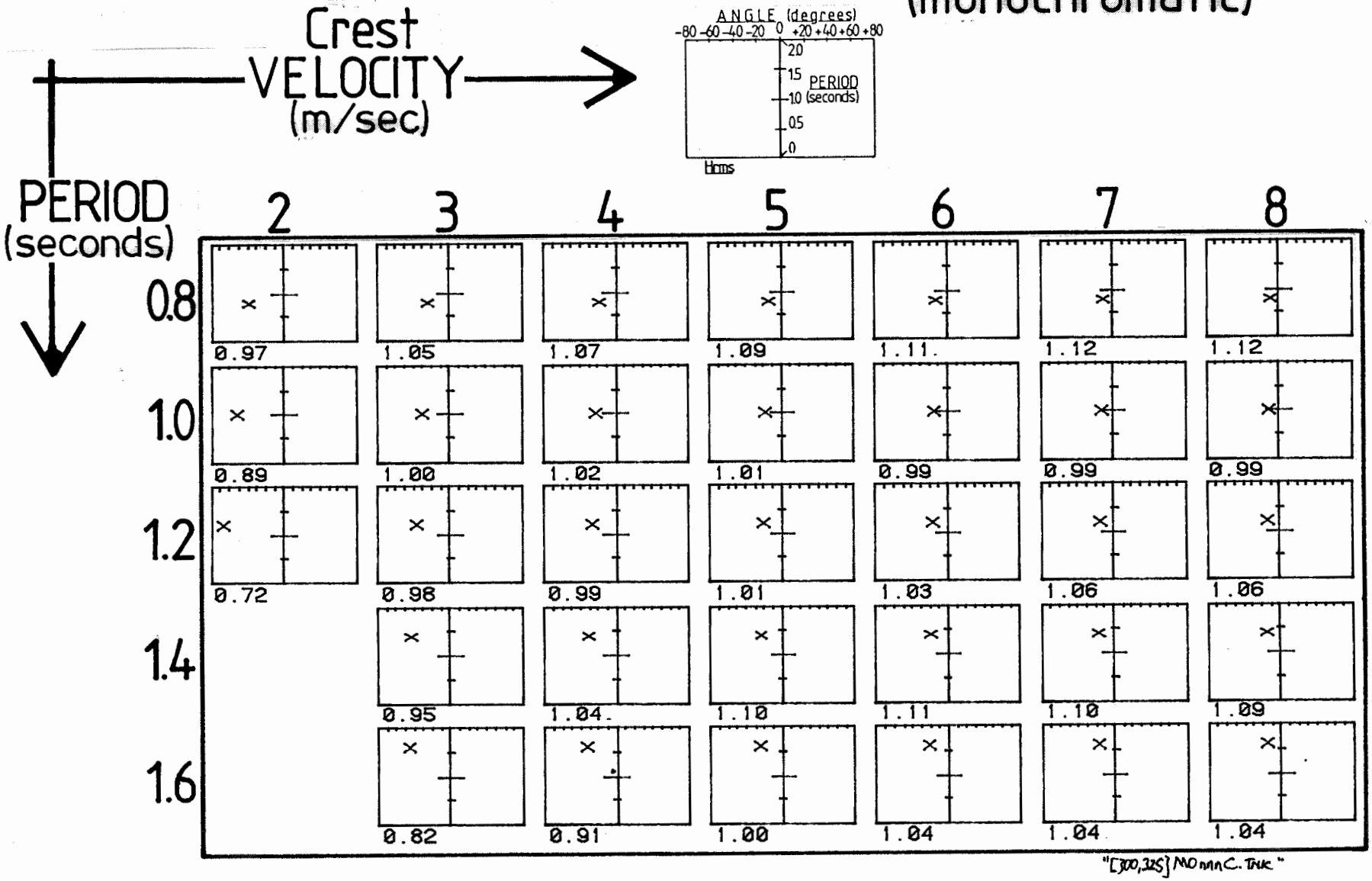

GRAPH 3.12

3.B POX-PLOTS WITH GHOST WAVEFRONTS Graphs 3.13 - 3.19

The restrictions on frequencies and angles due to the finite width of wavemakers are discussed in section 6.D.

An absolute upper tank limit exists at 2.26 hz, the frequency at which the wavelength is equal to wavemaker pitch. Between 1.6 hz and 2.26 hz the maximum permissible wavefront angle drops steadily from ±90° to 0°. Wavefronts transgressing this envelope acquire one or more 'ghost siblings' at the same frequency but at a different angle. Below 1.6 hz the theoretical angular limit is over 90°. Below 0.5 hz the wavemakers have too little displacement to work effectively. We have not yet made any measurements of the unwanted wavefronts but their amplitudes are visibly of the same order as the principal wavefront.

These modified pox-plots show the effect on our sea sets of using a simple rectangular limit (±70°, 0.5 - 3.0 hz) when calculating wavefront frequencies and angles. The limit has been over-drawn on each plot as a roughly horizontal line. Any intended wavefront below these lines acquires a ghost. Both wavefront and ghost are drawn as a dot. The number of ghosts is totalled at the top left of each plot. Naturally the effect is most obvious at high frequencies, so that in the scatter diagram set (graph 3.13), the seas at Te = 0.7 seconds have the most ghosts. The effect of angular offsets is to increase marginally the number of ghosts (graphs 3.14 & 3.15). On average the basic westerly set of South Uist spectra have 8 ghosting wavefronts, but this rises to 21 for the southerly set, and 14 for the northerly set (graphs 3.16 - 3.19).

Generally the effect of having too many fronts outside the tank limits is to widen the angular distribution of energy at short periods. Test work in monochromatic seas, (section 4.H, and more recent work still to be reported) suggests that the spine model is comparatively insensitive to short-period, off-axis wavefronts. Our wavemaking software will in future represent only those parts of spectra which fall within the tank limits. An override facility will allow deliberate transgressions.

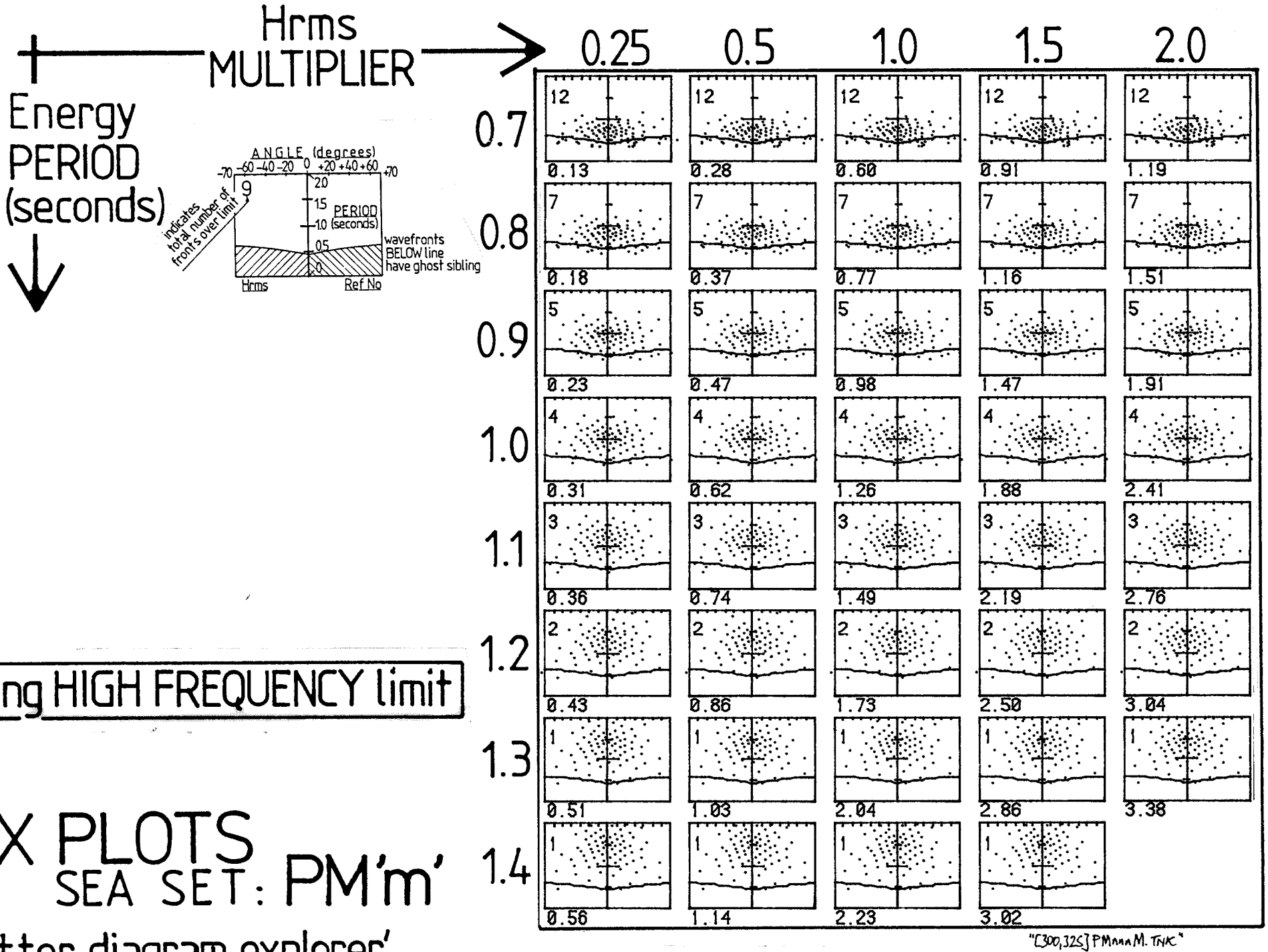

showing HIGH FREQUENCY limit

POX PLOTS
SEA SET: PM'm'

'scatter diagram explorer'

GRAPH 3.13

POX PLOTS
SEA SET: PM'a'

Offset ANGLE (degrees) →

Energy PERIOD (seconds) ↓

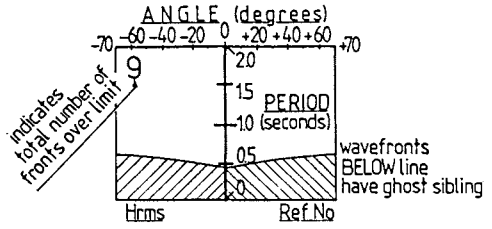

showing HIGH FREQUENCY limit

Energy PERIOD (seconds)	-40	-30	-20	-10	0	+10	+20	+30	+40
0.8	9 / 0.73	9 / 0.77	6 / 0.79	7 / 0.82	7 / 0.82	9 / 0.82	9 / 0.82	9 / 0.77	8 / 0.73
1.0	4 / 1.17	4 / 1.24	4 / 1.27	4 / 1.29	4 / 1.32	3 / 1.27	3 / 1.27	3 / 1.25	3 / 1.17
1.2	1 / 1.65	1 / 1.75	1 / 1.81	1 / 1.82	2 / 1.83	2 / 1.82	2 / 1.78	2 / 1.74	2 / 1.65
1.4	1 / 2.16	1 / 2.27	1 / 2.33	1 / 2.36	1 / 2.36	1 / 2.37	1 / 2.35	1 / 2.27	1 / 2.15
1.6	1 / 2.53	1 / 2.64	1 / 2.70	1 / 2.75	1 / 2.73	1 / 2.74	1 / 2.69	1 / 2.60	1 / 2.44

"[300,325] PMnnn A.TNK"

GRAPH 3.14

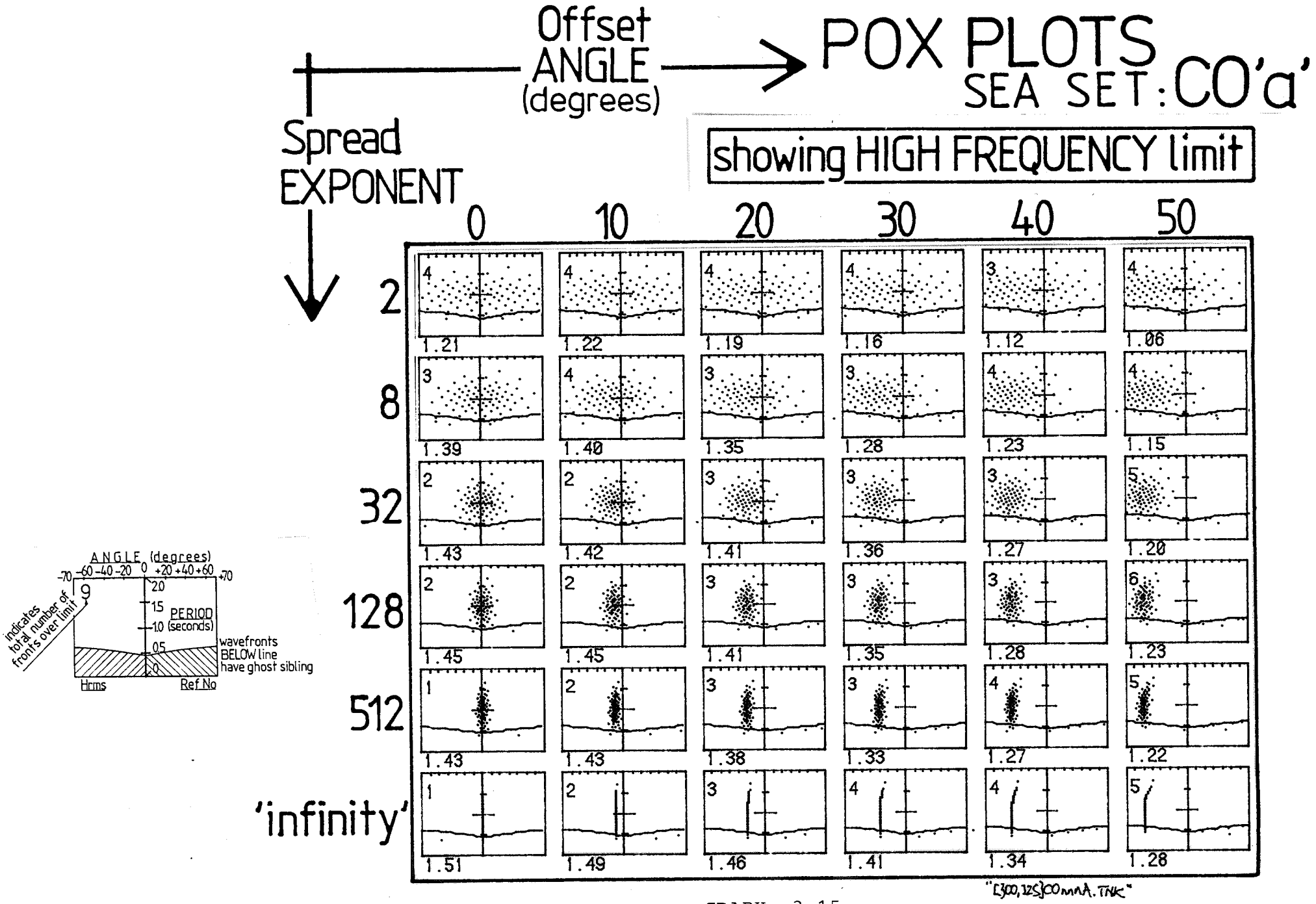
POX PLOTS
SEA SET: CO'a'
showing HIGH FREQUENCY limit
Offset
ANGLE
(degrees)
Spread
EXPONENT
0
10
20
30
40
50
2
8
32
128
512
'infinity'
1.21
1.22
1.19
1.16
1.12
1.06
1.39
1.40
1.35
1.28
1.23
1.15
1.43
1.42
1.41
1.36
1.27
1.20
1.45
1.45
1.41
1.35
1.28
1.23
1.43
1.43
1.38
1.33
1.27
1.22
1.51
1.49
1.46
1.41
1.34
1.28
"[300, 125]00 mnA. TNK"
ANGLE (degrees)
-70 -60 -40 -20 0 +20 +40 +60 +70
PERIOD (seconds)
20
15
10
05
0
Hrms
Ref No
indicates total number of fronts over limit
wavefronts BELOW line have ghost sibling

GRAPH 3.15

the 46 SPECTRA 'a' set

IOS data adjusted for 100m water depth and rescaled at 1/108

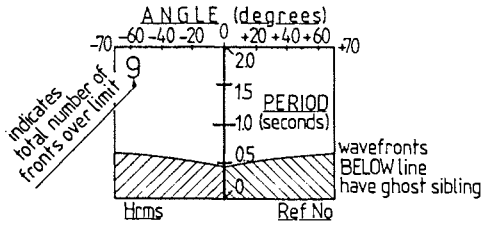

POX PLOTS SEA SET: SU 'a'

showing HIGH FREQUENCY limit

Nominal Westerly seas

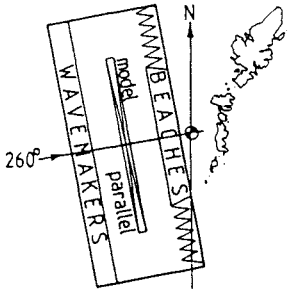

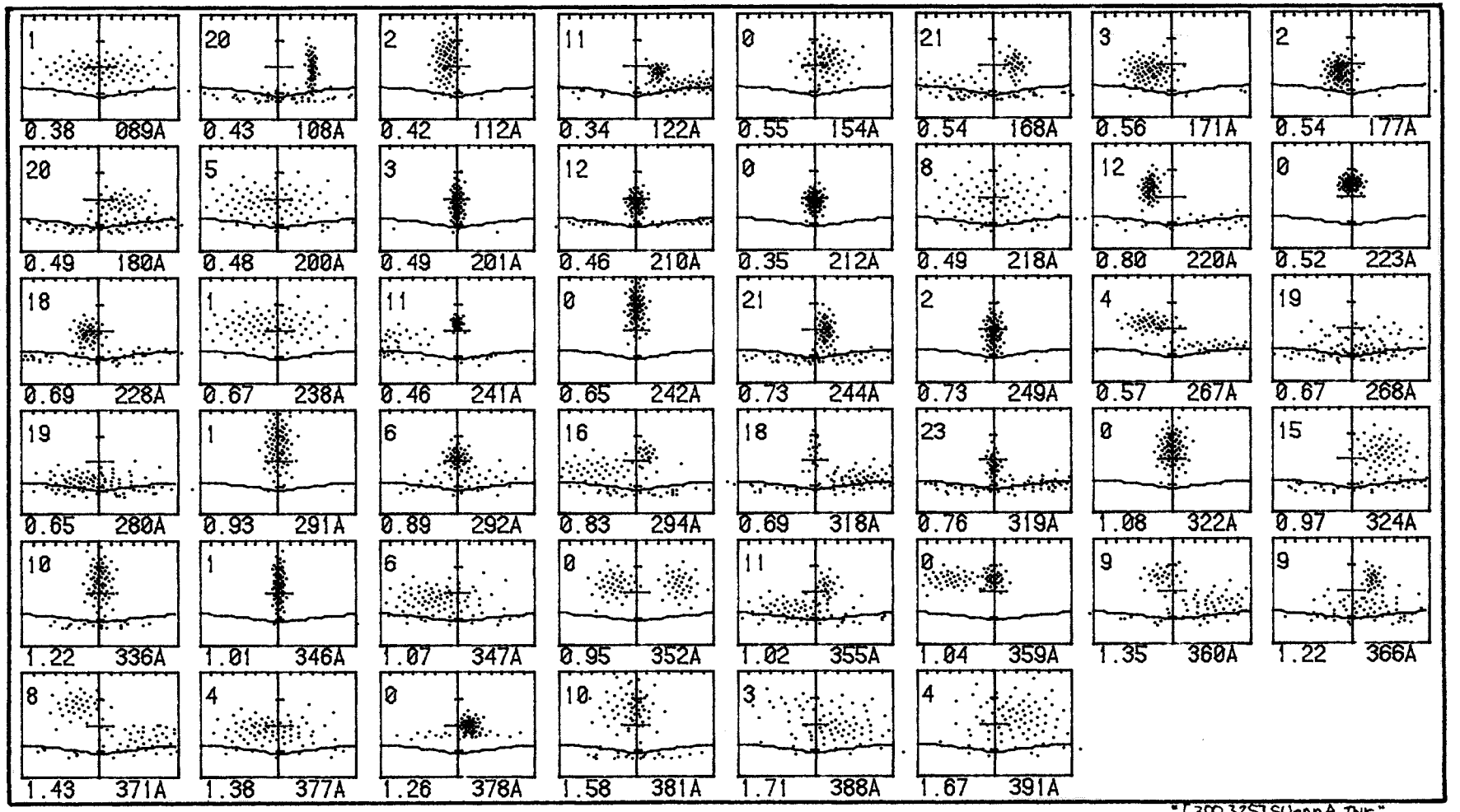

"[300,325]SUnnnA.TNK"

GRAPH 3.16

POX PLOTS
SEA SET: SU 'b'

showing HIGH FREQUENCY limit

the 46 SPECTRA 'b' set

IOS data adjusted for 100m water depth and rescaled at 1/108

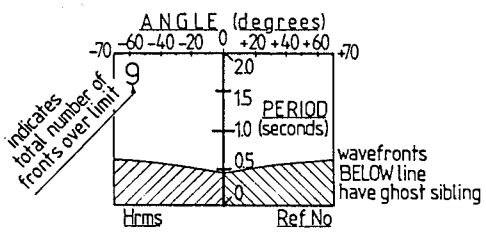

Southerly seas

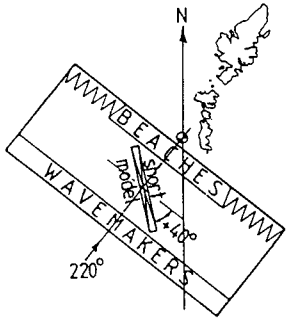

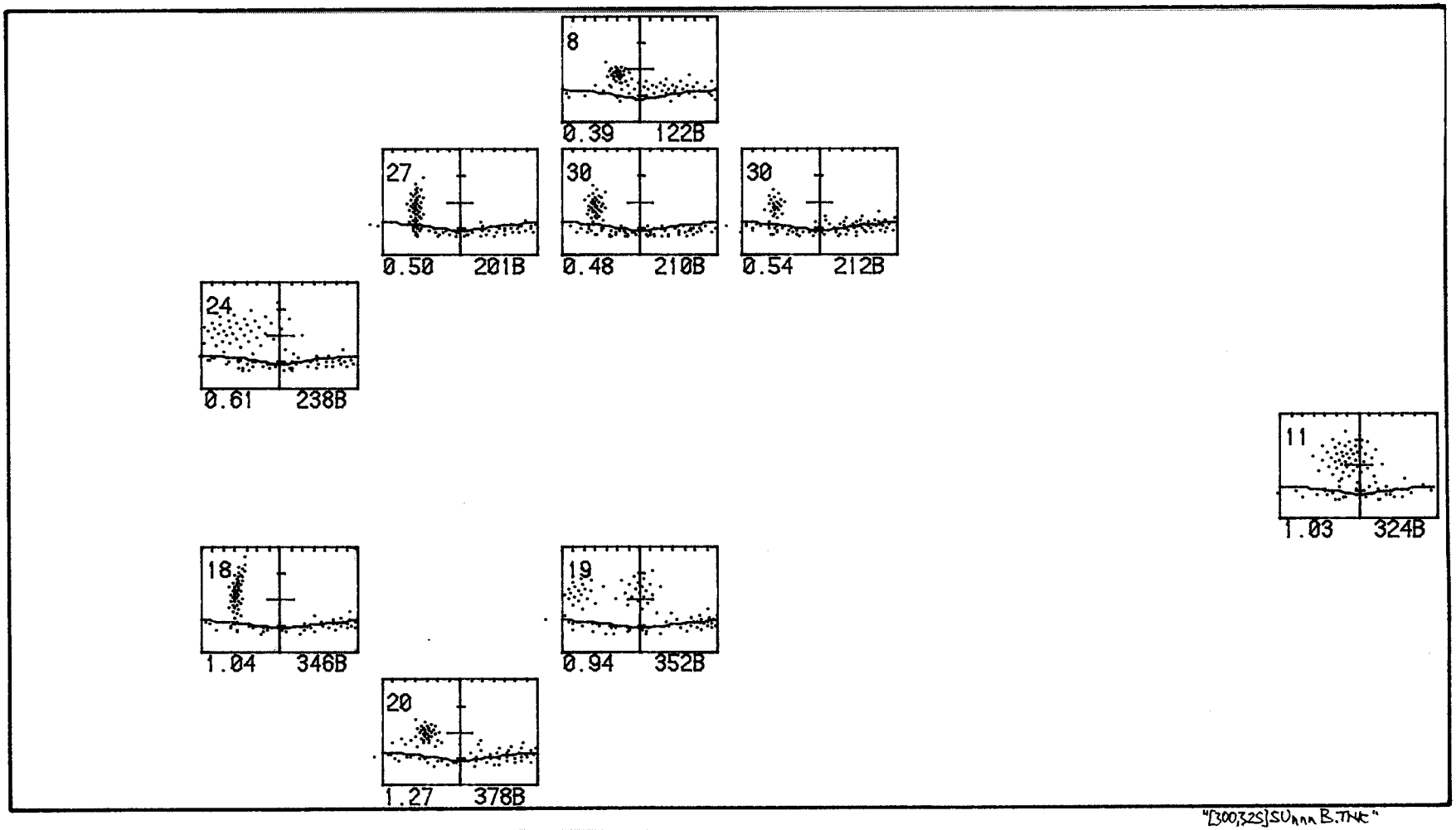

"[300,325]SUnnn B.THC"

GRAPH 3.17

POX PLOTS
SEA SET: SU 'c'

showing HIGH FREQUENCY limit

the 46 SPECTRA 'c' set

IOS data adjusted for 100m water depth and rescaled at 1/108

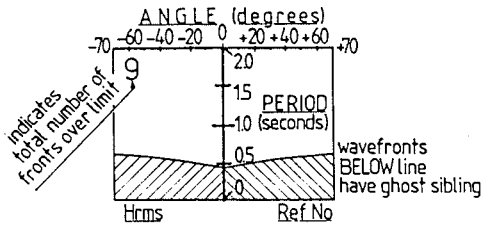

Northerly seas

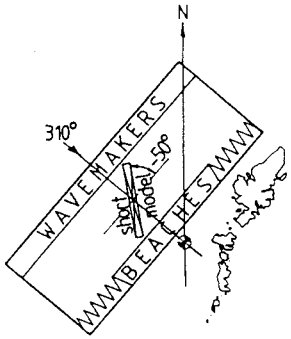

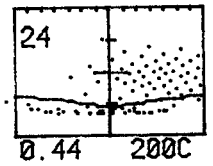

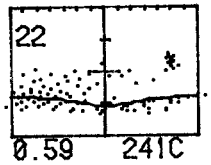

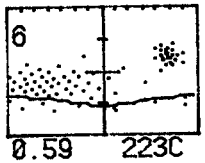

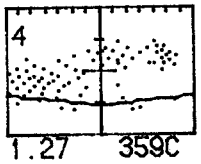

"D00325]SUnnC.TNK"

GRAPH 3.18

POX PLOTS
SEA SET: SU 'd'

showing HIGH FREQUENCY limit

the 46 SPECTRA 'd' set

mirrored Northerly seas

IOS data adjusted for 100m water depth and rescaled at 1/108

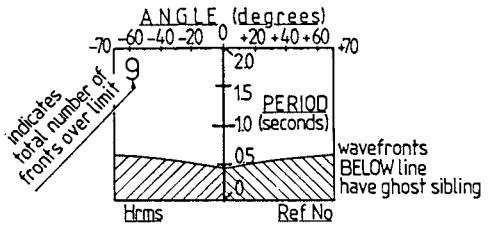

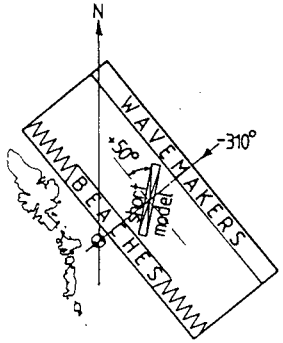

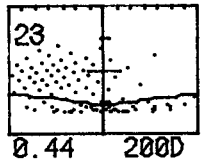

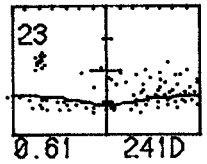

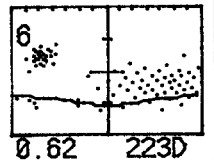

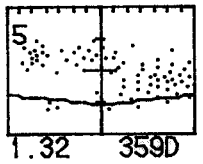

"[309,325] SU wave D. TRUC"

GRAPH 3.19

3.C 3D WAVE PLOTS

Introduction

3D plots add another dimension to pox-plots. They give a better impression of the overall size of seas, but they have lower resolution on the period/angle plane.

We include two separate groups of 3D plots:

In the 1st group - graphs 3.20 to 3.26 - the height of plot is proportional to wavefront amplitudes:

In the 2nd group - graphs 3.27 to 3.32 - the volume under the plot is proportional to total power in sea.

The layout of each page of 3D plots matches the corresponding page of pox-plots and bending moment test results. The range of periods and angles are the same. The vertical scales are unique to each page, so height comparisons between pages should not be made.

The nodes of each 3D plot form the bins of a 2-dimensional histogram. Each wavefront allocates scores to the bins in its vicinity according to a smoothing function.

The number of period and angle increments depends on the thickness of our plotter pens. We increase the resolution for the variable spread set in graph 3.22 by plotting at a larger scale and then reducing the whole page on a copier.

The Pierson-Moskowitz/Mitsuyasu spectra in graphs 3.20 & 3.21 are delightfully smooth. The cut-off enforced by the limited angular range of the tank is apparent on the right edge of many spectra.

We increased the period and angle resolution to try to show the dramatic change in angular distribution in graph 3.22. Ghost wavefronts show up as detached outcrops in the plots at the lower left.

Swell components show up clearly in the South Uist sets (graphs 3.23 - 3.26) but it is quite difficult to separate wind sea and old-wind sea components.

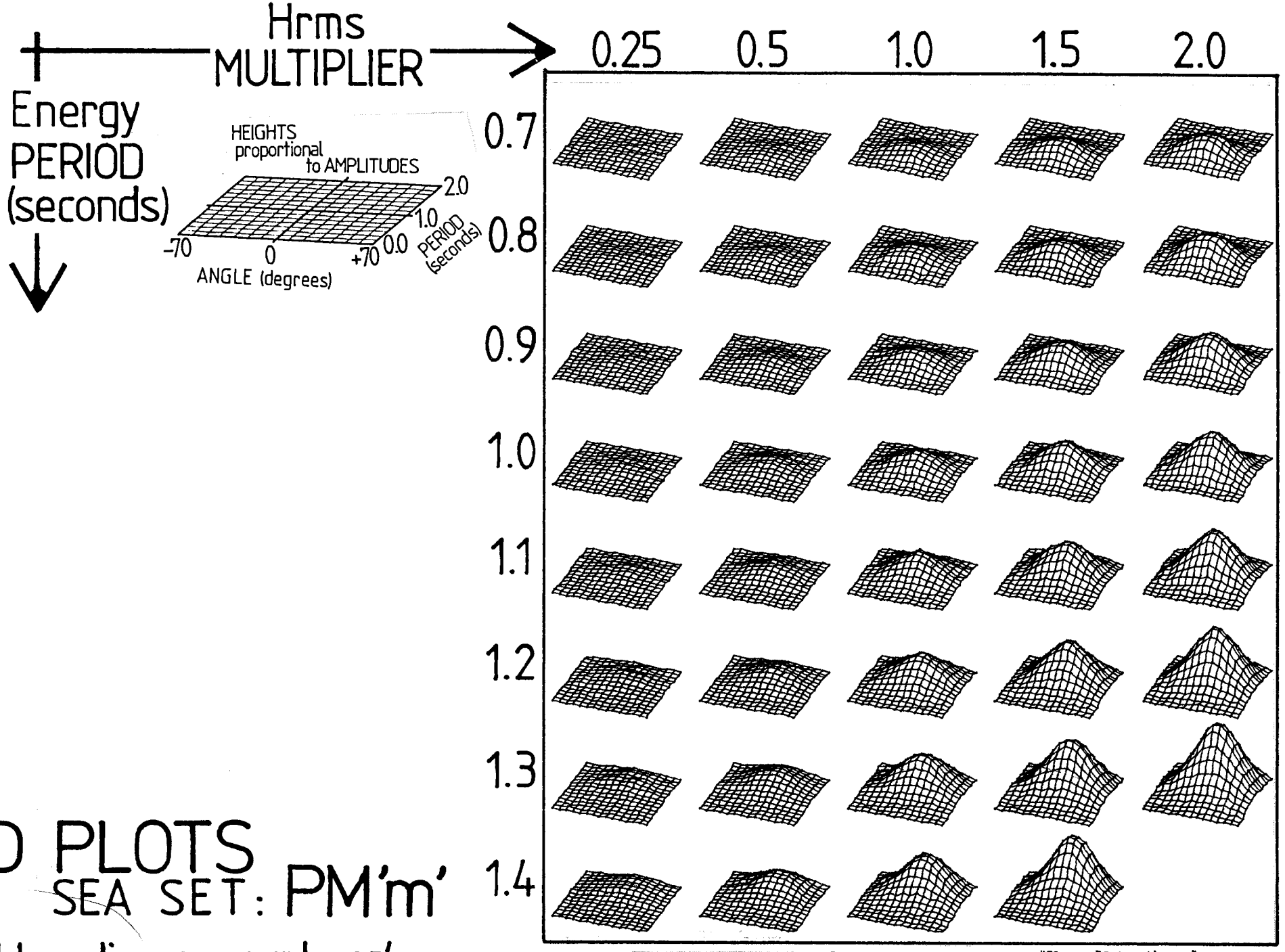

3D PLOTS
SEA SET: PM'm'

'scatter diagram explorer'

"[300,325] PMmmM. TNK"

GRAPH 3.20

3D PLOTS
SEA SET: PM'a'

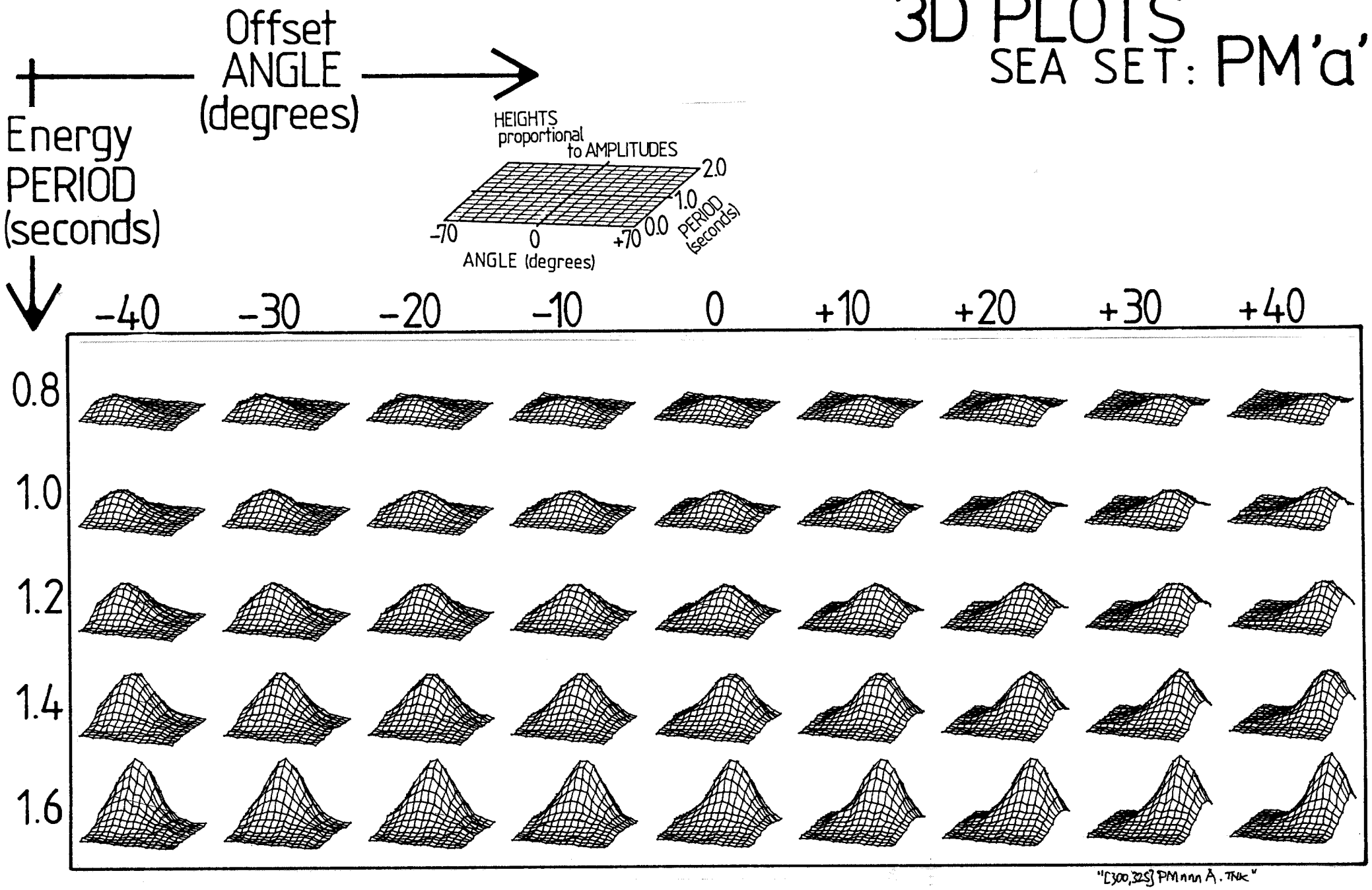

GRAPH 3.21

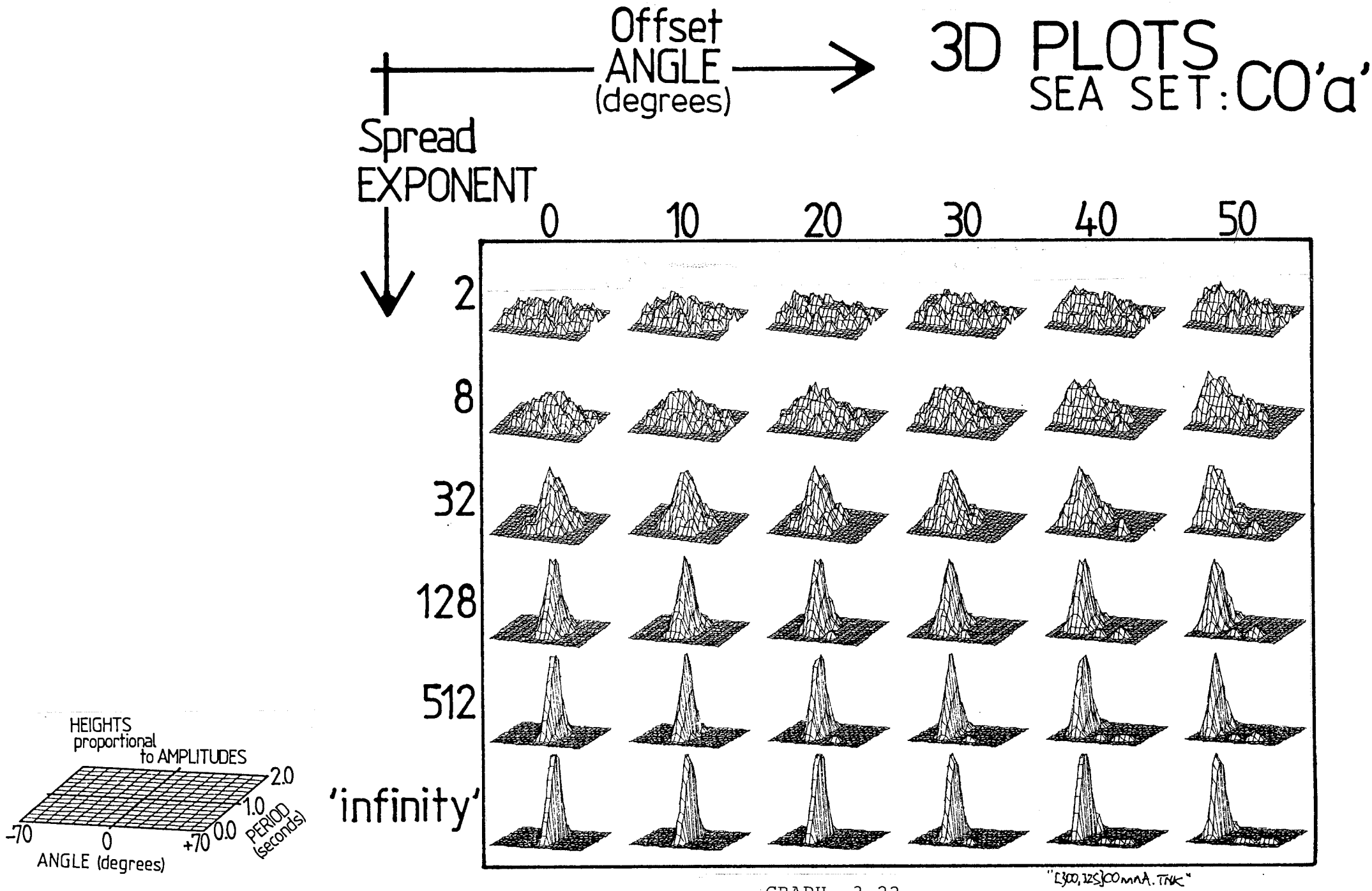
Offset
ANGLE
(degrees)
3D PLOTS
SEA SET: CO'a'
Spread
EXPONENT
0
10
20
30
40
50
2
8
32
128
512
'infinity'
HEIGHTS
proportional
to AMPLITUDES
2.0
1.0
0.0
PERIOD
(seconds)
-70
0
+70
ANGLE (degrees)
"[300,125]00mmA.TMK"

GRAPH 3.22

3D PLOTS
SEA SET: SU 'a'

the 46 SPECTRA

'a' set

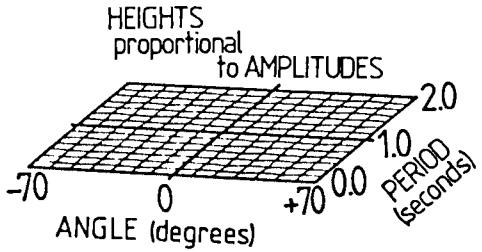

IOS data adjusted for 100m water depth and rescaled at 1/108

Nominal Westerly seas

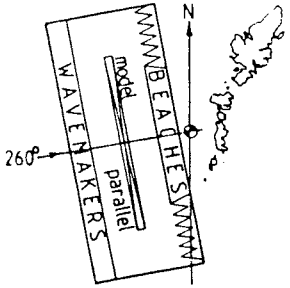

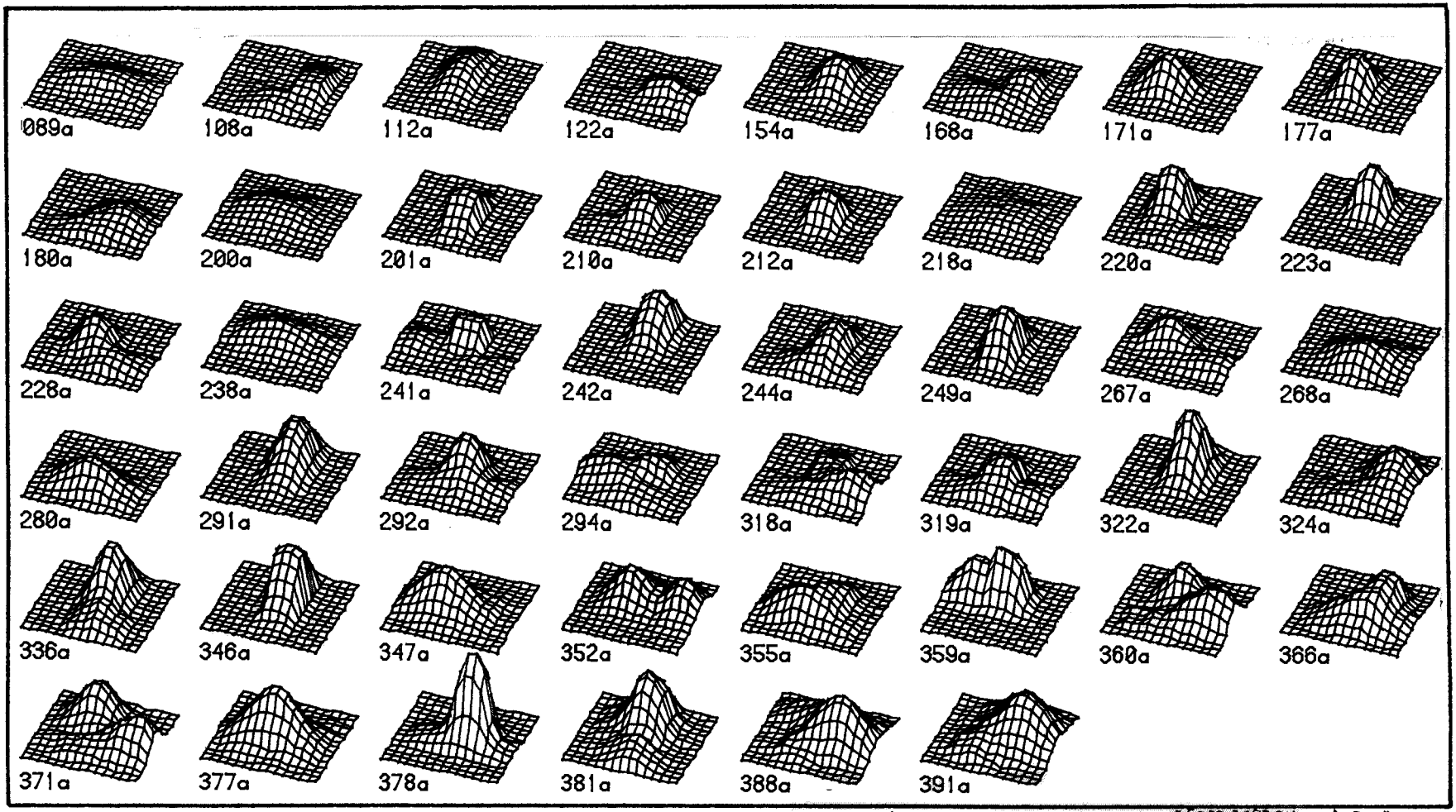

"[300,325]SUnnnA.TNK"

GRAPH 3.23

3D PLOTS
SEA SET: SU 'b'

the 46 SPECTRA 'b' set

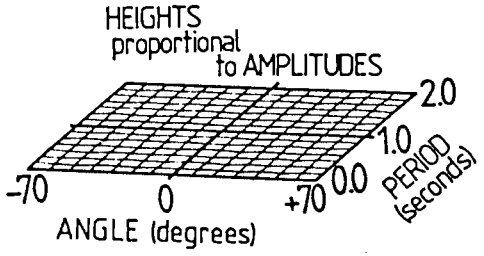

IOS data adjusted for 100m water depth and rescaled at 1/108

Southerly seas

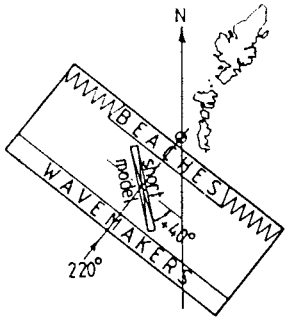

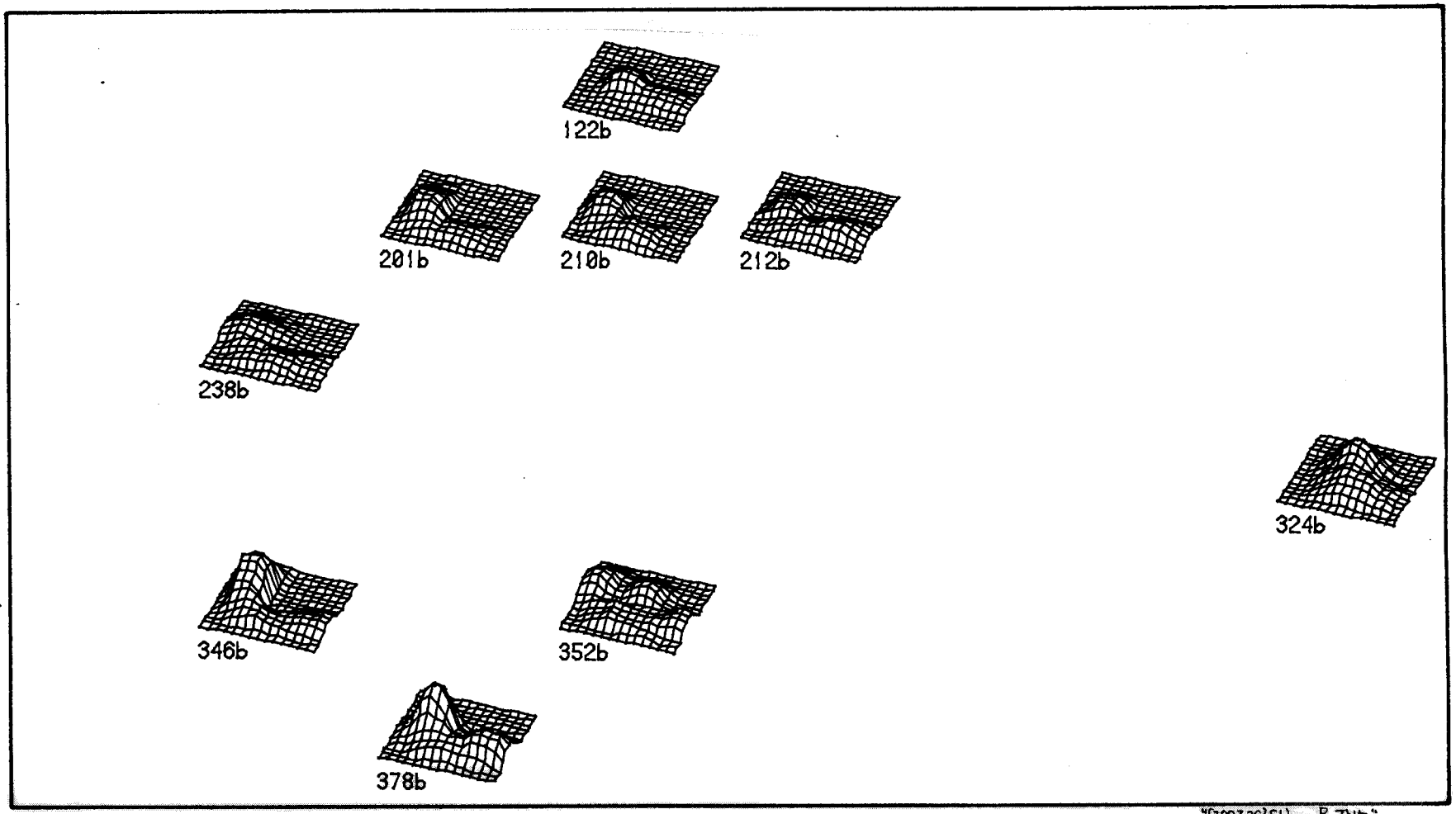

"[300,325]SU___B.TNC"

GRAPH 3.24

3D PLOTS
SEA SET: SU 'c'

the 46 SPECTRA

'c' set

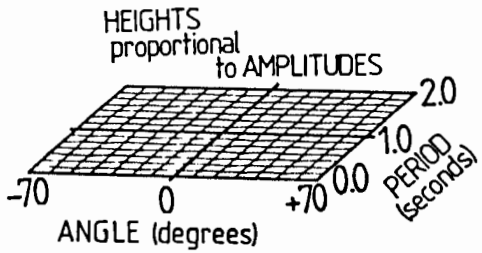

IOS data adjusted for 100m water depth and rescaled at 1/108

Northerly seas

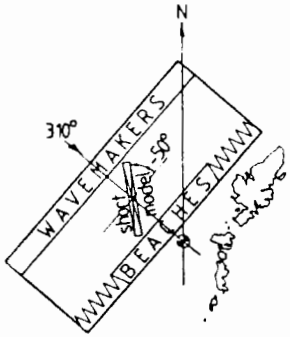

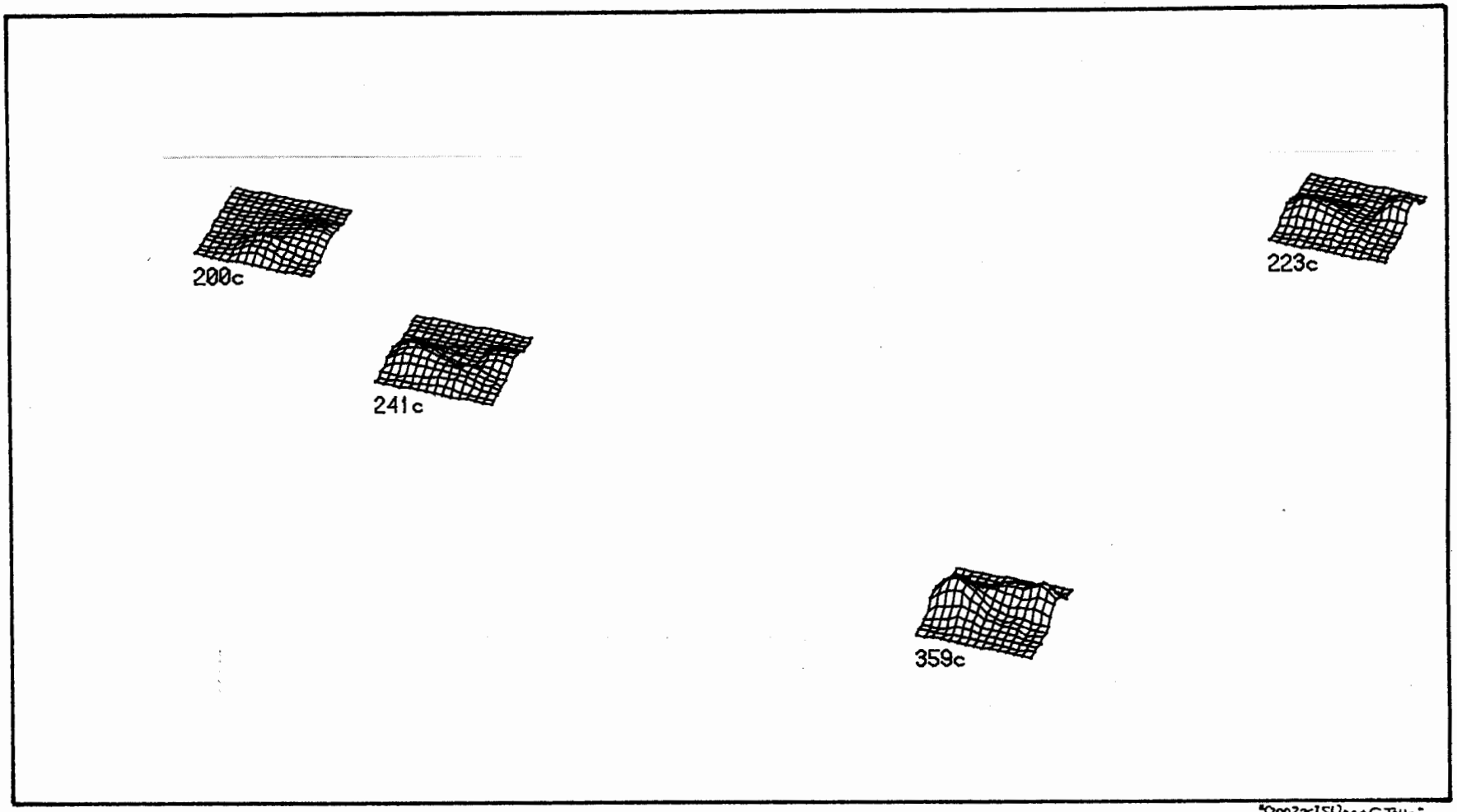

GRAPH 3.25

3D PLOTS
SEA SET: SU 'd'

the 46 SPECTRA 'd' set

mirrored Northerly seas

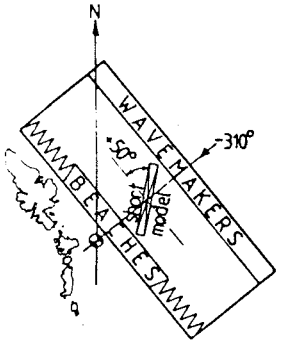

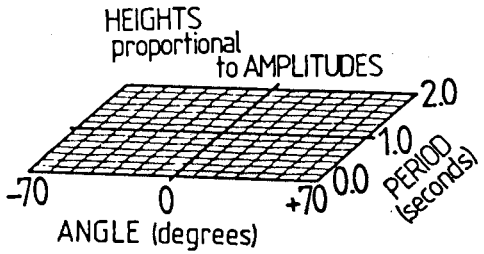

IOS data adjusted for 100m water depth and rescaled at 1/108

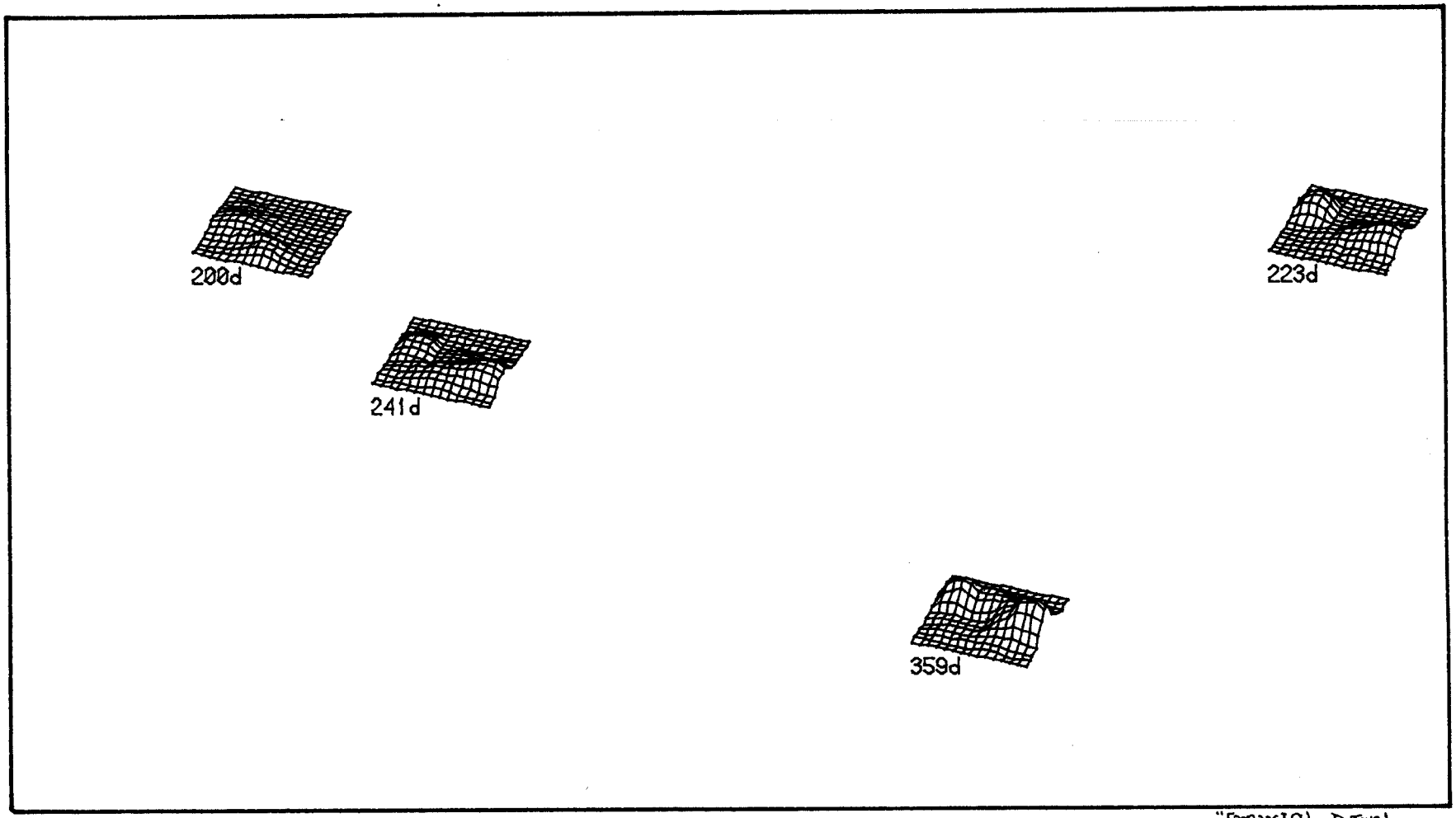

"[309,125] SU### D.TRUC"

GRAPH 3.26

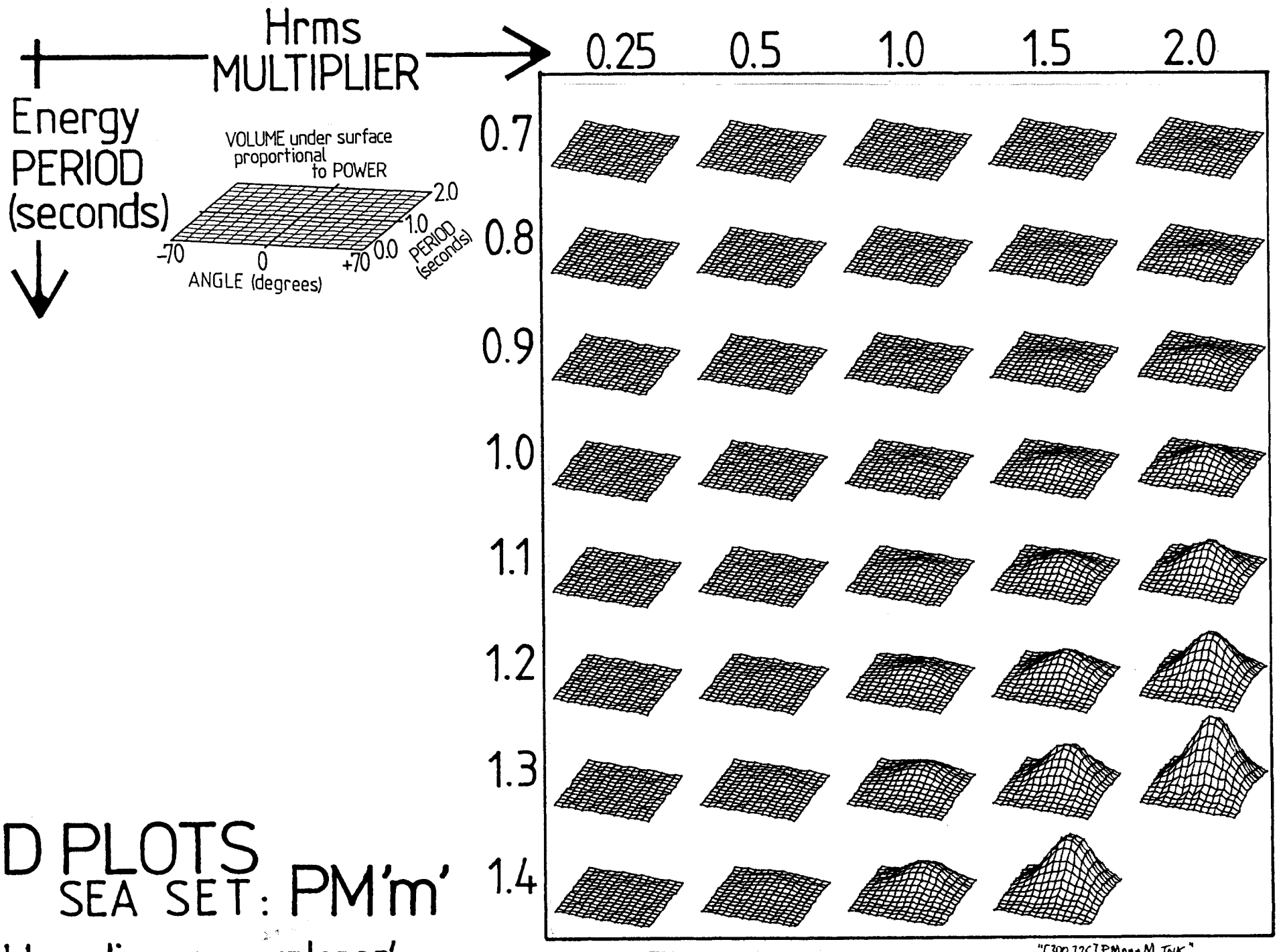

3D PLOTS
SEA SET: PM'm'

'scatter diagram explorer'

"[300,325]PMnnnM.TNK"

GRAPH 3.27

3D PLOTS
SEA SET: PM'a'

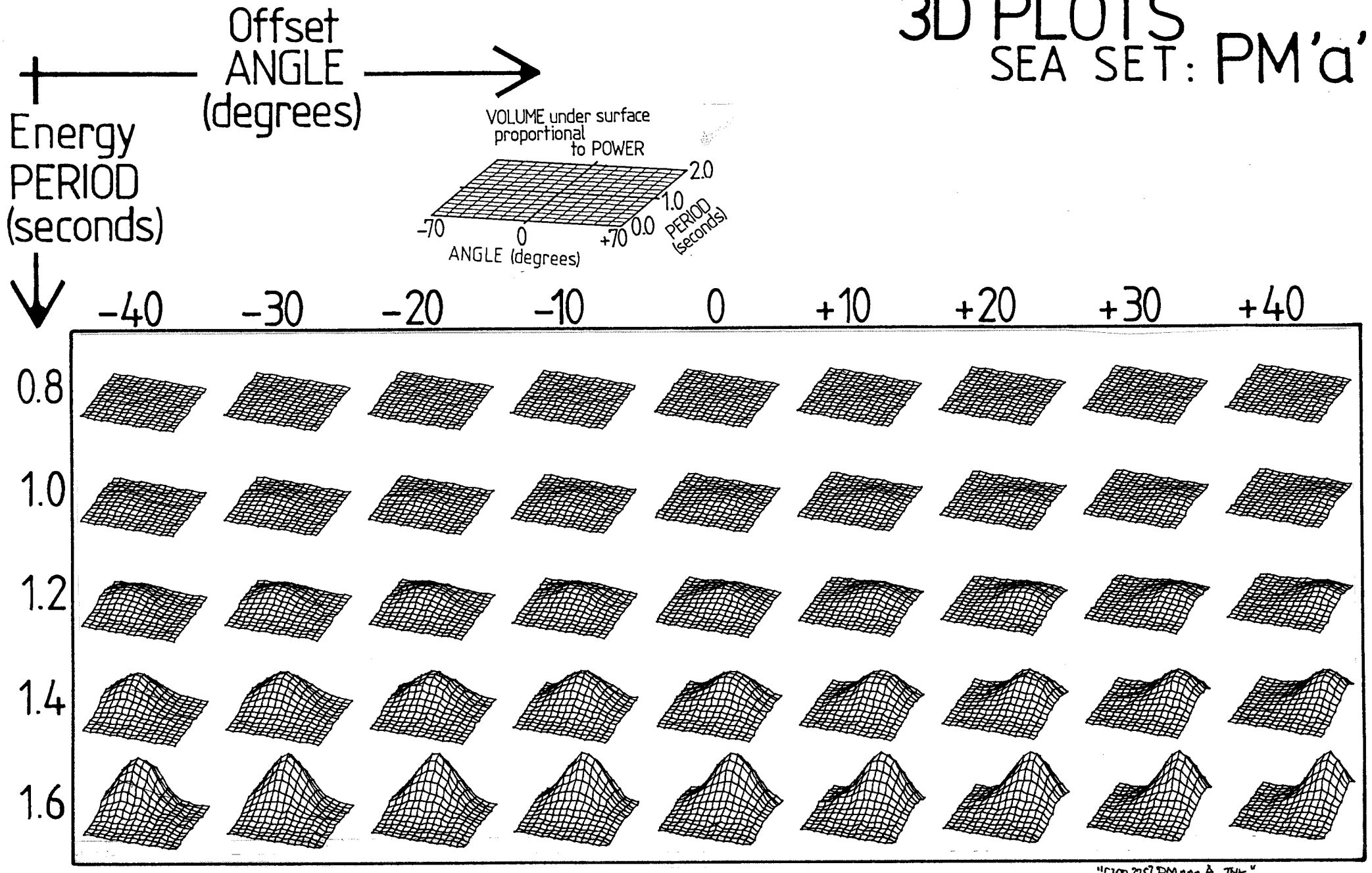

"C300,325]PM nnn A.TNK"

GRAPH 3.28

the 46 SPECTRA 'a' set

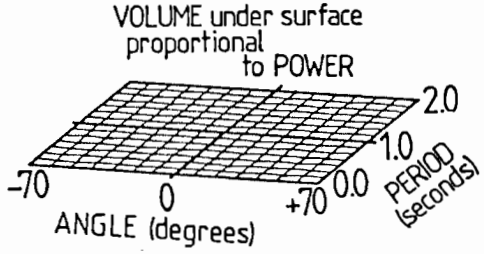

3D PLOTS SEA SET: SU 'a'

IOS data adjusted for 100m water depth and rescaled at 1/108

Nominal Westerly seas

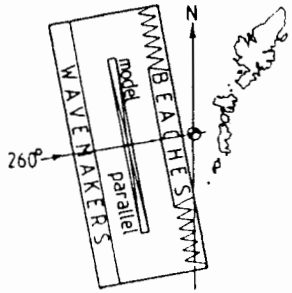

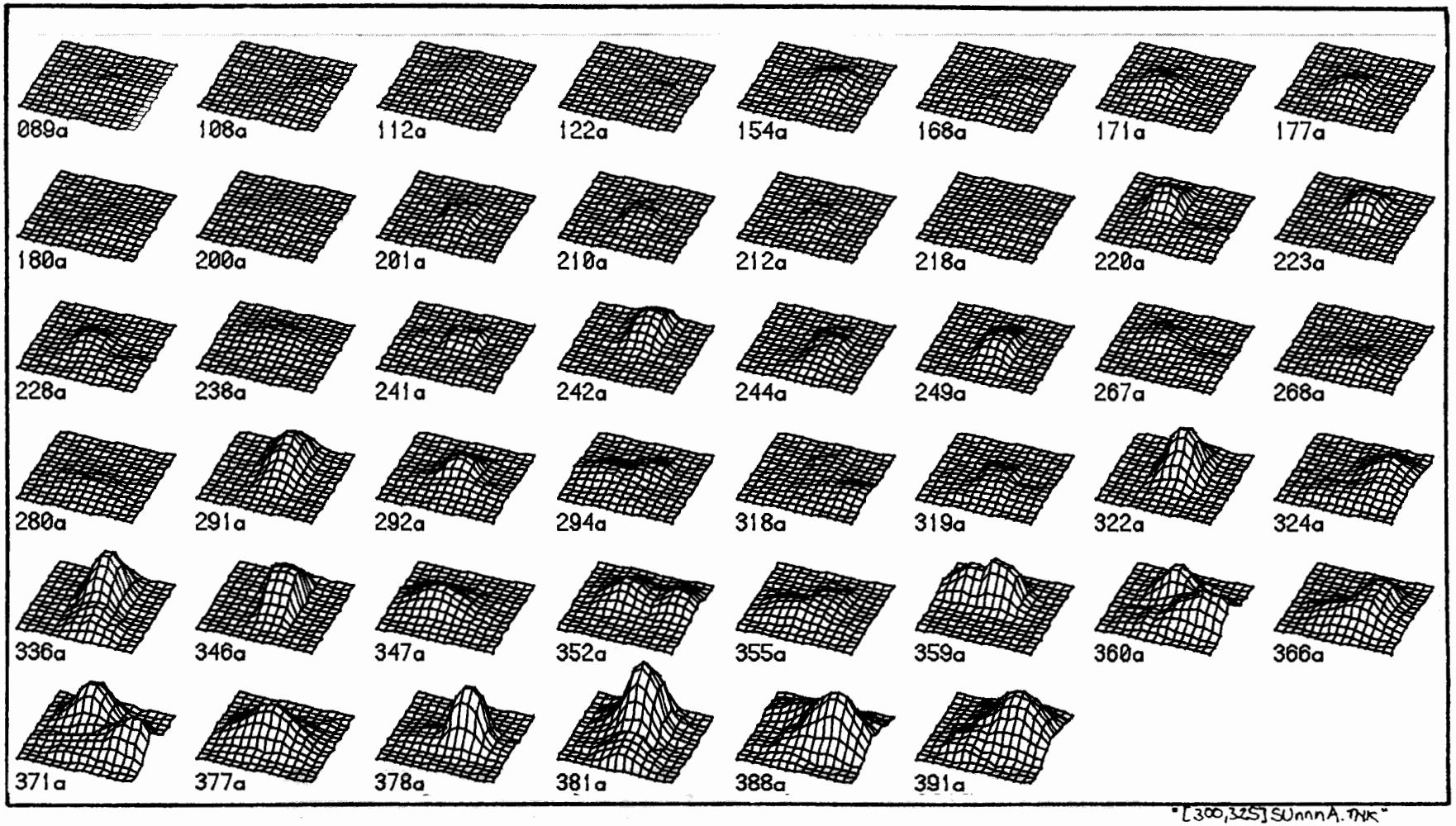

"[300,325]SUnnnA.TNK"

GRAPH 3.29

3D PLOTS
SEA SET: SU 'b'

the 46 SPECTRA 'b' set

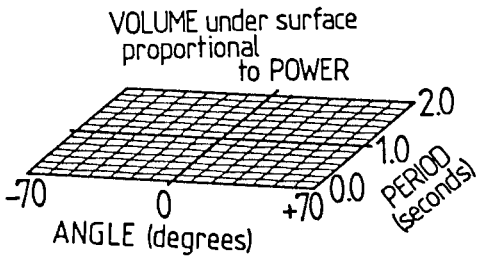

IOS data adjusted for 100m water depth and rescaled at 1/108

Southerly seas

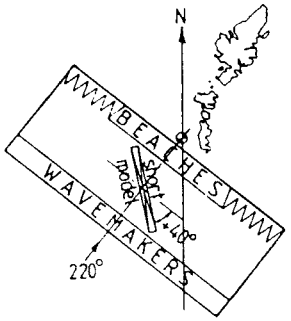

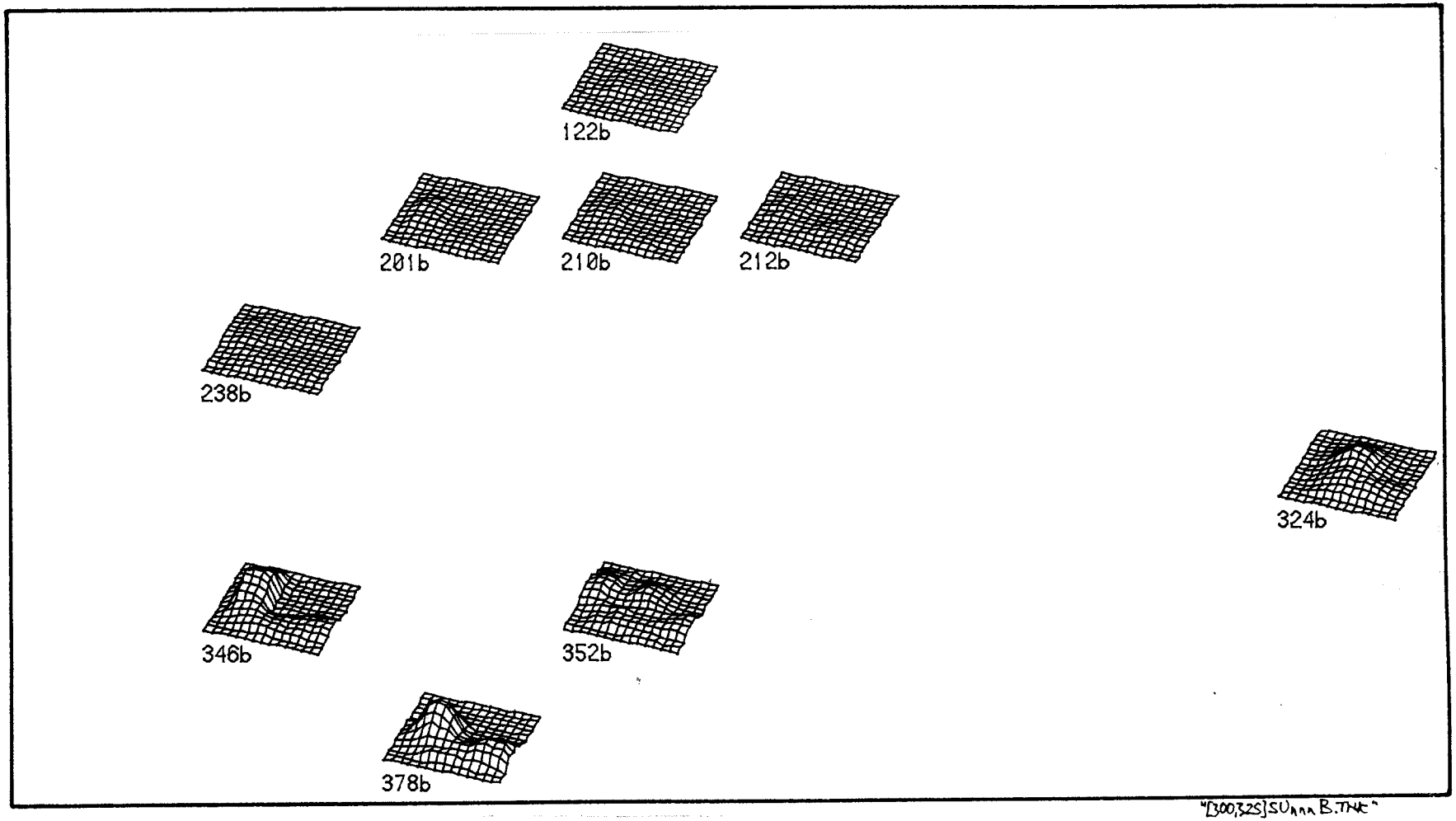

"[300,325]SU___B.THE"

GRAPH 3.30

3D PLOTS
SEA SET: SU 'c'

the 46 SPECTRA

'c' set

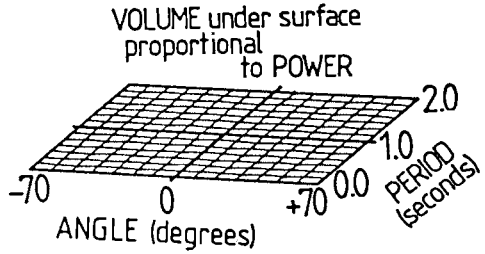

IOS data adjusted for 100m water depth and rescaled at 1/108

Northerly seas

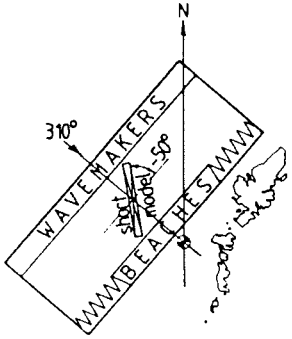

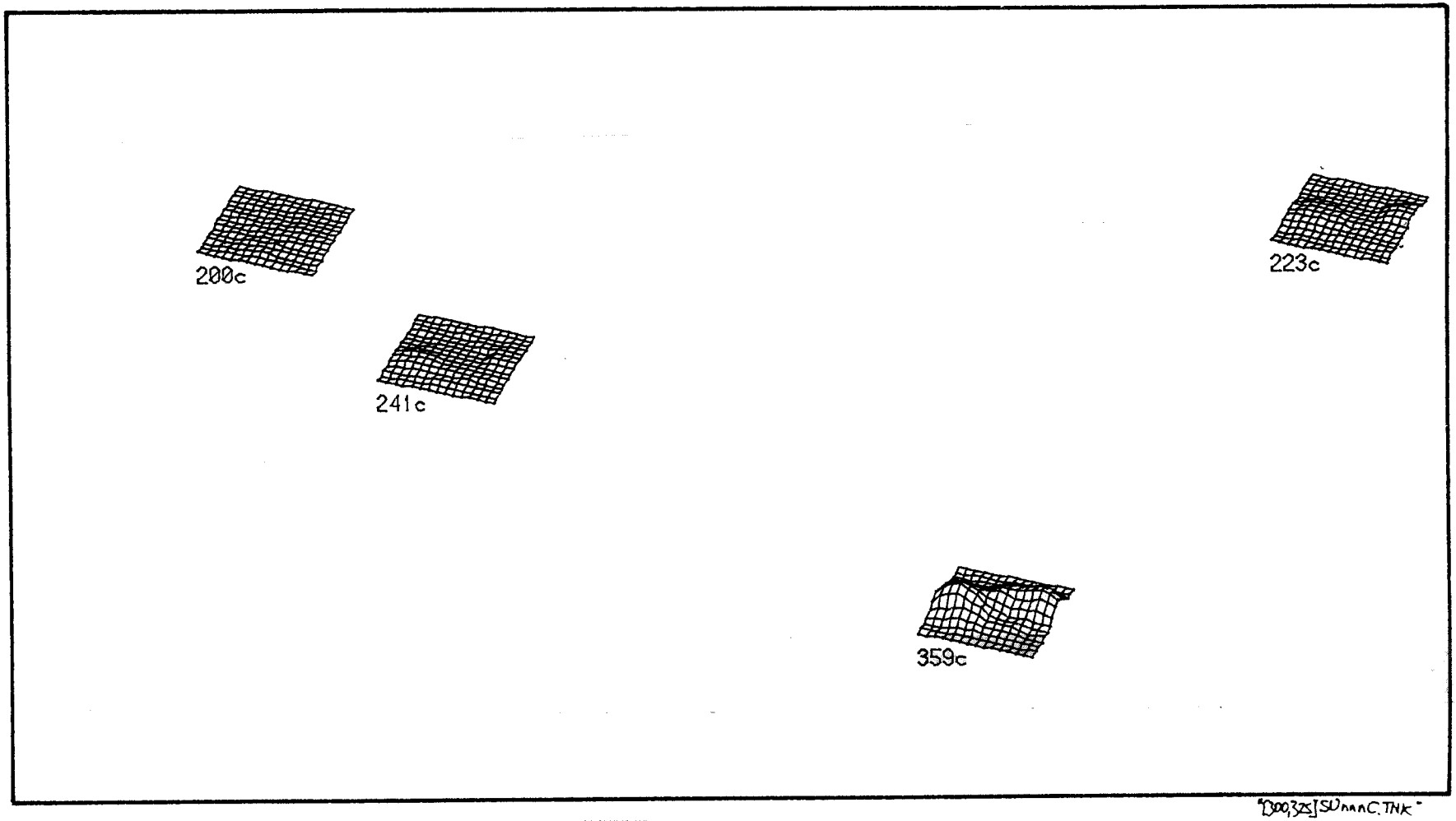

GRAPH 3.31

3D PLOTS
SEA SET: SU 'd'

the 46 SPECTRA

'd' set

mirrored Northerly seas

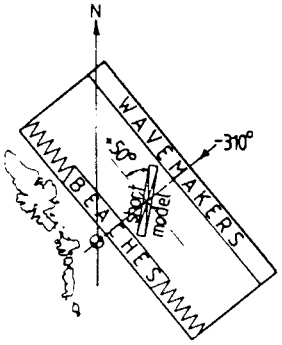

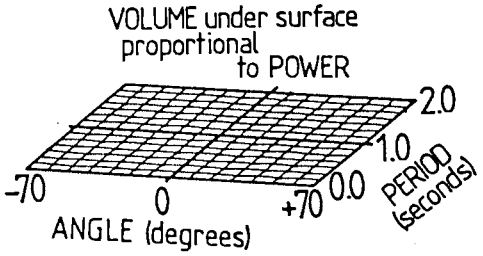

IOS data adjusted for 100m water depth and rescaled at 1/108

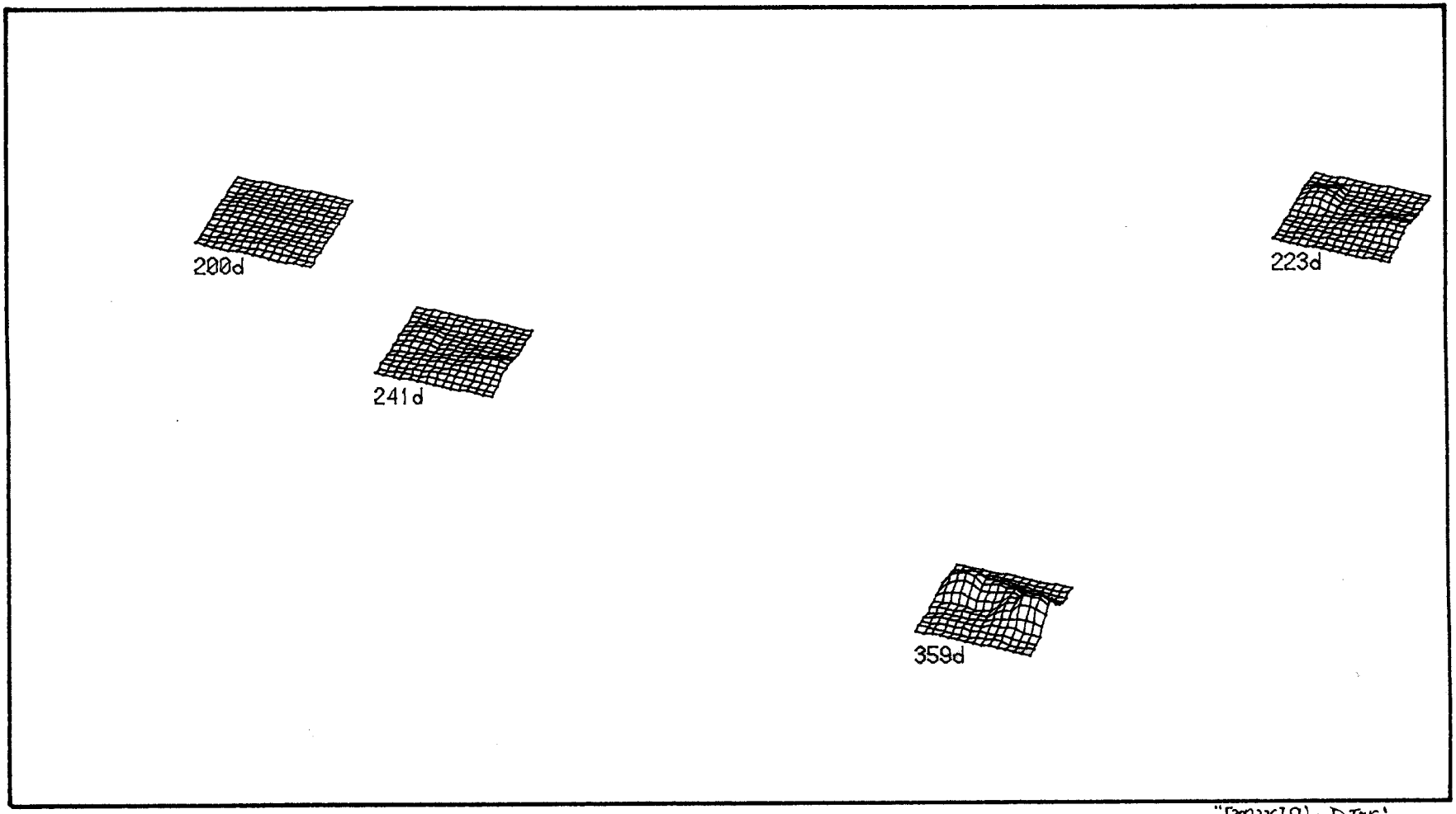

"[309,225] SU mm D.TNK"

GRAPH 3.32

4.A SCATTER DIAGRAM EXPLORING

Bending Moment Results

In graph 4.1 we draw sets of sub-graphs of the root mean square bending moment at each joint along the spine. The points are connected by straight lines but as there are usually so many joints we get the impression of a reasonably fair pattern.

As in most of the tests in this report we recorded 1024 measurements from each joint at a sampling rate of 20 Hertz. With 44 joints to the model each sub-graph is therefore based on 45,056 measurements and the array of 39 tests shown on this page needed 1,757,184 observations.

Bending moment scales are given on the right of the diagram. The units are Newton metres at model scale. They can be conveniently read with the aid of a pair of dividers. The most highly stressed joint on this page had an rms bending moment just under 10 Newton metres.

Tick marks along the top and bottom of the diagram allow us to identify joint numbers. At a scale of 107.7 the 44 joint model would cover nearly 1.9 kilometres of sea, equivalent to twelve wavelengths of a 10 second period wave.

Each sub-graph is laid out as a member of an array corresponding to the position of the sea state given in its corresponding pox-plot. In this case it would be the pox-plot on graph 3.2. The reader will find it helpful to refer backwards and forwards. The columns show the factor by which we multiply the Pierson Moskowitz norm for each of the values of Te shown in rows. Amplitude and period are of course interrelated in the Pierson Moskowitz formula. A x2 multiplier for a 1.4 second sea is very large, with power equivalent to 3.75 MWatts/metre at full scale.

The mean direction of this sea is at 90° to the length of the spine. The central regions show oscillations about a mean level with an increase at each end. Surge moments are always bigger than heave ones. The ratio is about two for small seas but falls for bigger ones.

This set of measurements was made at a stiffness of 1,000 Nm/radians with a whole spine length of 18 metres.

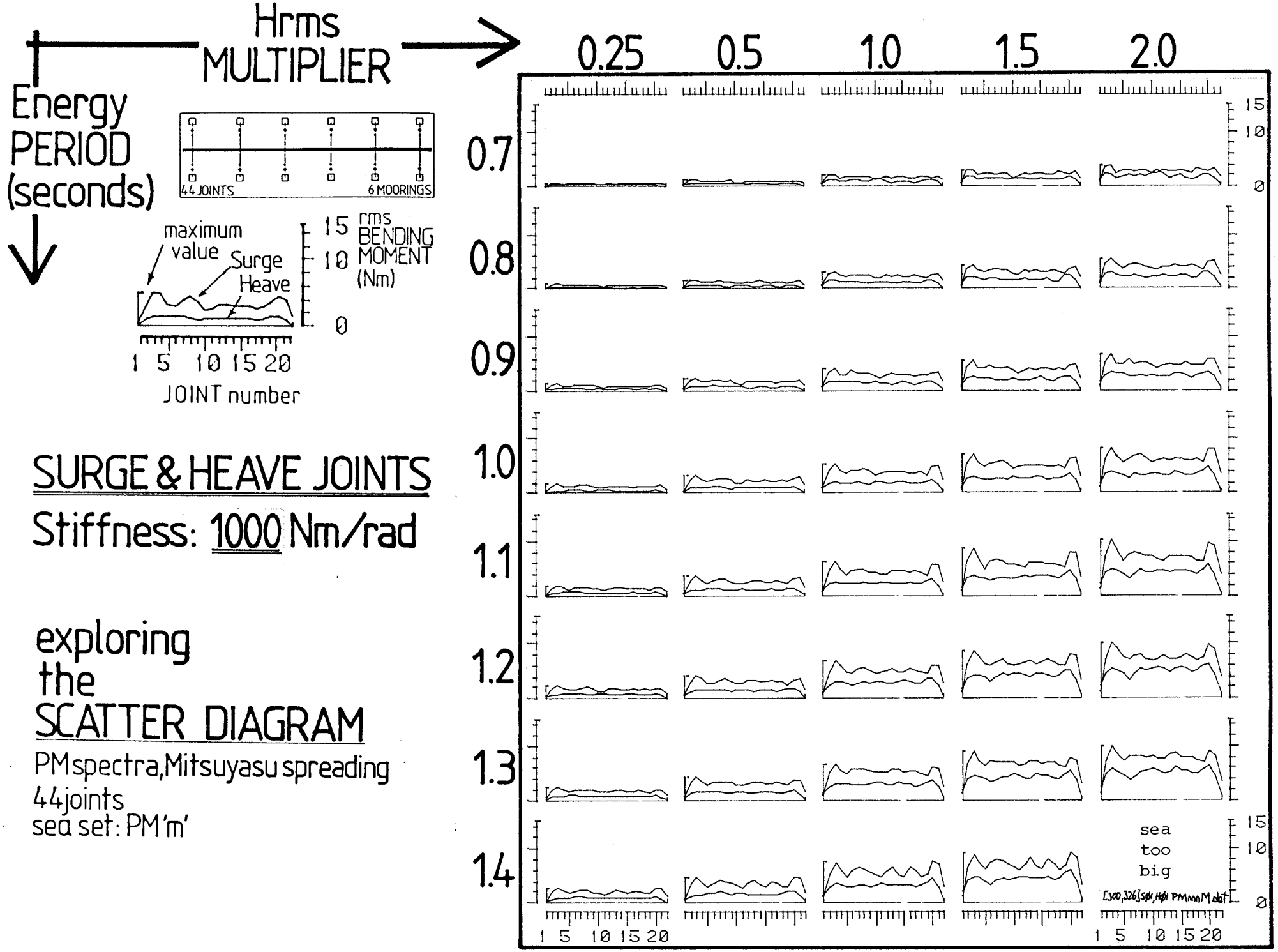

SURGE & HEAVE JOINTS

Stiffness: 1000 Nm/rad

exploring the SCATTER DIAGRAM

PM spectra, Mitsuyasu spreading
44 joints
sea set: PM 'm'

GRAPH 4.1

(4.A cont)

In graph 4.2 we have increased the stiffness to 3,500 N/m radian. The very big seas at this stiffness might have damaged our control motors so we leave blanks.

Hrms MULTIPLIER →

Energy PERIOD (seconds) ↓

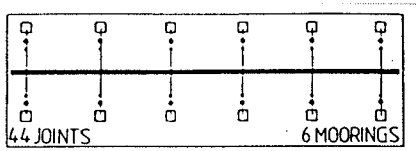

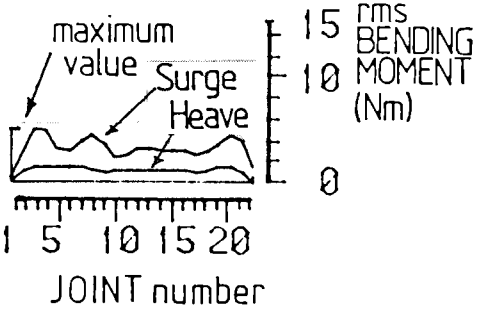

SURGE & HEAVE JOINTS

Stiffness: 3500 Nm/rad

exploring the SCATTER DIAGRAM

PM spectra, Mitsuyasu spreading
44 joints
sea set: PM 'm'

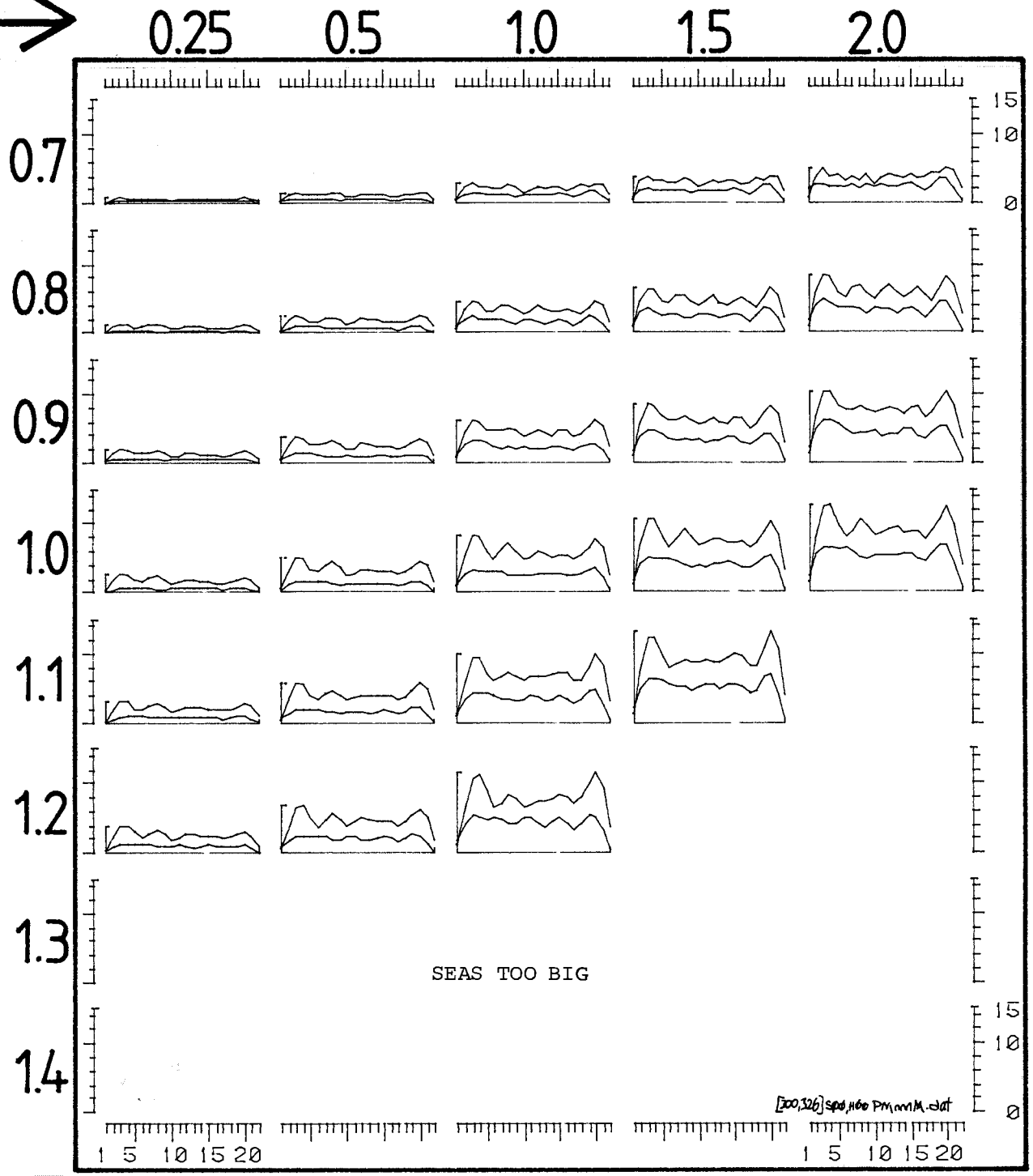

GRAPH 4.2

(4.A cont)

In graph 4.3 we re-plot only the surge results but superimpose projections to the right column and bottom row. This useful technique highlights the changes between each test condition. It looks as though surge bending moments are rising rather less rapidly than wave amplitude.

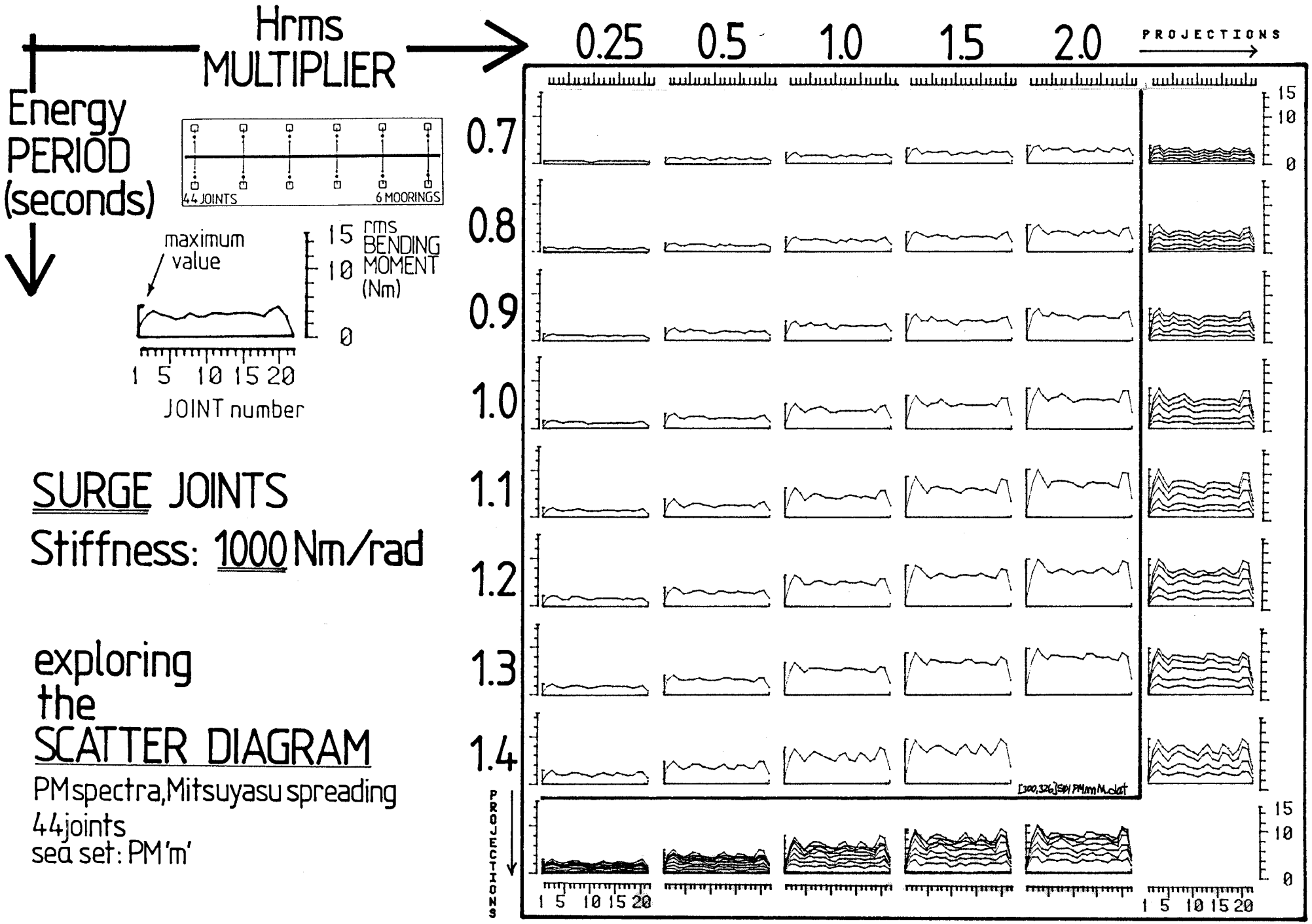
Hrms
MULTIPLIER
0.25
0.5
1.0
1.5
2.0
PROJECTIONS
Energy
PERIOD
(seconds)
0.7
0.8
0.9
1.0
1.1
1.2
1.3
1.4
44 JOINTS
6 MOORINGS
maximum
value
15
10
0
rms
BENDING
MOMENT
(Nm)
1 5 10 15 20
JOINT number
PROJECTIONS
SURGE JOINTS
Stiffness: 1000 Nm/rad
exploring
the
SCATTER DIAGRAM
PM spectra, Mitsuyasu spreading
44 joints
sea set: PM 'm'

GRAPH 4.3

(4.A cont)

In graph 4.4 we re-plot the surge data but divide each value by the measured value of Hrms for each test. We found that using a divisor of Hrms to the power 0.8 produces very close matching in the right hand column, suggesting that this is the right relationship between wave amplitude and bending moment for surge in all parts of the spine.

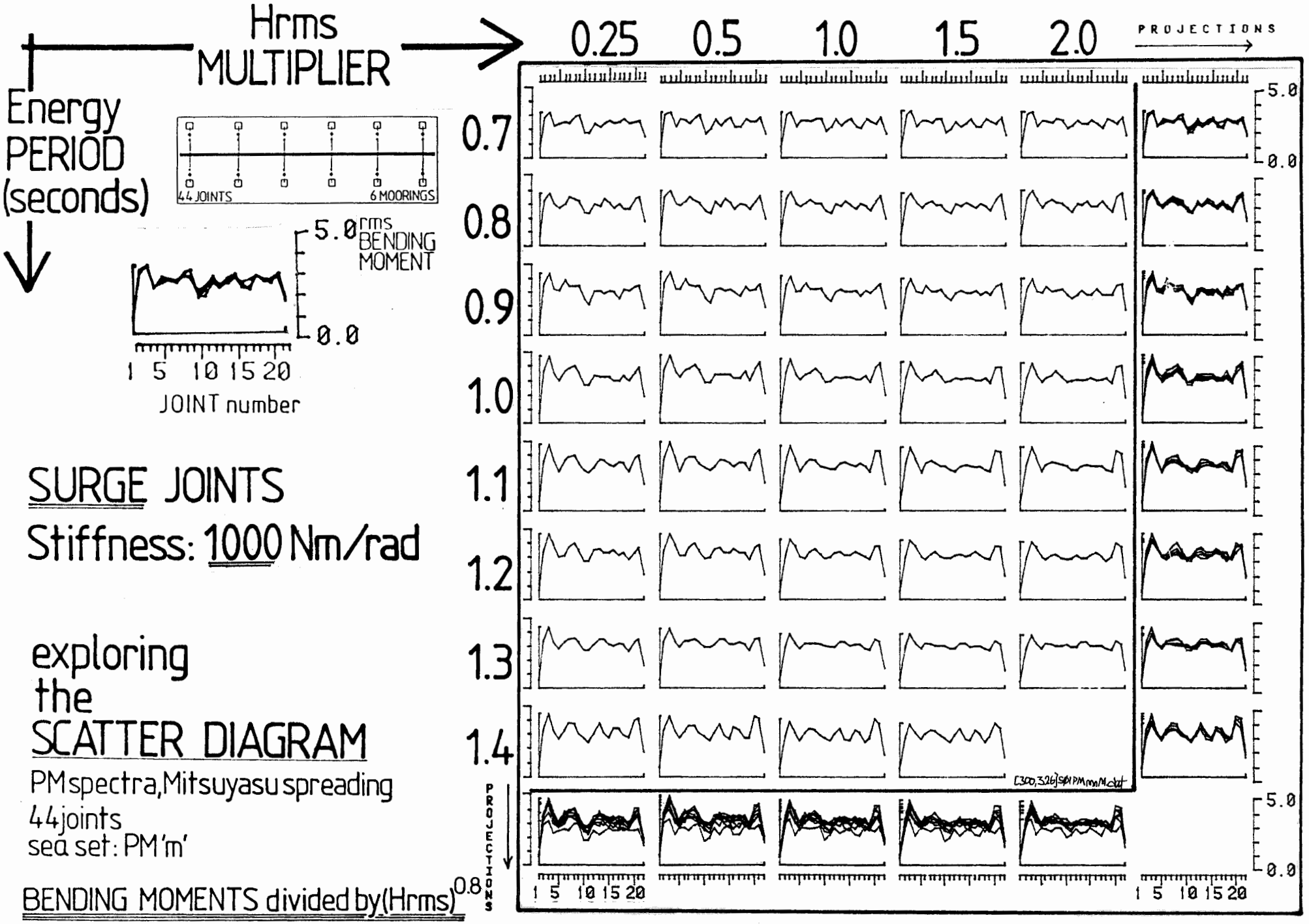
Hrms
MULTIPLIER
0.25
0.5
1.0
1.5
2.0
PROJECTIONS
Energy
PERIOD
(seconds)
0.7
0.8
0.9
1.0
1.1
1.2
1.3
1.4
44 JOINTS
6 MOORINGS
5.0
rms
BENDING
MOMENT
0.0
1 5 10 15 20
JOINT number
SURGE JOINTS
Stiffness: 1000 Nm/rad
exploring
the
SCATTER DIAGRAM
PM spectra, Mitsuyasu spreading
44 joints
sea set: PM 'm'
BENDING MOMENTS divided by (Hrms)^0.8
PROJECTIONS
5.0
0.0
1 5 10 15 20

GRAPH 4.4

(4.A cont)

In graph 4.5 we increase stiffness to 3500 Nm/rad and then for graph 4.6 we normalise by Hrms to the power 0.8, The same amplitude to bending moment rule applies.

In graphs 4.7 to 4.10 exactly the same procedure is carried out for heave but we found that the best normaliser was Hrms to the first power.

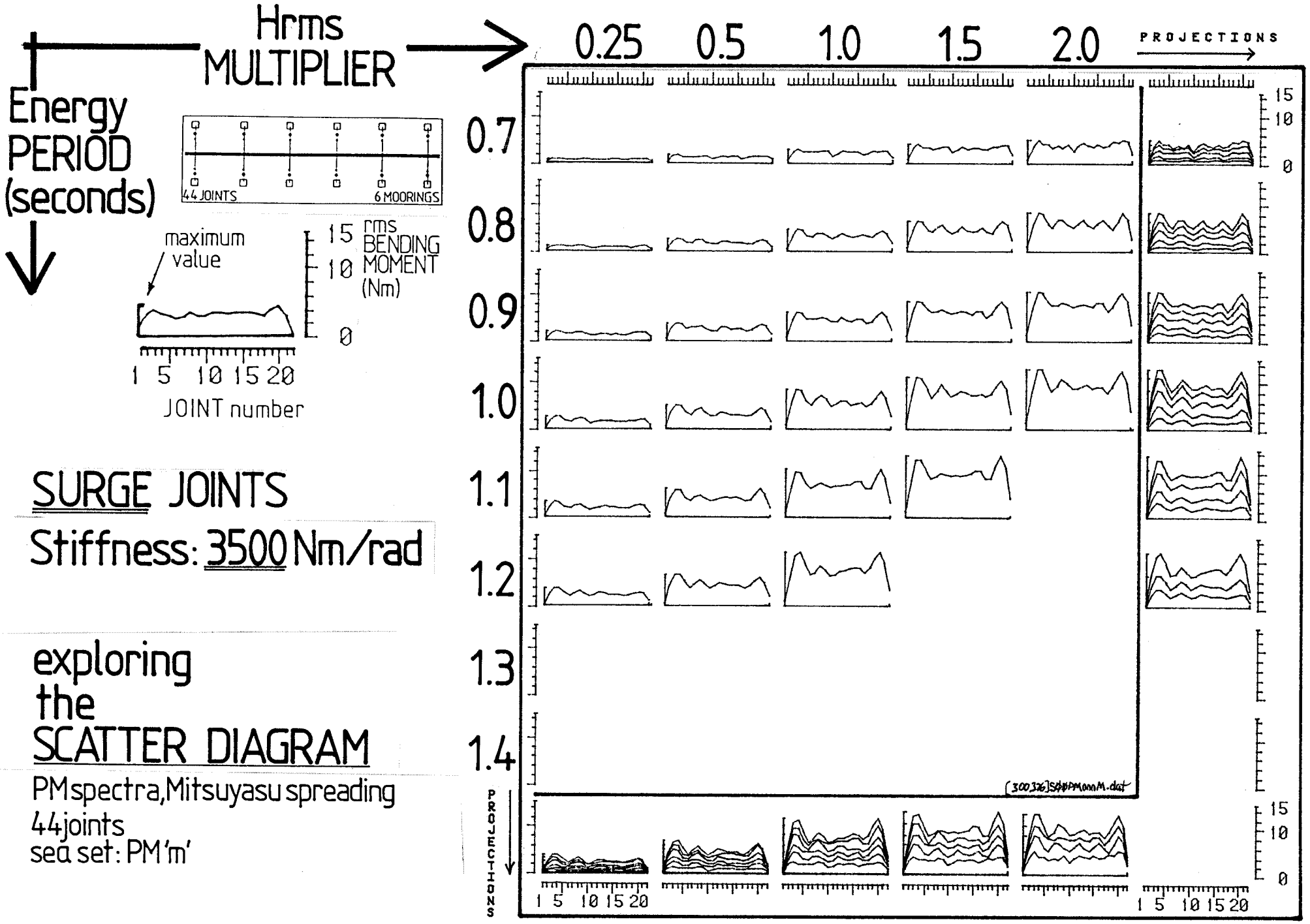
Hrms
MULTIPLIER
0.25
0.5
1.0
1.5
2.0
PROJECTIONS
Energy
PERIOD
(seconds)
0.7
0.8
0.9
1.0
1.1
1.2
1.3
1.4
44 JOINTS
6 MOORINGS
maximum
value
15
10
0
rms
BENDING
MOMENT
(Nm)
1 5 10 15 20
JOINT number
SURGE JOINTS
Stiffness: 3500 Nm/rad
exploring
the
SCATTER DIAGRAM
PM spectra, Mitsuyasu spreading
44 joints
sea set: PM 'm'
PROJECTIONS
[300326]S##PMmmM.dat

GRAPH 4.5

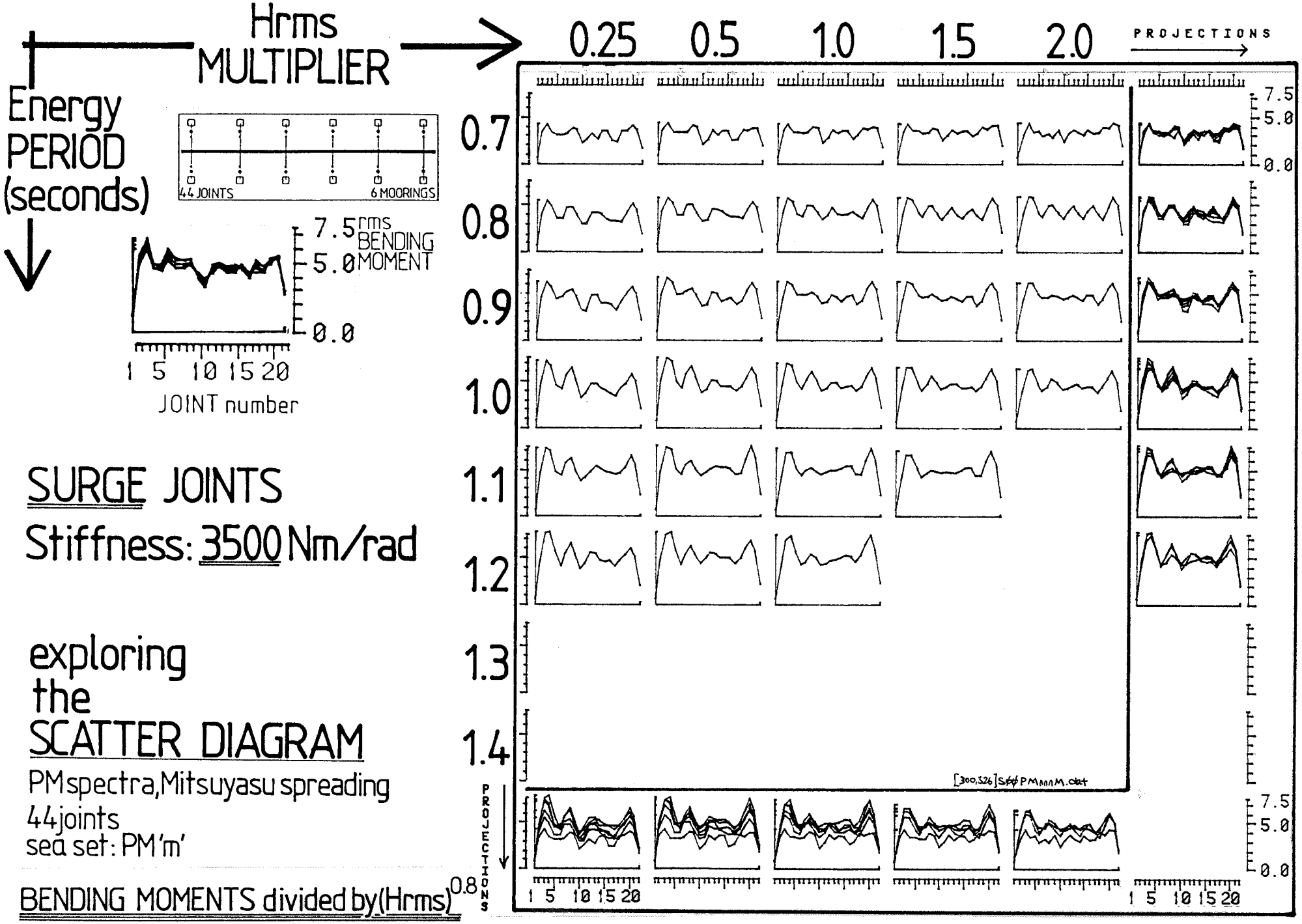
Hrms
MULTIPLIER
0.25 0.5 1.0 1.5 2.0
PROJECTIONS
Energy
PERIOD
(seconds)
0.7
0.8
0.9
1.0
1.1
1.2
1.3
1.4
44 JOINTS
6 MOORINGS
7.5
5.0
0.0
rms
BENDING
MOMENT
1 5 10 15 20
JOINT number
SURGE JOINTS
Stiffness: 3500 Nm/rad
exploring
the
SCATTER DIAGRAM
PM spectra, Mitsuyasu spreading
44 joints
sea set: PM 'm'
BENDING MOMENTS divided by (Hrms)^0.8
[300,326] S#f PMmmM.dat

GRAPH 4.6

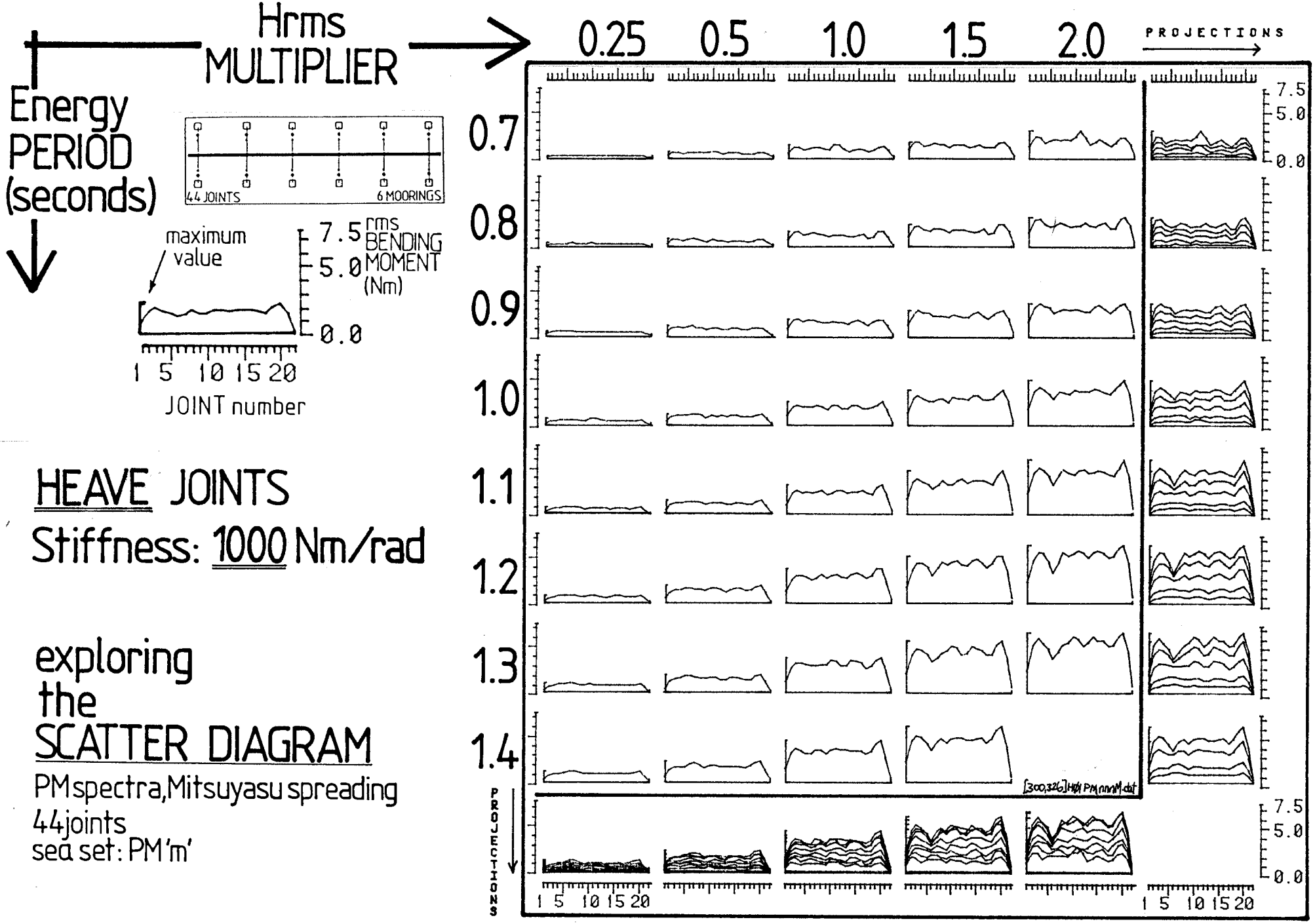
Hrms
MULTIPLIER
0.25
0.5
1.0
1.5
2.0
PROJECTIONS
Energy
PERIOD
(seconds)
0.7
0.8
0.9
1.0
1.1
1.2
1.3
1.4
44 JOINTS
6 MOORINGS
maximum
value
7.5
5.0
0.0
rms
BENDING
MOMENT
(Nm)
1 5 10 15 20
JOINT number
HEAVE JOINTS
Stiffness: 1000 Nm/rad
exploring
the
SCATTER DIAGRAM
PM spectra, Mitsuyasu spreading
44 joints
sea set: PM 'm'

GRAPH 4.7

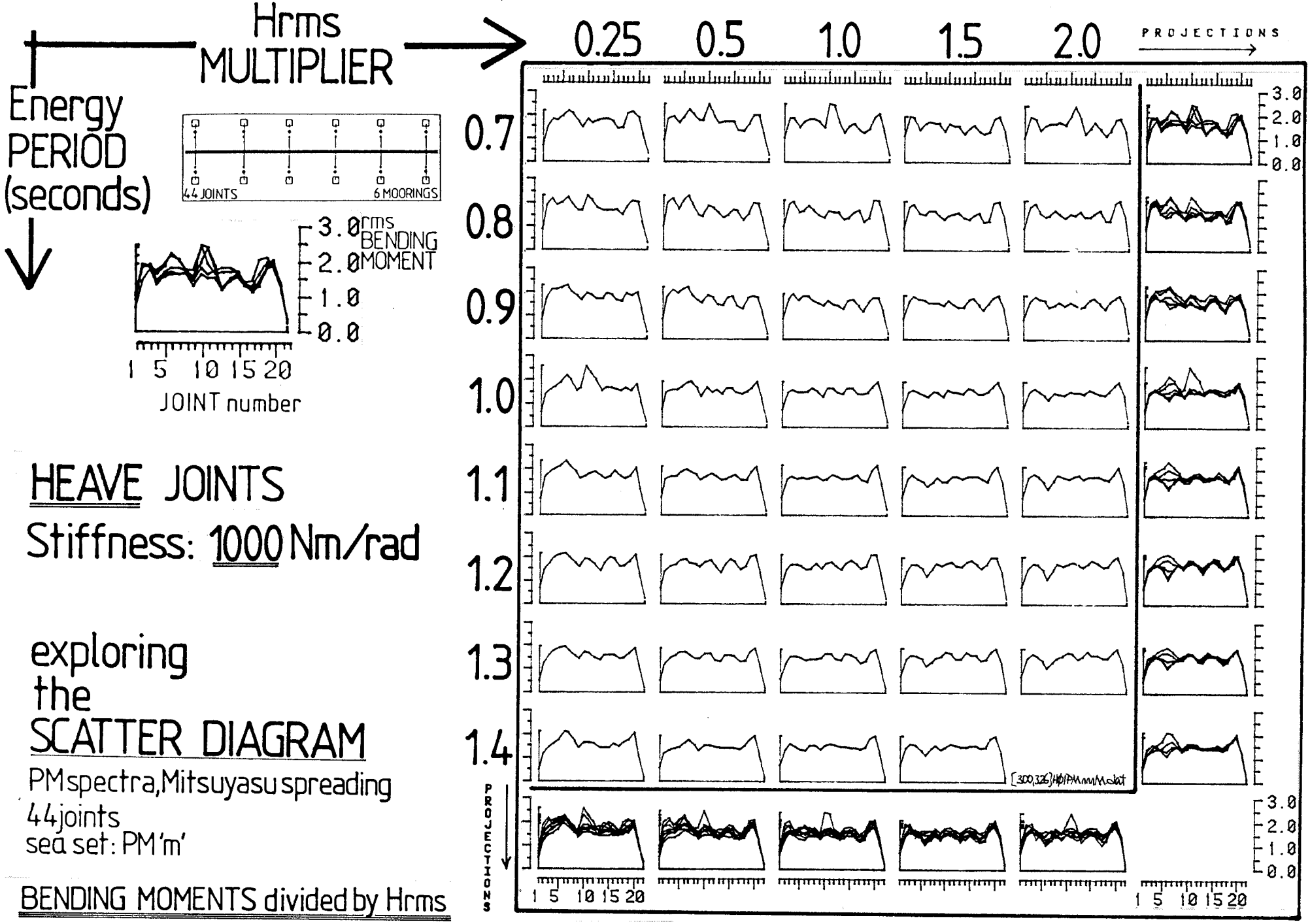
Hrms
MULTIPLIER
0.25 0.5 1.0 1.5 2.0
PROJECTIONS
Energy
PERIOD
(seconds)
44 JOINTS
6 MOORINGS
3.0 rms BENDING
2.0 MOMENT
1.0
0.0
1 5 10 15 20
JOINT number
0.7
0.8
0.9
1.0
1.1
1.2
1.3
1.4
PROJECTIONS
HEAVE JOINTS
Stiffness: 1000 Nm/rad
exploring
the
SCATTER DIAGRAM
PM spectra, Mitsuyasu spreading
44 joints
sea set: PM 'm'
BENDING MOMENTS divided by Hrms

GRAPH 4.8

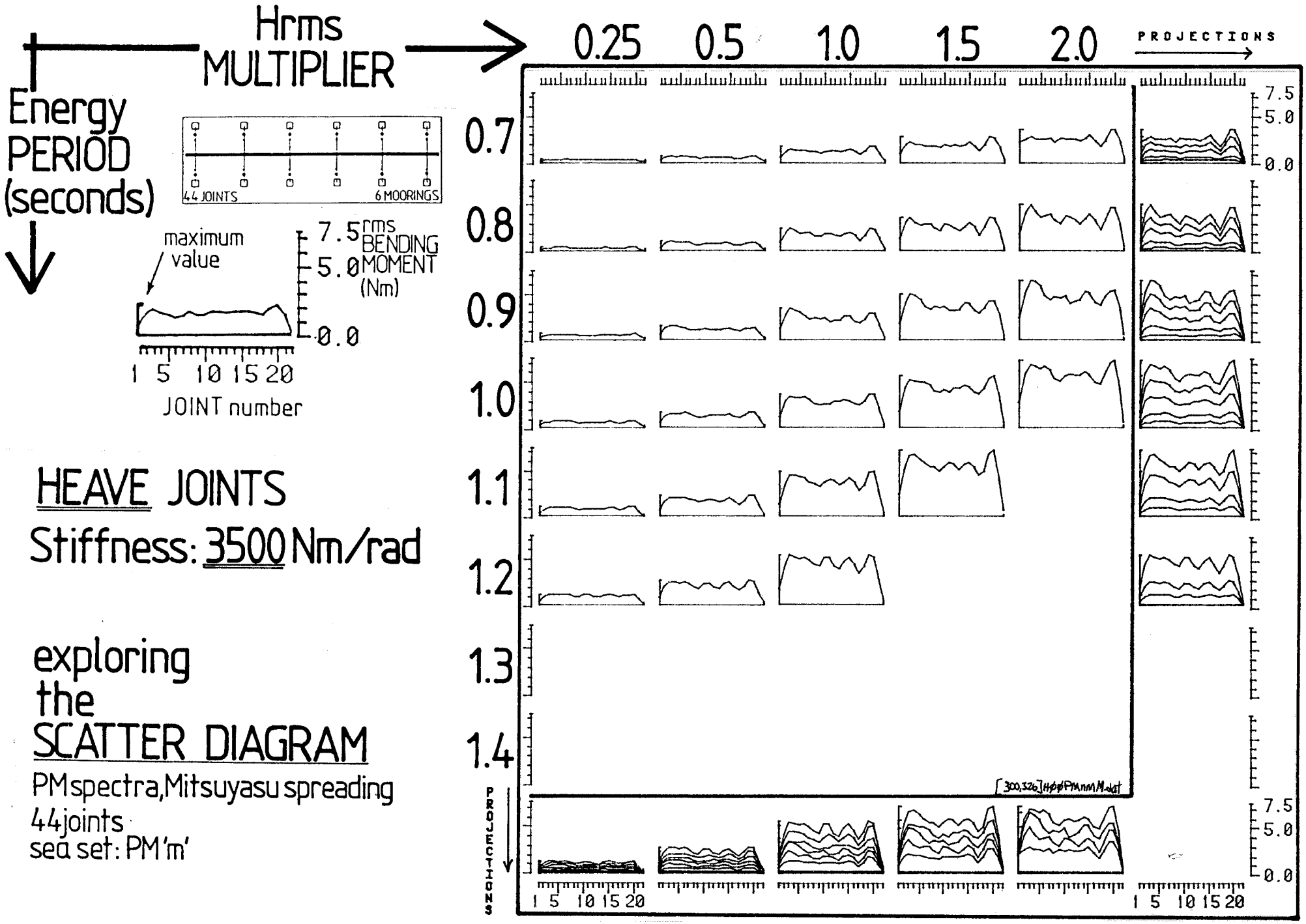
Hrms
MULTIPLIER
0.25
0.5
1.0
1.5
2.0
PROJECTIONS
Energy
PERIOD
(seconds)
0.7
0.8
0.9
1.0
1.1
1.2
1.3
1.4
44 JOINTS
6 MOORINGS
maximum
value
7.5
5.0
0.0
rms
BENDING
MOMENT
(Nm)
1 5 10 15 20
JOINT number
HEAVE JOINTS
Stiffness: 3500 Nm/rad
exploring
the
SCATTER DIAGRAM
PM spectra, Mitsuyasu spreading
44 joints
sea set: PM 'm'
PROJECTIONS
1 5 10 15 20

GRAPH 4.9

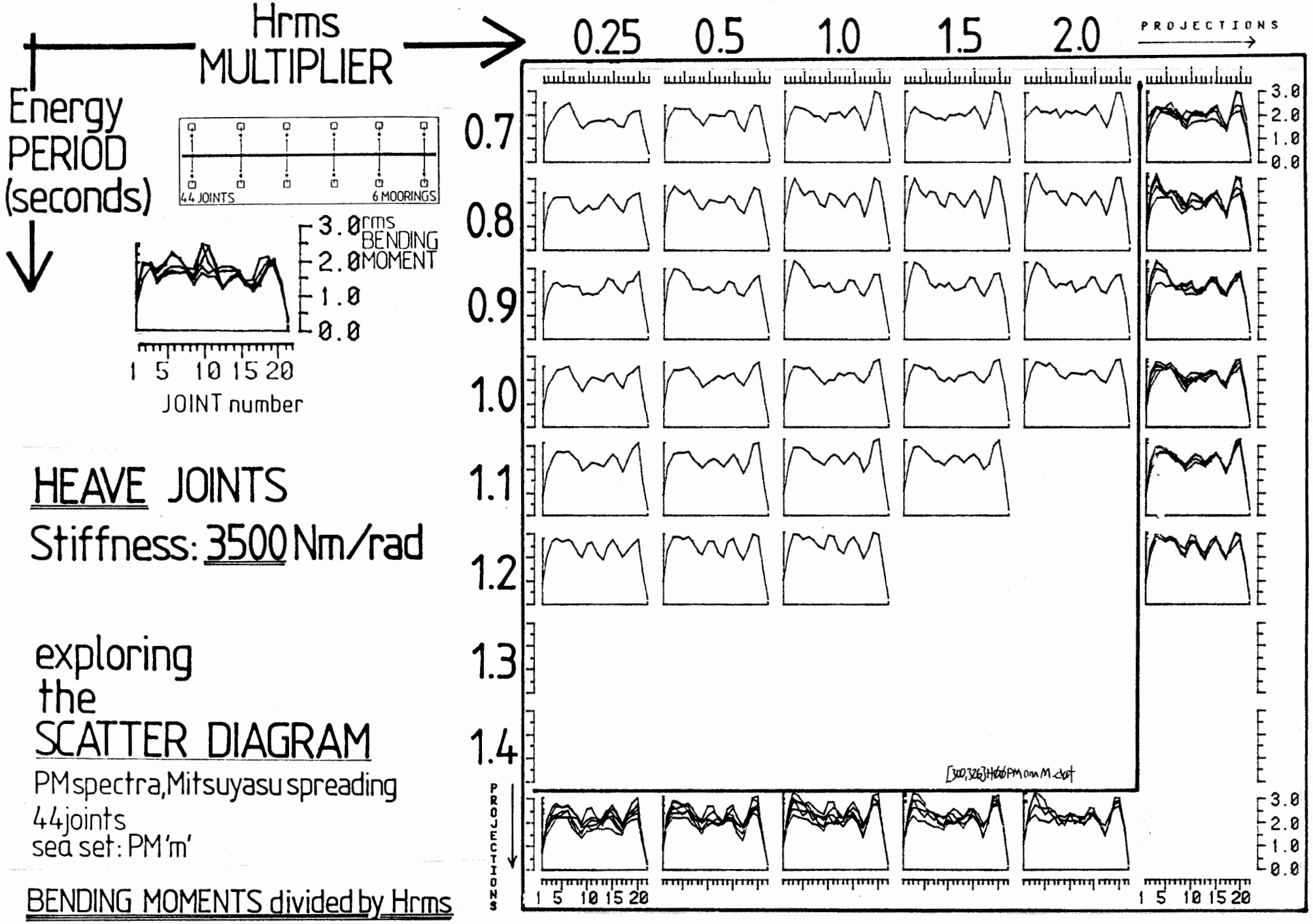
Hrms
MULTIPLIER
0.25
0.5
1.0
1.5
2.0
PROJECTIONS
Energy
PERIOD
(seconds)
0.7
0.8
0.9
1.0
1.1
1.2
1.3
1.4
44 JOINTS
6 MOORINGS
3.0 rms BENDING MOMENT
2.0
1.0
0.0
1 5 10 15 20
JOINT number
HEAVE JOINTS
Stiffness: 3500 Nm/rad
exploring
the
SCATTER DIAGRAM
PM spectra, Mitsuyasu spreading
44 joints
sea set: PM 'm'
BENDING MOMENTS divided by Hrms

GRAPH 4.10

(4.A cont)

Having shown the distribution of bending moment along the spine we now want to extract the rules for other variables. Graph 4.11 plots the root mean square bending moment for all joints in the model for heave and surge against Hrms at each energy period.

Heave families are very straight, confirming the Hrms to the first power rule. Surge values show the Hrms to the power 0.8 effect.

Heave period curves are all close, showing that period is having very little effect. Surge periods are also fairly close except for the shortest period of 0.7 seconds.

Graph 4.12 shows that increasing the stiffness to 3500 Nm/radians raises the slope but not by as much as 3.5. It also seems to separate the surge period curves.

In graph 4.13 we are plotting similar data but draw lines for each joint. The stiffness is 1000 Nm/radian. We can see the bunched results for the central region, two or three joints with higher values near the end and low ones at the very end. We must remember that heave and surge joints alternate.

Heave linearity is evident even with such scattered points. Surge non-linearity is also clear.

In 4.14 we repeat the procedures for an increased stiffness of 3500 Nm/radian. Everything is exactly as expected.

exploring the SCATTER DIAGRAM

BENDING MOMENTS

PM Spectra, Mitsuyasu, 44joints
(varying Hrms Multiplier & Energy Period)

SURGE

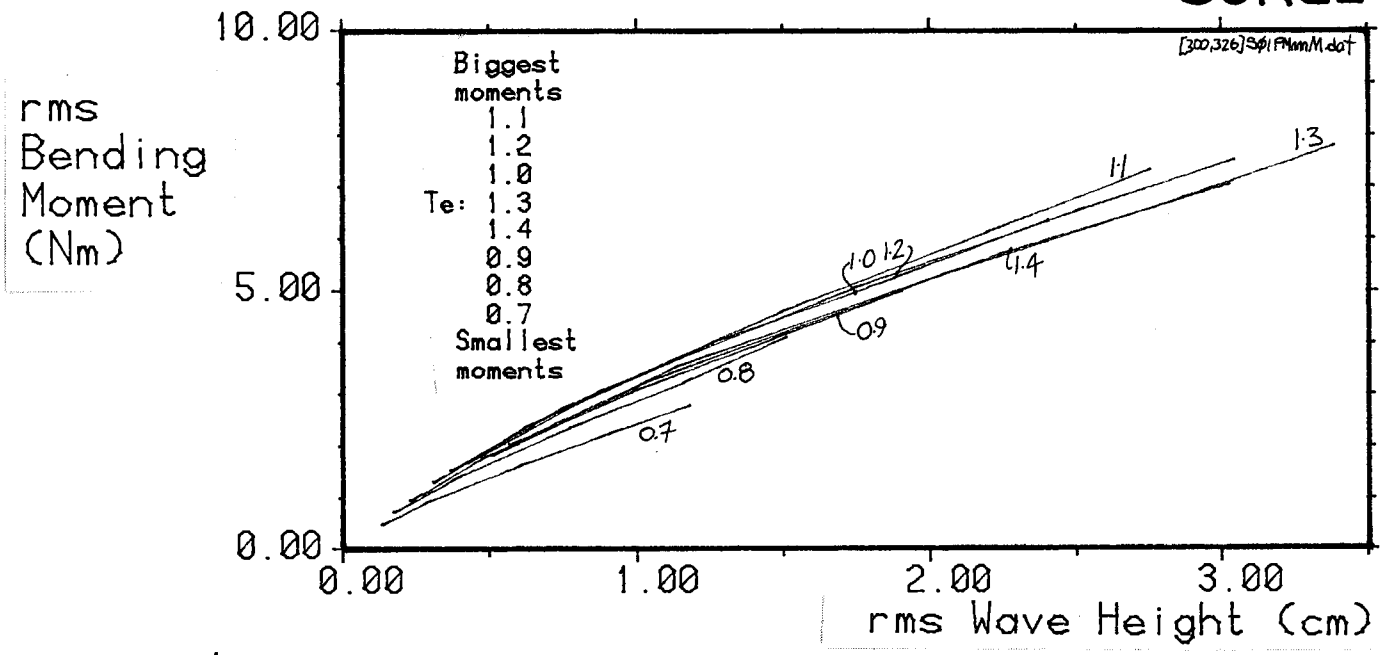

HEAVE

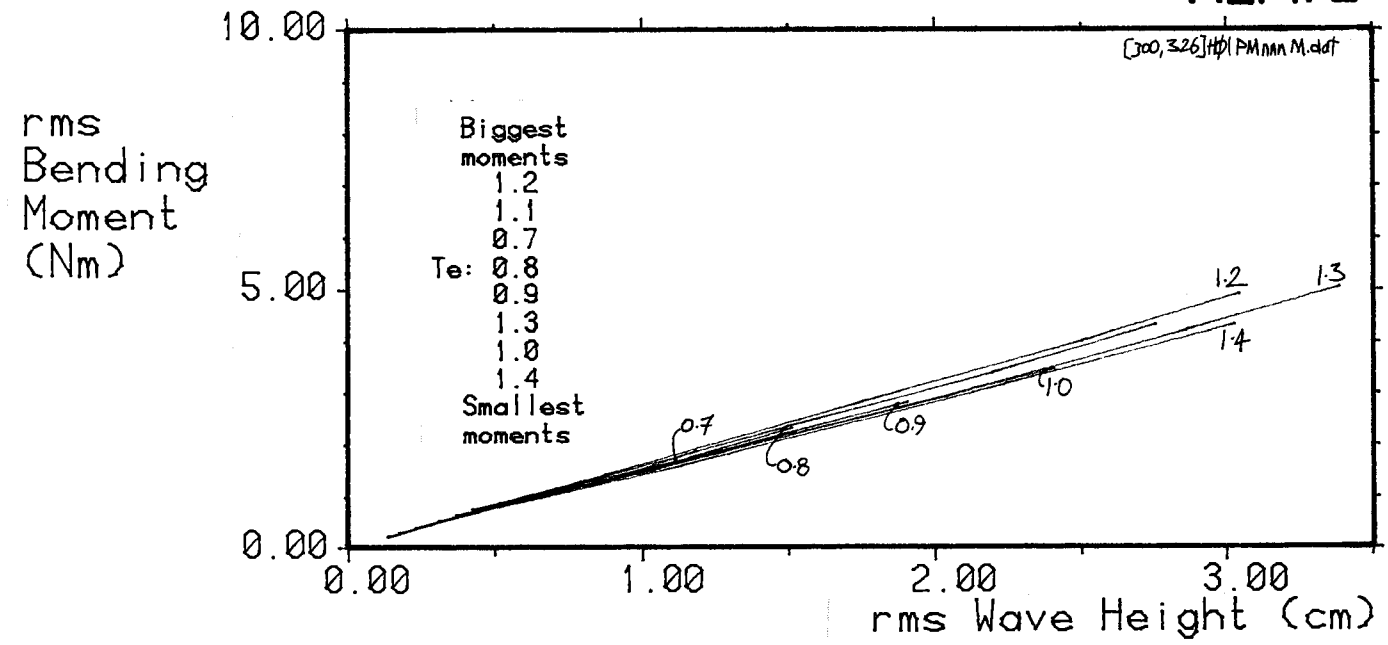

STIFFNESS 1000 Nm/rad

RMS values averaged over whole spine and grouped in families according to Te

GRAPH 4.11

exploring the SCATTER DIAGRAM

BENDING MOMENTS

PM Spectra, Mitsuyasu, 44joints
(varying Hrms Multiplier & Energy Period)

SURGE

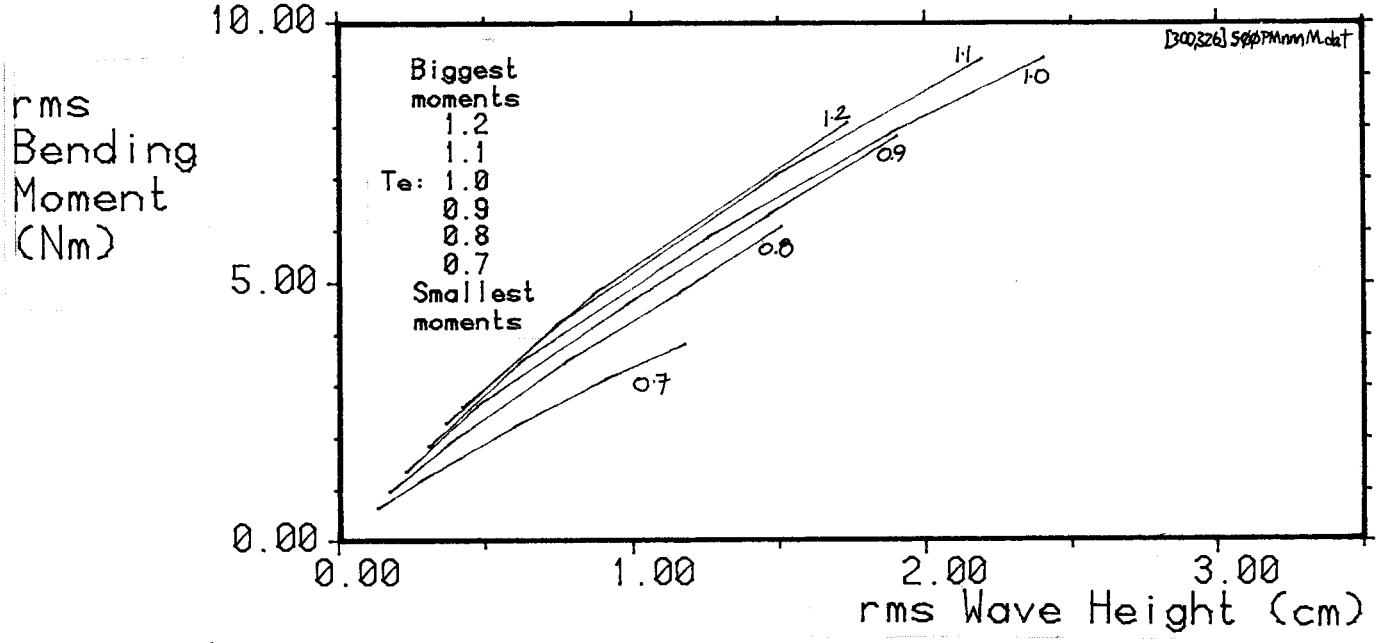

HEAVE

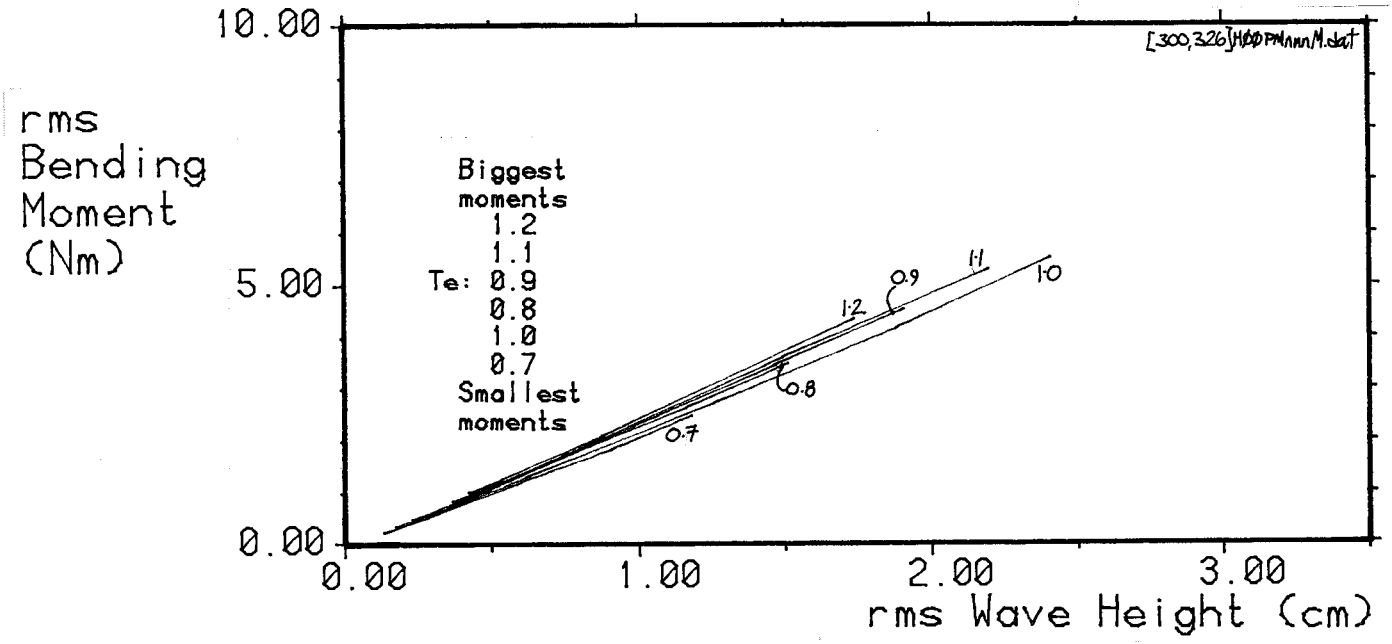

STIFFNESS 3500 Nm/rad

RMS values averaged over whole spine and grouped in families according to Te

GRAPH 4.12

exploring the SCATTER DIAGRAM

BENDING MOMENTS

PM Spectra, Mitsuyasu, 44joints
(varying Hrms Multiplier & Energy Period)

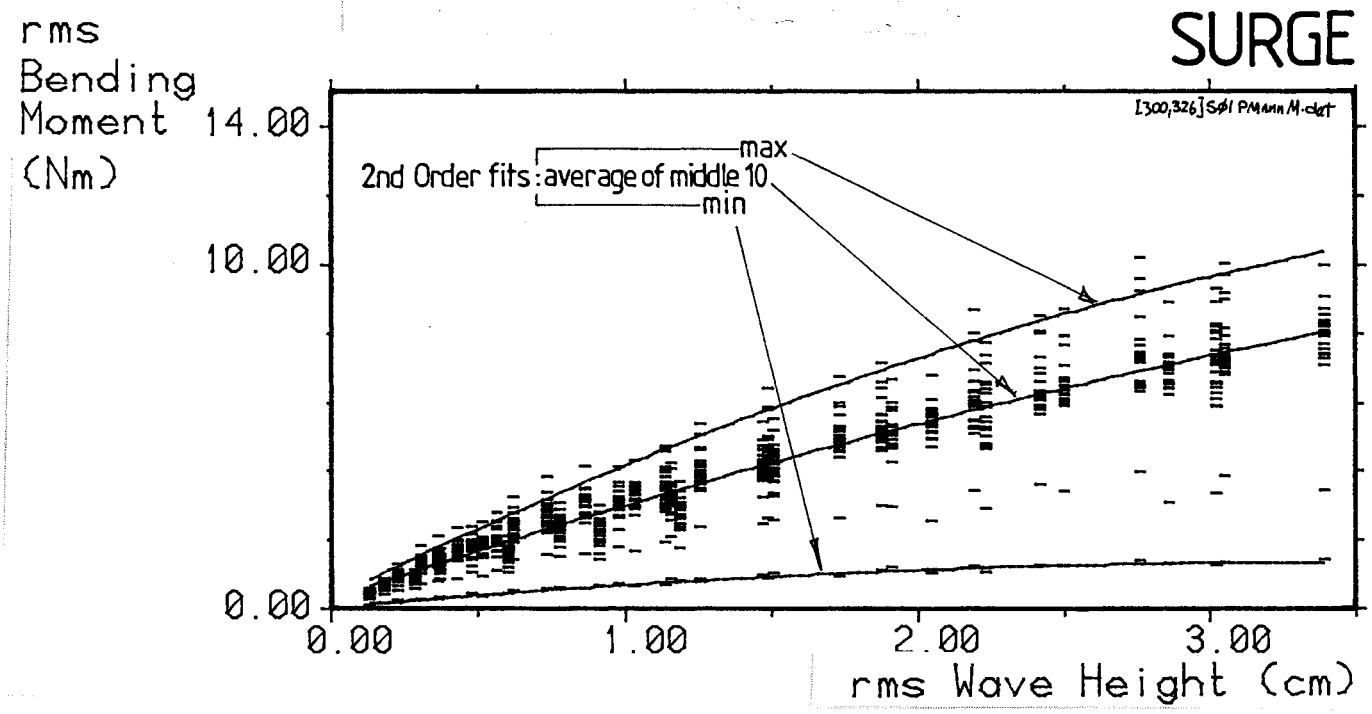

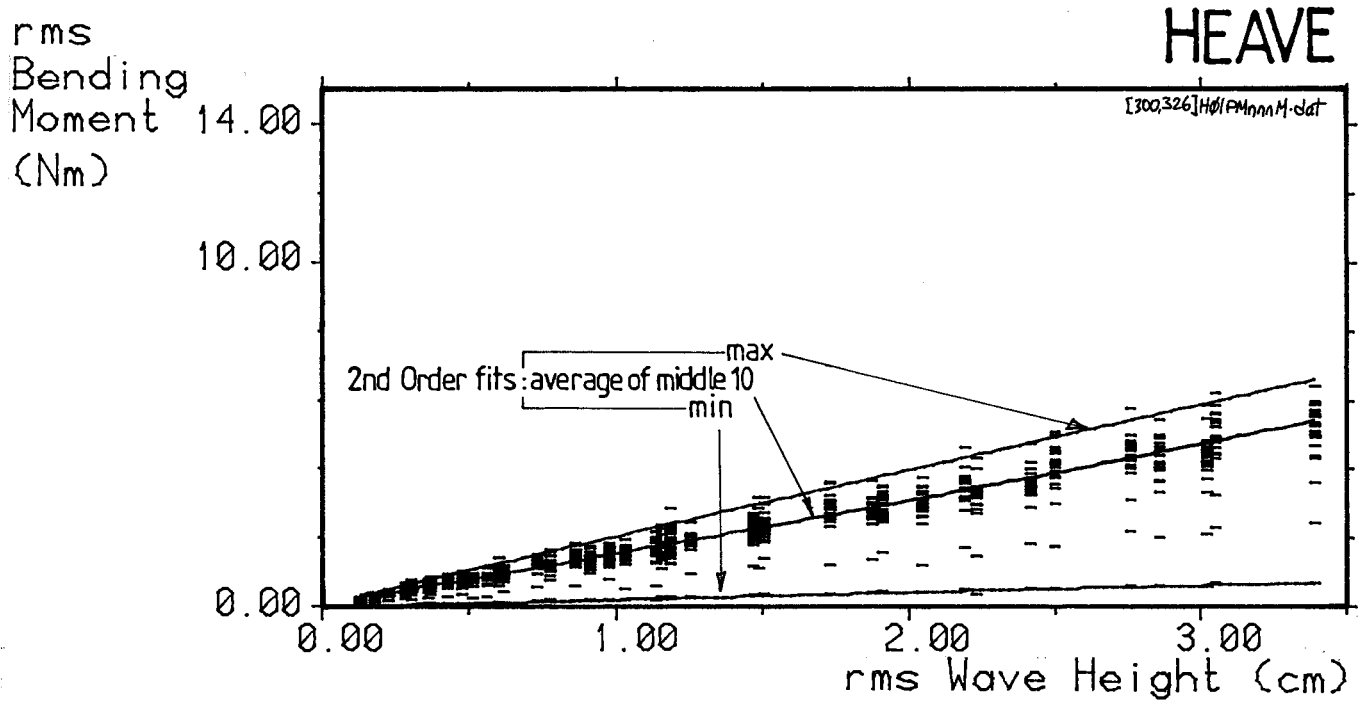

STIFFNESS 1000 Nm/rad

RMS values at EVERY JOINT
with curves fitted

GRAPH 4.13

exploring the SCATTER DIAGRAM

BENDING MOMENTS

PM Spectra, Mitsuyasu, 44joints
(varying Hrms Multiplier & Energy Period)

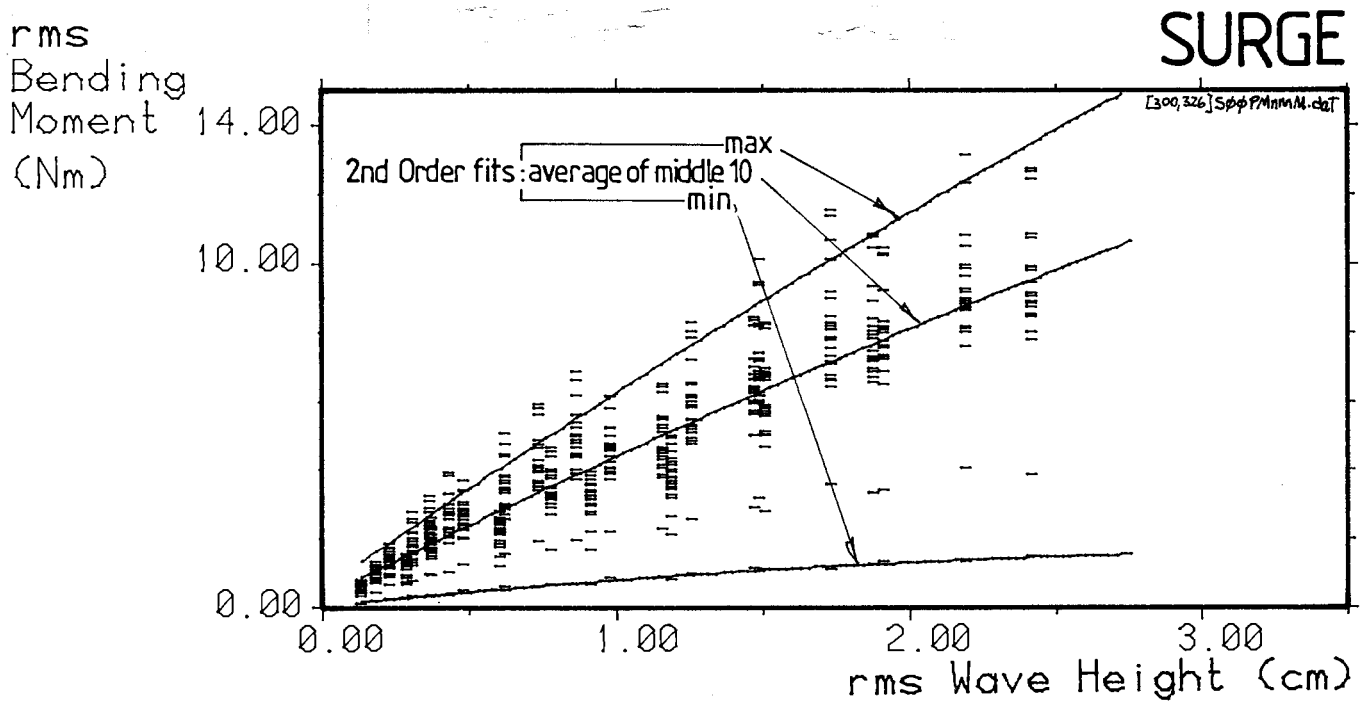

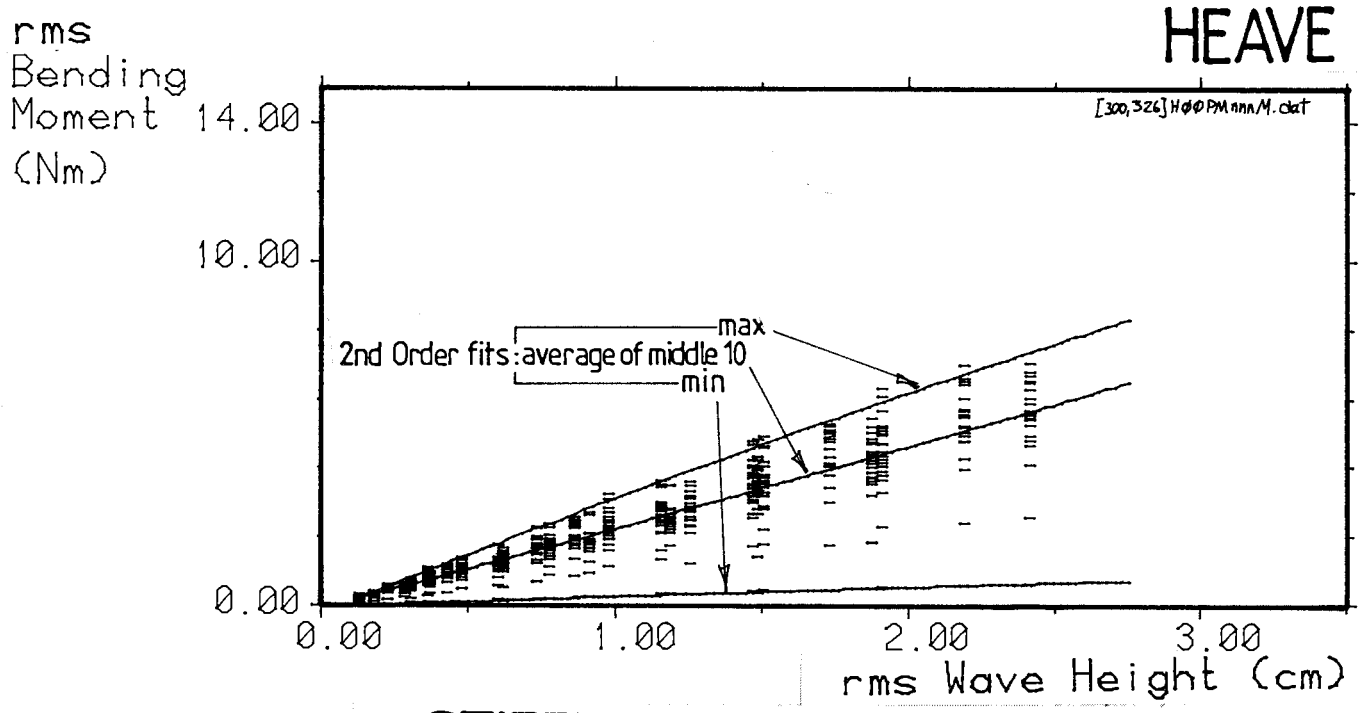

STIFFNESS 3500 Nm/rad

RMS values at EVERY JOINT
with curves fitted

GRAPH 4.14

exploring the SCATTER DIAGRAM

BENDING MOMENTS

PM Spectra, Mitsuyasu, 44joints
(varying Hrms Multiplier & Energy Period)

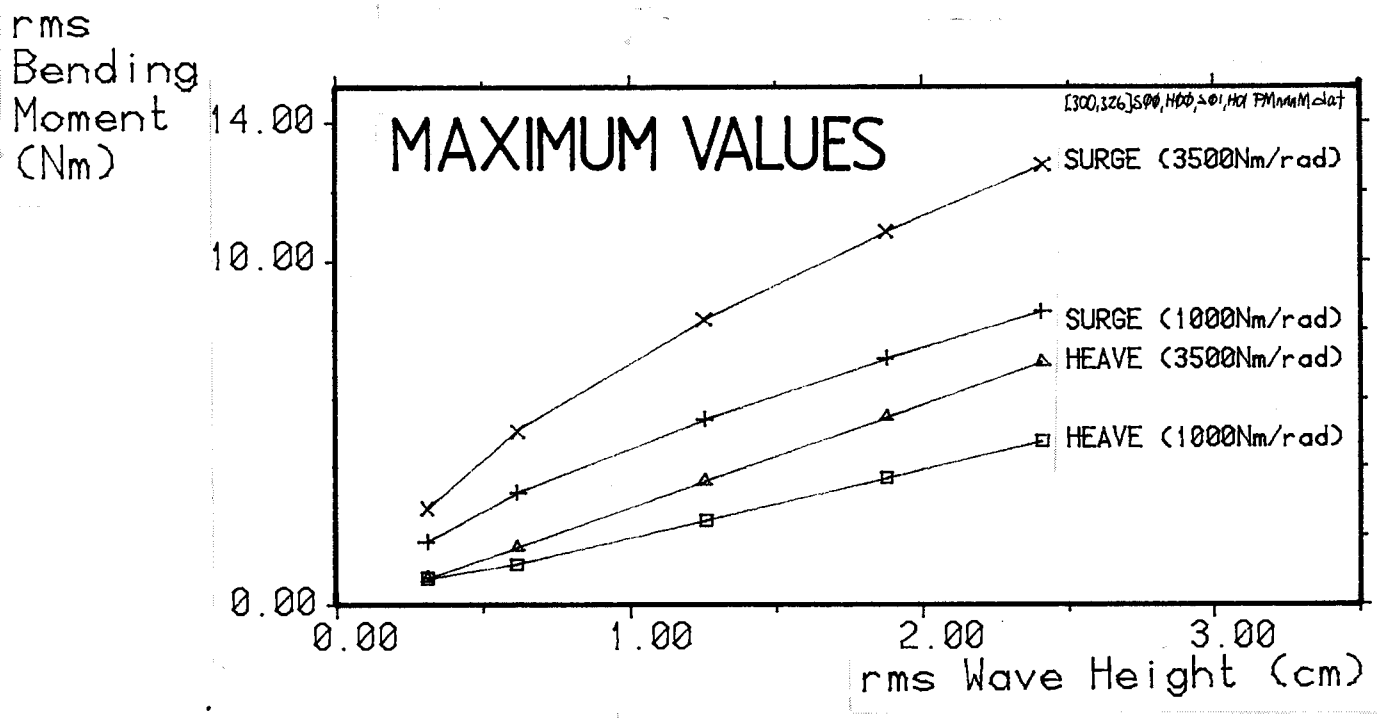

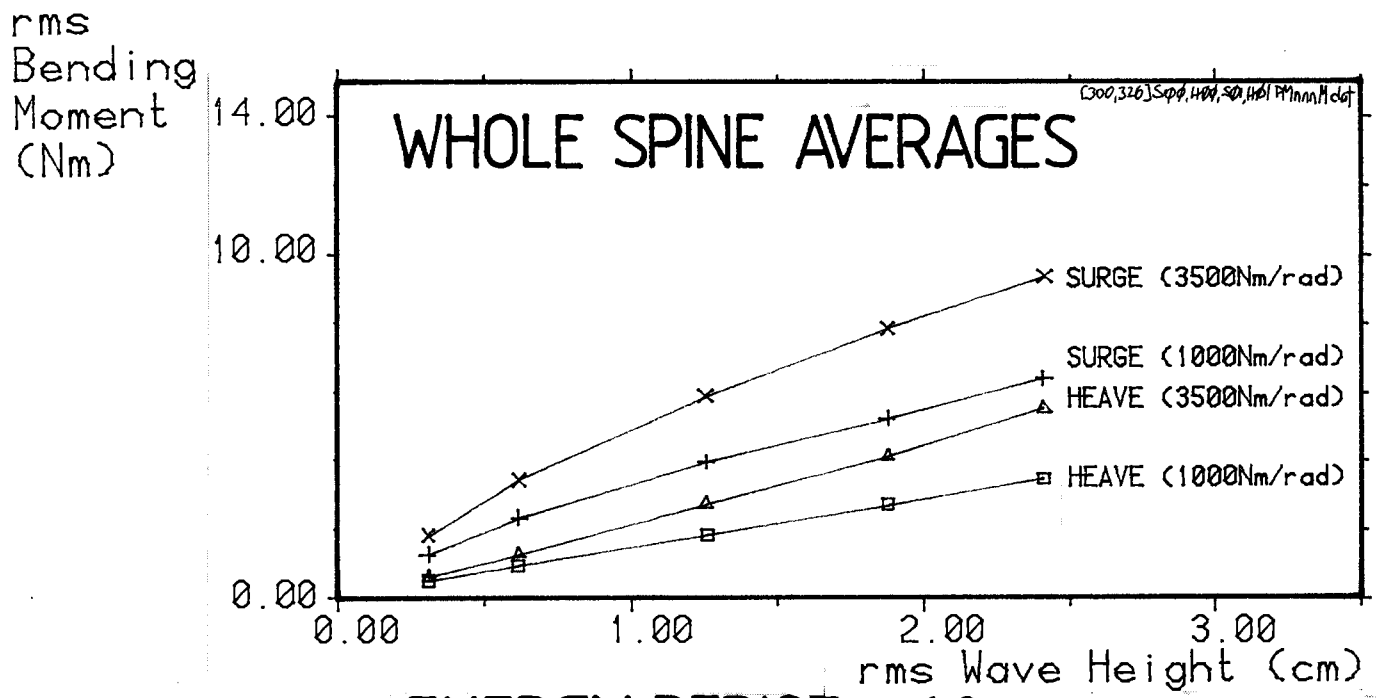

ENERGY PERIOD : 1.0sec

Comparisons of SURGE and HEAVE values
for 2 stiffnesses, at fixed Te

GRAPH 4.15

(4.A cont)

In graph 4.15 we extract the maximum value and the whole spine averages for heave and surge for the two stiffnesses. We were surprised to see the heave lines for two stiffness values intersecting at very low wave amplitudes. We prefer to use data from larger samples but a similar effect is indicated for the whole spine averages and we are inclined to trust the result.

The maximum root mean square surge value is more than twenty times the yield limit of our 1981 reference design. The peak instantaneous value would have been about three times the rms value and so the peak-to-yield ratio would be about sixty. Our preference for controlled yield points seems to be sound.

Graph 4.16 shows the relationship of bending moment to wave period for constant Hrms. The maximum values occur in the centre of the useful energy-generating band but the reduction to either side is barely detectable except for the very stiffest conditions. Energy period is the least important variable.

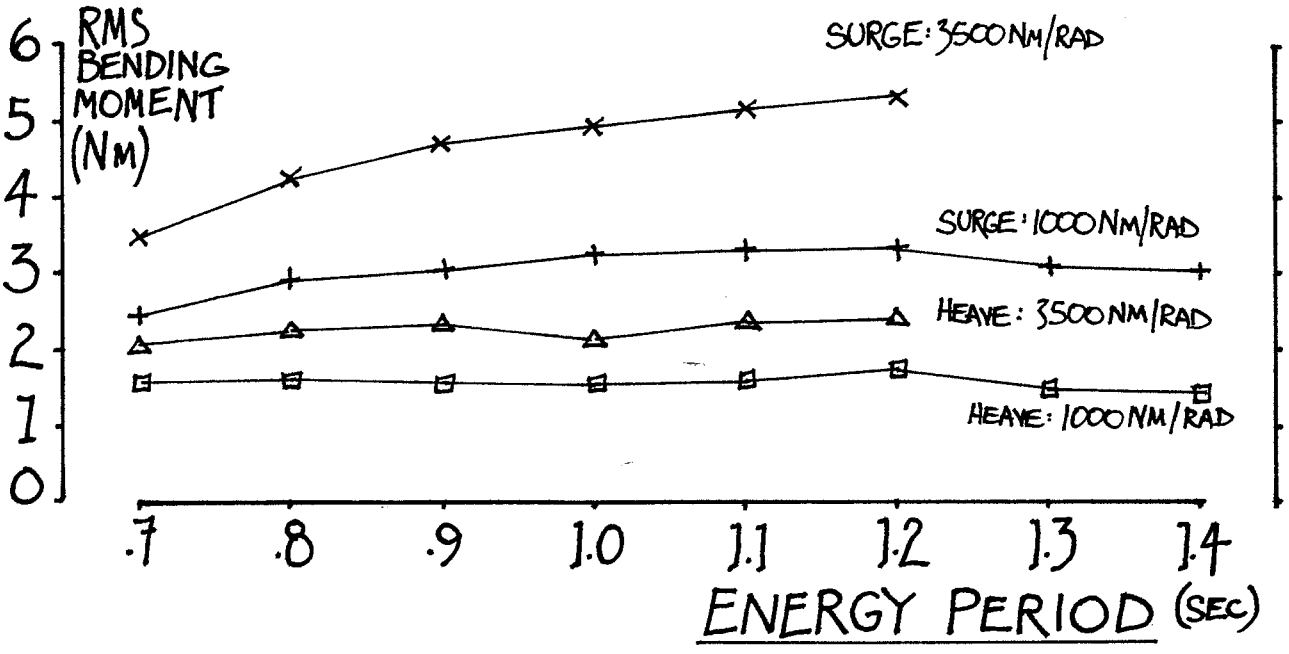

GRAPH 4.16 rms bending moments (average for all joints) against energy period, for Hrms = 1.0cm

(4.A cont)

Graph 4.17 shows superimposed simultaneous plots of surge moment against heave moment for every joint of a 36 joint model in a 1.0 sec PM $\cos^2$ sea. The joint stiffness was 1,000 Nm/rad. The heave data were obtained by taking the average values of the heave moment at either of the surge joints.

This method of deriving a synthetic heave measurement for a notional heave sensor at the position of a surge joint is open to some question because the correlation coefficient between the two heave joints is only 0.8. However we found that the rms value of the synthetic time series is on average only 1% lower than the value of the true time series.

The plot allows us to judge the accuracy of our estimate that there is about 90° phase shift between the two channels. It is interesting to compare this with page 28 of our slamming test report (ref L).

Each dot represents a probability density of 1 in 18,432.

It is premature to claim that the cost of post-tensioning steel and joint power plant can be reduced by as much as 25% because these measurements were taken without the torque limit which would have occurred at 1.5 Nm. Furthermore we should recall that the narrow tank variable coefficient work shows that, in many sea states, the required heave stiffness is a little greater than that for surge. Nevertheless there are some grounds to hope for savings in capital cost.

Instantaneous Bending Moments
SURGE against HEAVE

36 joints x 512 samples
1 sec, PM, Cos^2
stiffness: 1000 Nm/rad

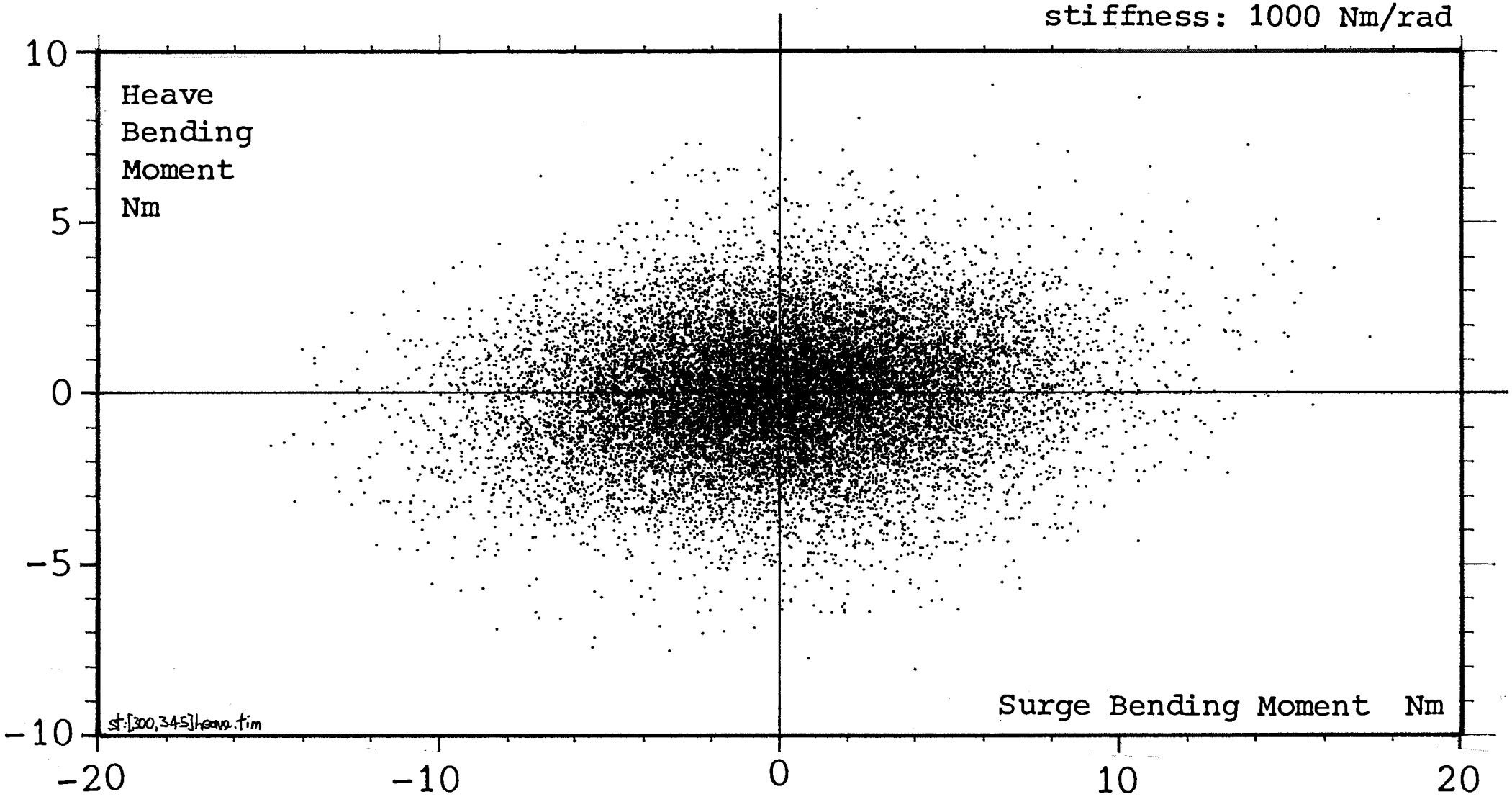

GRAPH 4.17

4.B EFFECTS OF VARYING JOINT STIFFNESS

We wanted to know:

a) How do spine bending moments vary with joint stiffness?

b) Are surge bending moments independent of heave stiffness?

c) Are heave bending moments independent of surge stiffness?

We used the same Pierson-Moskowitz sea throughout with an energy period of 1 second, a measured Hrms of 1.26cm and Mitsuyasu spreading. The spine was 18 metres long with 44 active joints and 6 moorings.

We varied surge and heave stiffness independently in 6 steps between 250 and 8000 Nm/rad, doubling the value at each change.

Graph 4.20 shows the basic results with bending moment arrays for surge and heave plotted together. Except where otherwise marked, the top curve in each plot is surge. The heave arrays tend to be about half the size of the surge arrays for equal surge and heave stiffnesses. Surge bending moments tend to be about 50% higher near the ends than they are in the middle, but in heave the results are more even.

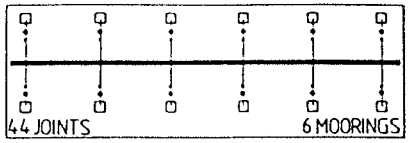

effect of JOINT STIFFNESS on Bending Moments

independently varying Surge and Heave stiffness

SAME sea throughout: 1.0sec,PM,Mitsuyasu, (pm104m)

Hrms: 1.26cm 44 joints

SURGE & HEAVE joints

SURGE Stiffness Nm/rad →

HEAVE Stiffness Nm/rad ↓

250 500 1000 2000 4000 8000

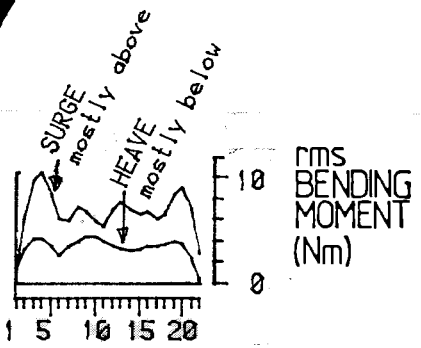

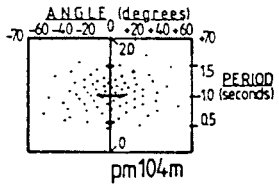

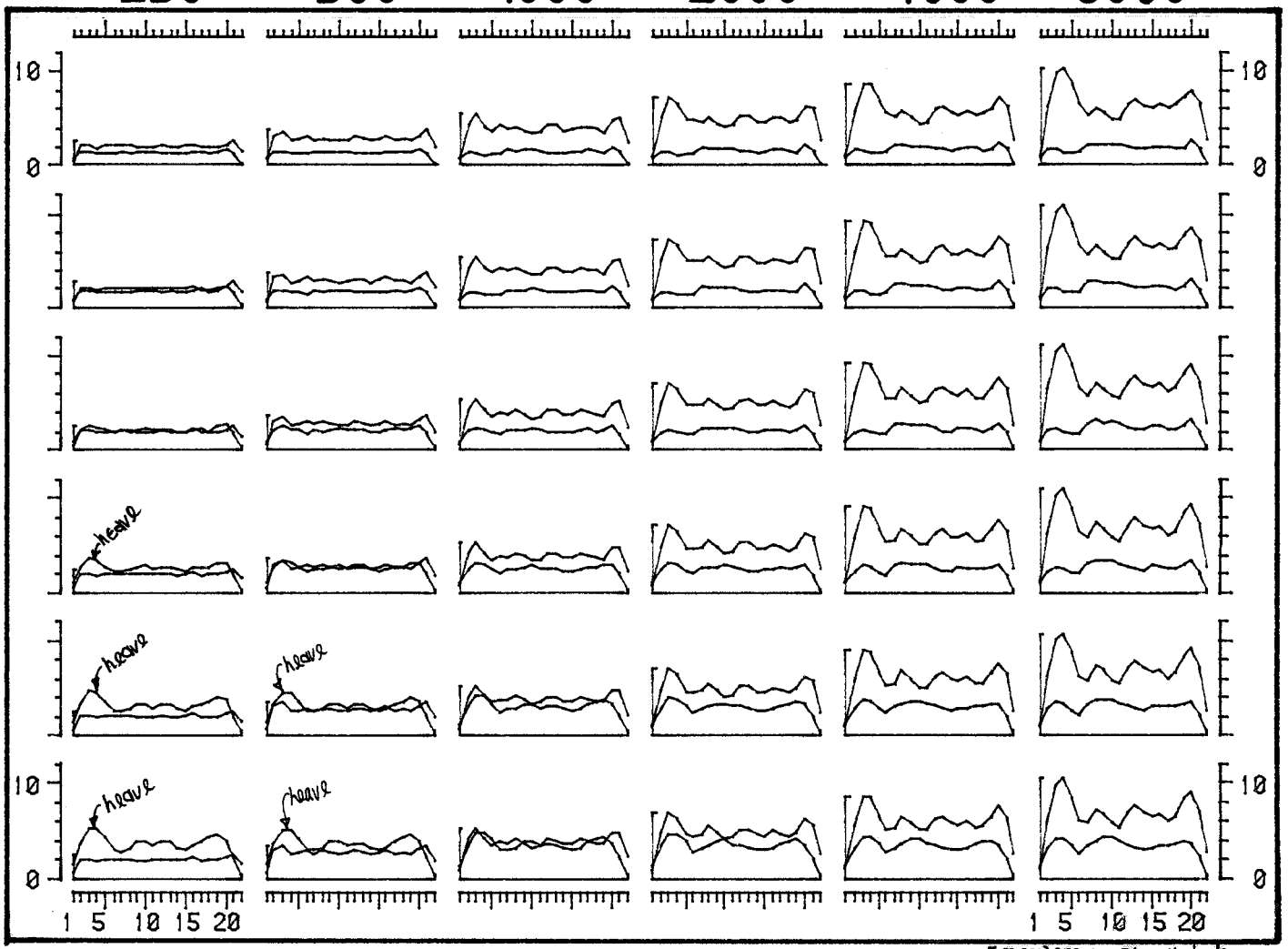

[500,326] SO2 HO2 PMammM.dat

GRAPH 4.20

(4.B cont)

Graphs 4.21 and 4.22 show the data separately in surge and heave with the arrays also collected together into 'projections' at the ends of rows and the bottoms of columns. We find this a useful way of summarising the effects of the 2 variables. Note that the surge vertical scale is twice the heave one.

On the surge page (graph 4.21), the right hand column of projections summarises the effect of varying surge stiffness. Each doubling of stiffness produces an approximately equal increment in the bending moment. The row of projections at the bottom shows that surge stiffness variations have very little effect on heave bending moments.

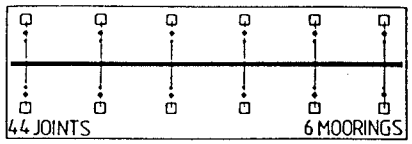

effect of JOINT STIFFNESS on Bending Moments

independently varying Surge and Heave stiffness

SAME sea throughout: 1.0 sec, PM, Mitsuyasu, (pm104m)

Hrms: 1.26cm 44 joints

SURGE joints

SURGE Stiffness Nm/rad

HEAVE Stiffness Nm/rad

250 500 1000 2000 4000 8000

PROJECTIONS

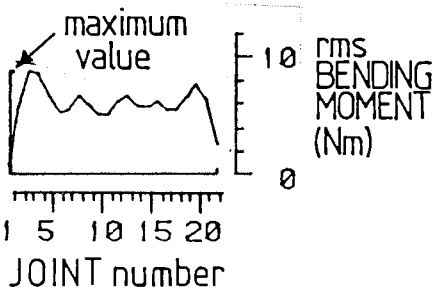

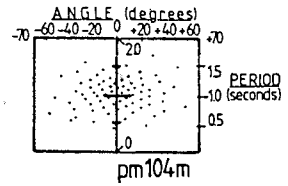

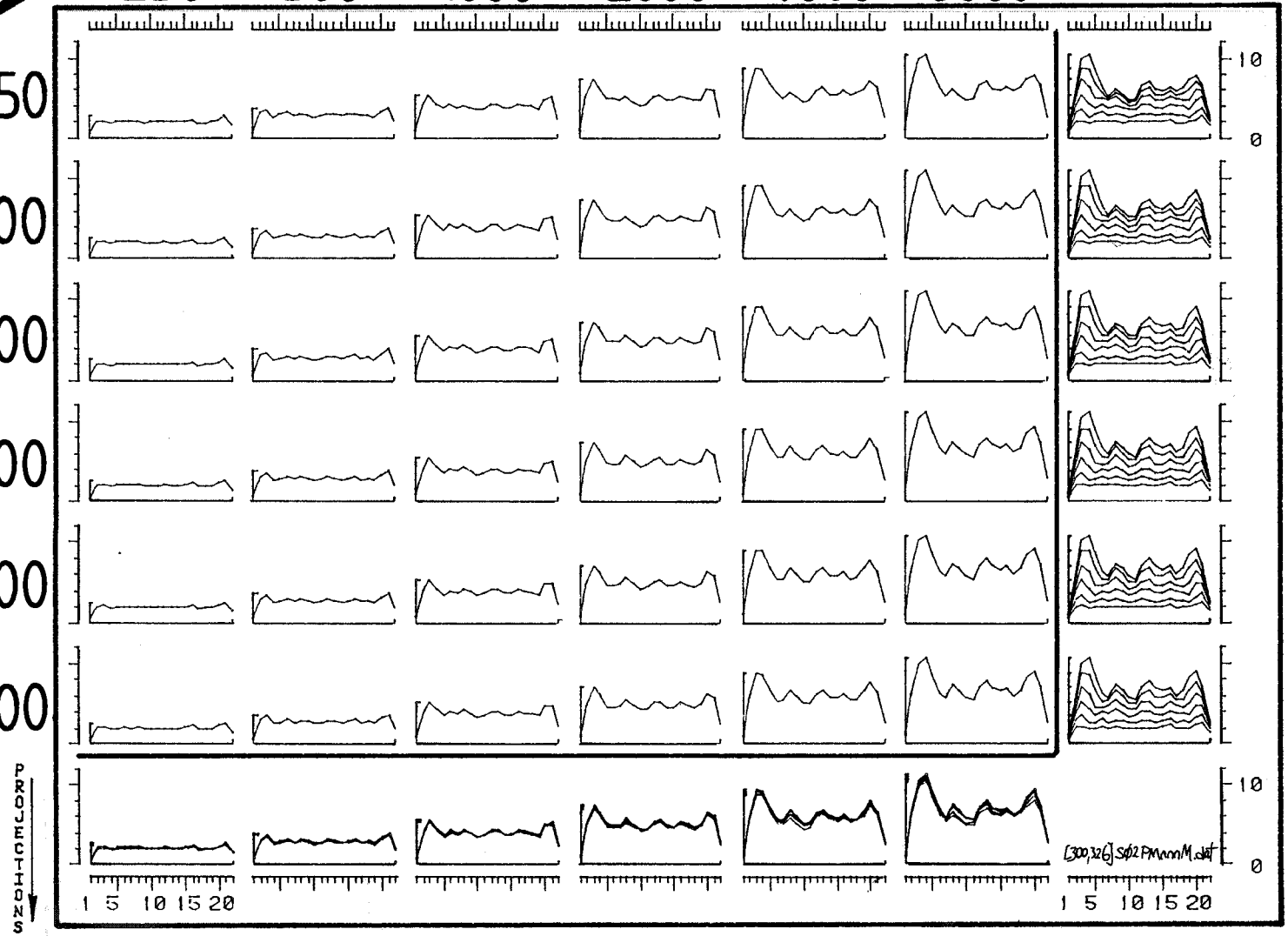

GRAPH 4.21

(4.B cont)

On the heave page, (graph 4.22) the row of projections at the bottom again shows that heave bending moment increments are about constant for doublings of stiffness. But the column of projections at the right shows a little more 'crosstalk' than is visible on the surge page. At low heave stiffnesses heave bending moments in the middle of the spine tend to increase with surge stiffness, while at high heave stiffnesses bending moments at the ends tend to get smaller. However the effects are small and it is safe to say that, for engineering purposes, the two directions are independent. We cannot relieve the surge bending moments by running away in heave. We had hoped that this would be possible when we discovered the death valley effect (see page 4.1 of our 4th year report, ref b).

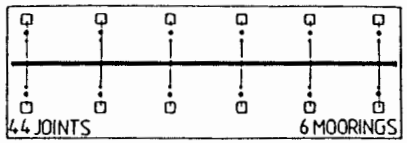

effect of JOINT STIFFNESS on Bending Moments

independently varying Surge and Heave stiffness

SAME sea throughout: 1.0sec,PM,Mitsuyasu, (pm104m)

Hrms: 1.26cm 44 joints

HEAVE joints

SURGE Stiffness Nm/rad

HEAVE Stiffness Nm/rad

250 500 1000 2000 4000 8000

PROJECTIONS

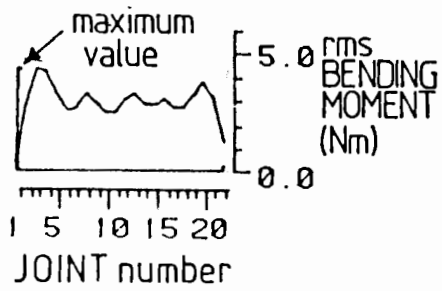

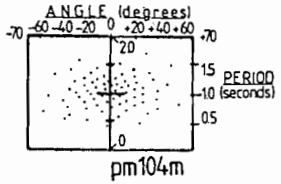

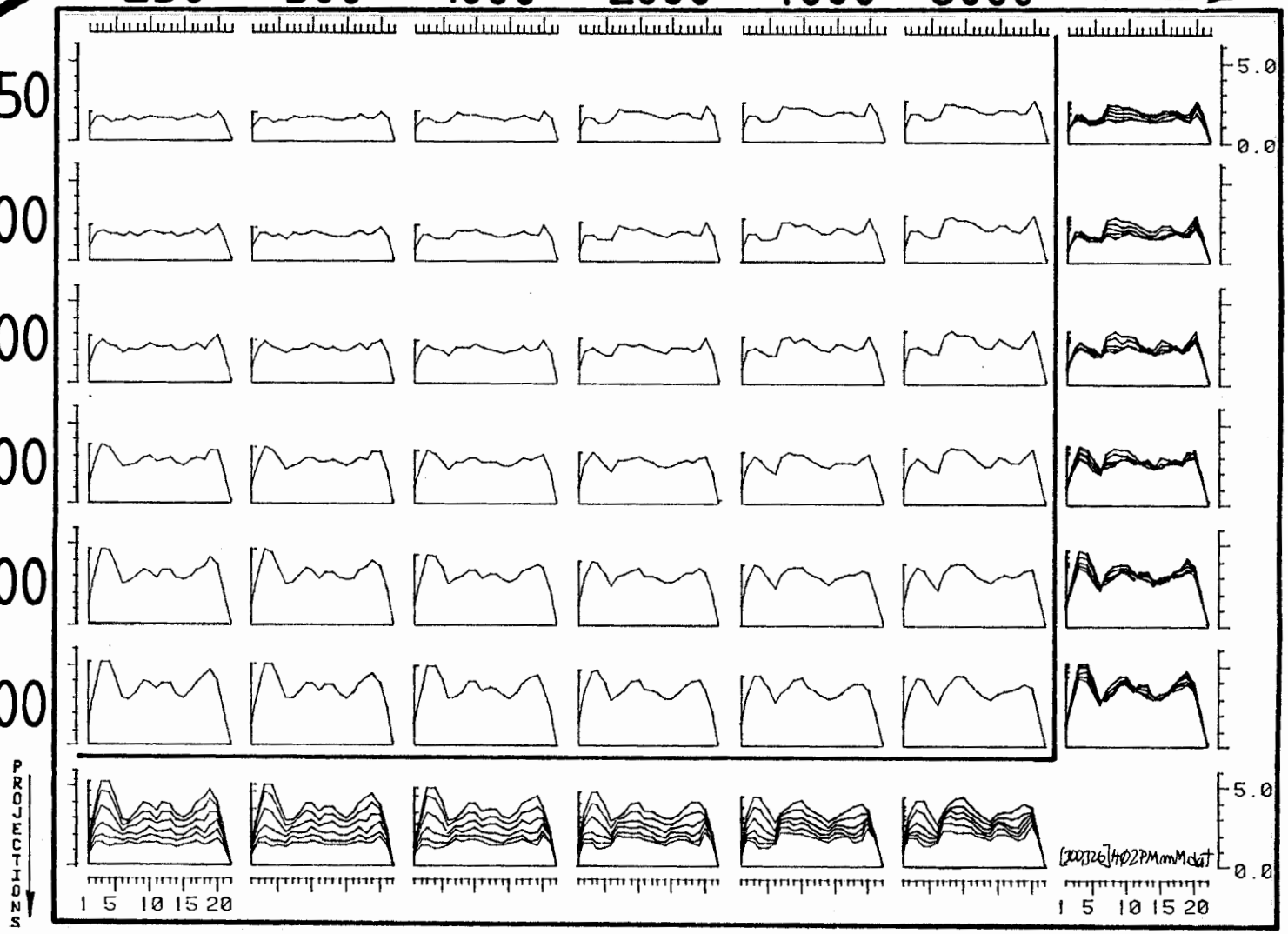

GRAPH 4.22

(4.B cont)

Summary of Effects of Varying Joint Stiffness: graphs 4.23 and 4.24

Graph 4.23 shows the data re-plotted to illustrate the relationship between stiffness and bending moment.

Separate curves are drawn in surge and heave for:

1. the rms bending for the most highly stressed joint;

2. the average of the rms bending moment for the middle six joints;

3. the average of the rms bending moments of all the joints.

The top graph has a linear horizontal stiffness scale, and the bottom one has a log scale.

The curvatures at the left on the upper plot do not suggest zero bending moments for zero applied stiffnesses, and some residual reaction forces at the joint are clearly indicated. The joint control system (see section 2) had a rather low closed loop-gain of about 2.7 in the configuration used for the lowest stiffness experiments, implying that the background stiction and damping of the joints would only be reduced to about 40% of the inherent values. Since these experiments we have altered feed back current values to allow more loop-gain at very low stiffness.

The log plots are remarkably straight from 500 Nm/rad upwards. However the higher stiffness values will in fact be modified by the inherent compliance of the spine units (see section 6.E), so that the bending moment graphs should really be compressed horizontally at the right. This is done on the next page.

effect of JOINT STIFFNESS on Bending Moments

independently varying Surge and Heave stiffness

44 joints 1.0sec,PM,Mitsuyasu, Hrms: 1.26cm

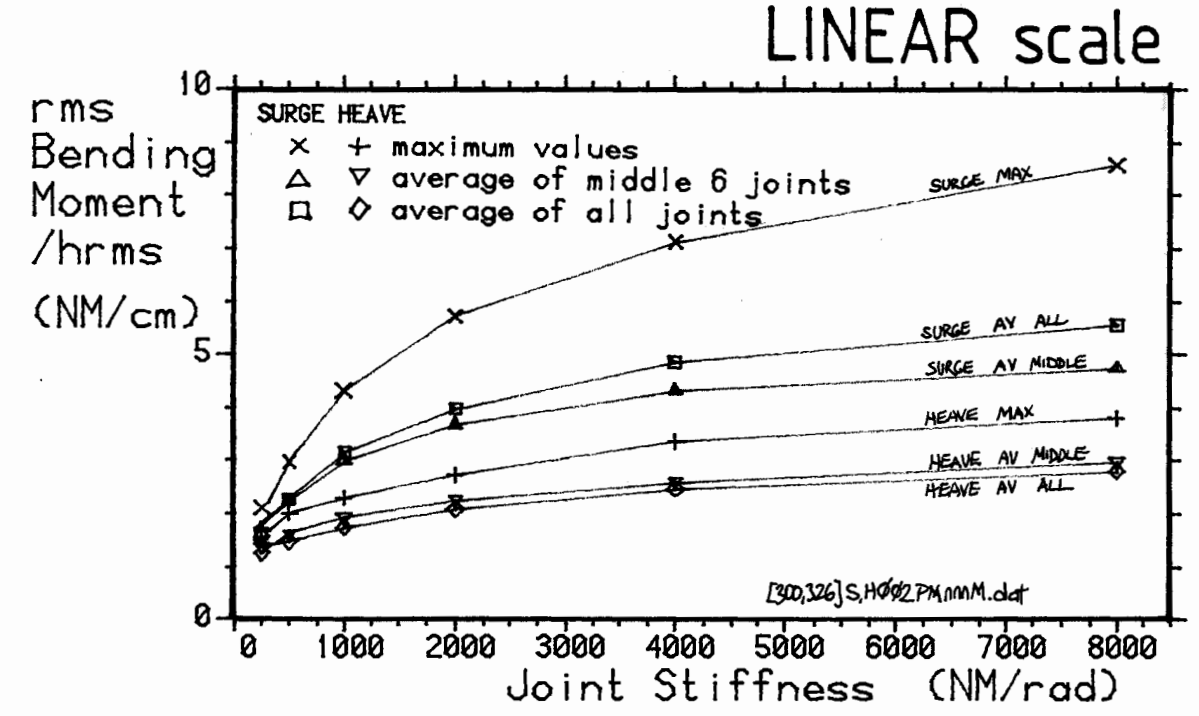

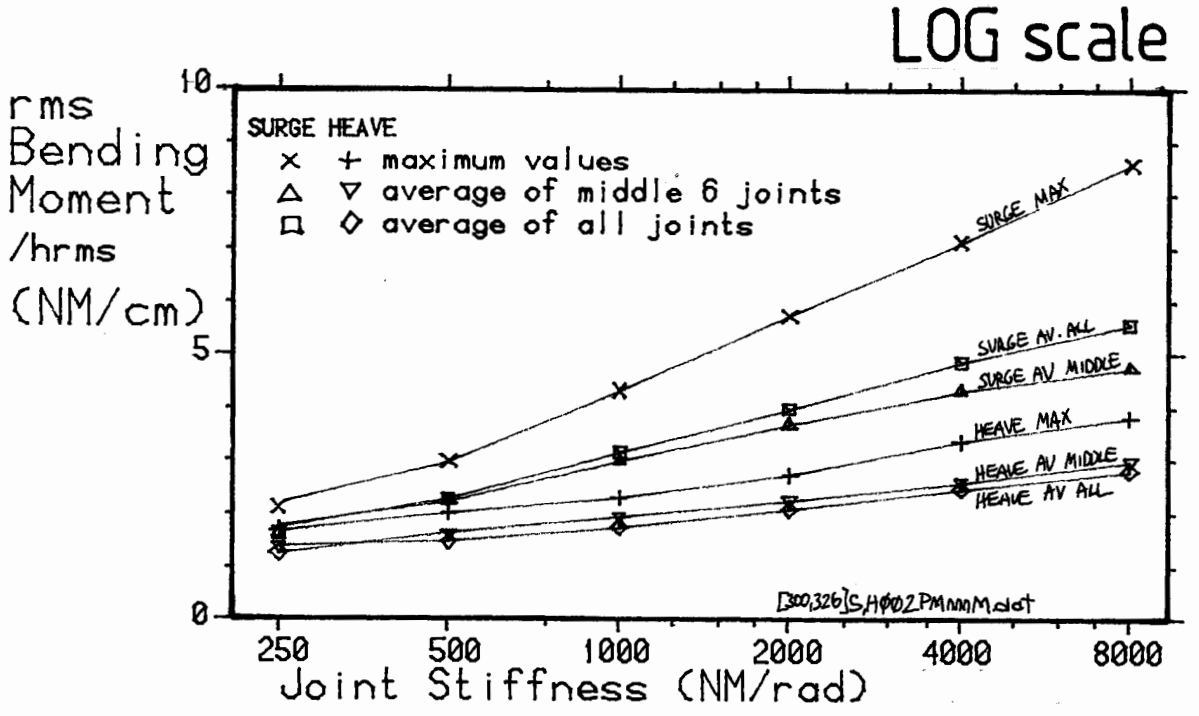

GRAPH 4.23

(4.B cont)

Graph 4.24 shows rms bending moments plotted against stiffness with the nominal stiffness values 'corrected' using the values suggested in table 6.7 (section 6.E). Upward tendencies are visible in the log plots for the maximum values, though the average values for the whole spine are fairly linear over the range of stiffnesses from 1000 to 5000 Nm/rad.

The results of variable coefficient control in the narrow tank lead us to believe that the desirable joint stiffness will be much lower than we had expected when the model was designed and we do not propose to improve high stiffness performance.

effect of JOINT STIFFNESS on Bending Moments

with estimated stiffness CORRECTIONS

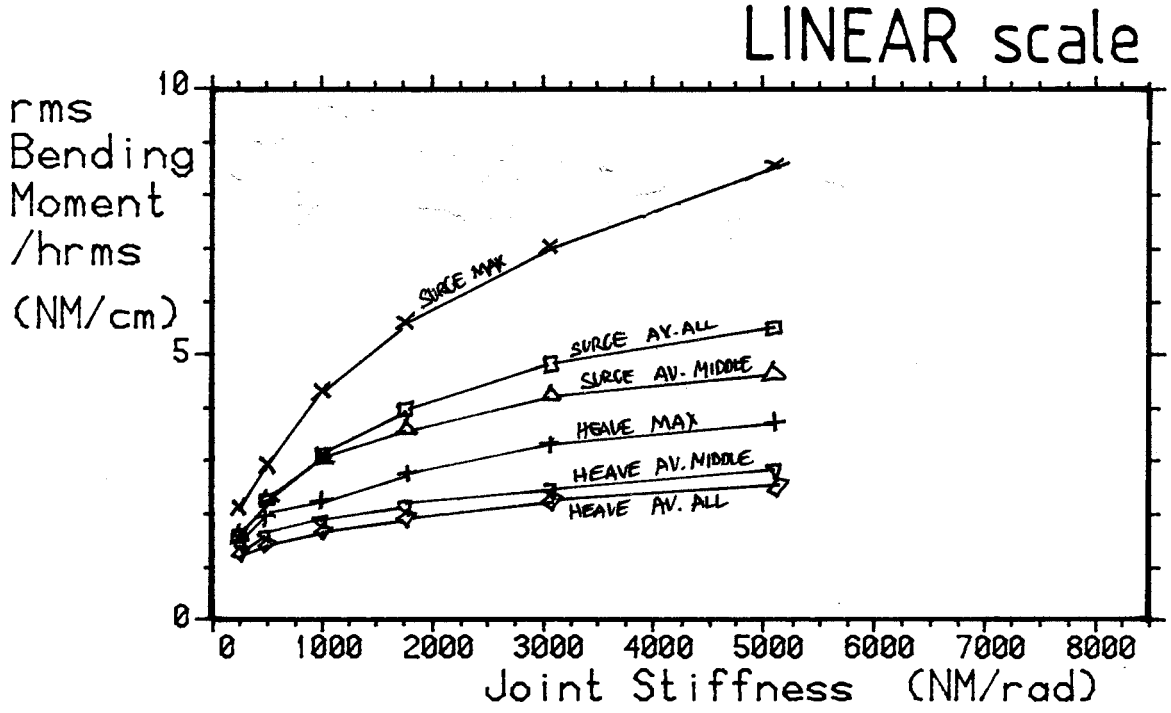

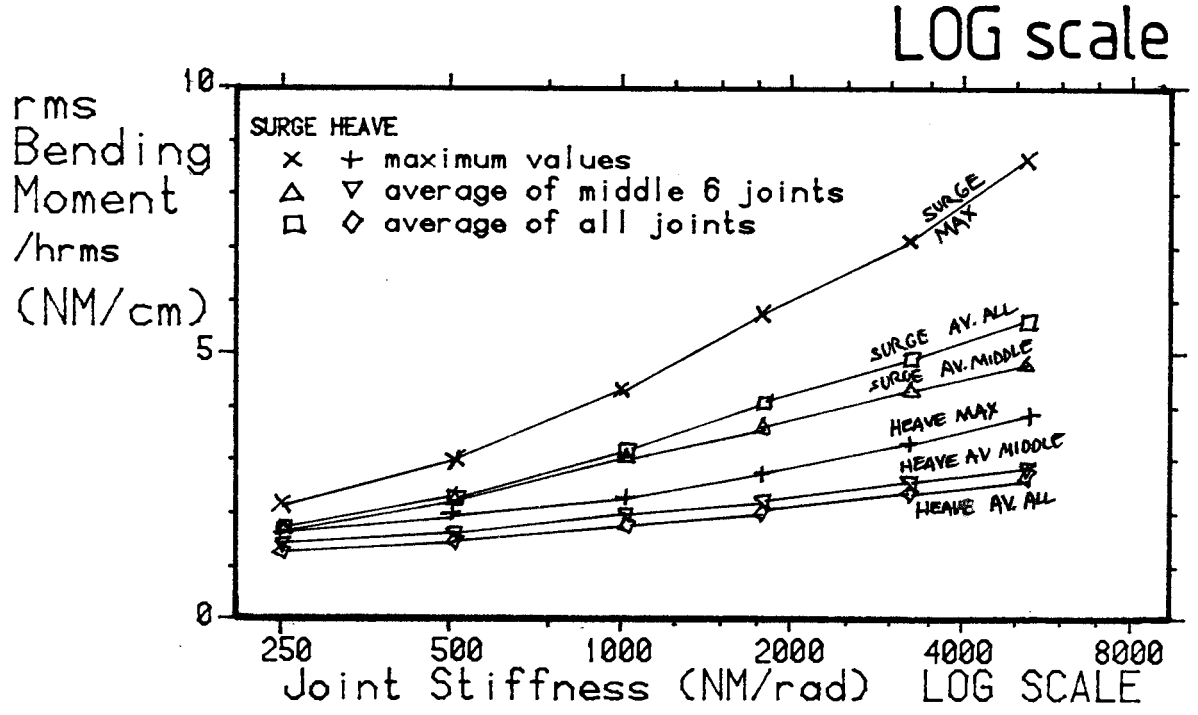

GRAPH 4.24

4.C EFFECT OF VARYING SEA OFFSET ANGLE AND ENERGY PERIOD

All previous tests used seas with a mean approach angle of 90°, i.e. westerlies hitting a spine lying north-south.

In this section we vary both the approach direction and the energy period. The amplitude was held to the Pierson Moskowitz norm for each energy period. Stiffness was 1000 Nm/rad throughout and the Mitsuyasu spread was used throughout. The pox-plot for these tests is that of graph 3.4. The results are given in graph 4.30.

Central approach directions have equal amplifications of bending moments at each end as expected from previous work.

Offset approach angles raise the moments at the down-wave end and depress those at the windward end. The ratio approaches 3:1 for 40 degree offset.

When surge bending moments are normalised by division by Hrms to the power 0.8 we can see on graph 4.31 a flat central region for low values of Te but at the longest ones there is a rise with distance along the spine.

The accumulations projected to the right-hand column show a very nice symmetry, at least as far as a Te of 1.4 seconds. They also show that there is more bending moment skew at longer Te.

Graph 4.32 shows the same effects are present but less pronounced for normalised heave.

effect on Bending Moment of varying SEA OFFSET ANGLE and ENERGY PERIOD

Offset ANGLE (degrees) →

Energy PERIOD (seconds) ↓

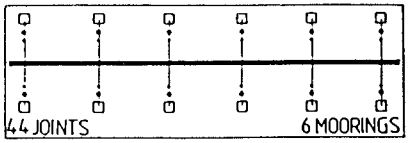

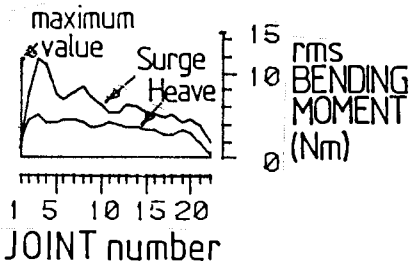

44 joints

Stiffness: 1000 Nm/rad

PM spectra, Mitsuyasu spreading; sea set: PM 'a'

SURGE & HEAVE

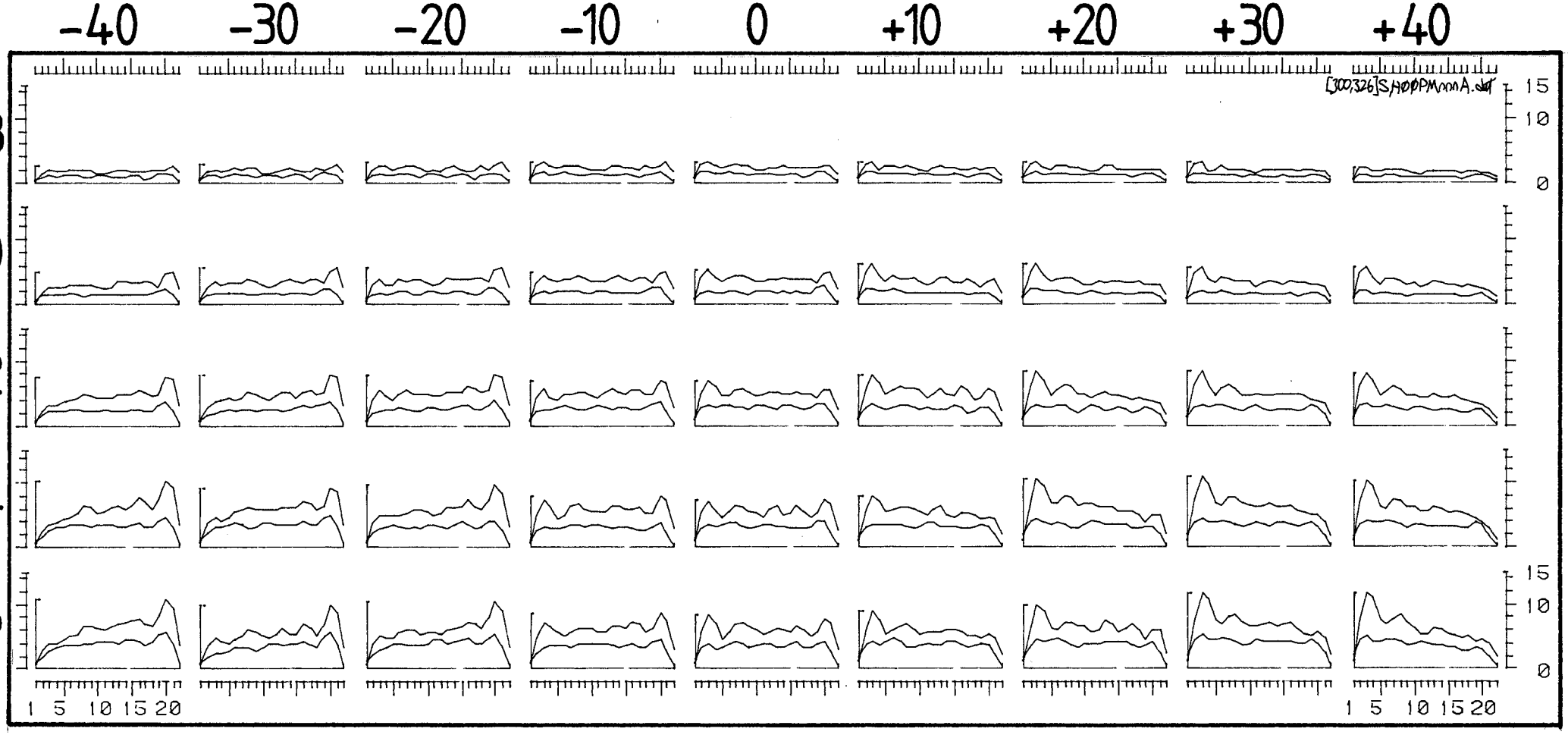

GRAPH 4.30

effect on Bending Moment of varying SEA OFFSET ANGLE and ENERGY PERIOD

Stiffness: 1000 Nm/rad 44 joints
PM spectra, Mitsuyasu spreading; sea set: PM 'a'

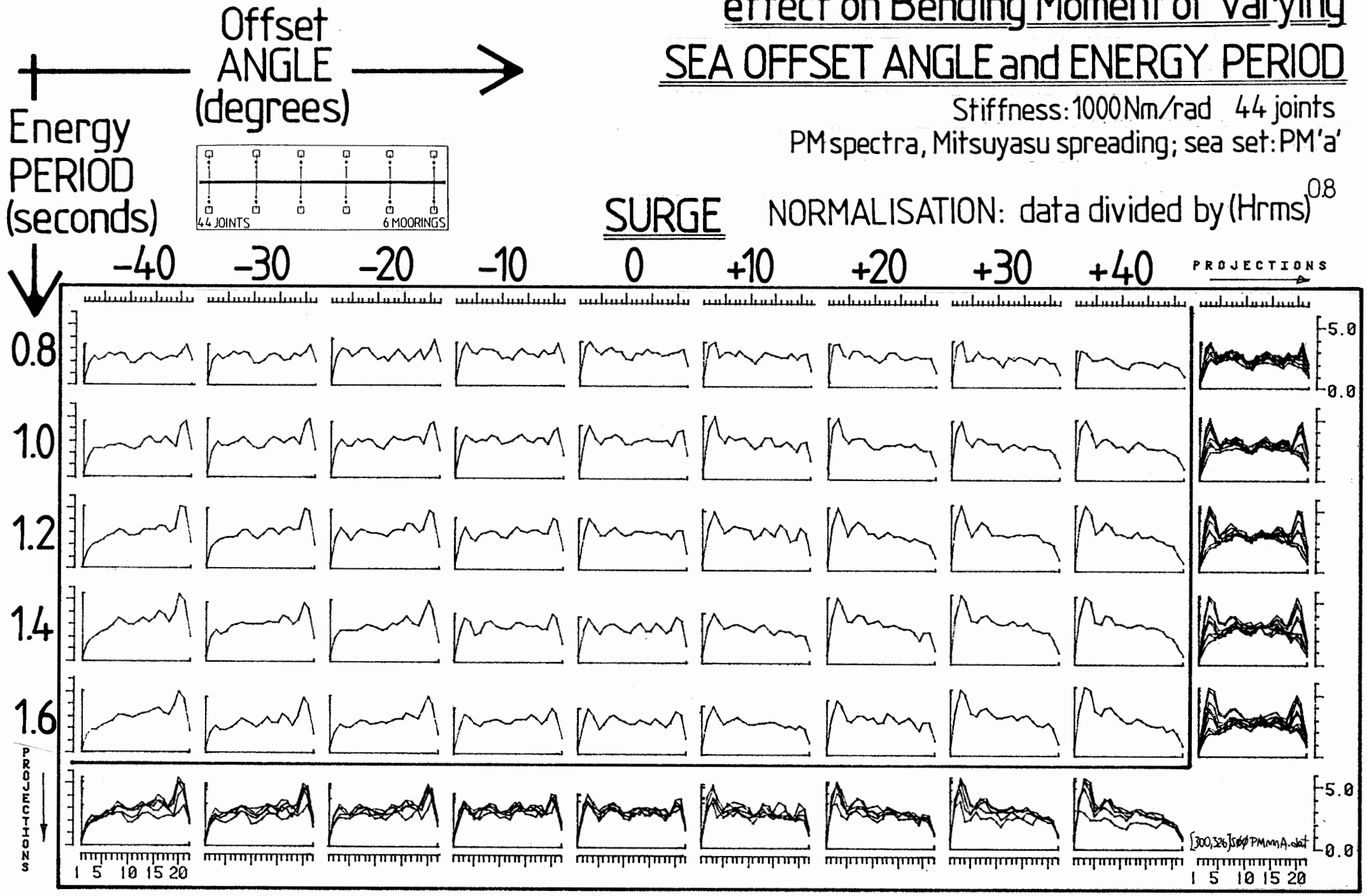

GRAPH 4.31

effect on Bending Moment of varying SEA OFFSET ANGLE and ENERGY PERIOD

Stiffness: 1000 Nm/rad 44 joints
PM spectra, Mitsuyasu spreading; sea set: PM 'a'

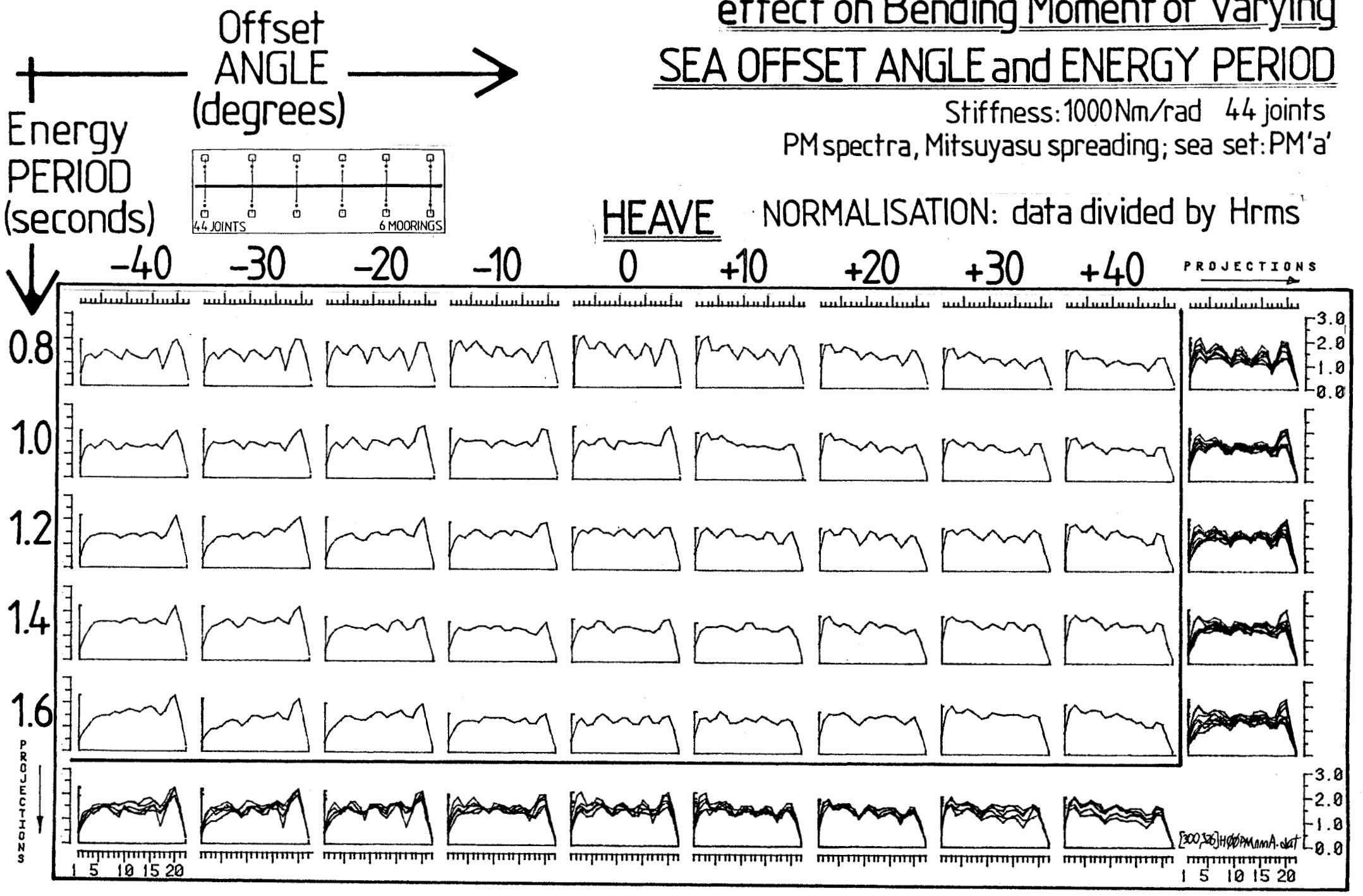

GRAPH 4.32

4.D EFFECT OF VARYING SEA OFFSET ANGLE AND SPREAD

In this series we varied angular spread (the value of **S** in the $\mathbf{Cos^S}$ spreading function) and angular offset, keeping energy period constant at 1 second and stiffness constant at 100 Nm/rad. The pox-plot is given in graph 3.5.

It is not surprising to see in graph 4.40 that narrow spreads generate wide variations of bending moments for small offset angles whereas wide seas with **s = 2** show no change with angle. A spread of **s = 2** is a little wider than Mitsuyasu. The Mitsuyasu function is more tightly bunched at its central periods and angles (see pox-plots 3.4 and 3.5).

It is very unusual to see that, for 10 degrees offset and the narrowest spread, the heave moments at one joint exceed the surge value.

The normalised results on graphs 4.41 and 4.42 show that heave maxima occur at about 10 degrees of offset whereas surge maxima are at 20°.

effect on Bending Moments of varying SEA OFFSET ANGLE and SPREAD

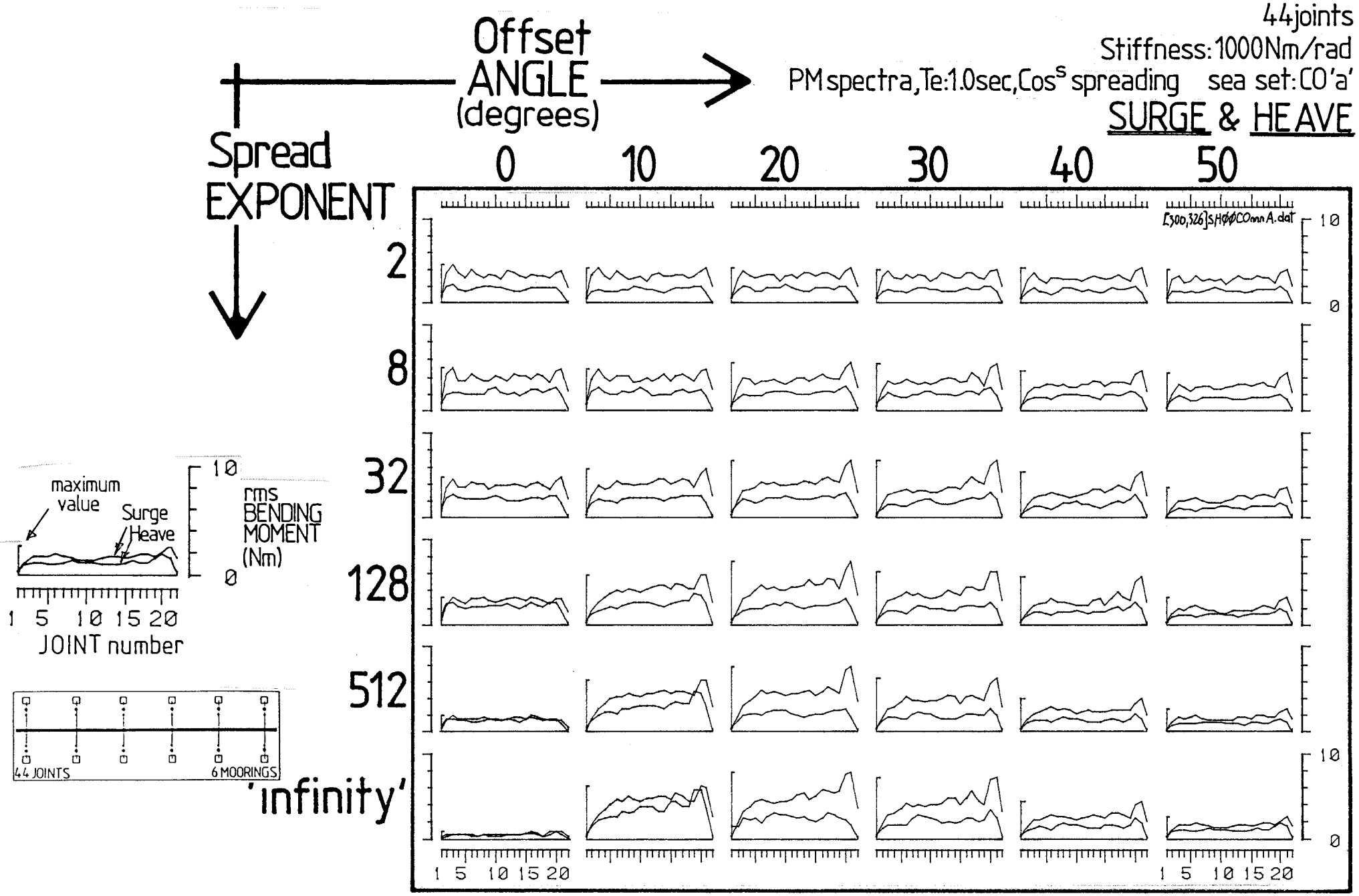

GRAPH 4.40

effect on Bending Moments of varying SEA OFFSET ANGLE and SPREAD

Stiffness: 1000Nm/rad 44joints

PM spectra, Te: 1.0sec, Cos^s spreading sea set: C0'a'

NORMALISATION: data divided by $(Hrms)^{0.8}$

Offset ANGLE (degrees) →

Spread EXPONENT ↓

0 10 20 30 40 50 PROJECTIONS →

2

8

32

128

512

'infinity'

PROJECTIONS ↓

5.0 0.0

1 5 10 15 20

this page:
SURGE
Bending Moments

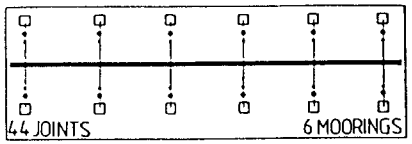

GRAPH 4.41

effect on Bending Moments of varying SEA OFFSET ANGLE and SPREAD

Stiffness: 1000Nm/rad 44joints

PM spectra, Te: 1.0sec, Cos^s spreading sea set: CO'a'

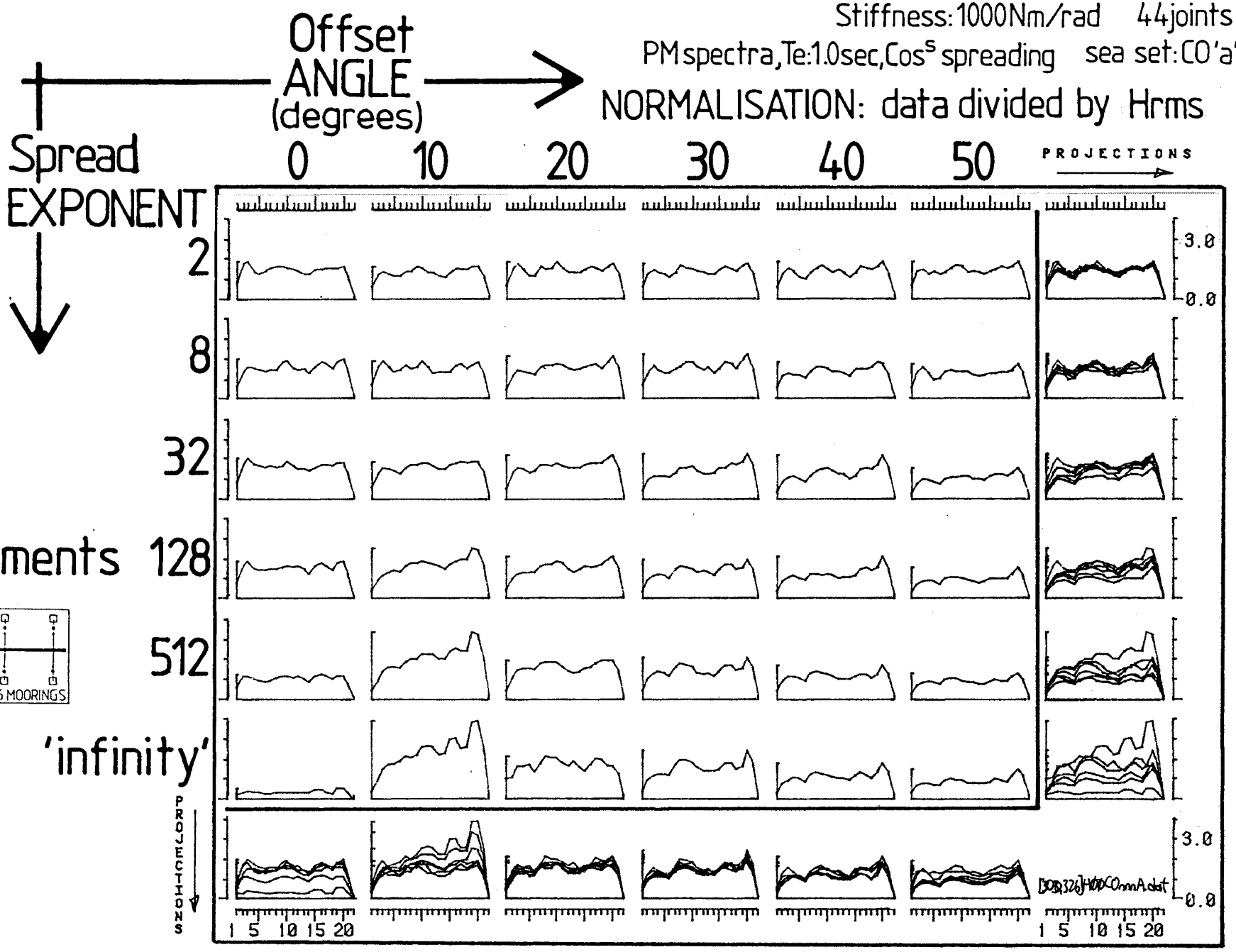

this page:

HEAVE

Bending Moments

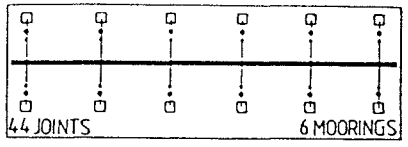

GRAPH 4.42

4.E BENDING MOMENTS IN THE SOUTH UIST SPECTRA

In this series of tests we use the IOS set of 46 spectra measured at South Uist. (The selection procedure is described in section 6.G).

The surge and heave bending moments of the 46 'a' set are shown on graph 4.50. Model length was increased to 48 joints and the stiffness was held at 1000 Nm/radian. It is interesting to look at the normalised surge results in graph 4.51 in which bending moments are divided by measured $Hrms^{0.8}$. Compare results for seas 220 and 223 and then look at their pox-plots on graph 3.6.

We see little end-enhancement for low spread seas, for example 201, 210, 212, and some asymmetrical enhancements predictable from our earlier offset tests.

In normalised heave (graph 4.52,in which scale is doubled) we see much less difference between seas. Look again at 220 and 223.

Test 378 shows relatively more enhancement than for the corresponding surge result.

Bending Moments in the South Uist 46 SPECTRA

48 joints Stiffness: 1000 Nm/rad

sea set: SU'a'

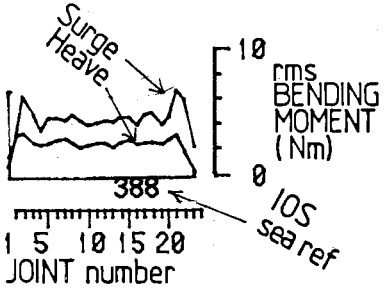

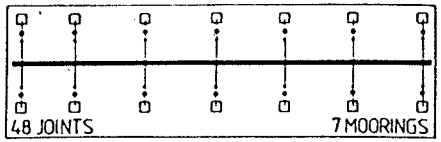

SURGE & HEAVE joints

the 46 SPECTRA 'a' set

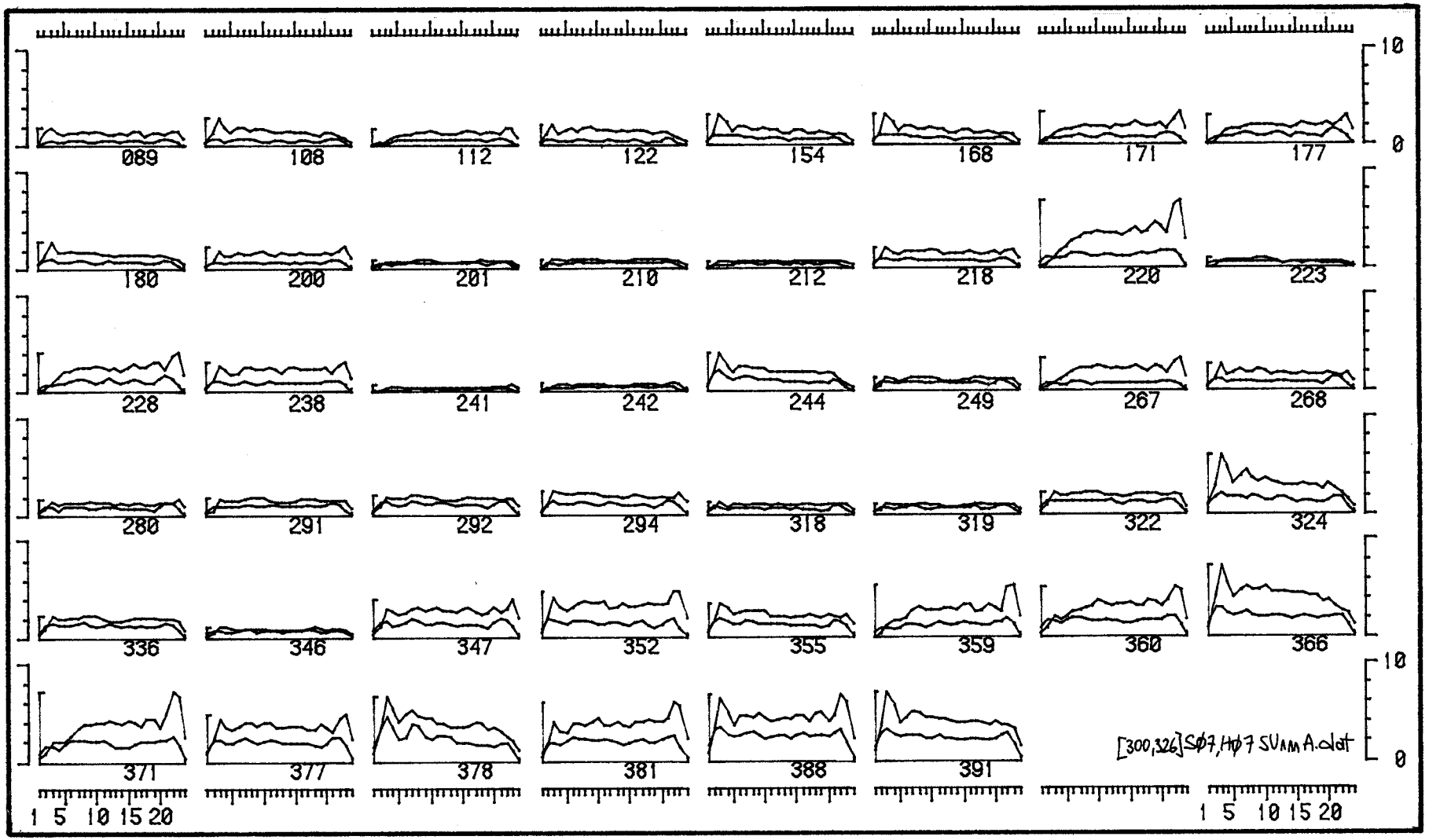

GRAPH 4.50

Bending Moments in the South Uist 46 SPECTRA

NORMALISATION : data divided by $(Hrms)^{0.8}$

48 joints Stiffness: 1000 Nm/rad

sea set: SU'a'

SURGE joints

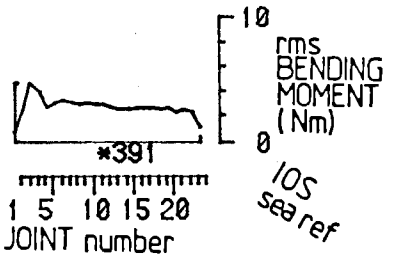

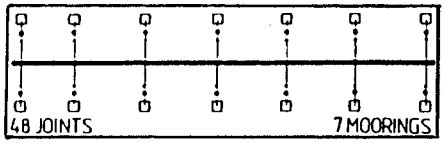

the 46 SPECTRA 'a' set

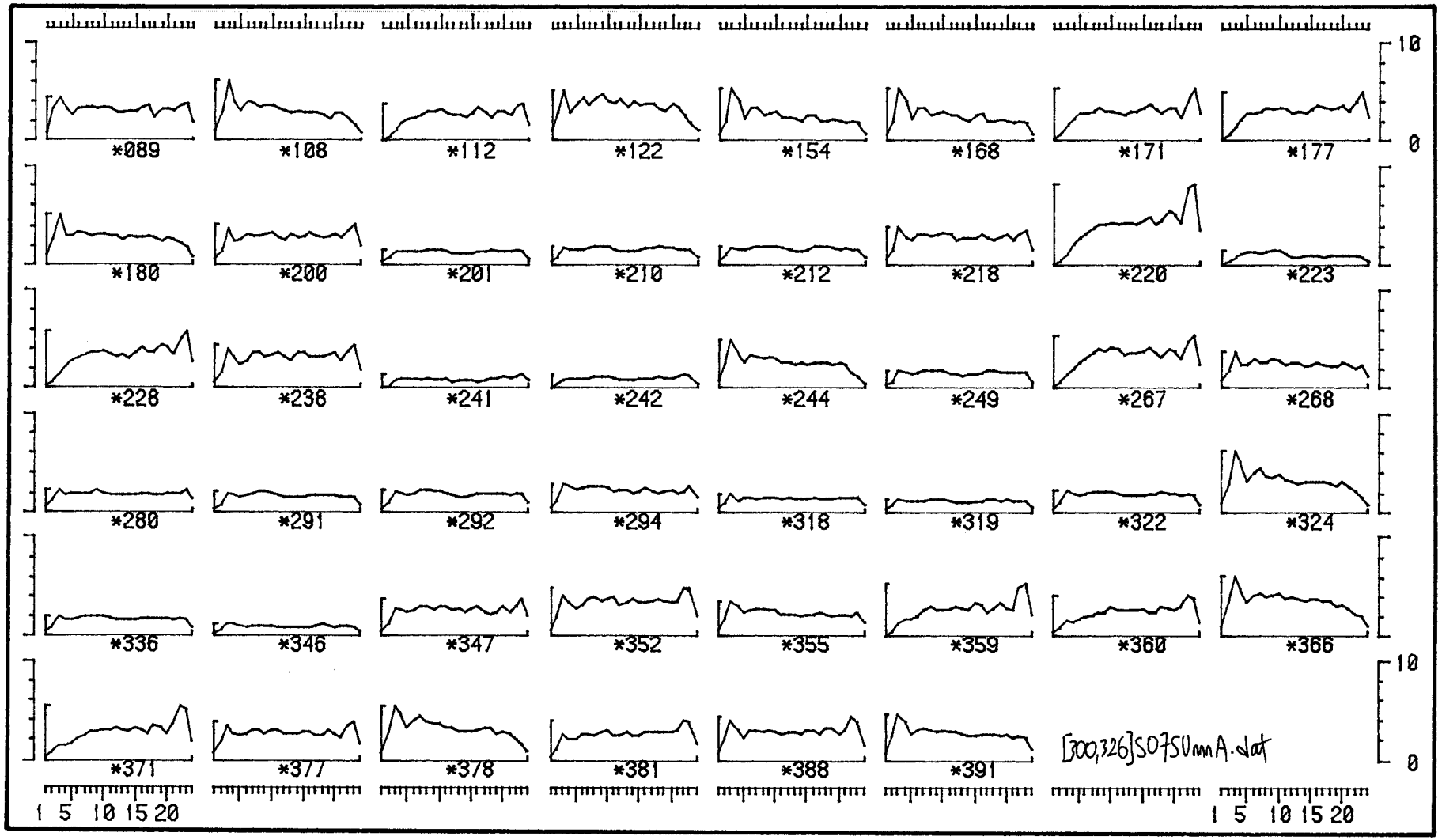

GRAPH 4.51

Bending Moments in the South Uist 46 SPECTRA

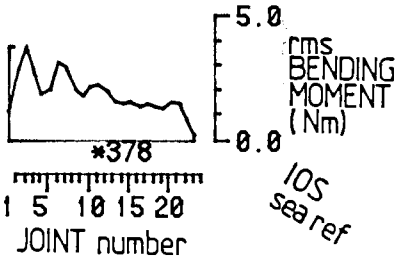

NORMALISATION : data divided by Hrms

48 joints Stiffness: 1000 Nm/rad

sea set: SU'a'

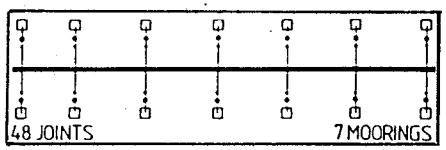

HEAVE joints

the 46 SPECTRA 'a' set

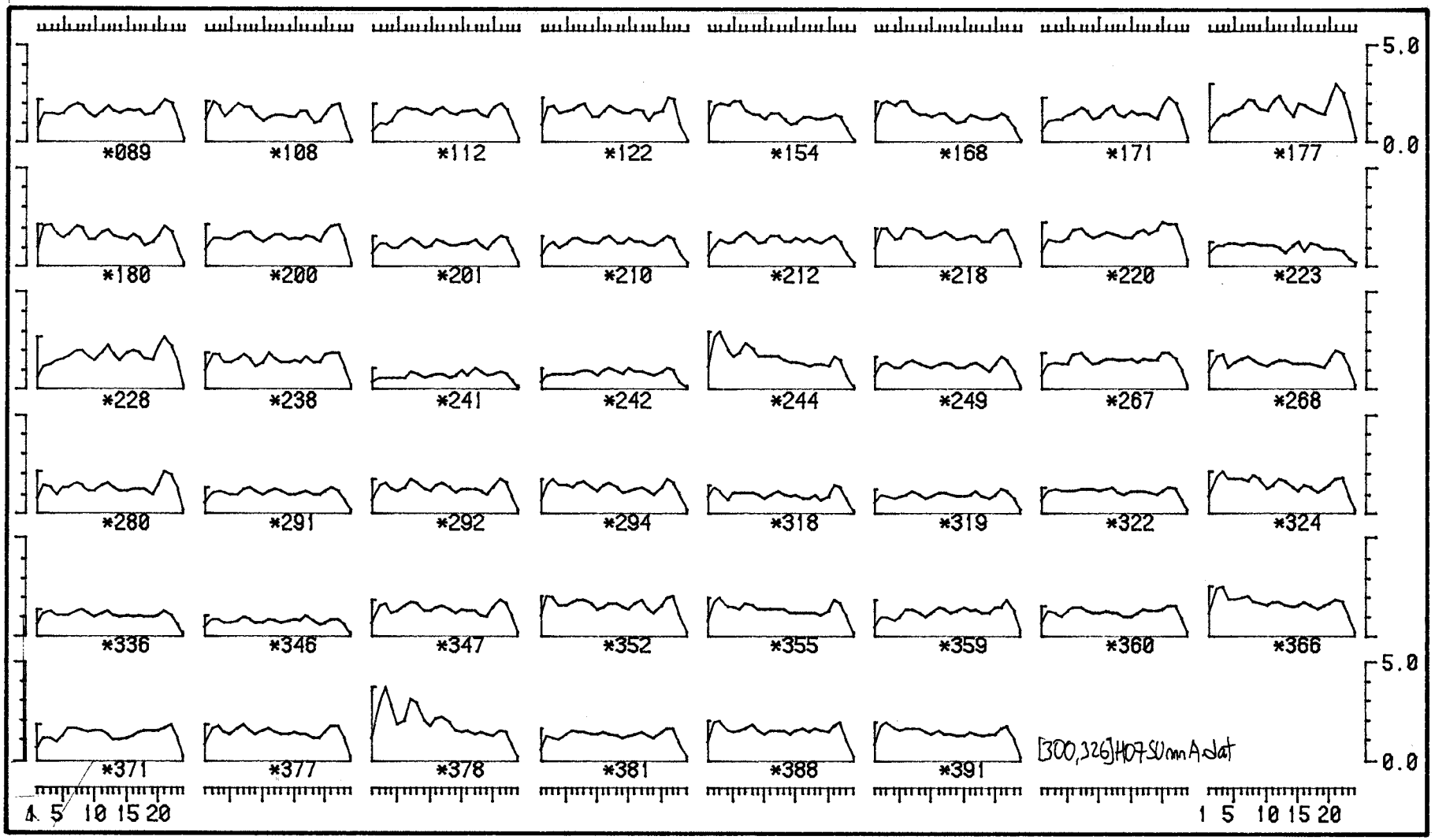

GRAPH 4.52

(4.E cont)

For the next series of tests we varied the total model length, keeping the 46 'a' set and 1000 Nm/rad joint stiffness.

The results on graph 4.53 are for 36 joints and on graph 4.54 are for 22 joints. For graph 4.55 we use a 22 joint model swung round to the South 'b' series of seas. The results are close to the 'a' series with the exception of sea number 3.78. Relevant pox-plots are graphs 3.6 and 3.7.

Graph 4.56 shows the results of testing 22 joints in the 'd' series seas. The mirror image reversal for sea 359 is beautifully shown. There is a wide difference for sea 223 between graph 4.56 and 4.54. Again the pox-plots on 3.9 and 3.6 show why.

The series of graphs 4.57 to 4.61 is an exact repeat of the previous group with the stiffness increased to 3500 Nm/rad. The shapes of the arrays are similar, and the only obvious effect of changing stiffness is to increase bending moments in all joints and in all seas.

Bending Moments in the South Uist 46 SPECTRA

36 joints Stiffness: 1000 Nm/rad

sea set: SU 'a'

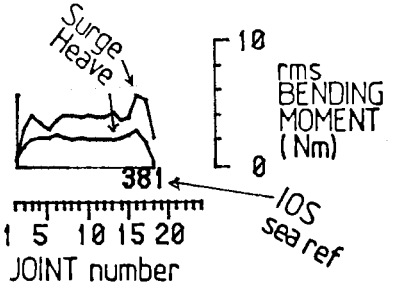

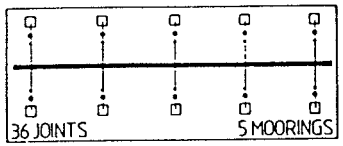

SURGE & HEAVE joints

the 46 SPECTRA 'a' set

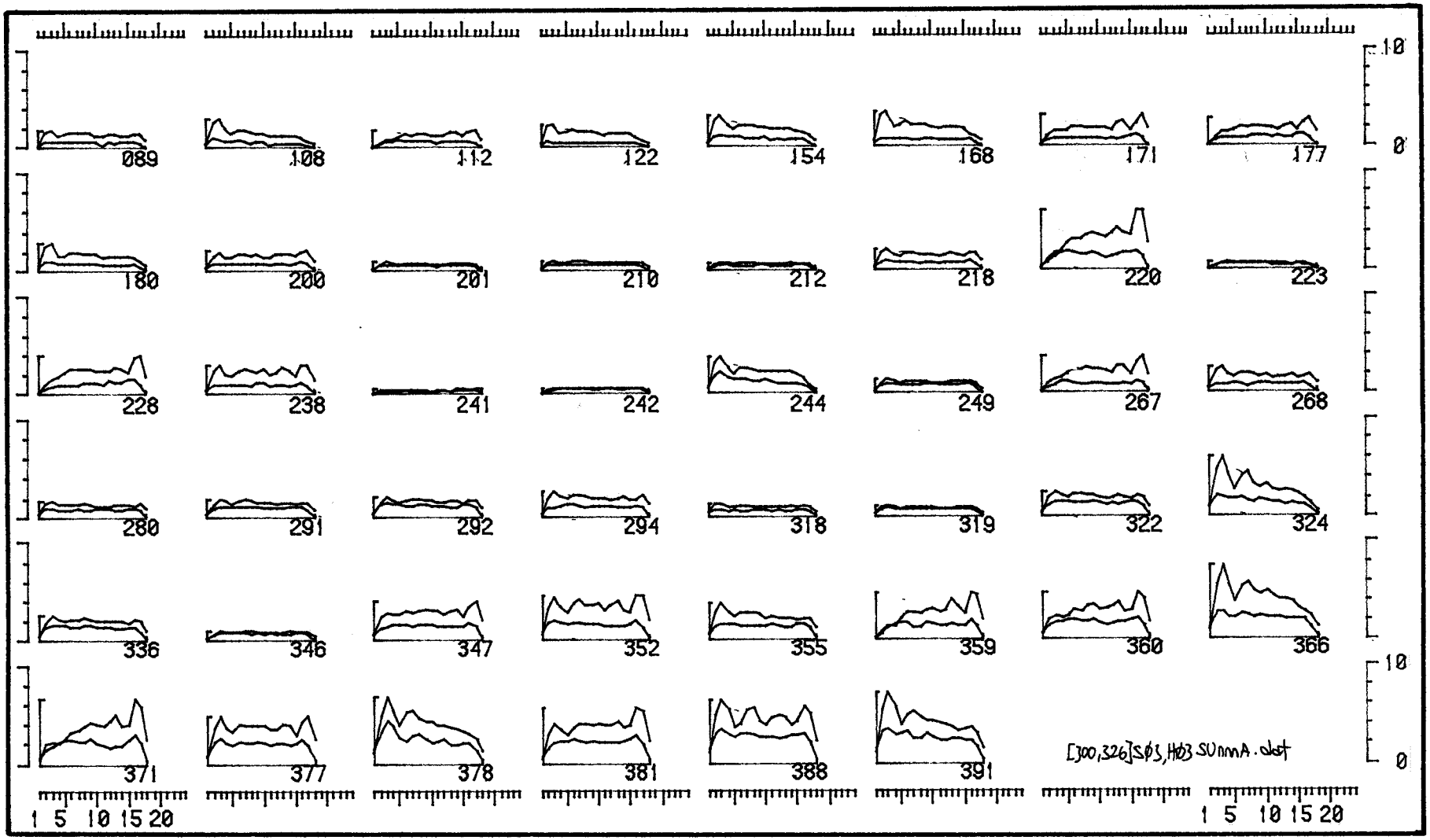

GRAPH 4.53

Bending Moments in the South Uist 46 SPECTRA

22 joints Stiffness: 1000 Nm/rad

sea set: SU 'a'

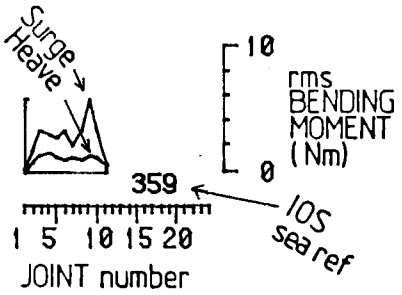

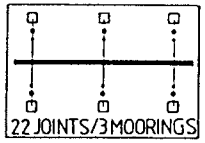

SURGE & HEAVE joints

the 46 SPECTRA 'a' set

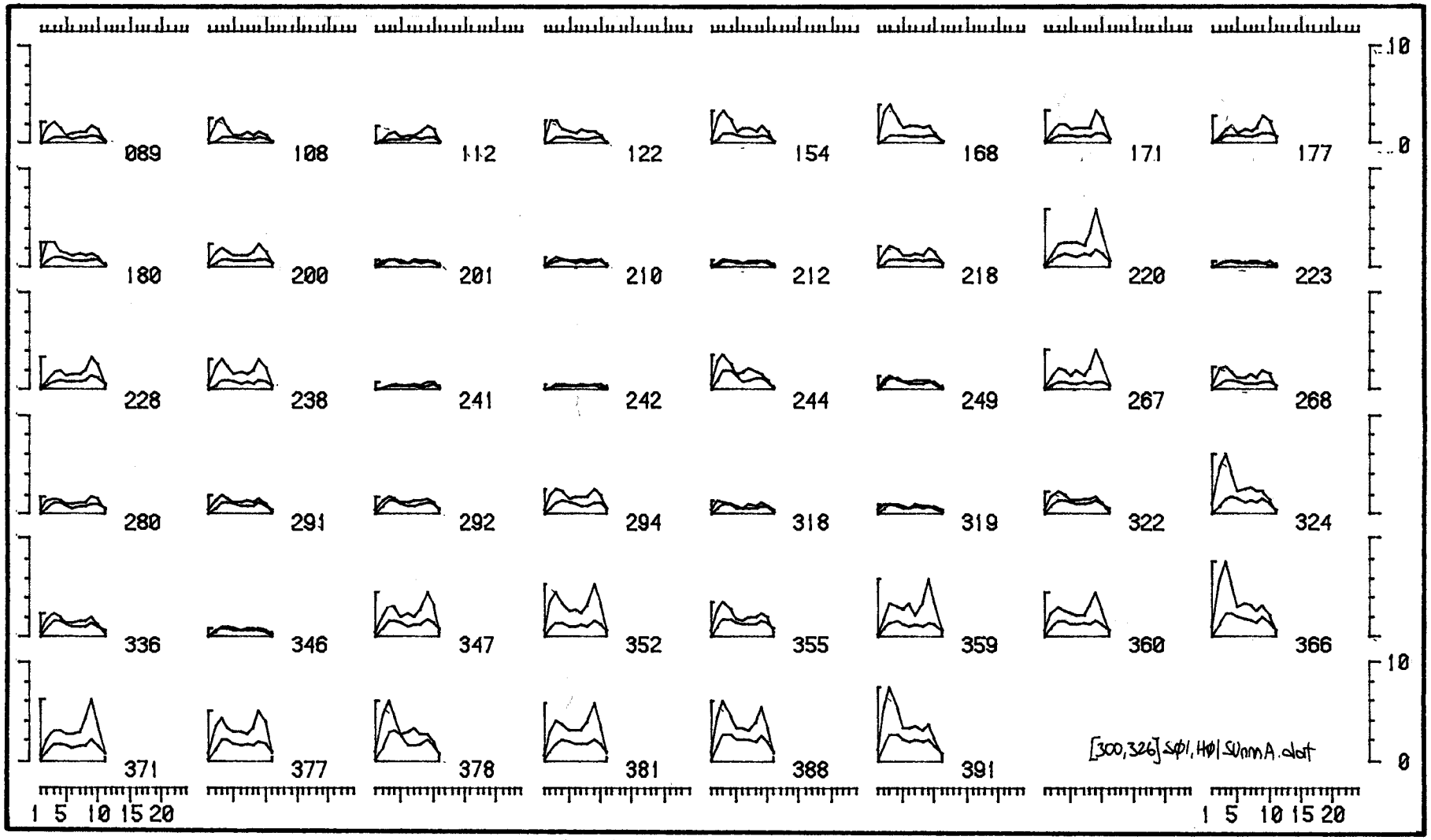

GRAPH 4.54

Bending Moments in the South Uist 46 SPECTRA

22 joints Stiffness: 1000 Nm/rad

sea set: SU 'b'

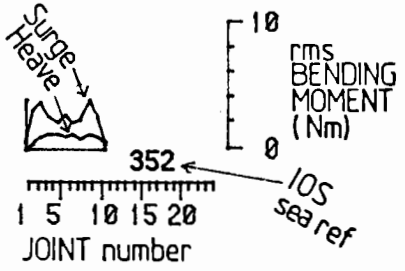

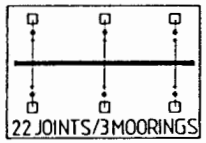

SURGE & HEAVE joints

the 46 SPECTRA 'b' set

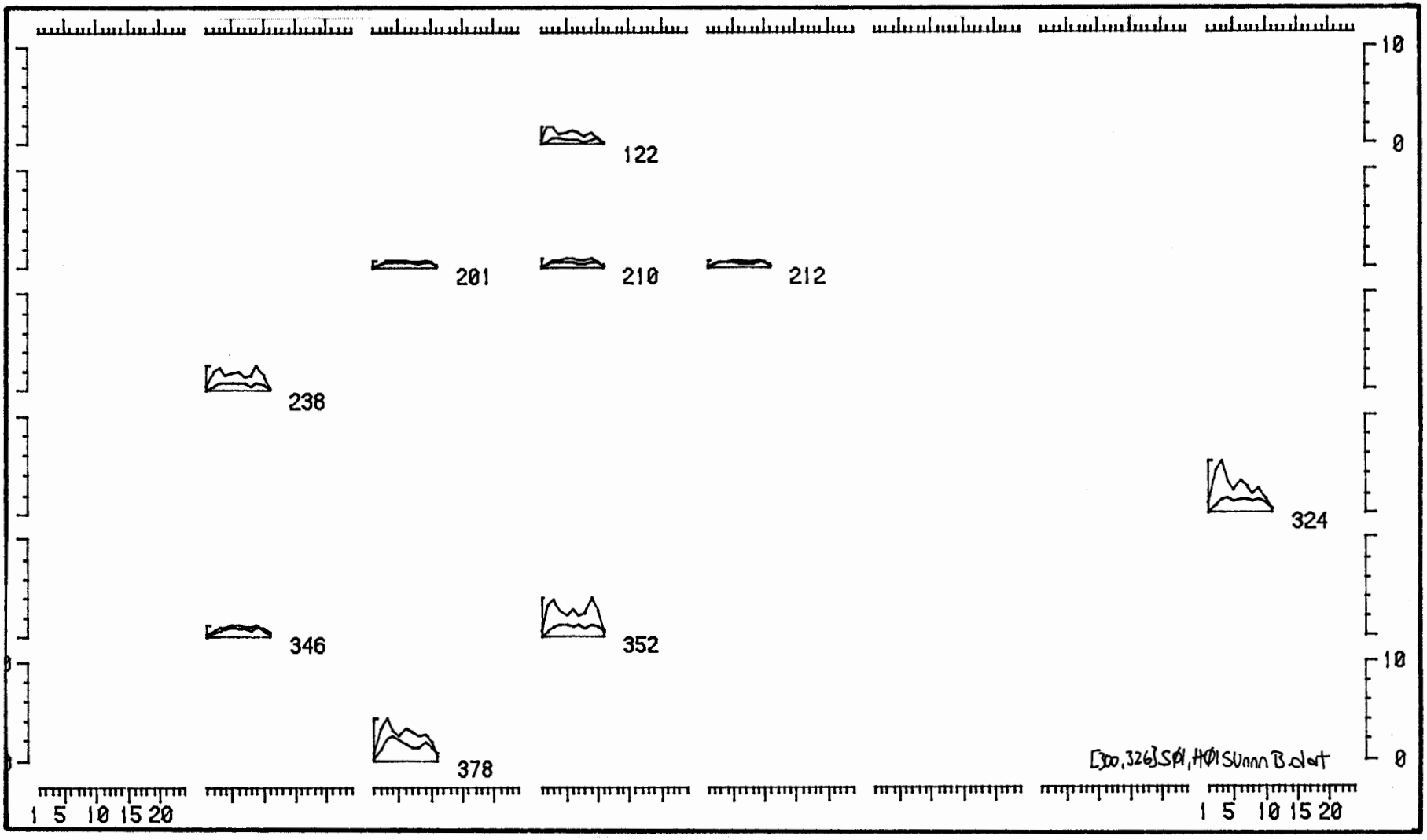

GRAPH 4.55

Bending Moments in the South Uist 46 SPECTRA

22 joints Stiffness: 1000 Nm/rad

sea set: SU 'd'

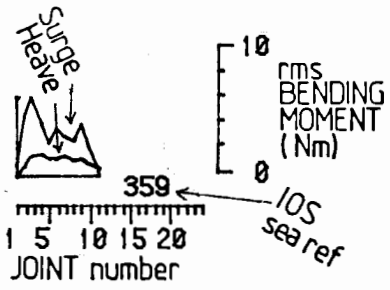

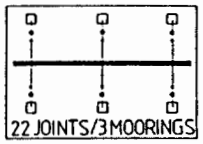

SURGE & HEAVE joints

the 46 SPECTRA 'd' set

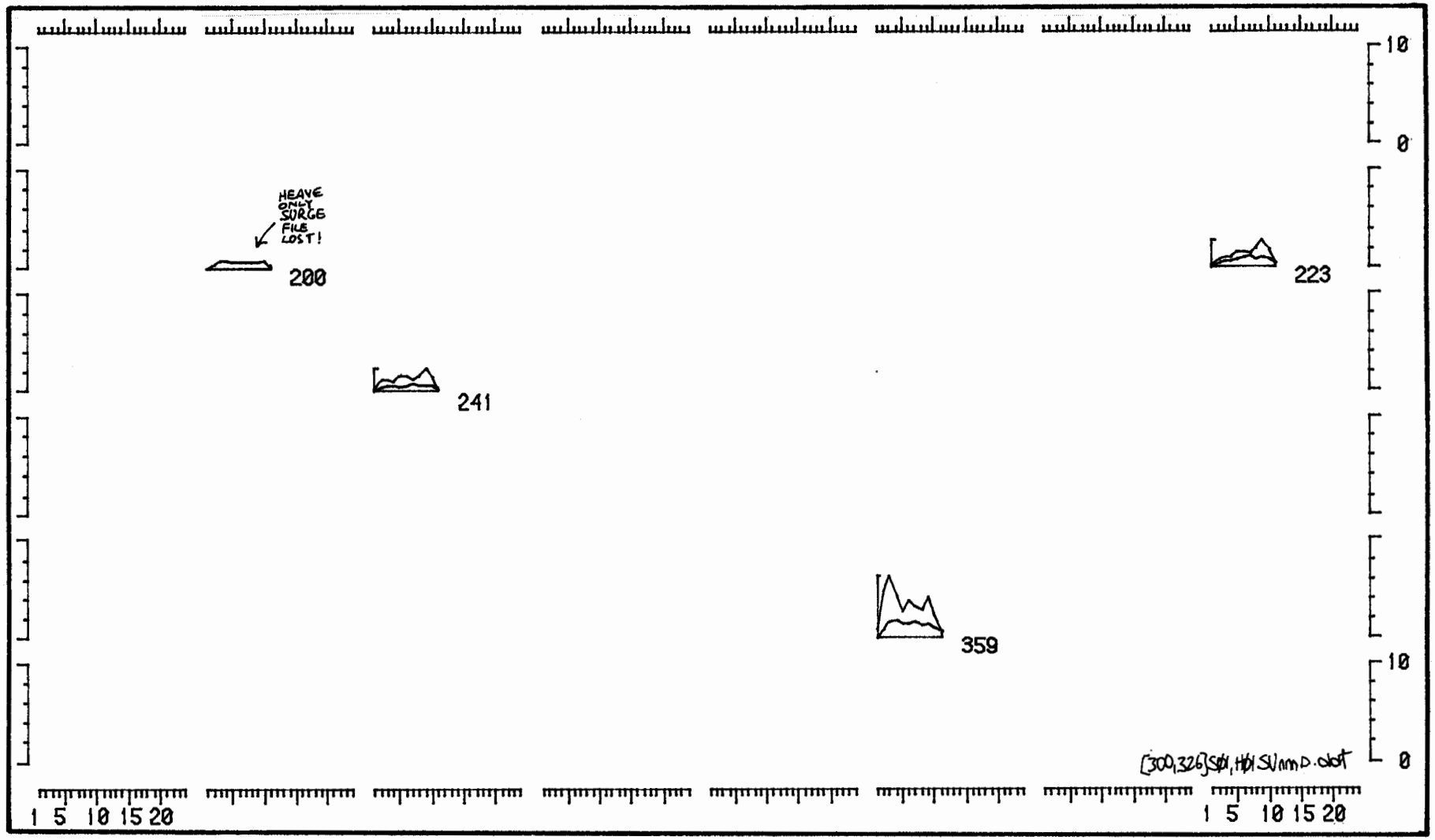

GRAPH 4.56

Bending Moments in the South Uist 46 SPECTRA

48 joints Stiffness: 3500 Nm/rad

sea set: SU 'a'

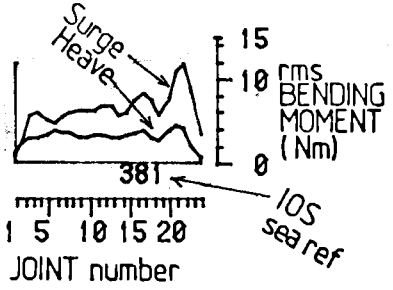

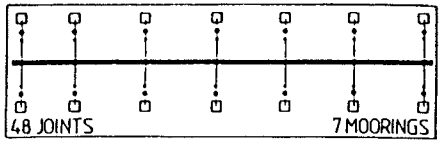

SURGE & HEAVE joints

the 46 SPECTRA 'a' set

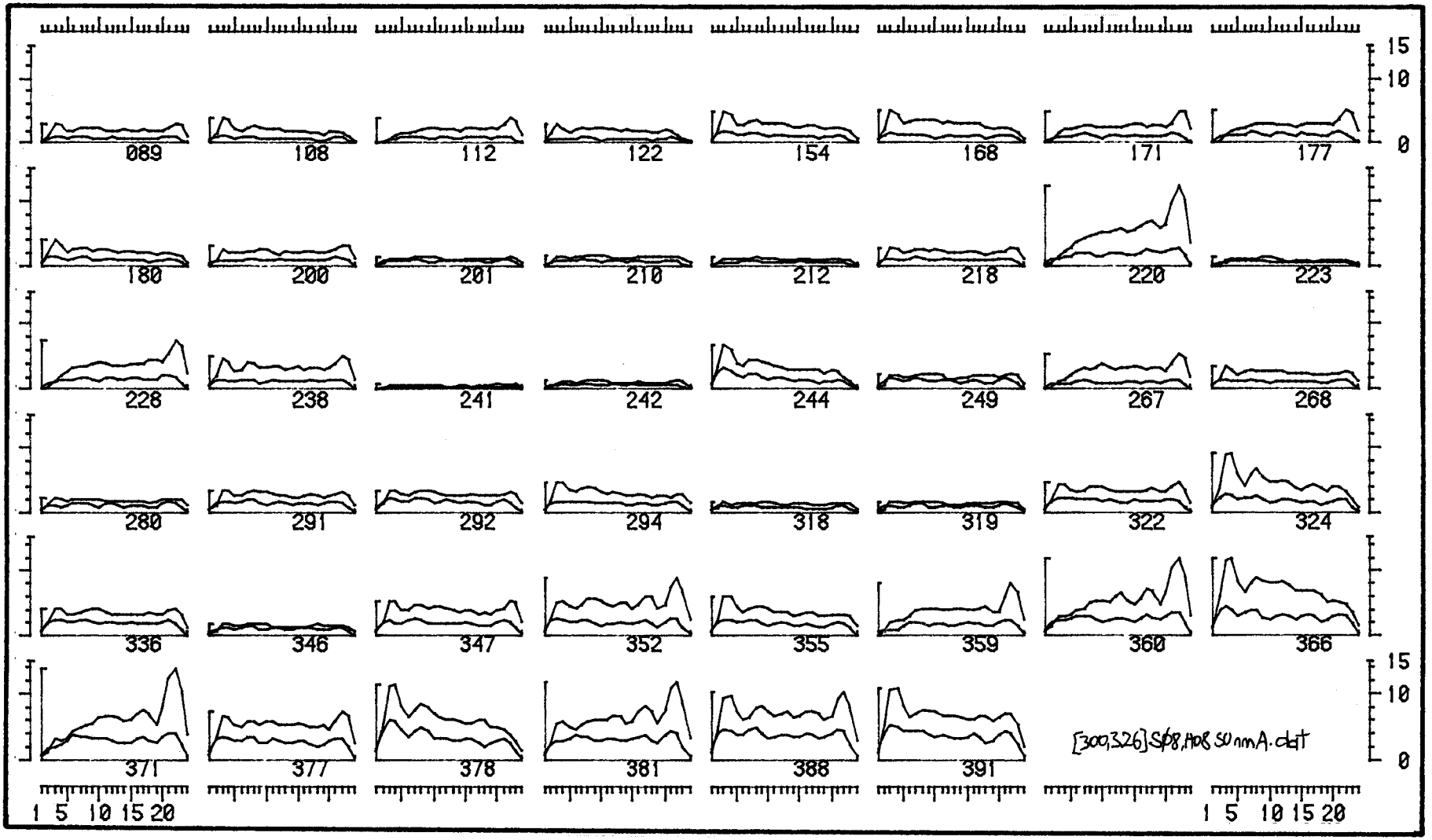

GRAPH 4.57

Bending Moments in the South Uist 46 SPECTRA

36 joints Stiffness: 3500 Nm/rad

sea set: SU 'a'

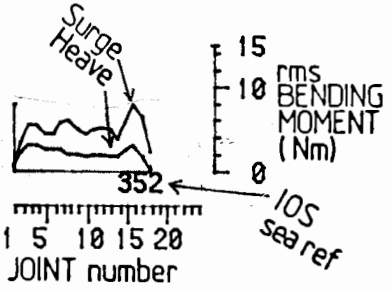

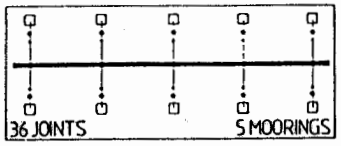

SURGE & HEAVE joints

the 46 SPECTRA 'a' set

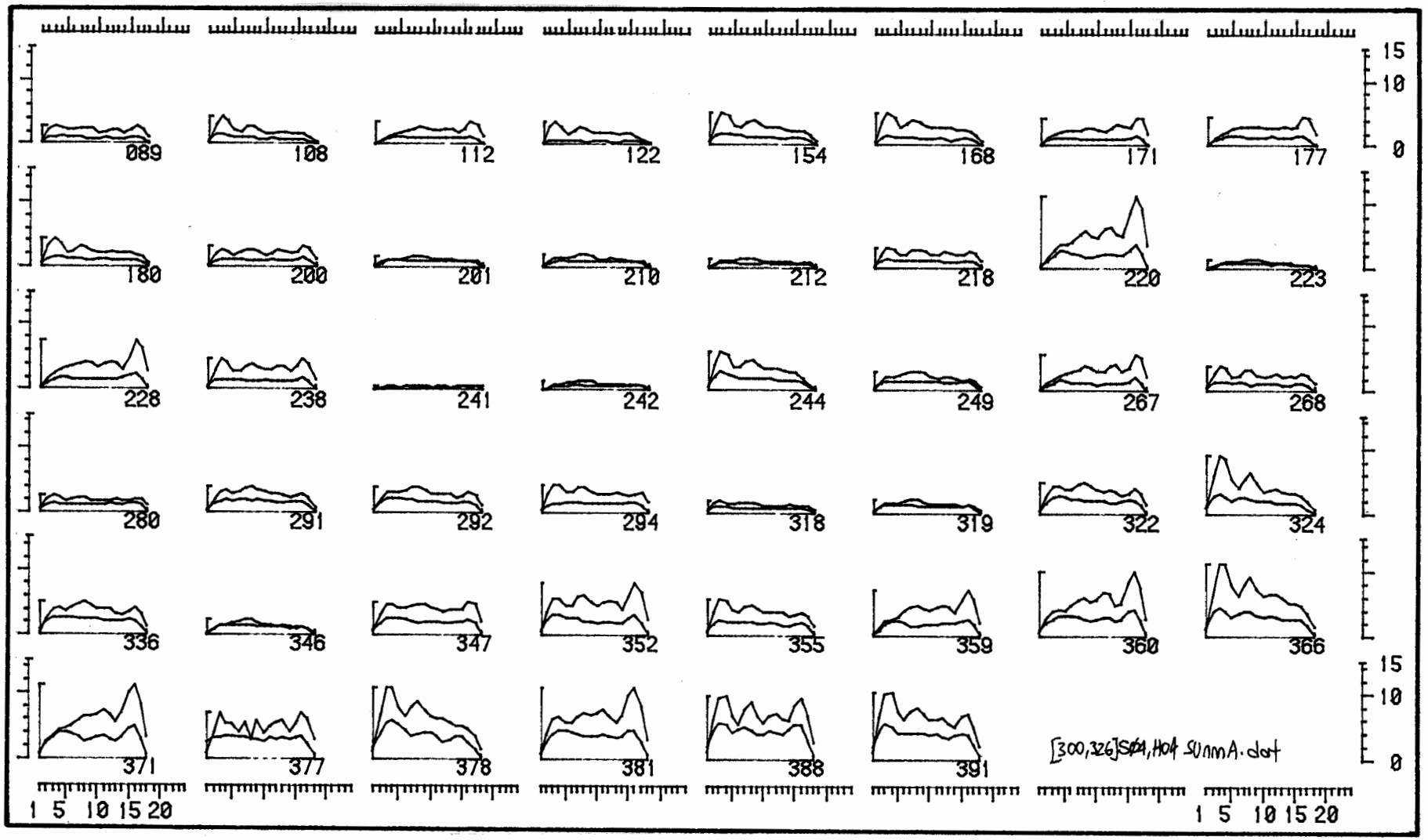

GRAPH 4.58

Bending Moments in the South Uist 46 SPECTRA

22 joints Stiffness: 3500 Nm/rad

sea set: SU 'a'

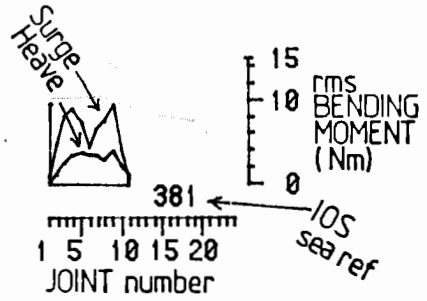

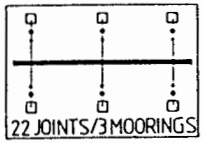

SURGE & HEAVE joints

the 46 SPECTRA 'a' set

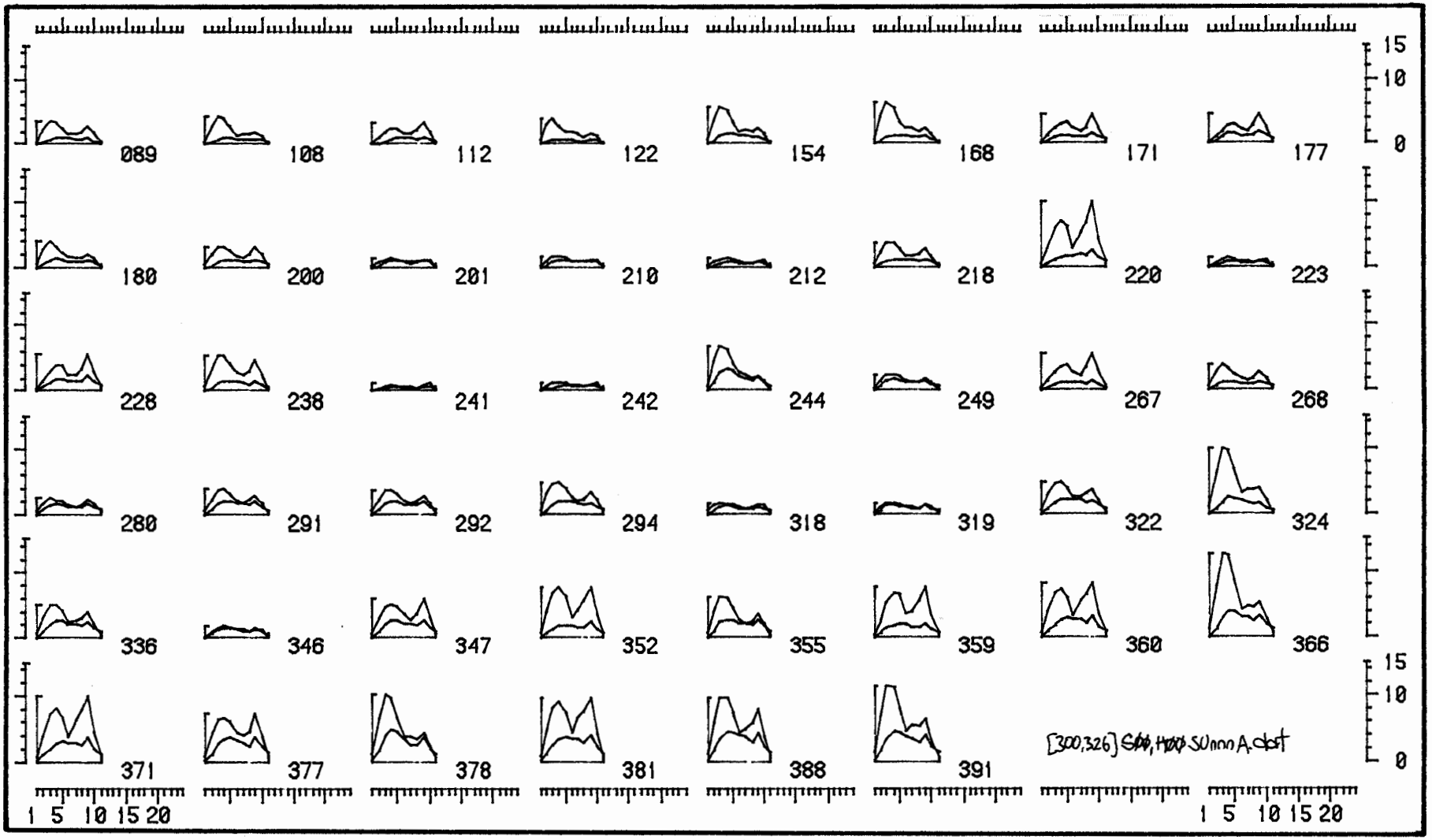

GRAPH 4.59

Bending Moments in the South Uist 46 SPECTRA

22 joints Stiffness: 3500 Nm/rad

sea set: SU 'b'

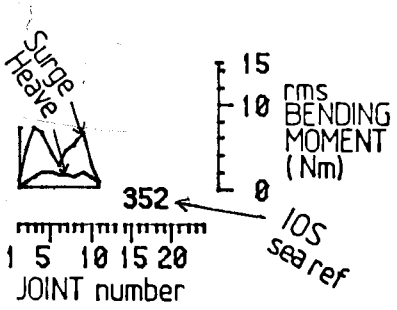

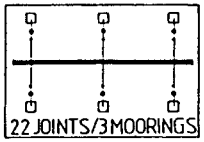

SURGE & HEAVE joints

the 46 SPECTRA 'b' set

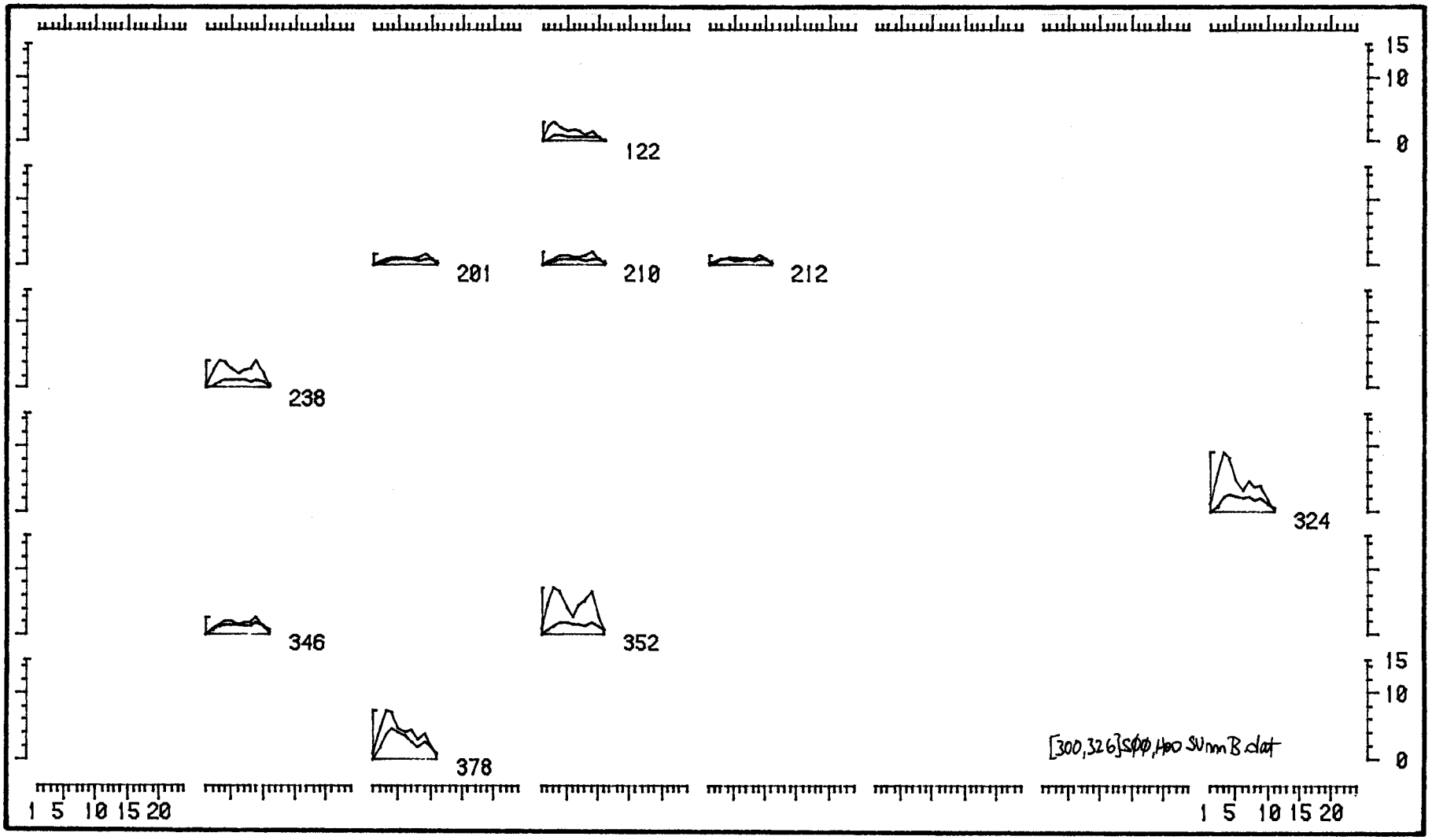

GRAPH 4.60

Bending Moments in the South Uist 46 SPECTRA

22 joints Stiffness: 3500 Nm/rad

sea set: SU 'd'

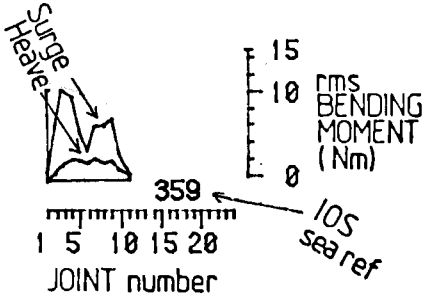

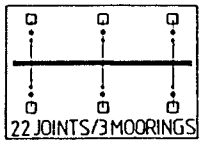

SURGE & HEAVE joints

the 46 SPECTRA 'd' set

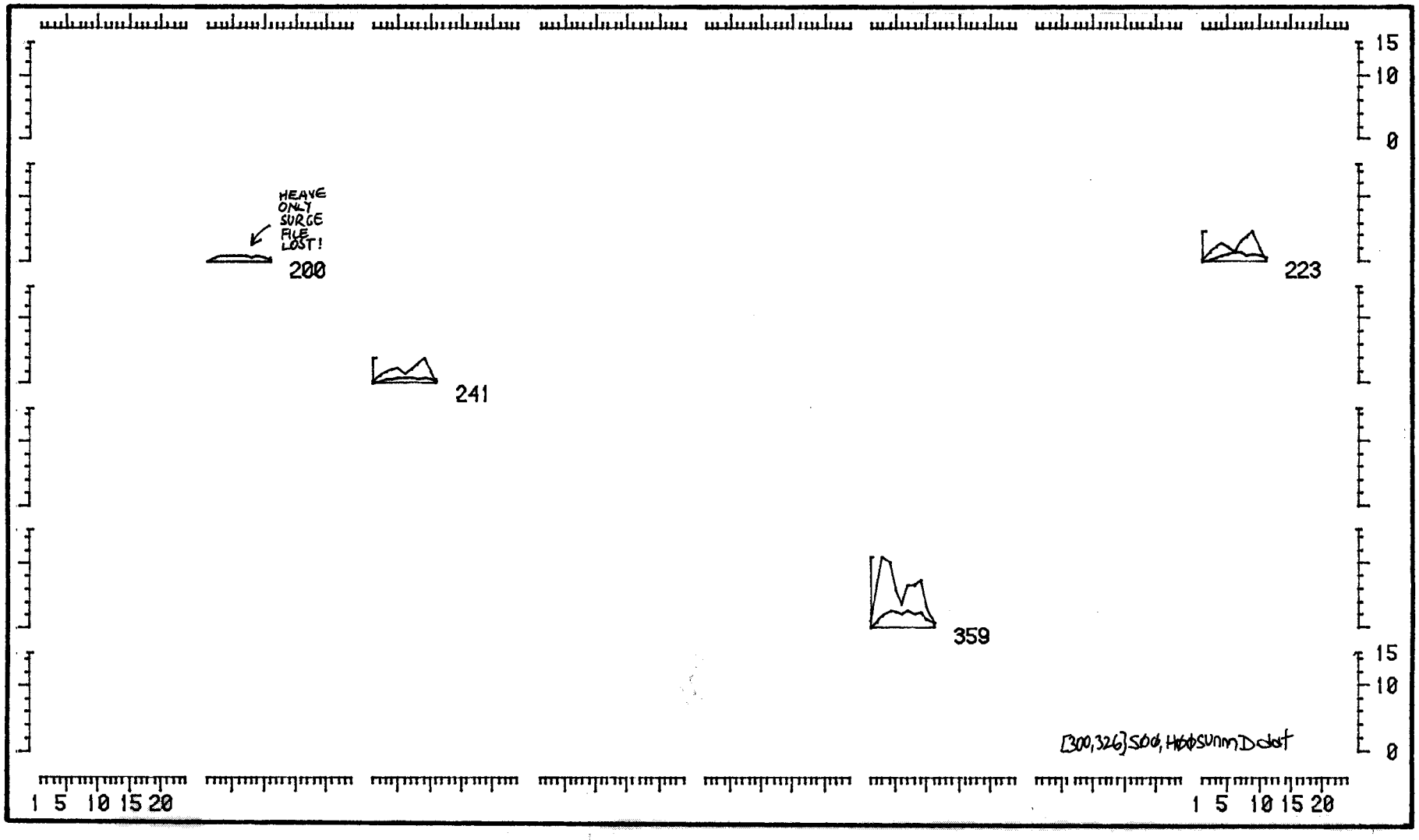

GRAPH 4.61

4.F EFFECT OF STIFFNESS VARIATIONS IN SOUTH UIST SEAS

In this series of experiments the 46 'a' set seas are used on a 48 joint model with three different stiffness values; 1000, 3500 and 5000 Nm/rad.

Graphs 4.70 and 4.71 show the raw data for the three stiffnesses.

Graphs 4.72 and 4.73 show them normalised by division by Hrms.

The very small heave bending moments for sea 122 look suspiciously jagged when normalised and we suspect a communication fault for the left hand half of the spine.

In general, the relationship of bending moments to stiffness follows the approximately logarithmic pattern shown in graph 4.23 of section 4B, with little change between stiffnesses of 3500 Nm/rad and 5000 Nm/rad. However, the difference between the down-wave peaks in strongly offset seas is greater than expected when the stiffness increases from 1000 Nm/rad to 3500 Nm/rad. Sea number 220 is again the obvious example. It is reasonable to hope that lower model stiffness will reduce the severity of down-wave enhancement.

Bending Moments in the South Uist 46 SPECTRA

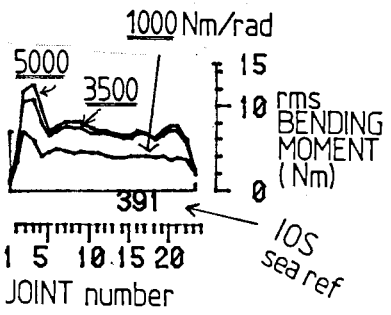

3 Stiffnesses: 1000,3500,5000 Nm/rad

48 joints Stiffness: 1000 Nm/rad

sea set: SU'a'

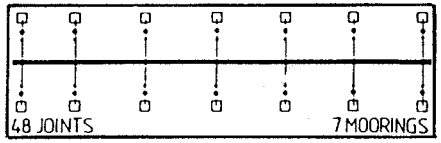

SURGE joints

the 46 SPECTRA 'a' set

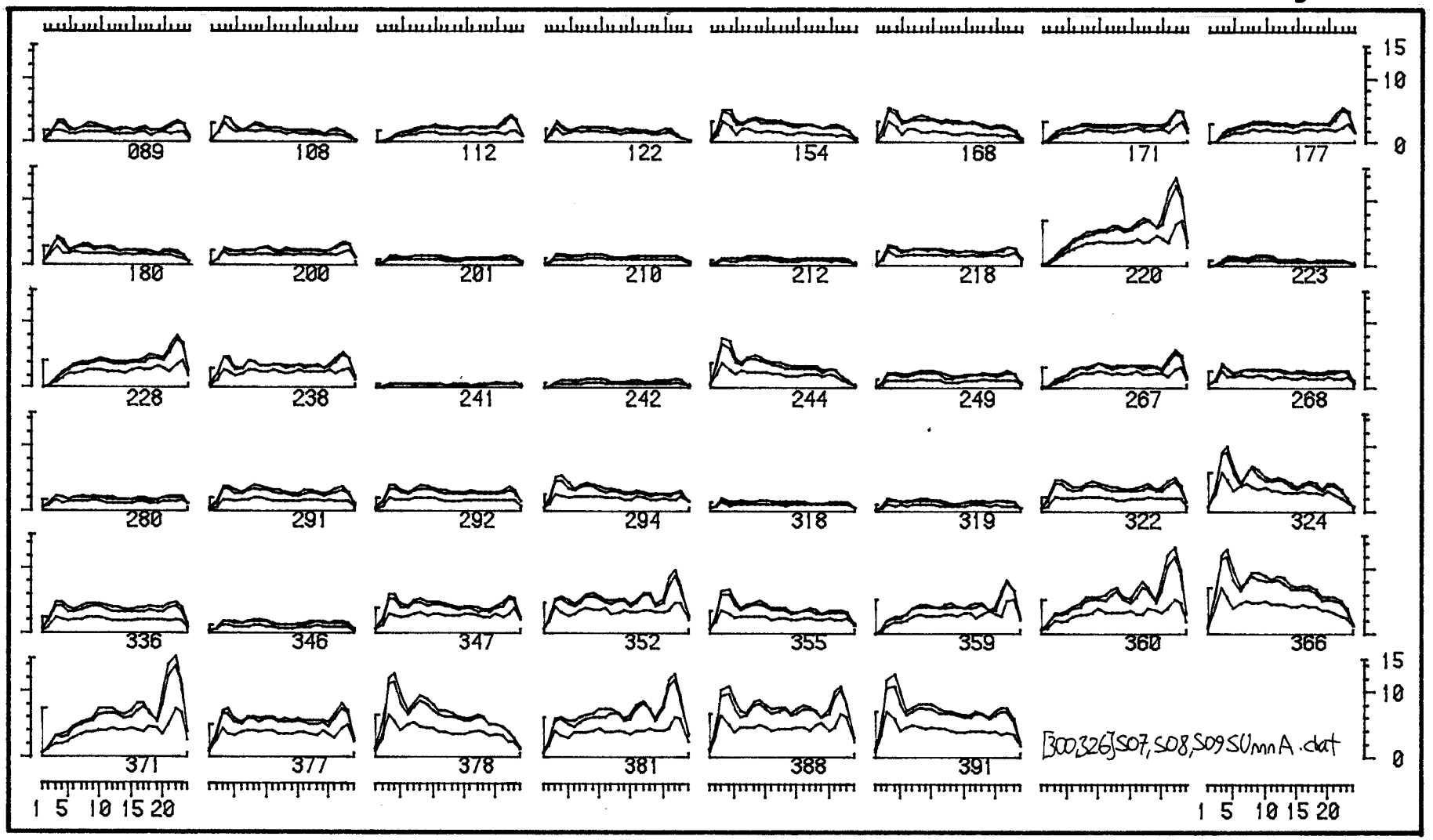

GRAPH 4.70

Bending Moments in the South Uist 46 SPECTRA

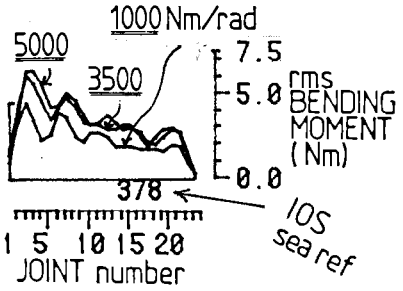

3 Stiffnesses: 1000, 3500, 5000 Nm/rad

48 joints Stiffness: 1000 Nm/rad

sea set: SU'a'

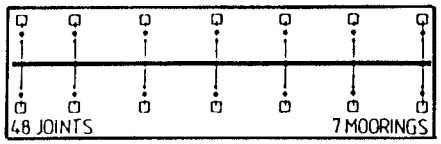

HEAVE joints

the 46 SPECTRA 'a' set

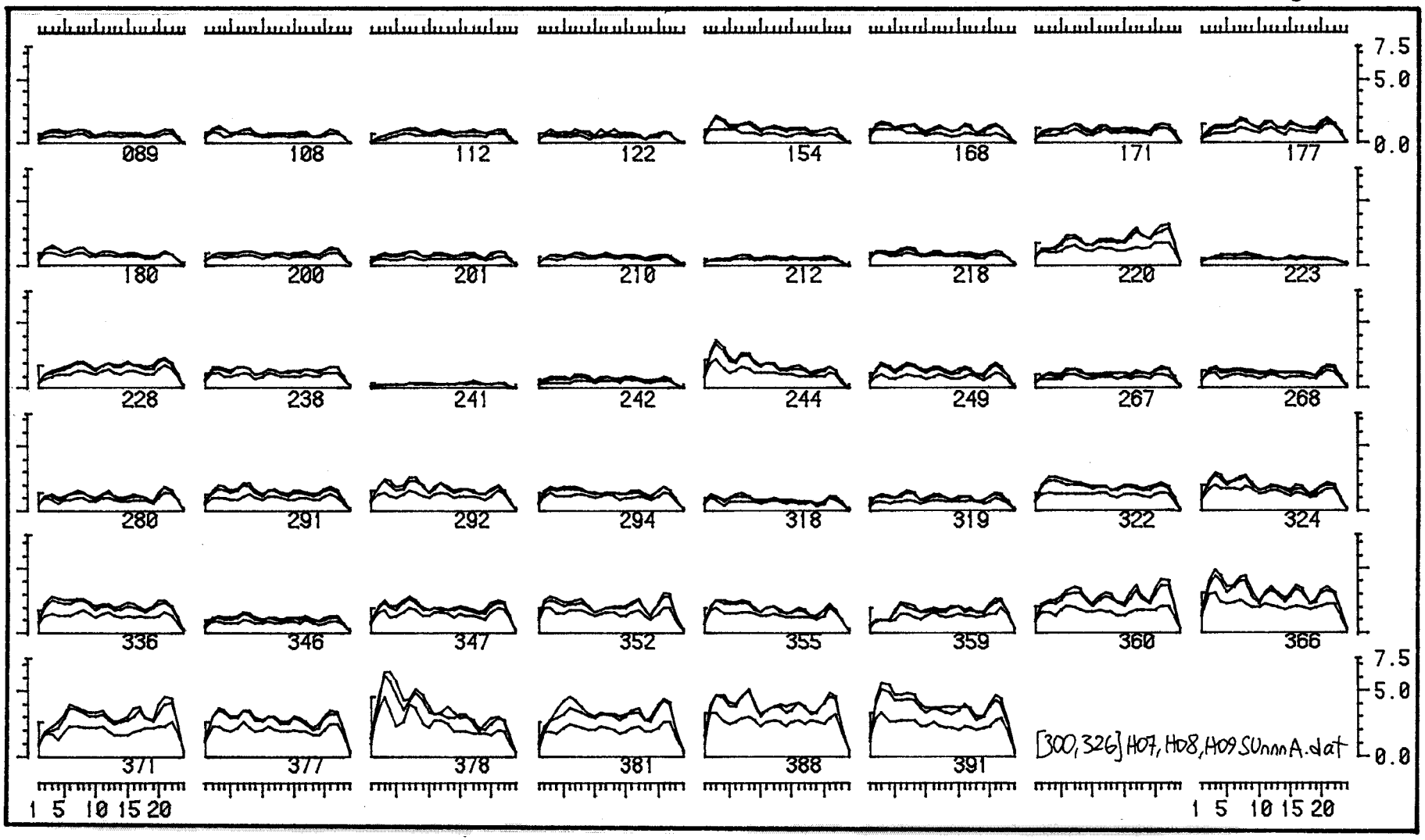

GRAPH 4.71

Bending Moments in the South Uist 46 SPECTRA

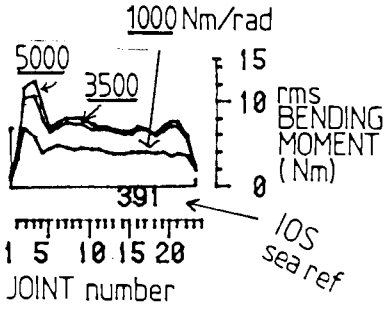

data 'normalised'
by dividing by $(Hrms)^{0.8}$

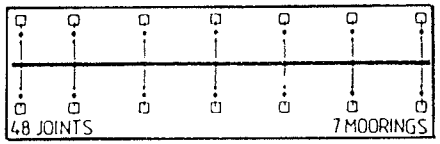

3 Stiffnesses: 1000, 3500, 5000 Nm/rad
48 joints
Stiffness: 1000 Nm/rad
sea set: SU'a'

SURGE joints

the 46 SPECTRA 'a' set

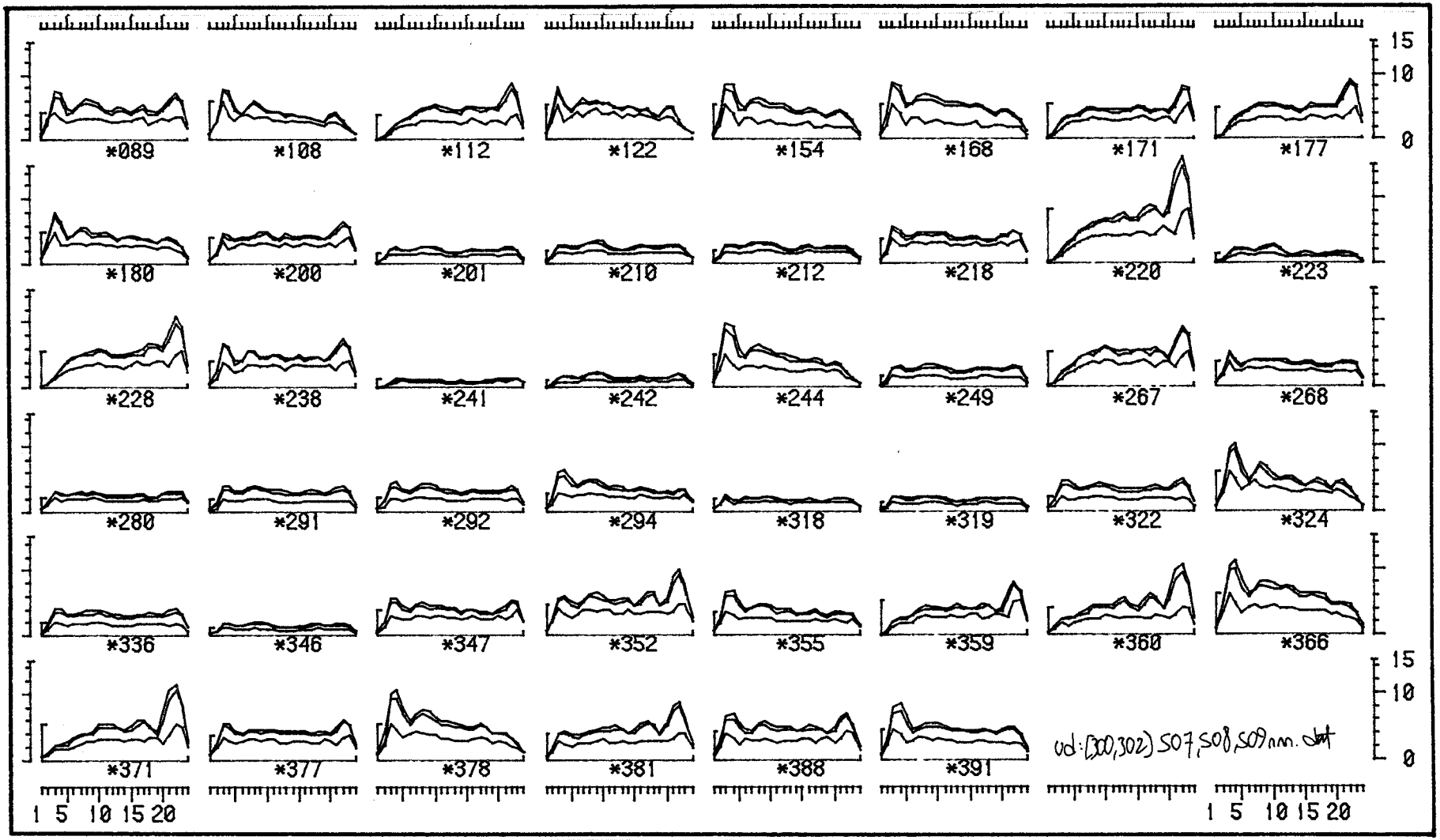

GRAPH 4.72

Bending Moments in the South Uist 46 SPECTRA

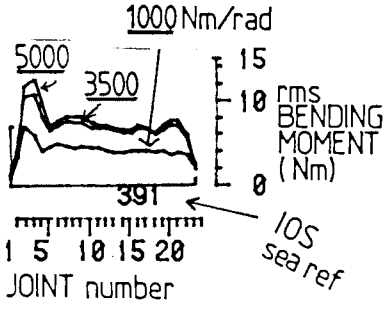

data 'normalised' by dividing by Hrms

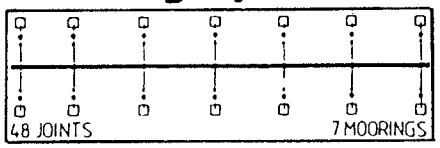

3 Stiffnesses: 1000, 3500, 5000 Nm/rad

48 joints Stiffness: 1000 Nm/rad

sea set: SU'a'

HEAVE joints

the 46 SPECTRA 'a' set

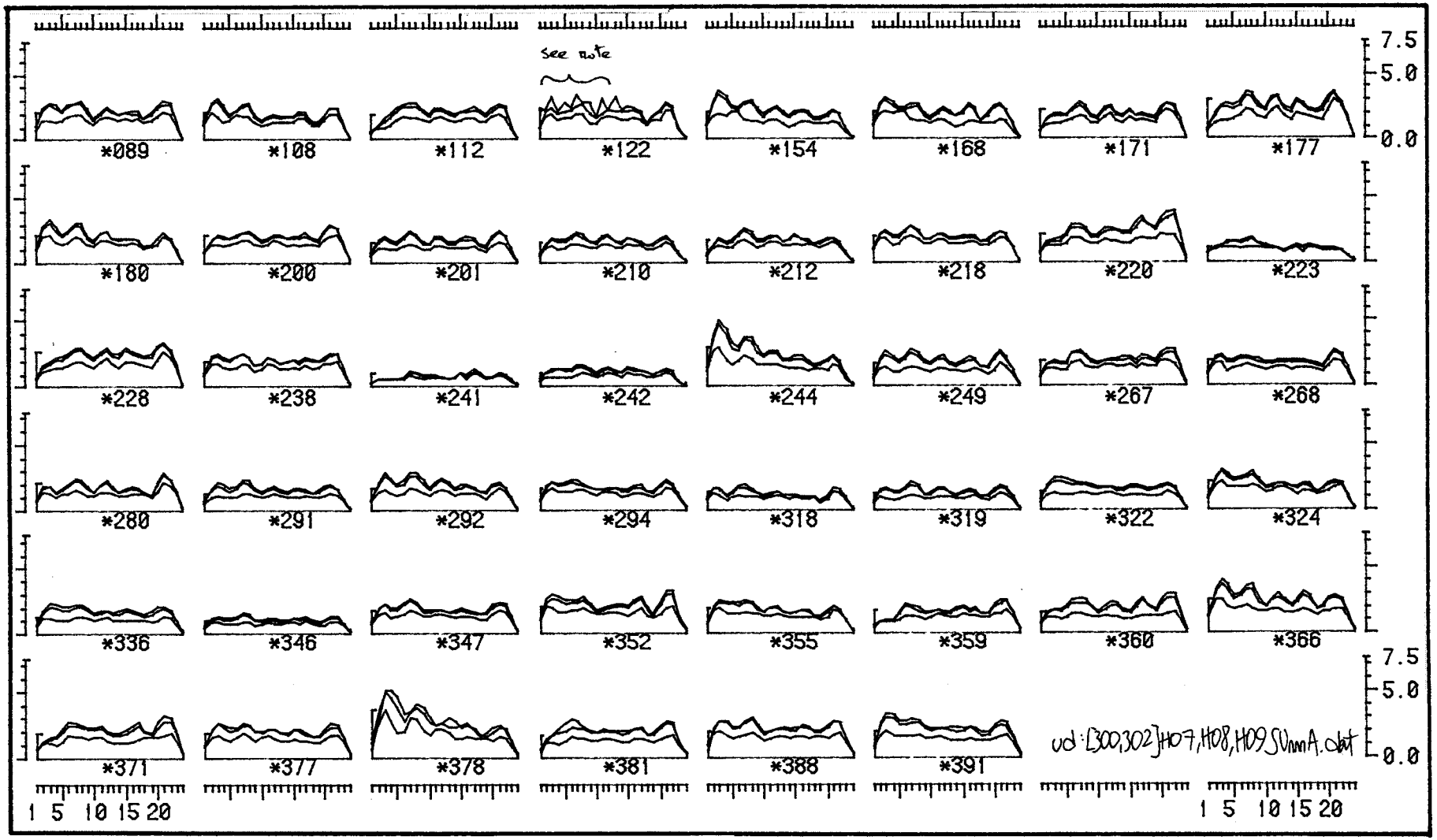

GRAPH 4.73

4.G SHAPE OF BENDING MOMENT DISTRIBUTION IN SOUTH UIST SEAS

In this section we are trying to show the shape of the distribution of bending moment along the spine. Data from the previous tests are scaled to make the maximum value the same for each test. For example in graph 4.80 the double hump in sea 223 was usually too small to show up well even in normalised plots.

We plot surge and heave separately for lengths of 48, 36 and 22 joints with stiffness held constant at 1000 Nm/rad.

Heave results are generally flatter than surge but seas 228, 224 and 378 are exceptions (see graph 4.83).

We are suspicious of the first three results on graph 4.83. The reduced moment for one joint in sea 089, which is adjacent to raised moments on either side, is characteristic of a loose model joint (see section 4.M).

Shortening the model by a factor of two has removed the asymmetry of 223, but in general shape is not much changed by shortening (see for example sea 366).

The shortest model was swung round to be tested in the 'b' and 'd' South Uist seas. The biggest changes are for sea 346 in graph 4.86 and 223 in graphs 4.88 and 4.89. All the others look very much like their 'a' series versions.

More length variations are given in section 4.K.

Note the striking similarity of seas 201, 210, 212, 291, 292, 322 and 336. We see that there are central moments very close in value to end peaks.

We can also notice the similarity of the pox-plots in graph 3.6.

Bending Moments in the South Uist 46 SPECTRA

self-scaled to show SHAPES of arrays

48 joints Stiffness: 1000 Nm/rad

sea set: SU'a'

SURGE joints

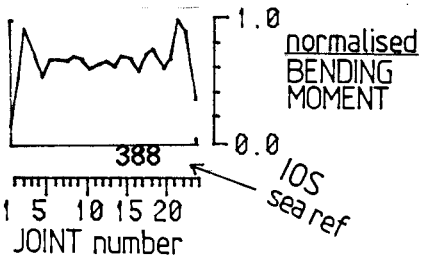

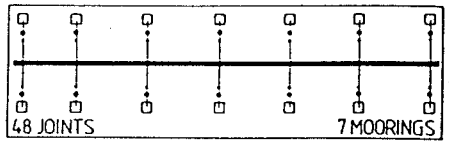

the 46 SPECTRA 'a' set

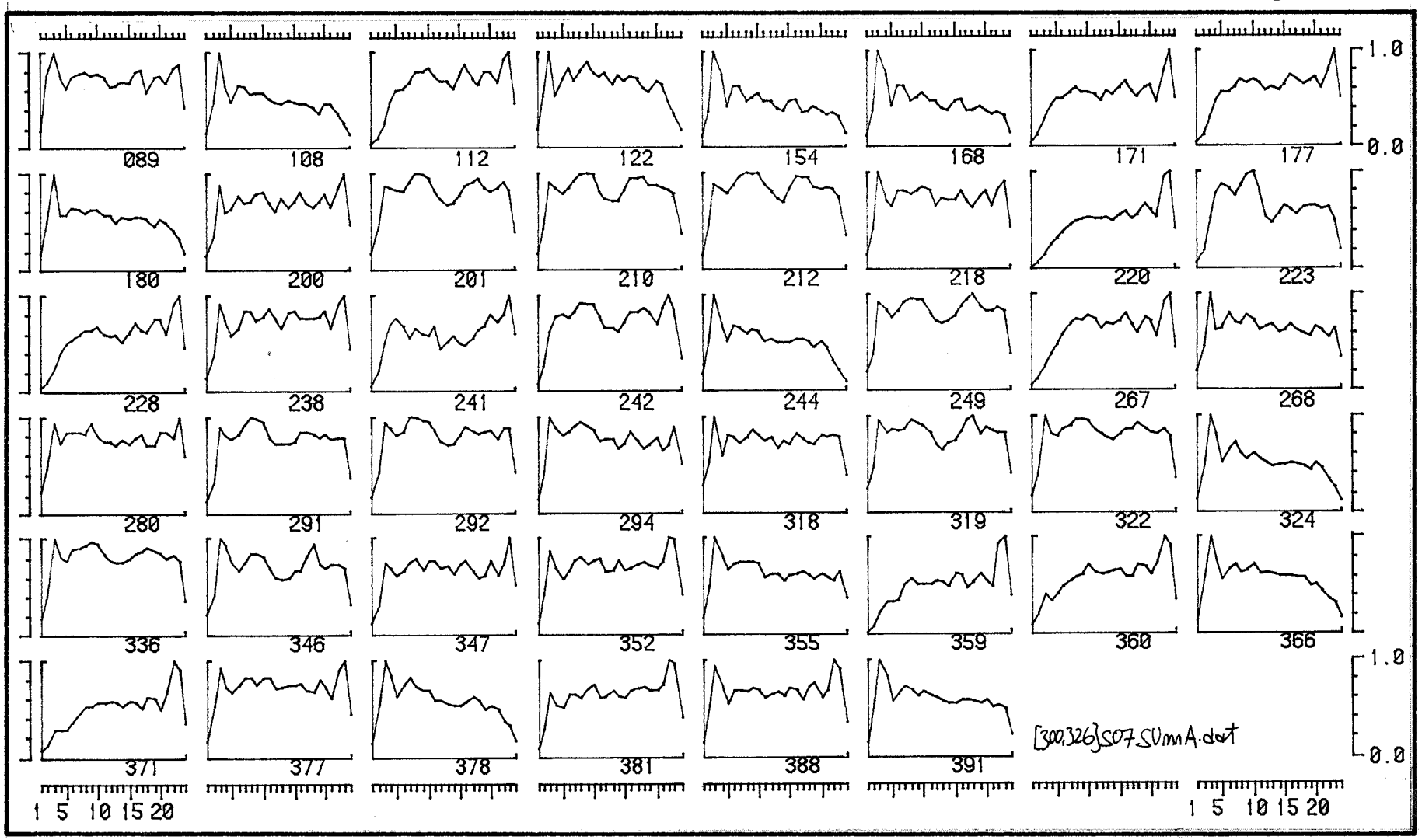

GRAPH 4.80

Bending Moments in the South Uist 46 SPECTRA

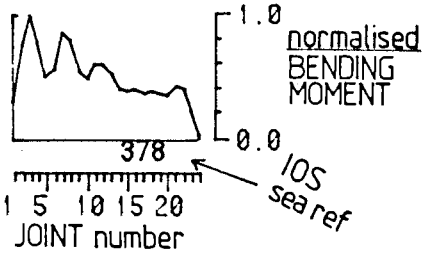

self-scaled to show SHAPES of arrays

48 joints Stiffness: 1000 Nm/rad

sea set: SU'a'

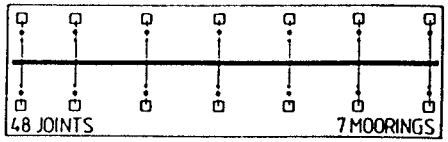

HEAVE joints

the 46 SPECTRA 'a' set

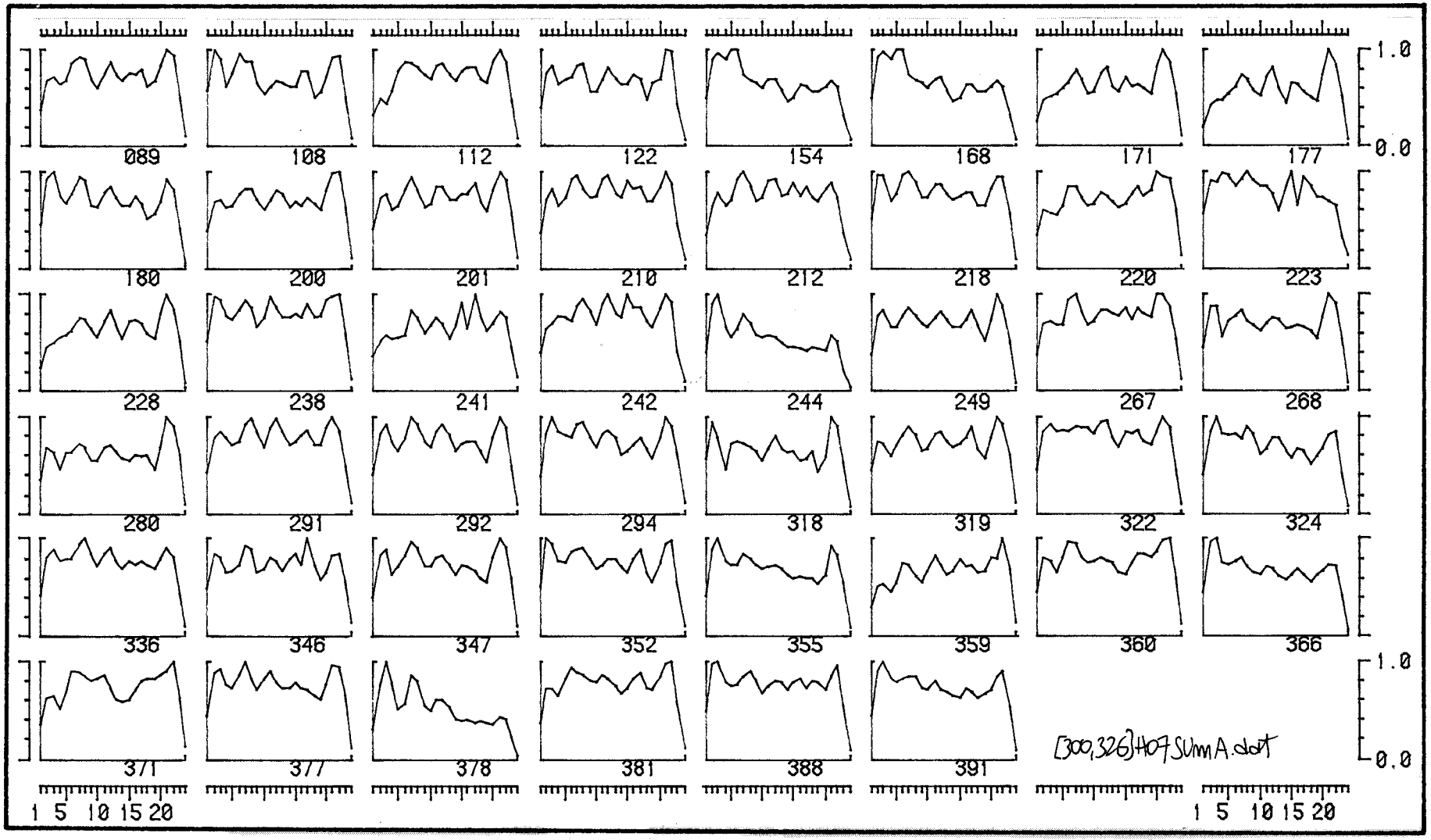

GRAPH 4.81

Bending Moments in the South Uist 46 SPECTRA

self-scaled to show SHAPES of arrays

36 joints Stiffness: 1000 Nm/rad

sea set: SU'a'

SURGE joints

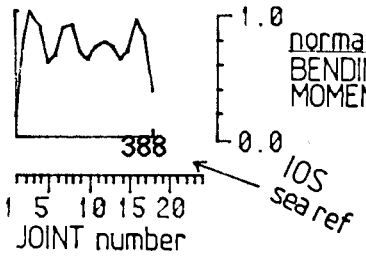

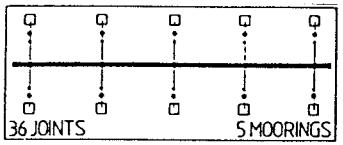

the 46 SPECTRA 'a' set

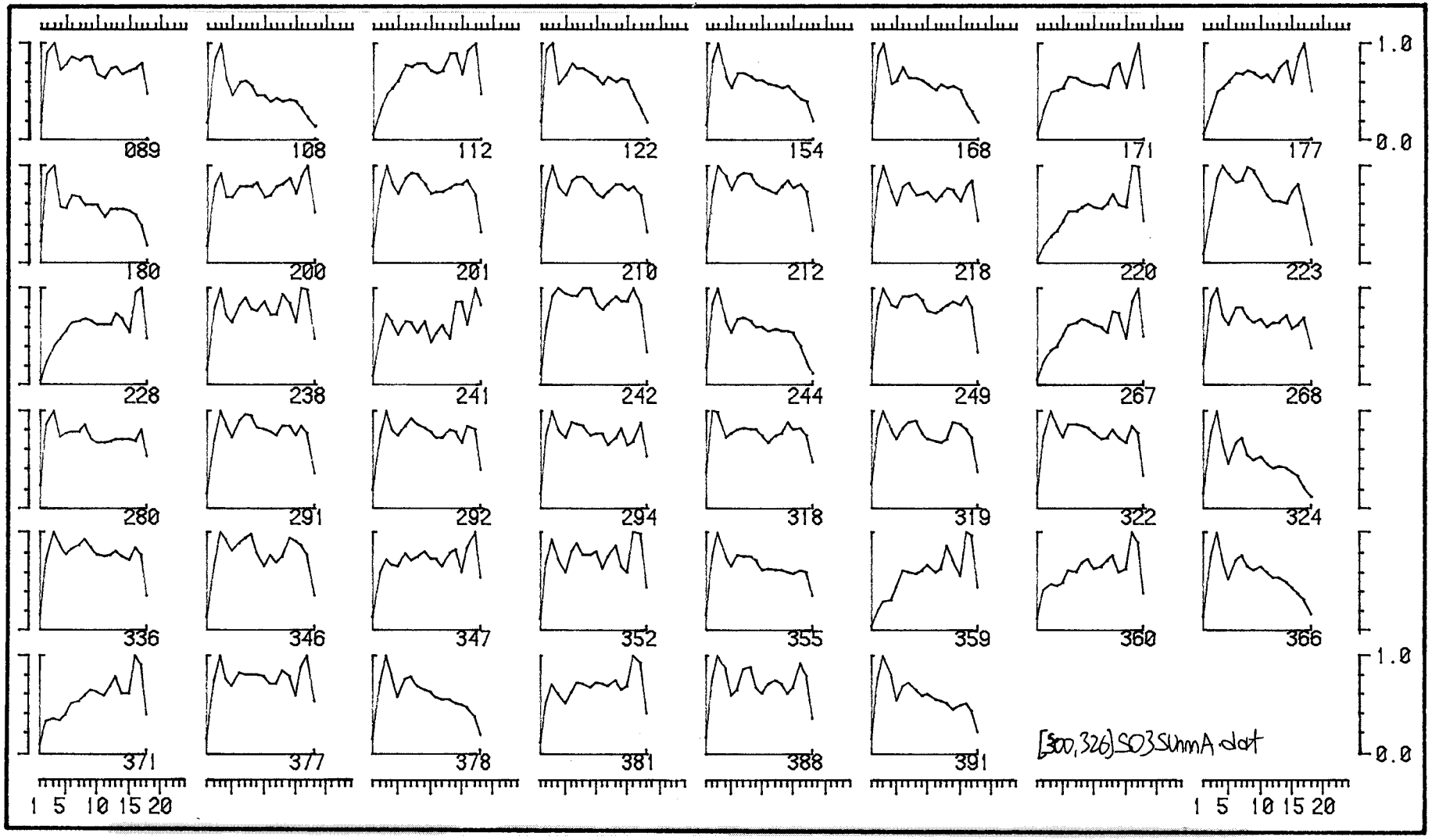

GRAPH 4.82

Bending Moments in the South Uist 46 SPECTRA

self-scaled to show SHAPES of arrays

36 joints Stiffness: 1000 Nm/rad

sea set: SU'a'

HEAVE joints

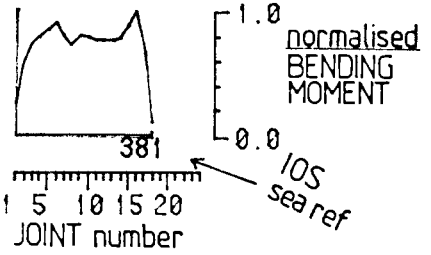

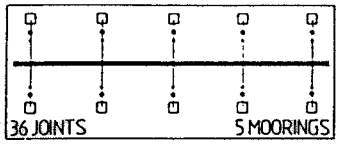

the 46 SPECTRA 'a' set

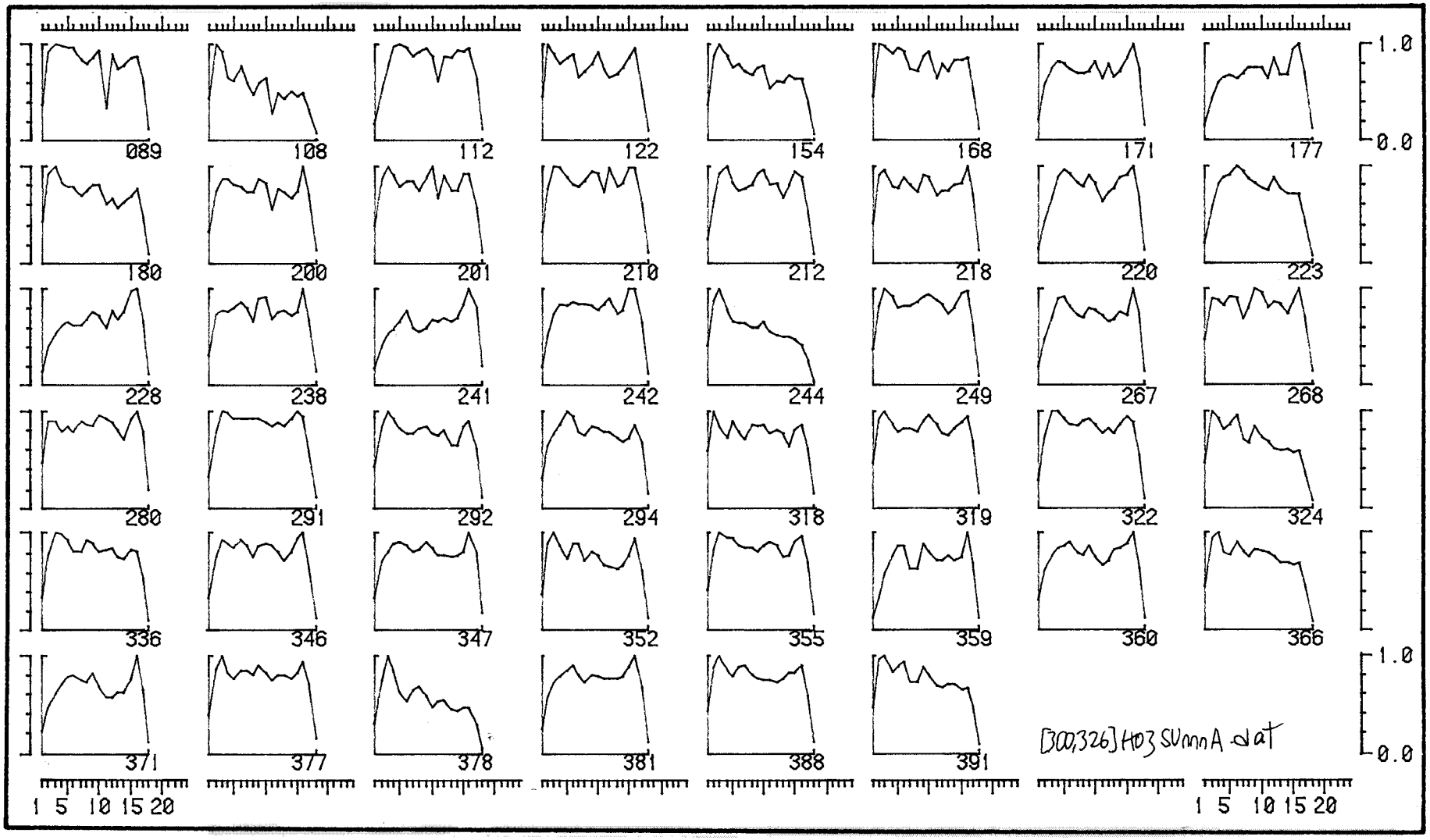

GRAPH 4.83

Bending Moments in the South Uist 46 SPECTRA

self-scaled to show SHAPES of arrays

22 joints Stiffness: 1000 Nm/rad

sea set: SU'a'

SURGE joints

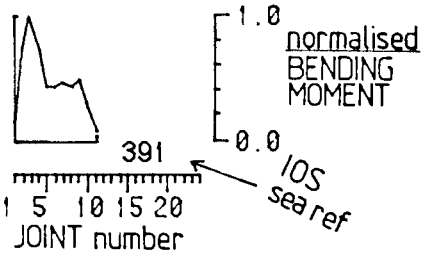

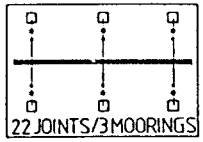

the 46 SPECTRA 'a' set

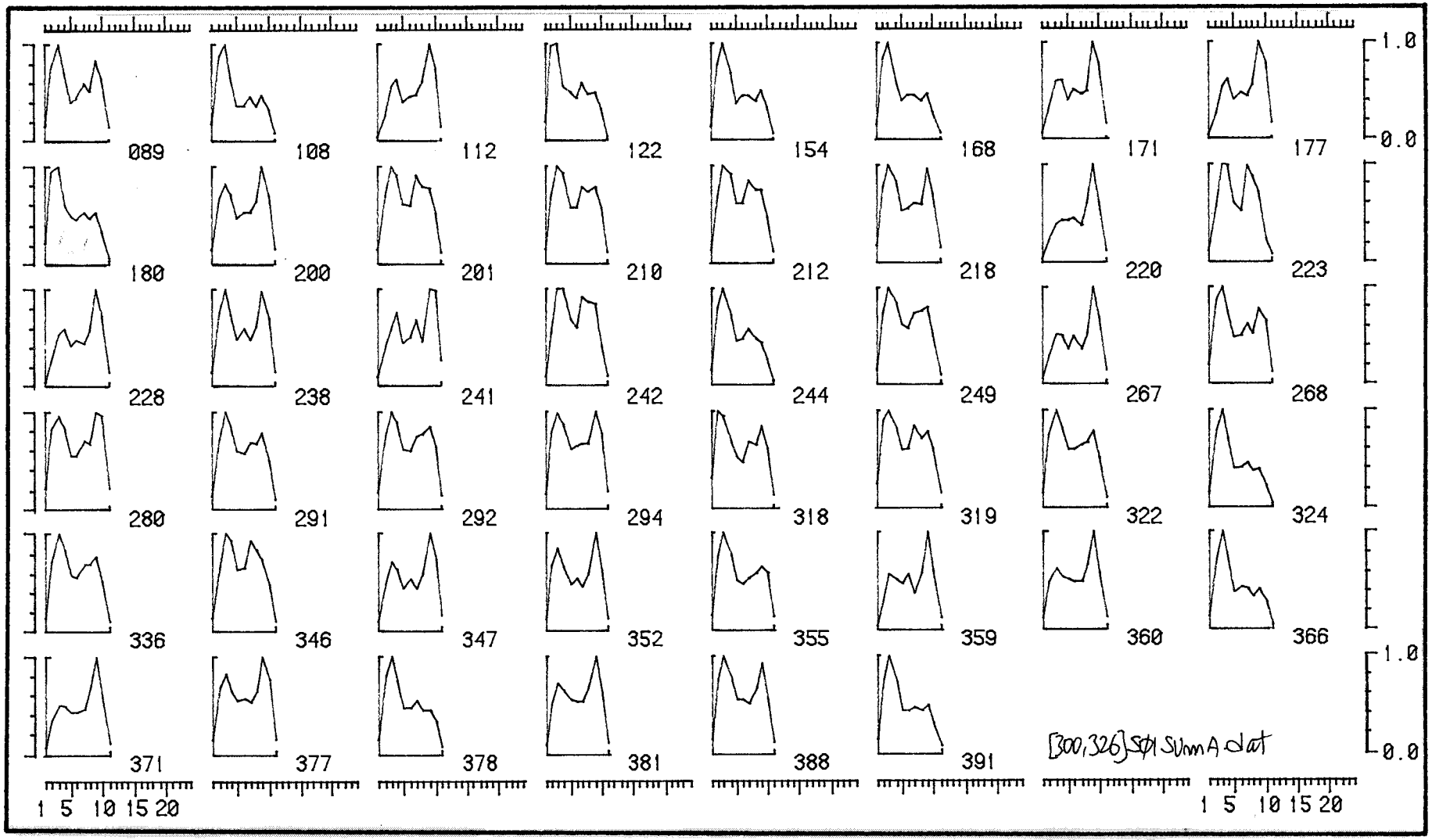

GRAPH 4.84

Bending Moments in the South Uist 46 SPECTRA

self-scaled to show SHAPES of arrays

22 joints Stiffness: 1000 Nm/rad

sea set: SU'a'

HEAVE joints

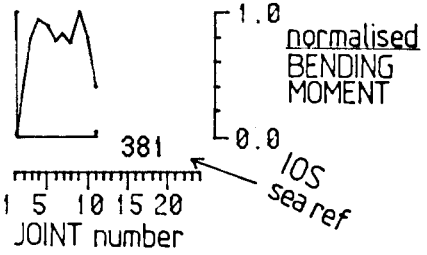

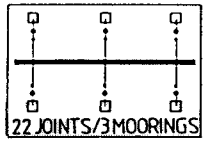

the 46 SPECTRA 'a' set

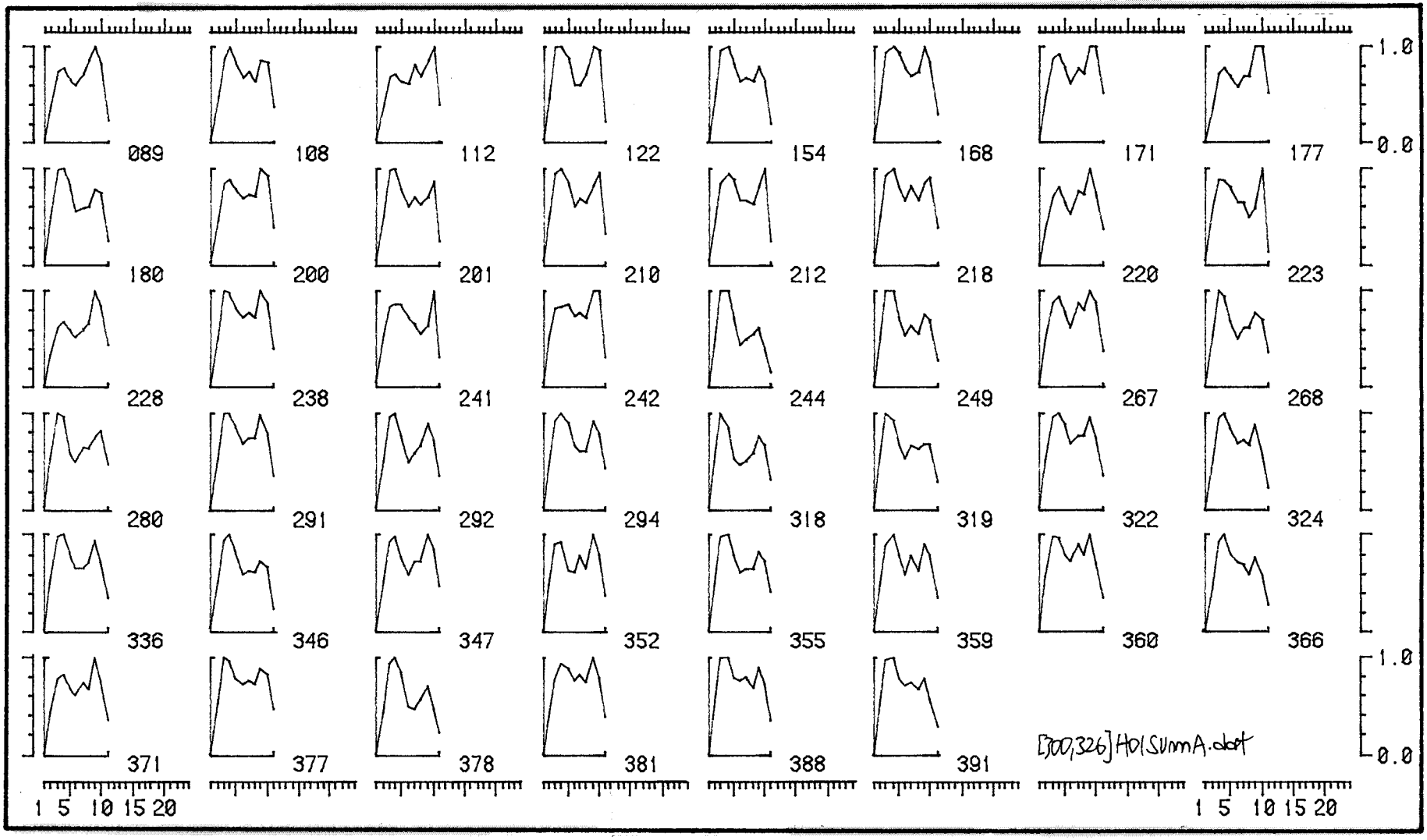

GRAPH 4.85

Bending Moments in the South Uist 46 SPECTRA

self-scaled to show SHAPES of arrays

22 joints Stiffness: 1000 Nm/rad

sea set: SU 'b'

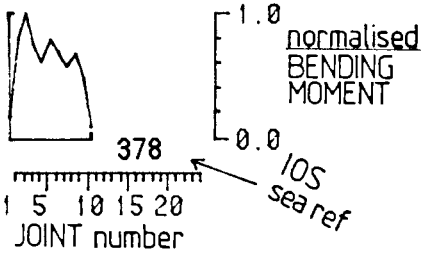

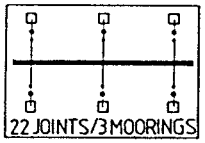

SURGE joints

the 46 SPECTRA 'b' set

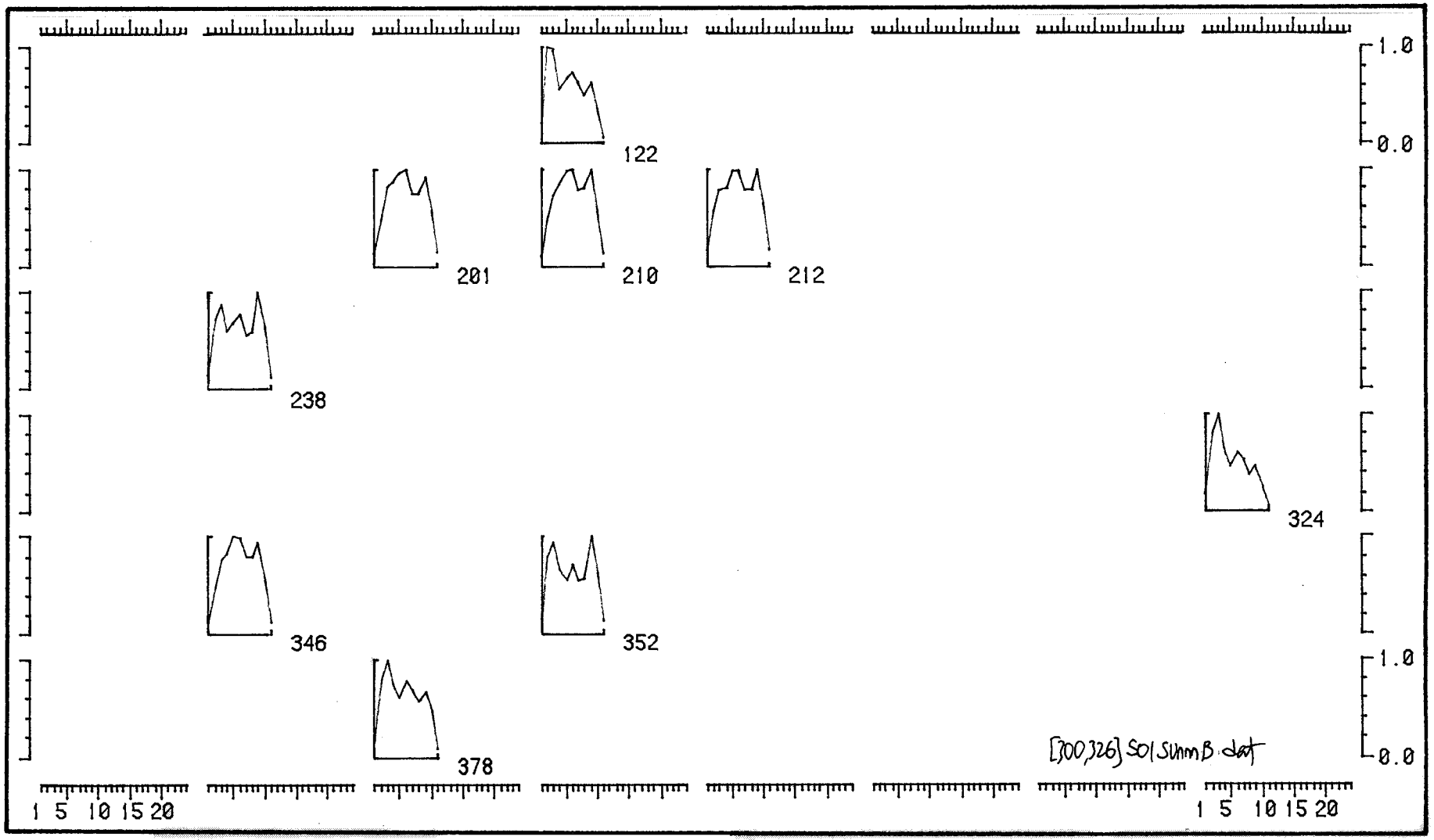

GRAPH 4.86

Bending Moments in the South Uist 46 SPECTRA

self-scaled to show SHAPES of arrays

22 joints Stiffness: 1000 Nm/rad

sea set: SU 'b'

HEAVE joints

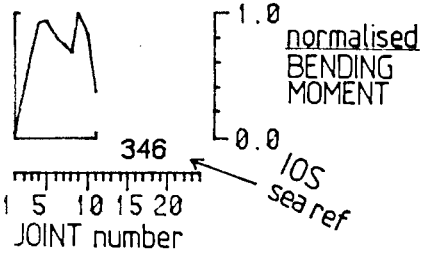

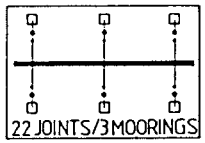

the 46 SPECTRA 'b' set

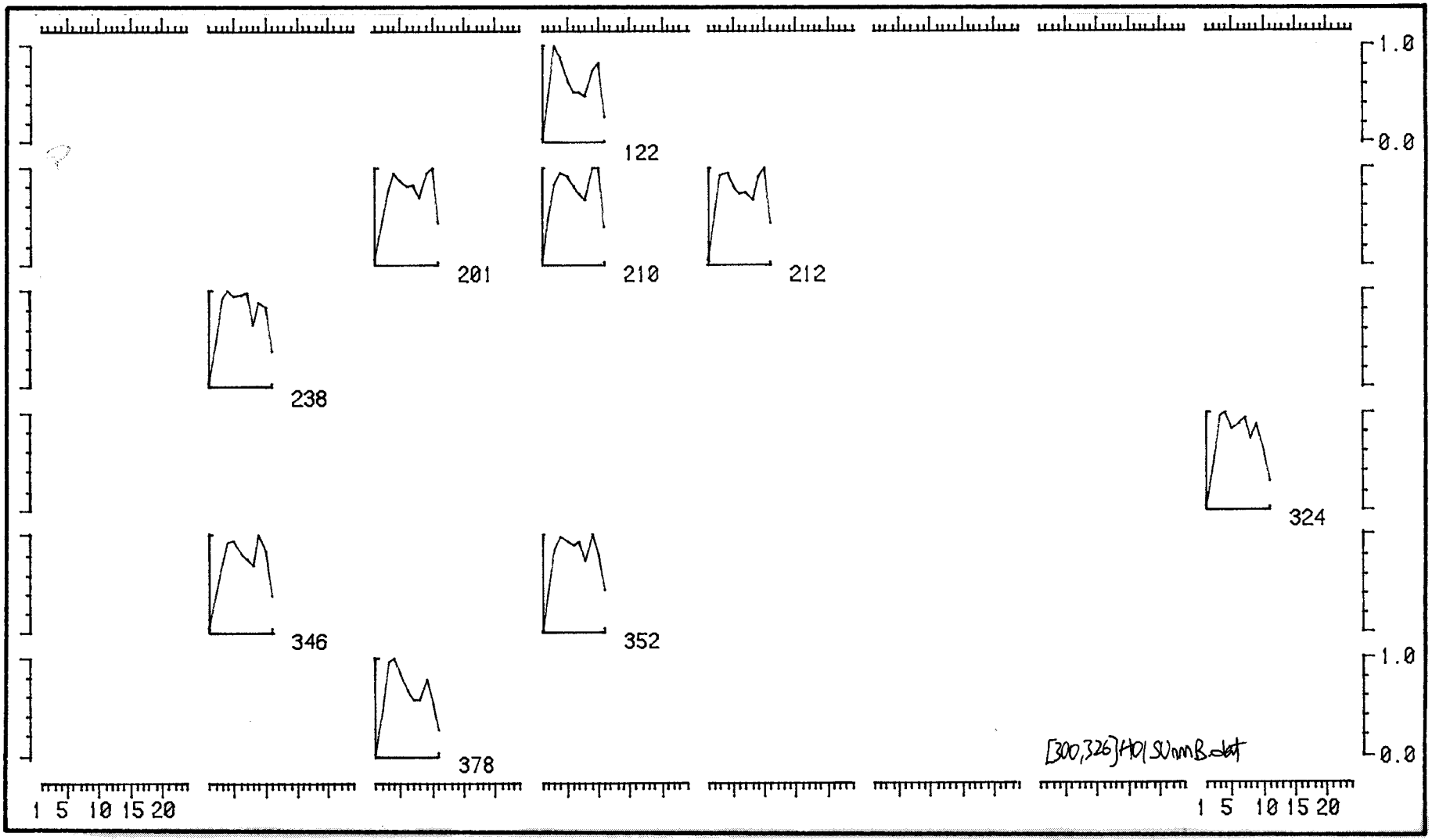

GRAPH 4.87

Bending Moments in the South Uist 46 SPECTRA

self-scaled to show SHAPES of arrays

22 joints Stiffness: 1000 Nm/rad

sea set: SU 'd'

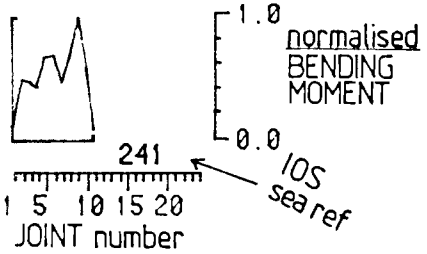

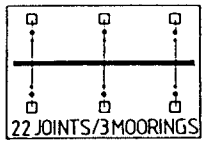

SURGE joints

the 46 SPECTRA 'd' set

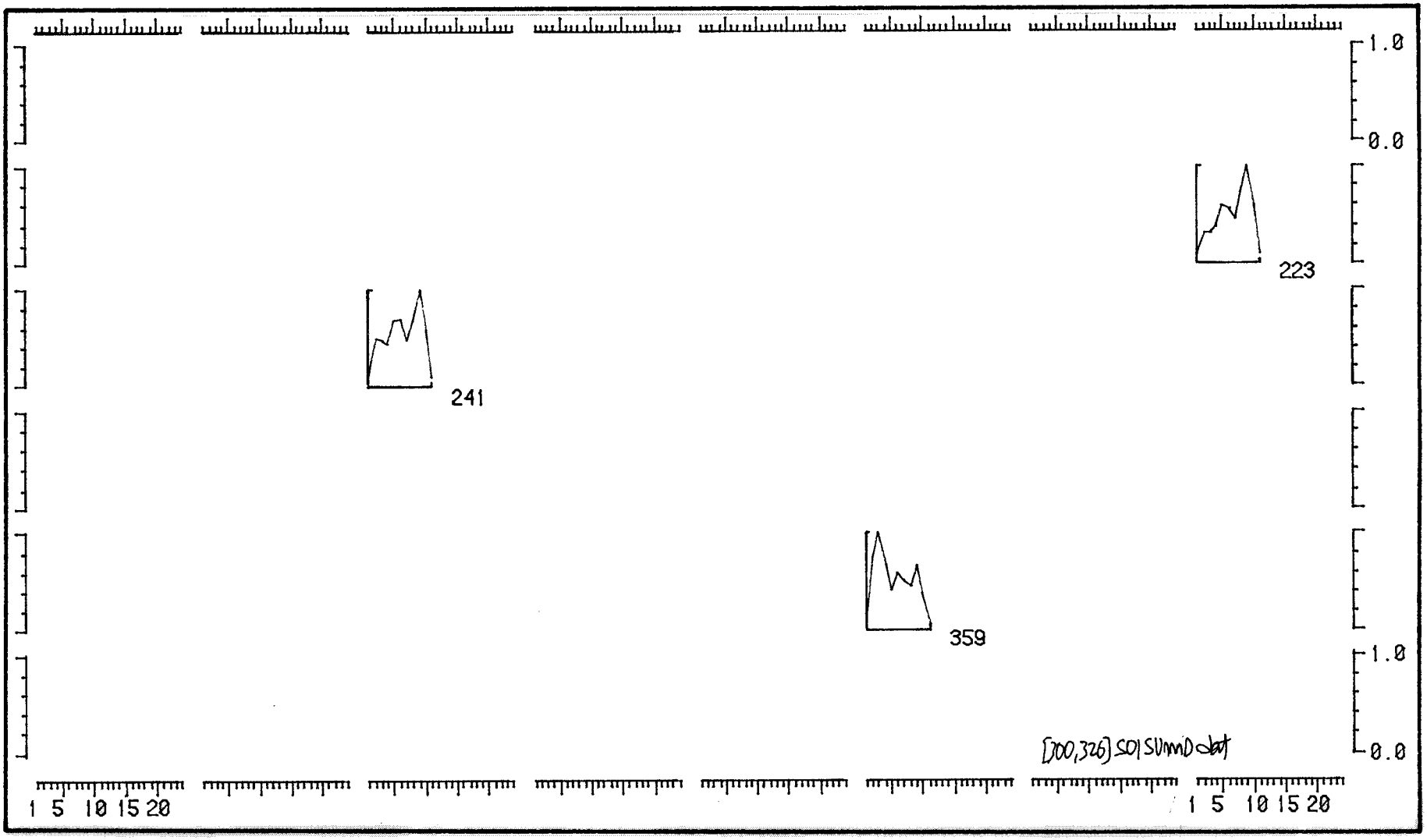

GRAPH 4.88

Bending Moments in the South Uist 46 SPECTRA

self-scaled to show SHAPES of arrays

22 joints Stiffness: 1000 Nm/rad

sea set: SU 'd'

HEAVE joints

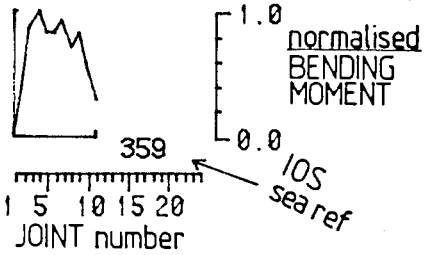

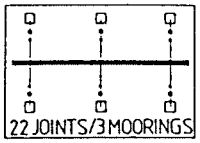

the 46 SPECTRA 'd' set

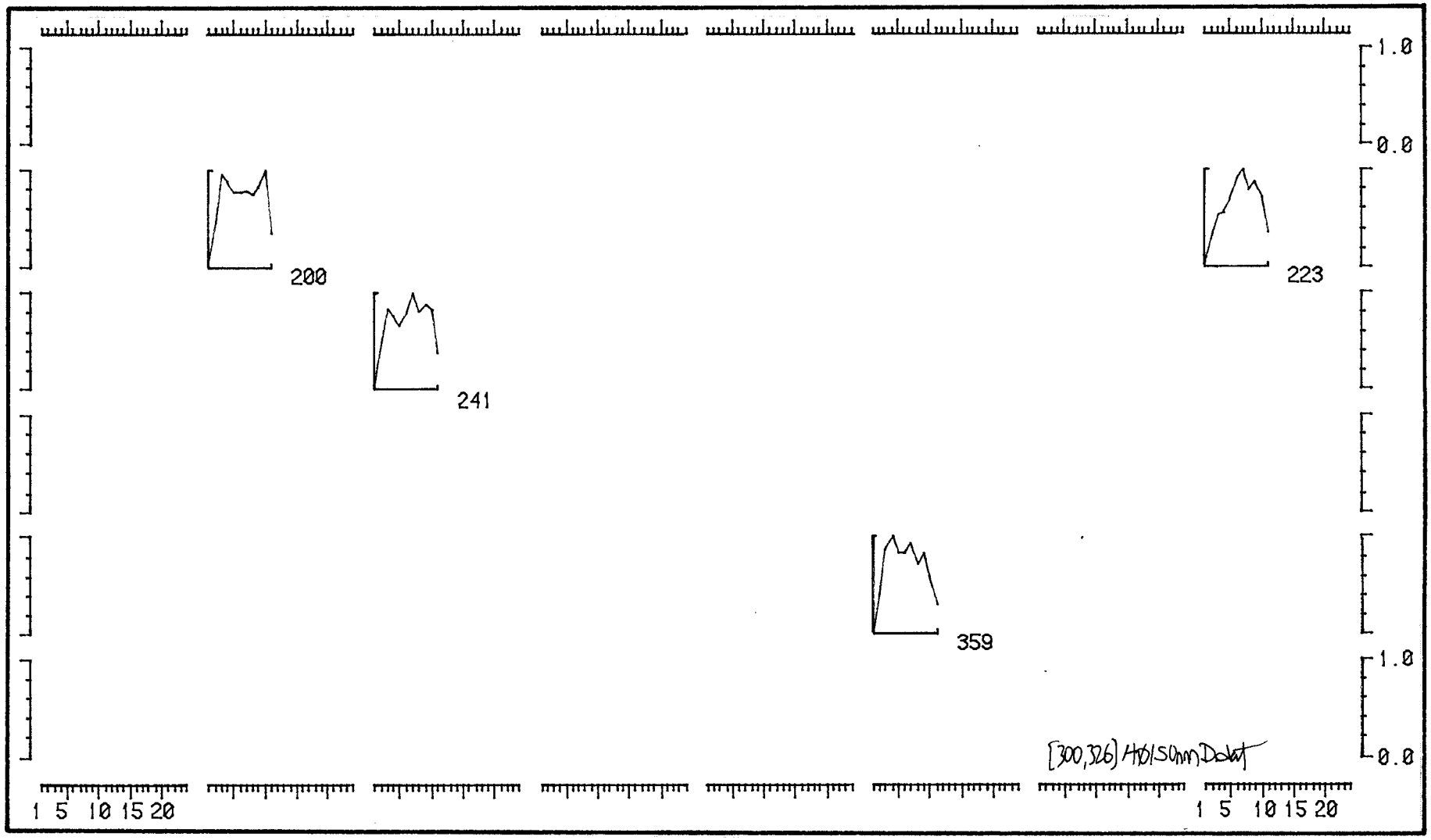

GRAPH 4.89

4.H BENDING MOMENTS IN ANGLED MONOCHROMATIC WAVES

By this stage in the tests it was clear to us that by far the most interesting phenomenon was the enhancement of bending moment at the down wave end of the spine. We formed a theory to explain the effect and carried out the next series of tests in monochromatic waves to test it.

We were interested in crest length, crest angle and crest velocity and we varied them together with energy period for two spine stiffnesses. The results are dramatic. Look at graph 4.90 for 40° crest angle and 1.6 seconds period. The surge trace shows growing cyclical variations of bending moment as we move along the spine. The behaviour is repeated for shorter periods and smaller offset angles so that a group of similar plots lie on a diagonal of the page. The violence of the variations seems to be growing as we move to longer period and bigger offsets. Despite the fact that the seas were nominally the same amplitude (1.414 cm) we get bending moment variation of at least 20:1 for the same offset angle and even more if we change offset and period.

In graphs 4.91 we have normalised the results by dividing by the measured value of wave amplitude to correct for any minor variations and superimposed rows and columns at bottom and right.

The heave results in graph 4.92 show slightly less dramatic changes but nevertheless the effect is clearly visible for 0.8 second period and -10 degrees of offset. The number of humps decreases from 4 to 2 as the period increases.

All the tests so far described in this section were carried out with a stiffness of 3500 Nm/rad. When in graph 4.93 we cut stiffness to 1000 Nm/rad we can see that the enhancement ridge is moved to bigger offset angles. Normalisation and superposition of rows and columns is as before.

effect on Bending Moments of varying CREST ANGLE and Energy Period

44 joints Stiffness: 3500 Nm/rad

monochromatic seas, Hrms: 1.414 cm sea set: MO 'a'

SURGE & HEAVE joints

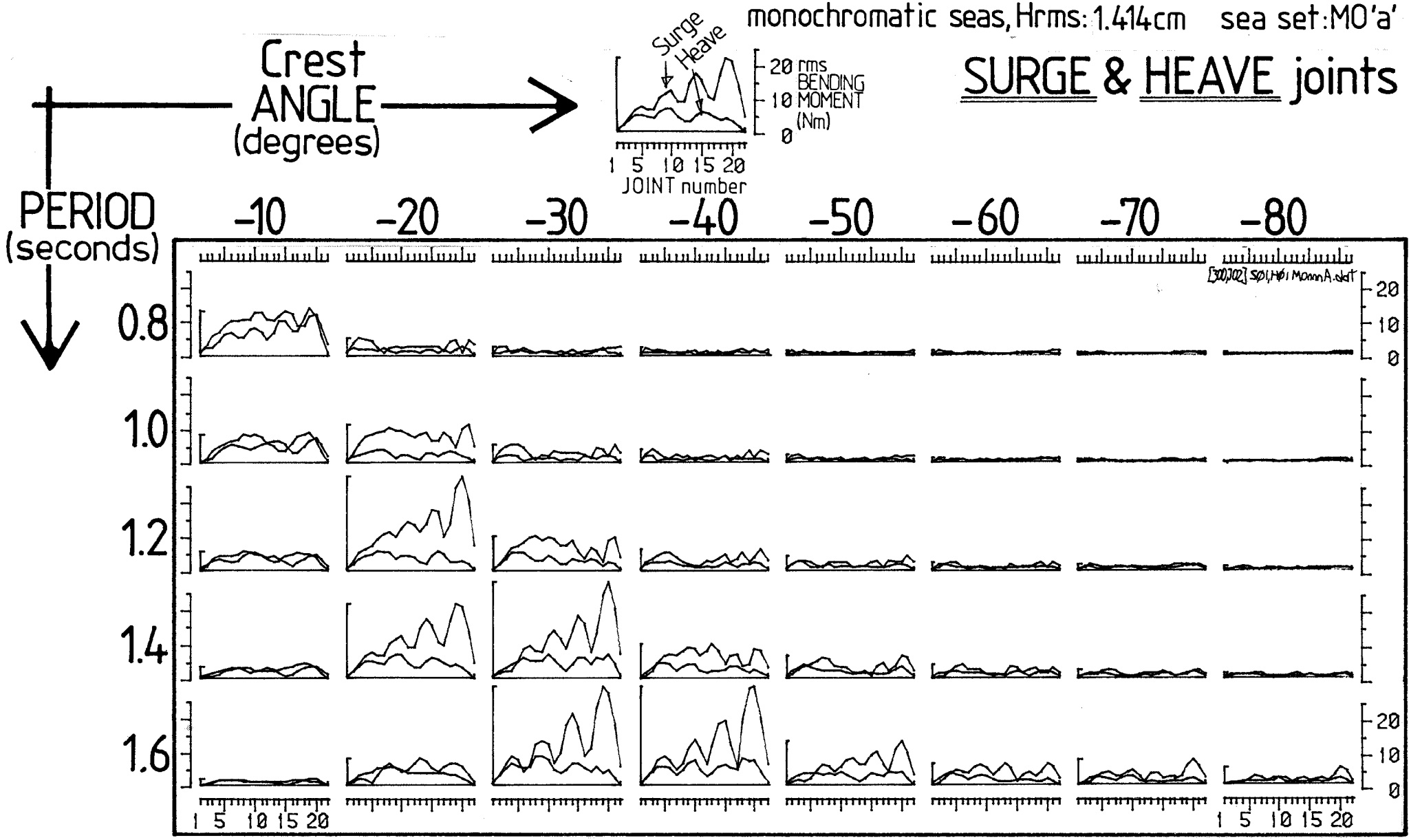

GRAPH 4.90

effect on Bending Moments of varying CREST ANGLE and Energy Period

44 joints Stiffness 3500 Nm/rad

monochromatic seas, Hrms: 1.414 cm sea set: MO'a'

NORMALISATION: data divided by $(Hrms)^{0.8}$ SURGE joints

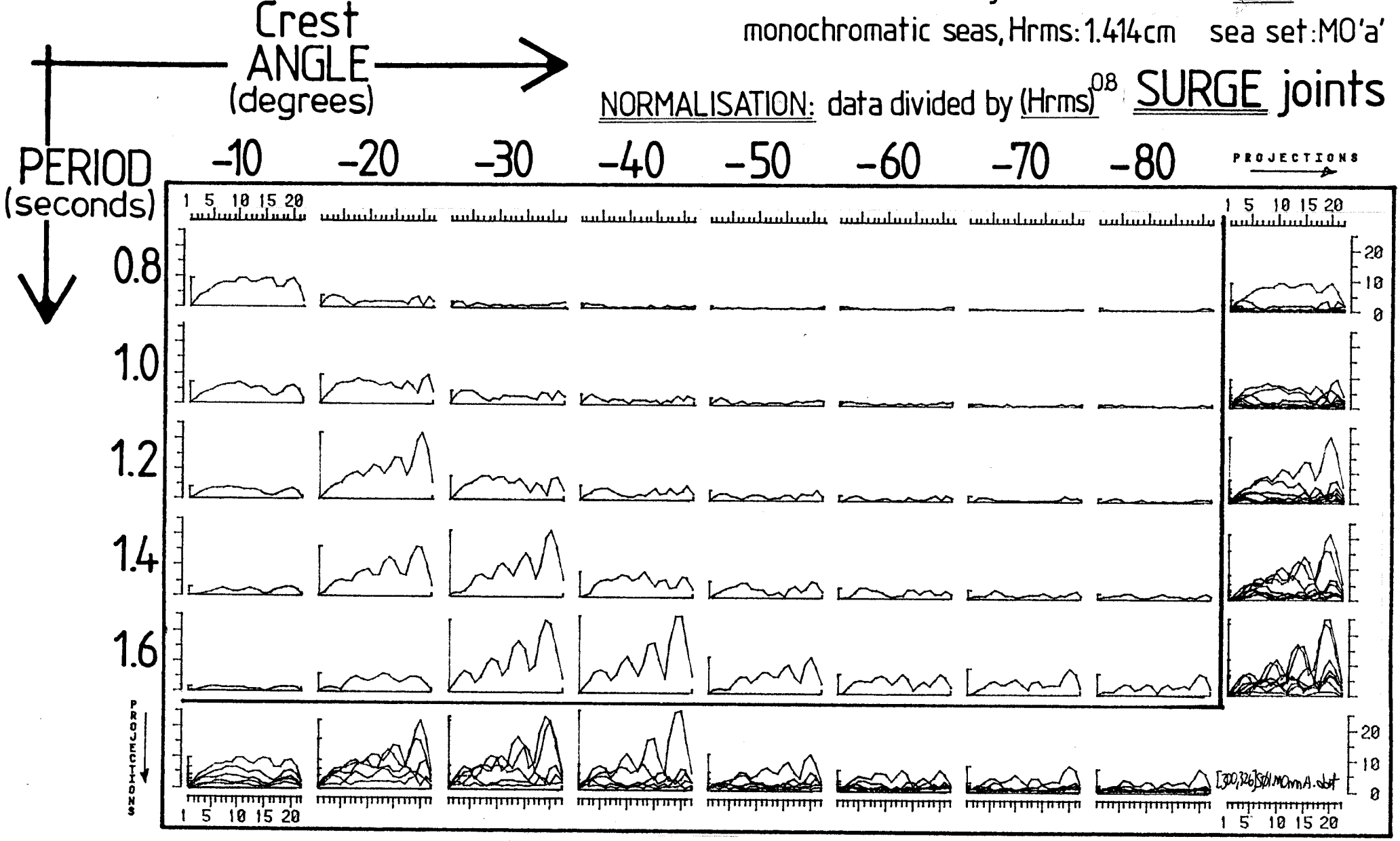

GRAPH 4.91

monochromatic seas

effect on Bending Moments of varying CREST ANGLE and Energy Period

44 joints Stiffness: 3500Nm/rad

monochromatic seas, Hrms: 1.414cm sea set: MO'a'

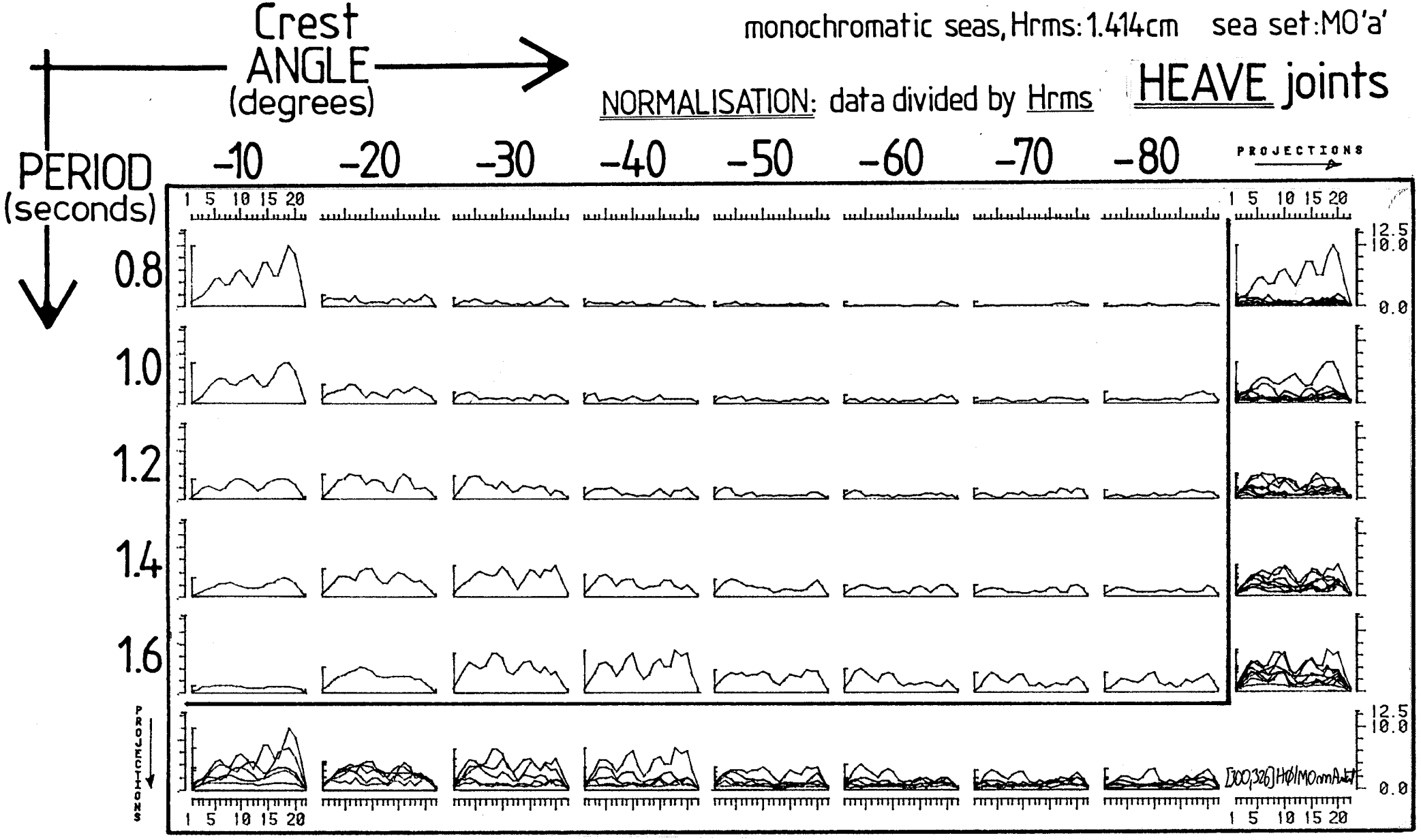

GRAPH 4.92

effect on Bending Moments of varying CREST ANGLE and Energy Period

44 joints Stiffness: 1000 Nm/rad

monochromatic seas, Hrms: 1.414cm sea set: MO'a'

NORMALISATION: data divided by $(Hrms)^{0.8}$ SURGE joints

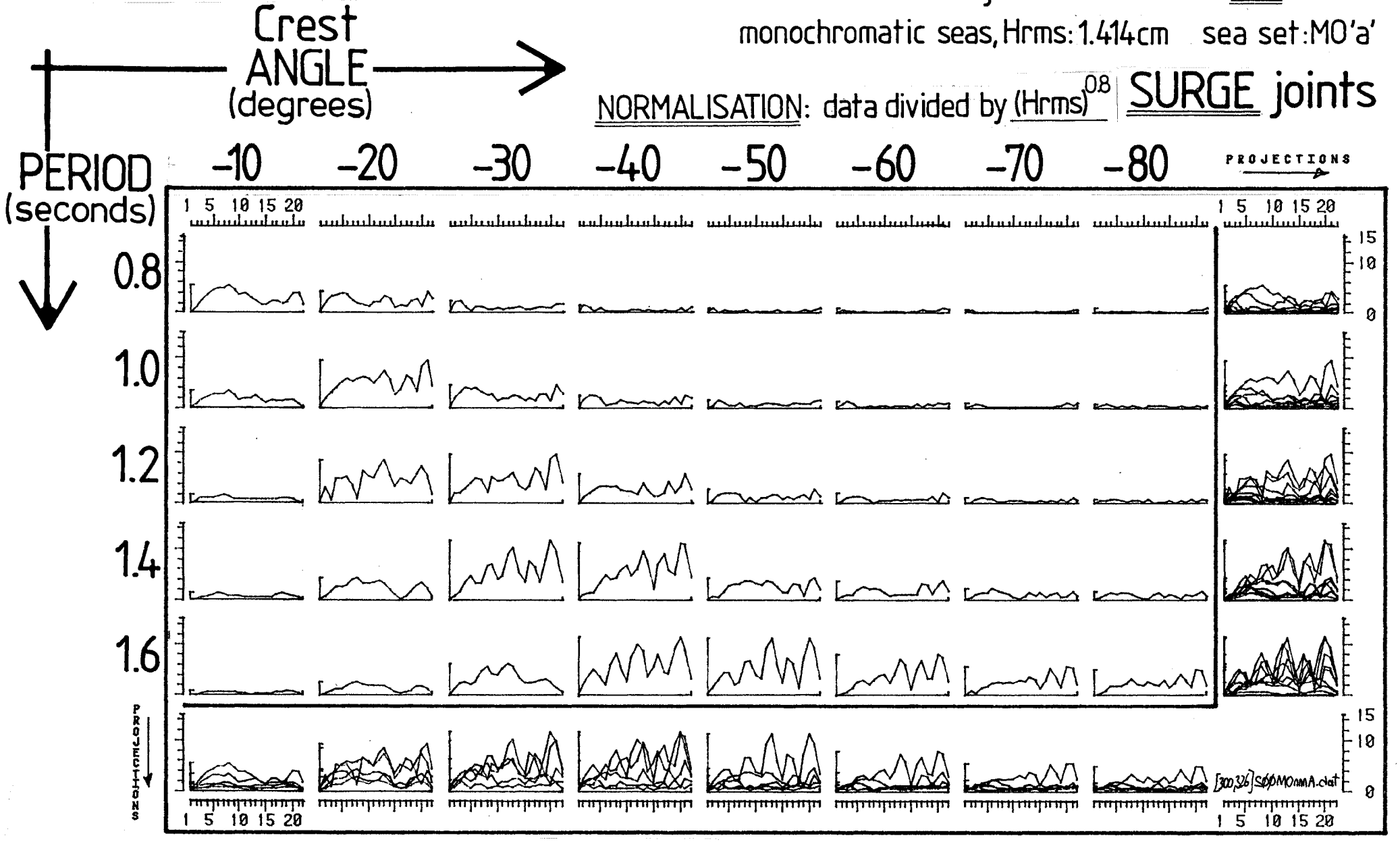

GRAPH 4.93

(4.H cont)

Next, in graphs 4.94 to 4.96, we carried out a fresh series of tests in which the variable is crest length. For a single wavefront sea we define crest length as the distance along the spine between points of the same phase. Some sub-graphs are missing because they would lie outside the tank envelope. Once again we see the same pattern of progressively increasing bending moments as we move down-wave along the spine. The oblique ridge has moved nearly to the vertical. The maximum surge values are between 5 and 6 metres crest length, independent of period.

Surge moments get worse with longer periods but in graph 4.96 the opposite is true for heave. Note the splendid effect for 6 metres at 1.0 second.

effect on Bending Moments of varying CREST LENGTH and Energy Period

44 joints Stiffness: 1000 Nm/rad

monochromatic seas, Hrms: 1.0cm sea set: MO 'b'

SURGE & HEAVE joints

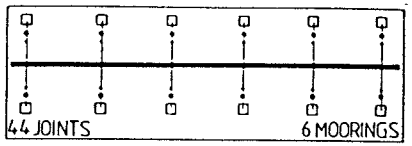

Crest LENGTH (metres)

PERIOD (seconds)

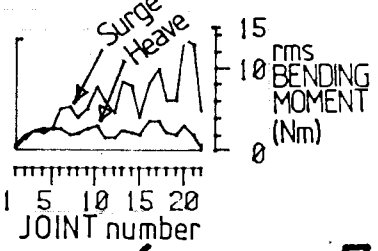

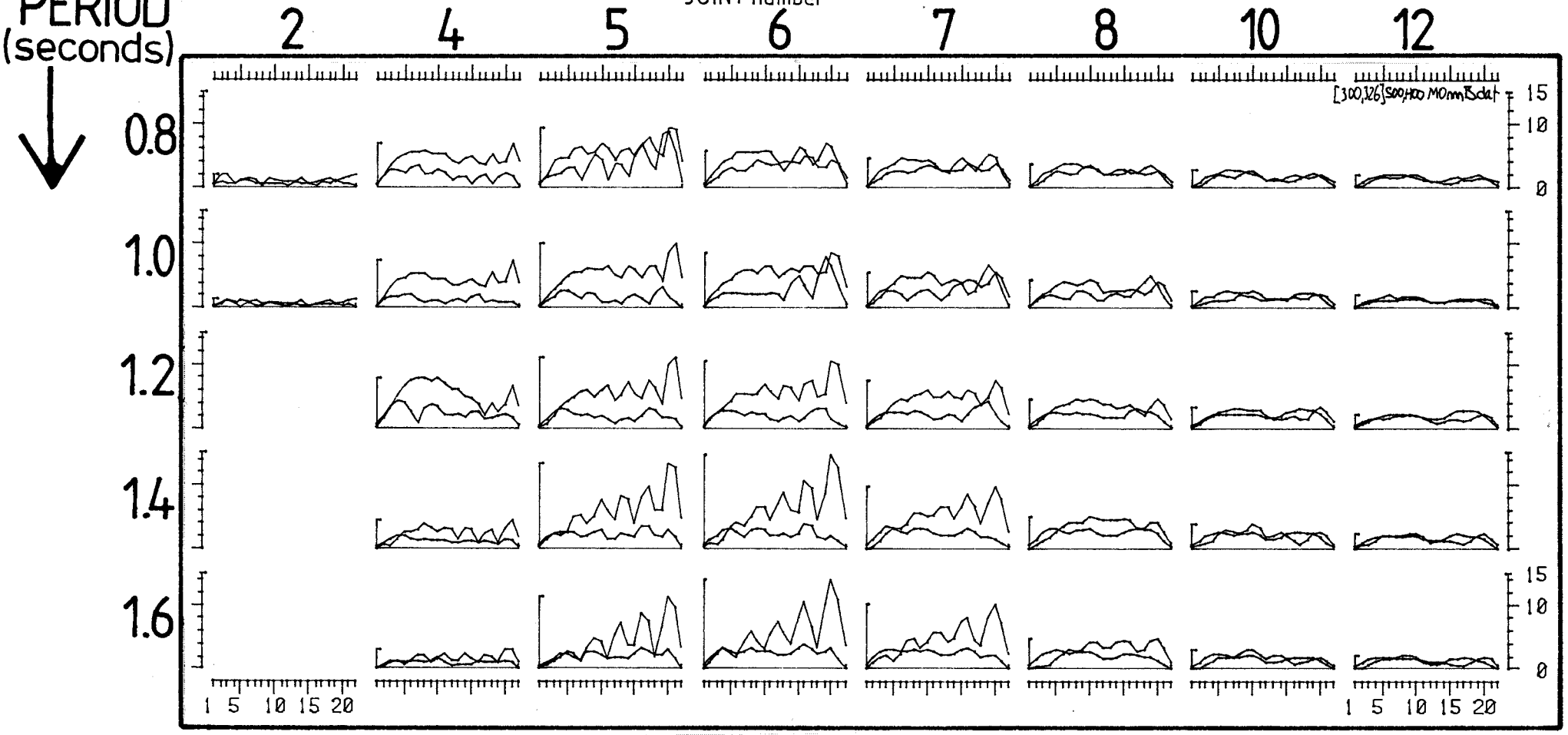

GRAPH 4.94

effect on Bending Moments of varying CREST LENGTH and Energy Period

44 joints Stiffness: 1000 Nm/rad

monochromatic seas, Hrms: 1.0cm sea set: MO 'b'

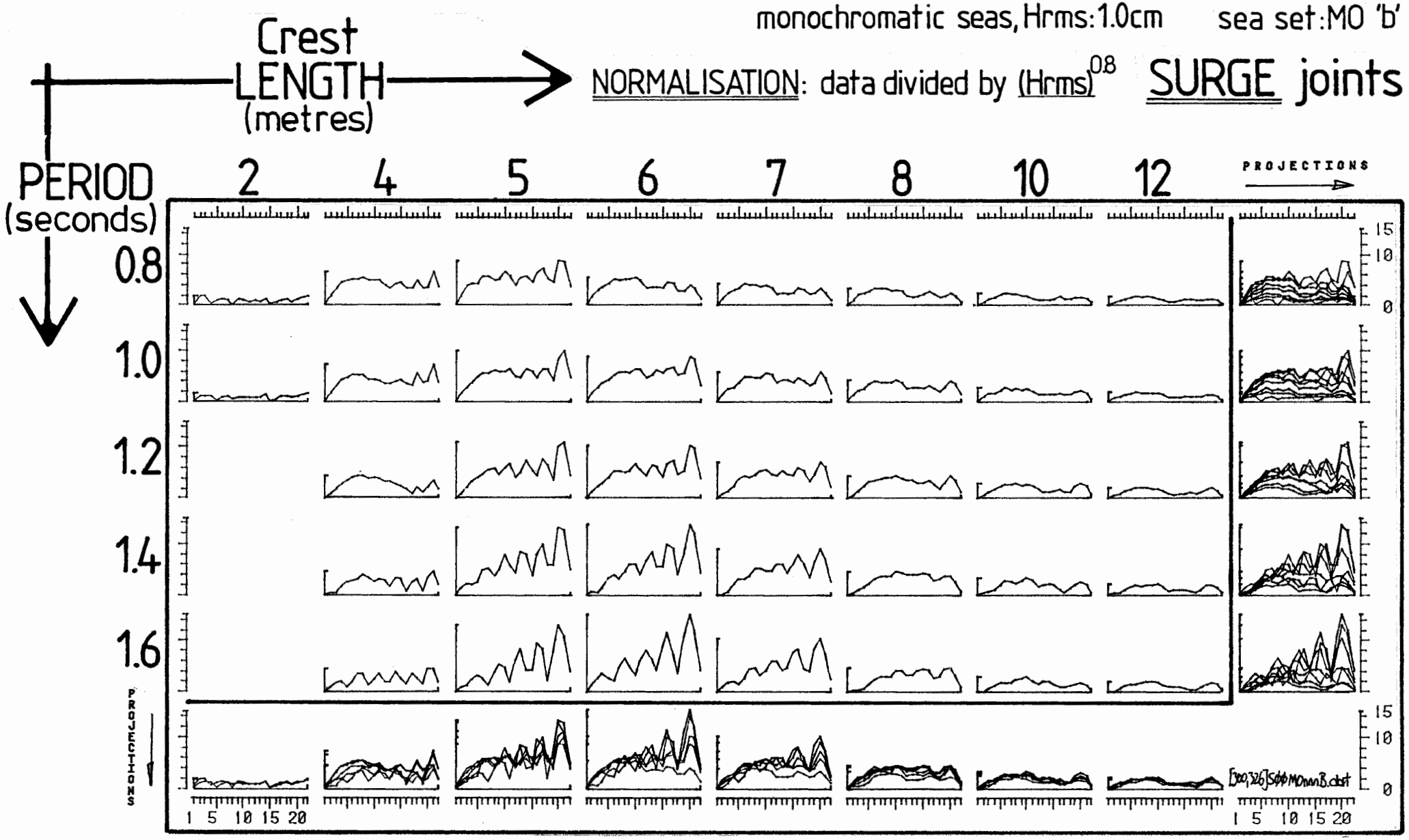

GRAPH 4.95

effect on Bending Moments of varying CREST LENGTH and Energy Period

44 joints Stiffness: 1000 Nm/rad

monochromatic seas, Hrms: 1.0cm sea set: MO 'b'

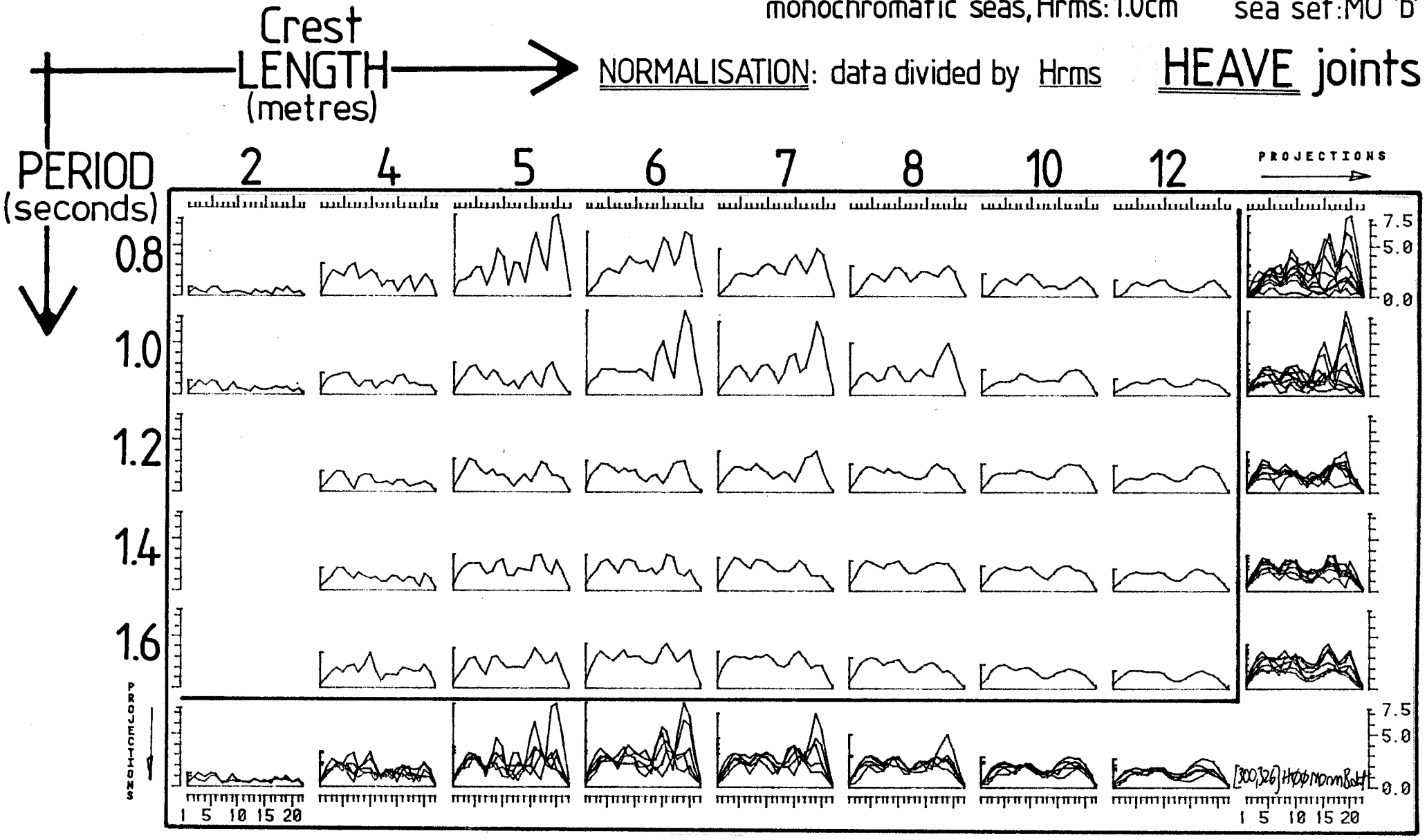

GRAPH 4.96

(4.H cont)

Our next variable is the velocity of the crest as it moves along the spine. Graph 4.97 shows heave and surge superimposed for a stiffness of 3500 Nm/rad. Peak surge values are always bigger than peak heave except in the top right test. The maximum enhancement for heave occurs at 8m/sec (it might still have been getting bigger) and 0.8 seconds whereas the surge effect is biggest at 4 m/sec and 1.6 seconds.

In graphs 4.98 and 4.99 we separate heave and surge and superimpose rows and columns to emphasise the wide range of variation. While one's eyes are naturally drawn to the most dramatic results we should not overlook the 8 m/sec 1.6 sec entry on graph 4.98, which has a peak-free flat response. This is what a naive expectation might have been but it is extremely rare for long spines. The only other examples in this report are for rather short lengths.

Next we reduced the stiffness to 1000 Nm/rad for graphs 4.100 to 4.102. Note that the vertical scale is also changed. In both surge and heave the maximum enhancement has moved to the left, i.e. toward slower crest velocities, and the number of humps has increased from 4 to 5.

monochromatic seas

effect on Bending Moments of varying CREST VELOCITY and Energy Period

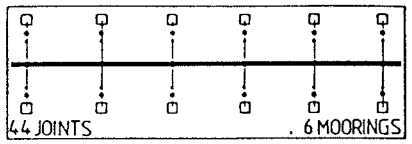

44 joints Stiffness: 3500 Nm/rad

monochromatic seas, Hrms: 1.0cm sea set: MO 'c'

SURGE & HEAVE joints

Crest VELOCITY (m/sec) →

PERIOD (seconds) ↓

2 3 4 5 6 7 8

0.8 1.0 1.2 1.4 1.6

heave

20 10 0

Surge
Heave

rms BENDING MOMENT (Nm)

20 10 0

1 5 10 15 20
JOINT number

GRAPH 4.97

effect on Bending Moments of varying CREST VELOCITY and Energy Period

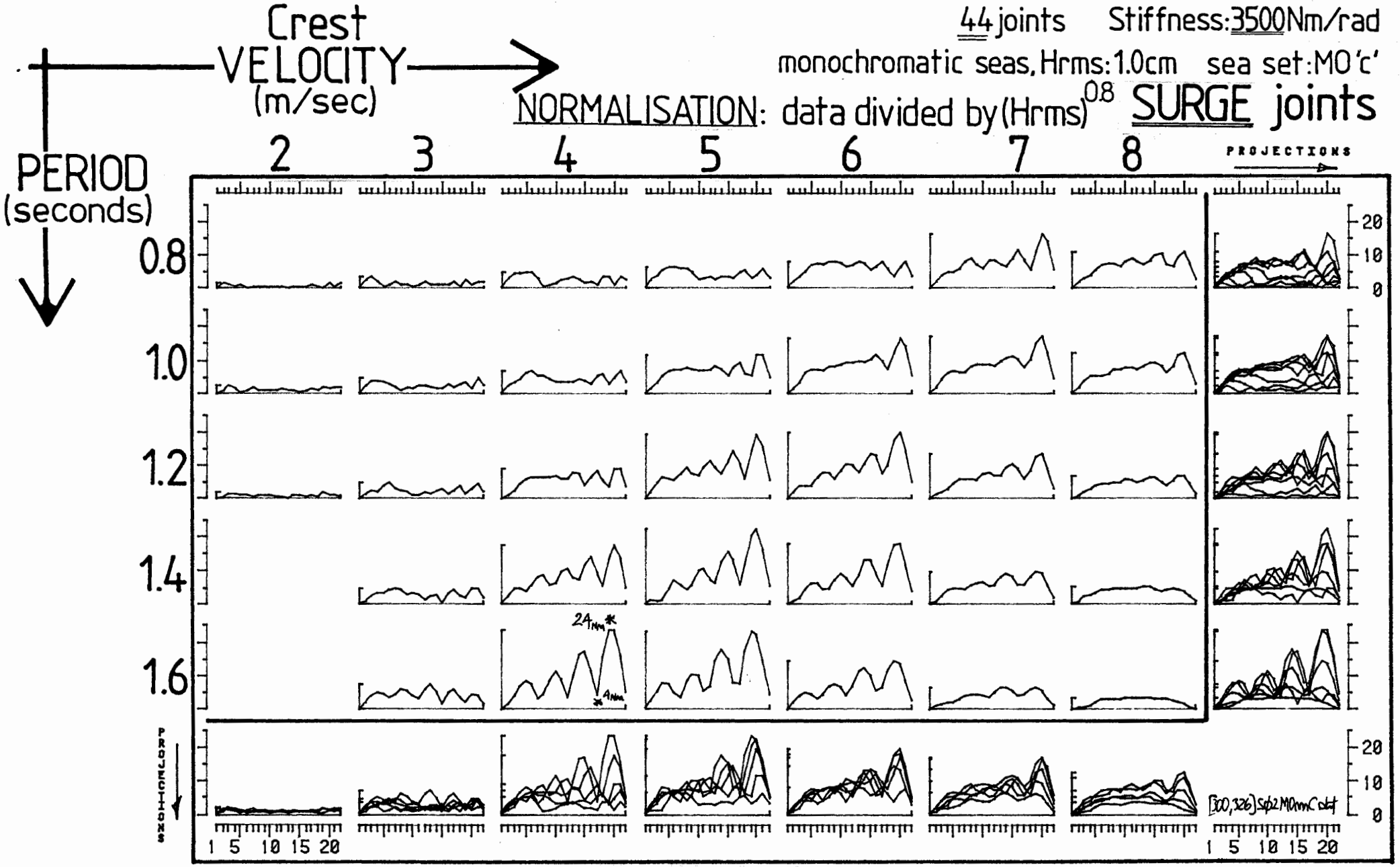

GRAPH 4.98

monochromatic seas

effect on Bending Moments of varying CREST VELOCITY and Energy Period

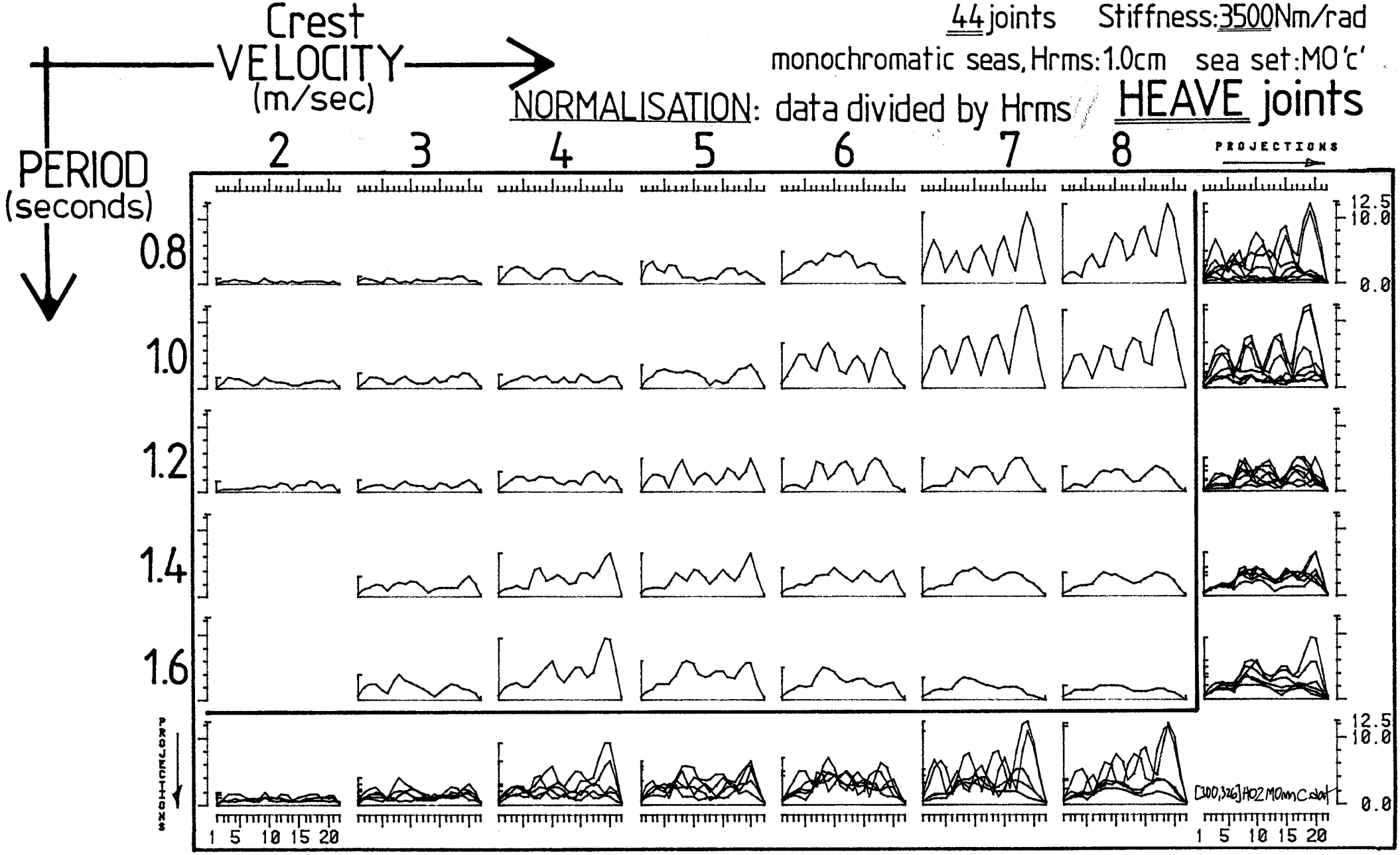

GRAPH 4.99

monochromatic seas

effect on Bending Moments of varying CREST VELOCITY and Energy Period

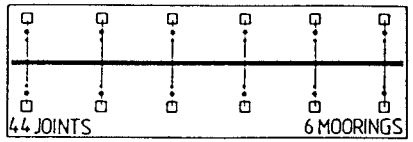

44 joints Stiffness: 1000 Nm/rad

monochromatic seas, Hrms: 1.0cm sea set: MO 'c'

SURGE & HEAVE joints

Crest VELOCITY (m/sec) →

PERIOD (seconds) ↓

2 3 4 5 6 7 8

0.8

1.0

1.2

1.4

1.6

15 10 0

1 5 10 15 20

Surge
Heave

15 rms BENDING MOMENT (Nm)
10
0

1 5 10 15 20
JOINT number

GRAPH 4.100

monochromatic seas

effect on Bending Moments of varying CREST VELOCITY and Energy Period

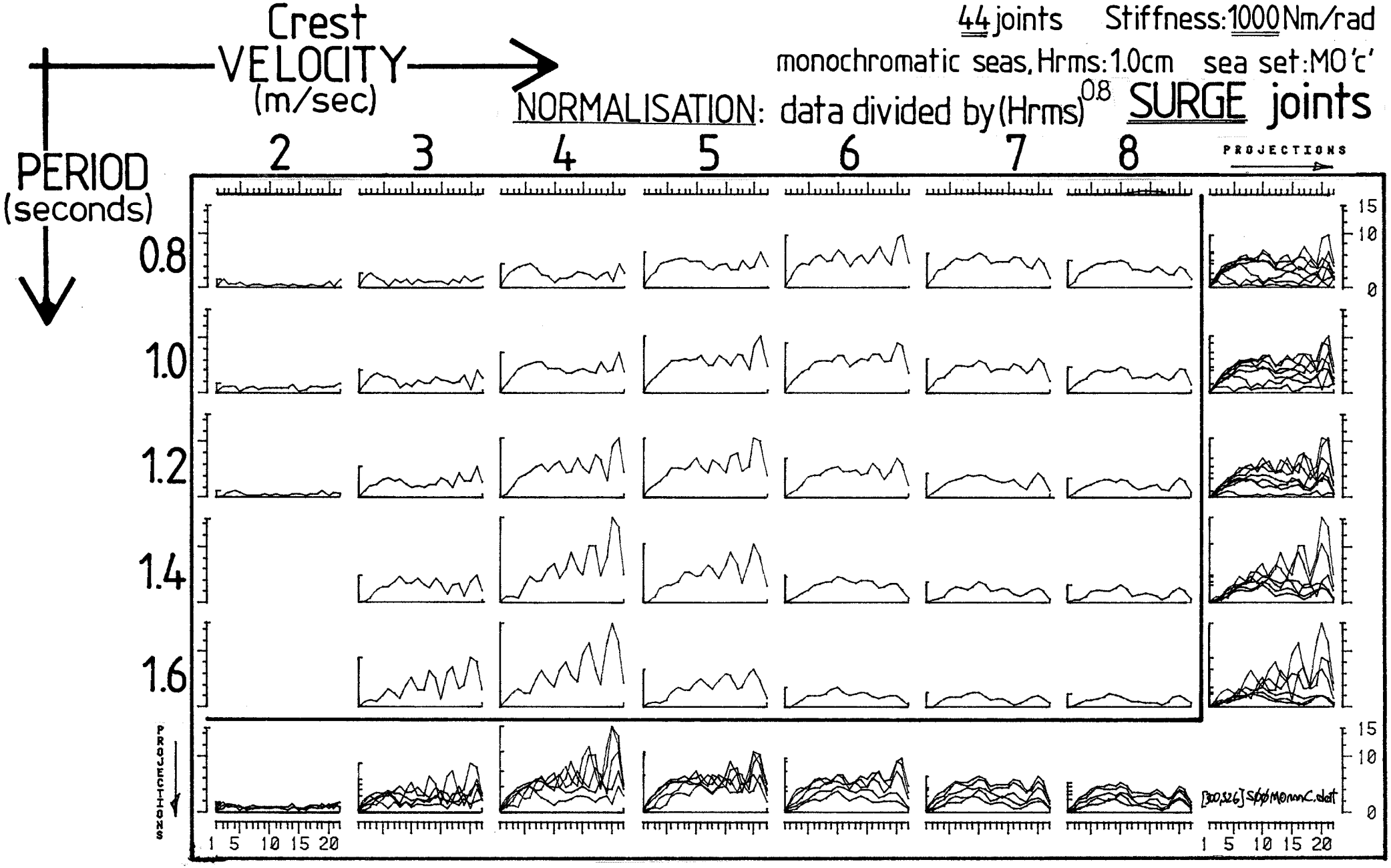

GRAPH 4.101

monochromatic seas

effect on Bending Moments of varying CREST VELOCITY and Energy Period

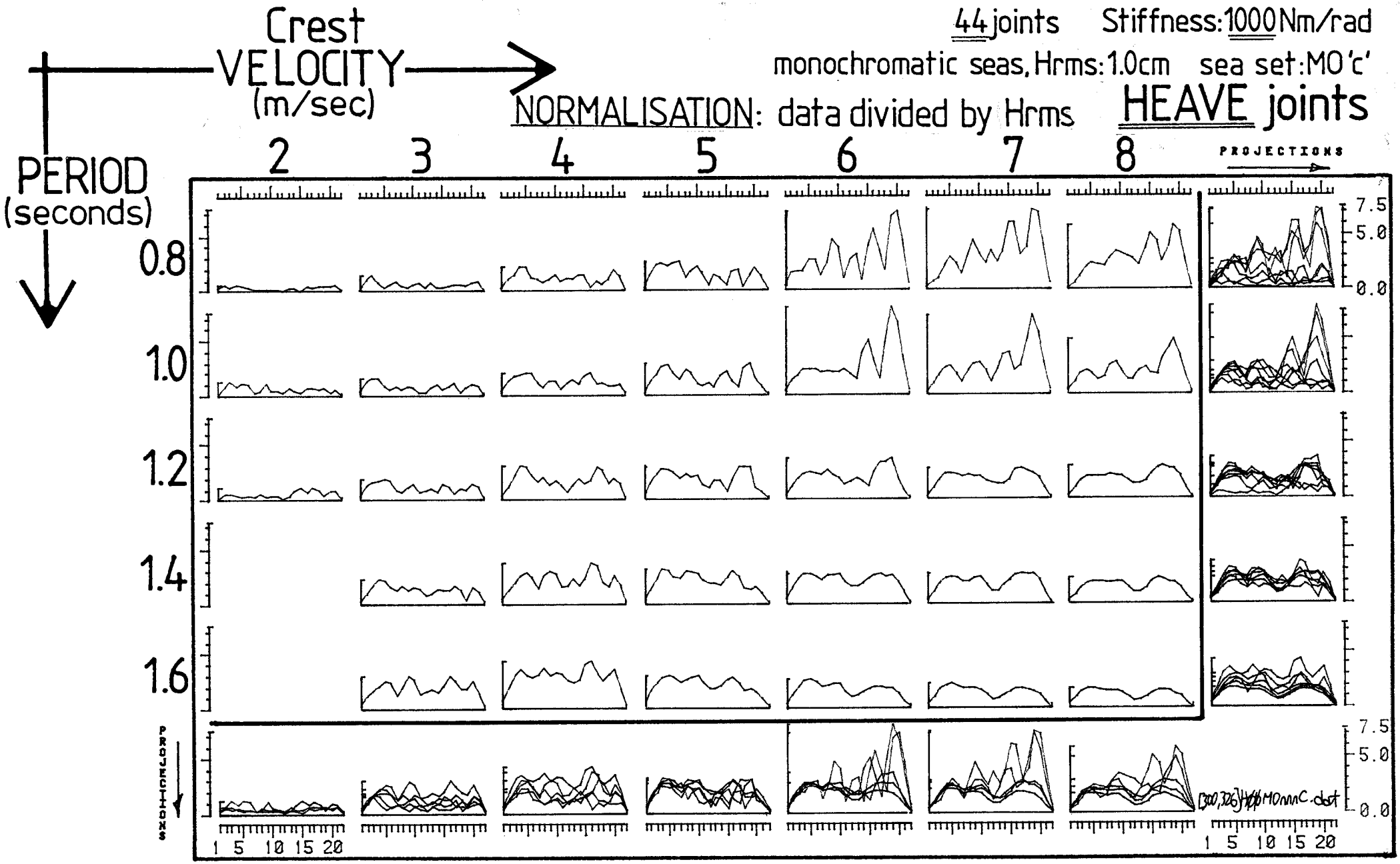

GRAPH 4.102

(4.H cont)

Our next variable was to test crest velocity against period for shorter lengths and two stiffnesses. Graph 4.103 for 28 joints shows that the maximum value of the peaks is about the same and occurs in nearly the same test conditions. There is only room for 2 or 3 peaks but otherwise the results are very close to those for longer lengths. Clearly the length is not the cause of the enhancement. The unusual zero ripple surge result for 8m/sec and 1.6 seconds on graph 4.98 does not occur on 4.104 although there are two such results for heave on 4.105.

Cutting the stiffness for the 28 joint spine (graphs 4.106 to 4.108) shows the same leftward movement of maximum enhancement and rather less ripple in surge for the higher velocities. Vertical scales are changed.

Cutting the length even more to 16 joints in graphs 4.109 to 4.111 for 3500 Nm/rad gives us lots of single hump results. There is a suspicion of double humps beginning in the top left diagonal of the diagram. The maximum value has dropped but nowhere near as much as a length squared rule would predict. Cutting the length by three has reduced peak bending moment to about two thirds. However, if we average the values of the highest peak of a long spine with its adjacent trough ((24 + 4.0) ÷ 2 = 14 Nm on graph 4.98) the result is less than the 16 Nm peak in the centre of a short spine on graph 4.110. We expect that bending moment enhancement will be usefully suppressed by the presence of joint generation and that power-generating joints in long spines will be subject to lower fluid loading than the concrete of short spines. The presence of ducks will also reduce the effects.

Graphs 4.112 to 4.114 show the 16 joint spine with stiffness reduced to 1,000 Nm/rad. Vertical scales are changed. In surge the arrays are more often doubly humped that at 3,500 Nm/rad. In heave the peak bending moments occur at a longer period and a shorter wave velocity.

monochromatic seas

effect on Bending Moments of varying CREST VELOCITY and Energy Period

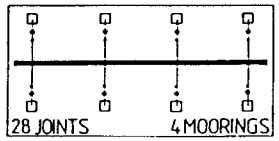

28 joints Stiffness: 3500 Nm/rad

monochromatic seas, Hrms: 1.0cm sea set: MO 'c'

SURGE & HEAVE joints

Crest VELOCITY (m/sec) →

PERIOD (seconds) ↓

2 3 4 5 6 7 8

0.8
1.0
1.2
1.4
1.6

rms BENDING MOMENT (Nm)

20 10 0

Surge Heave

1 5 10 15 20
JOINT number

GRAPH 4.103

monochromatic seas

effect on Bending Moments of varying CREST VELOCITY and Energy Period

28 joints Stiffness: 3500 Nm/rad

monochromatic seas, Hrms: 1.0cm sea set: MO 'c'

NORMALISATION: data divided by $(Hrms)^{0.8}$ SURGE joints

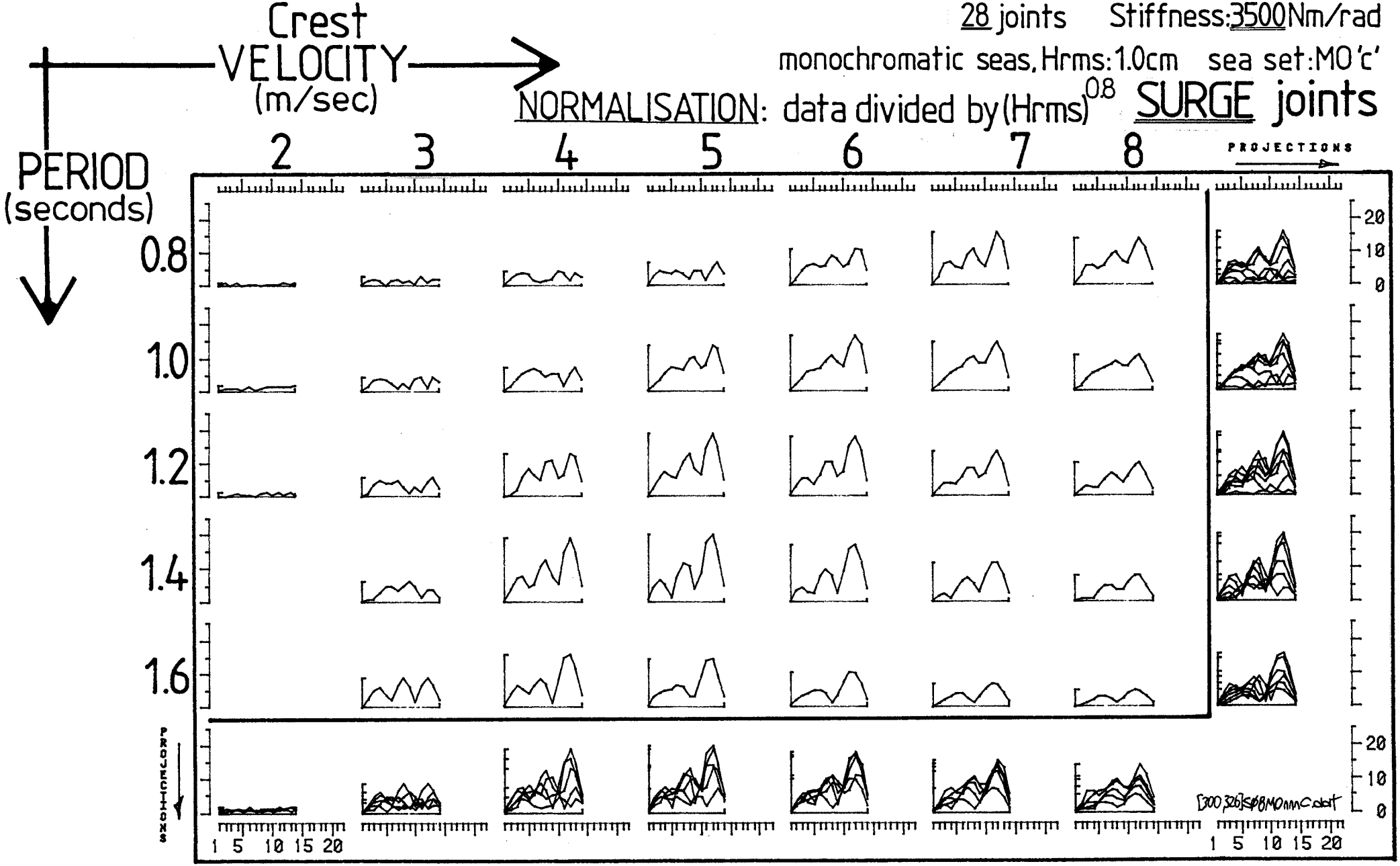

GRAPH 4.104

monochromatic seas

effect on Bending Moments of varying CREST VELOCITY and Energy Period

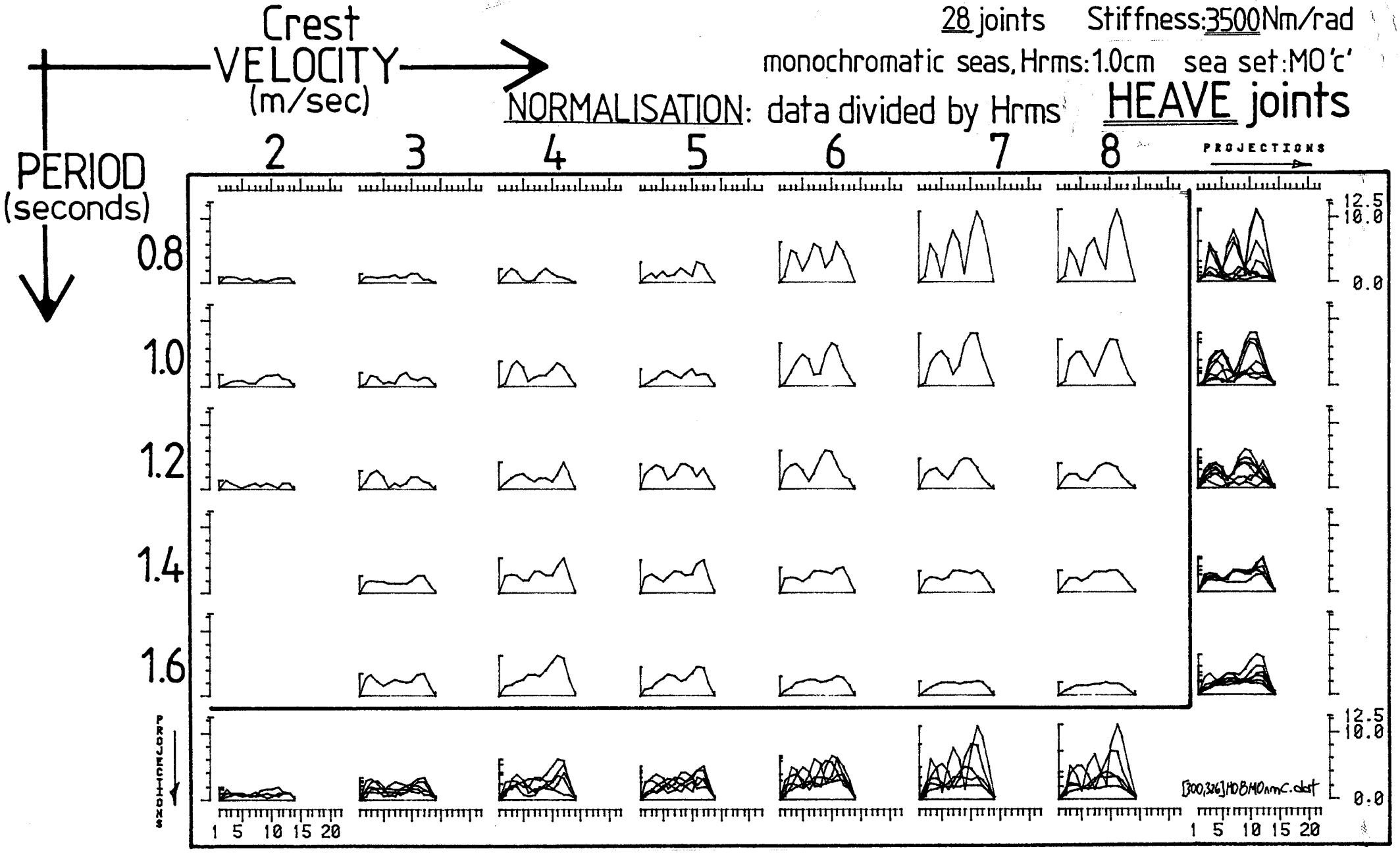

GRAPH 4.105

monochromatic seas

effect on Bending Moments of varying CREST VELOCITY and Energy Period

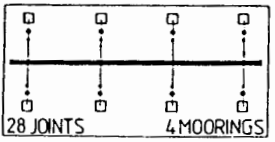

28 joints Stiffness: 1000 Nm/rad

monochromatic seas, Hrms: 1.0cm sea set: MO 'c'

SURGE & HEAVE joints

Crest VELOCITY (m/sec) →

PERIOD (seconds) ↓

2 3 4 5 6 7 8

0.8

1.0

1.2

1.4

1.6

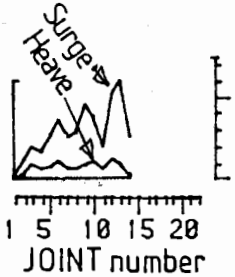

GRAPH 4.106

monochromatic seas

effect on Bending Moments of varying CREST VELOCITY and Energy Period

28 joints Stiffness: 1000 Nm/rad

monochromatic seas, Hrms: 1.0cm sea set: MO 'c'

NORMALISATION: data divided by $(Hrms)^{0.8}$ SURGE joints

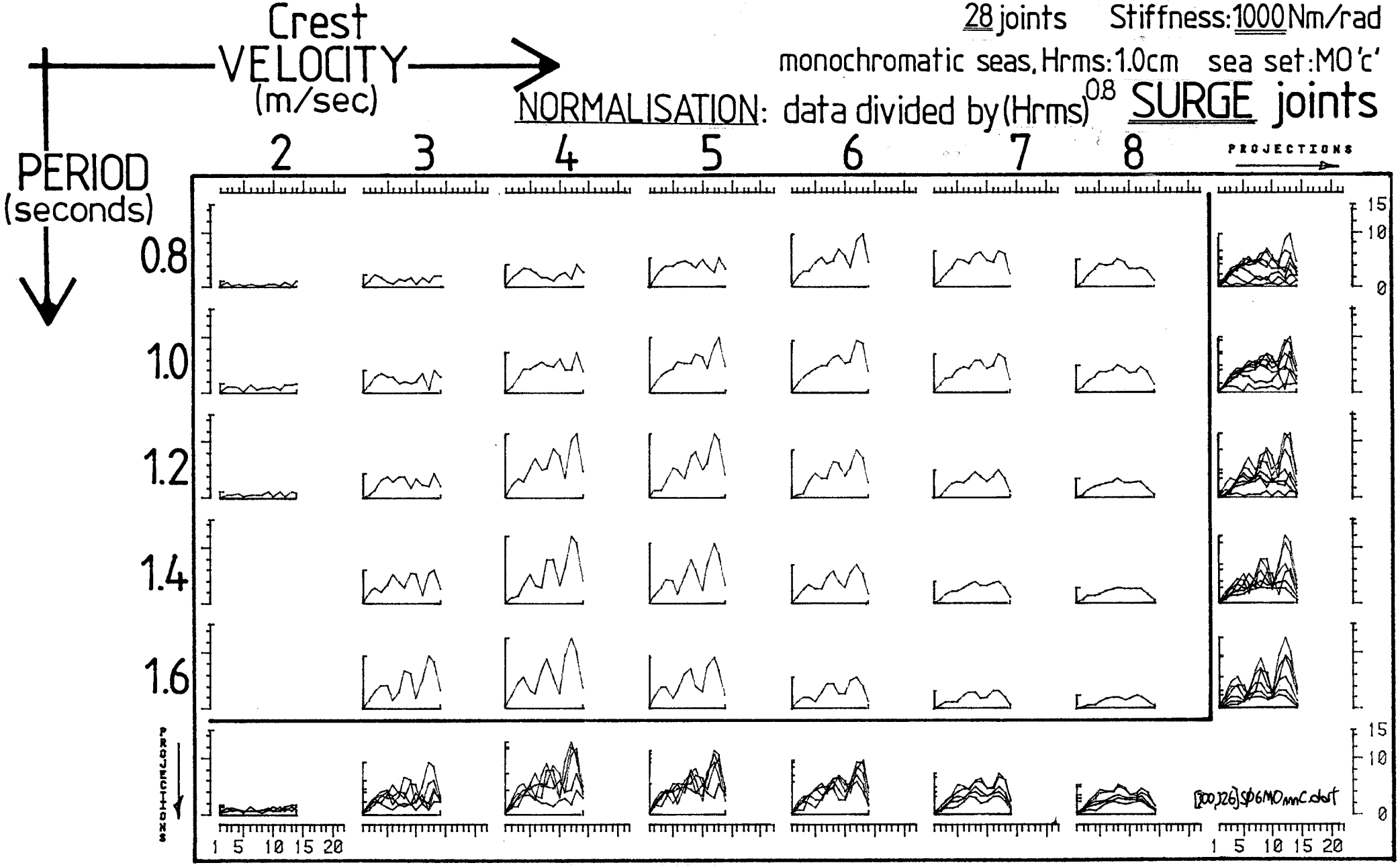

GRAPH 4.107

monochromatic seas

effect on Bending Moments of varying CREST VELOCITY and Energy Period

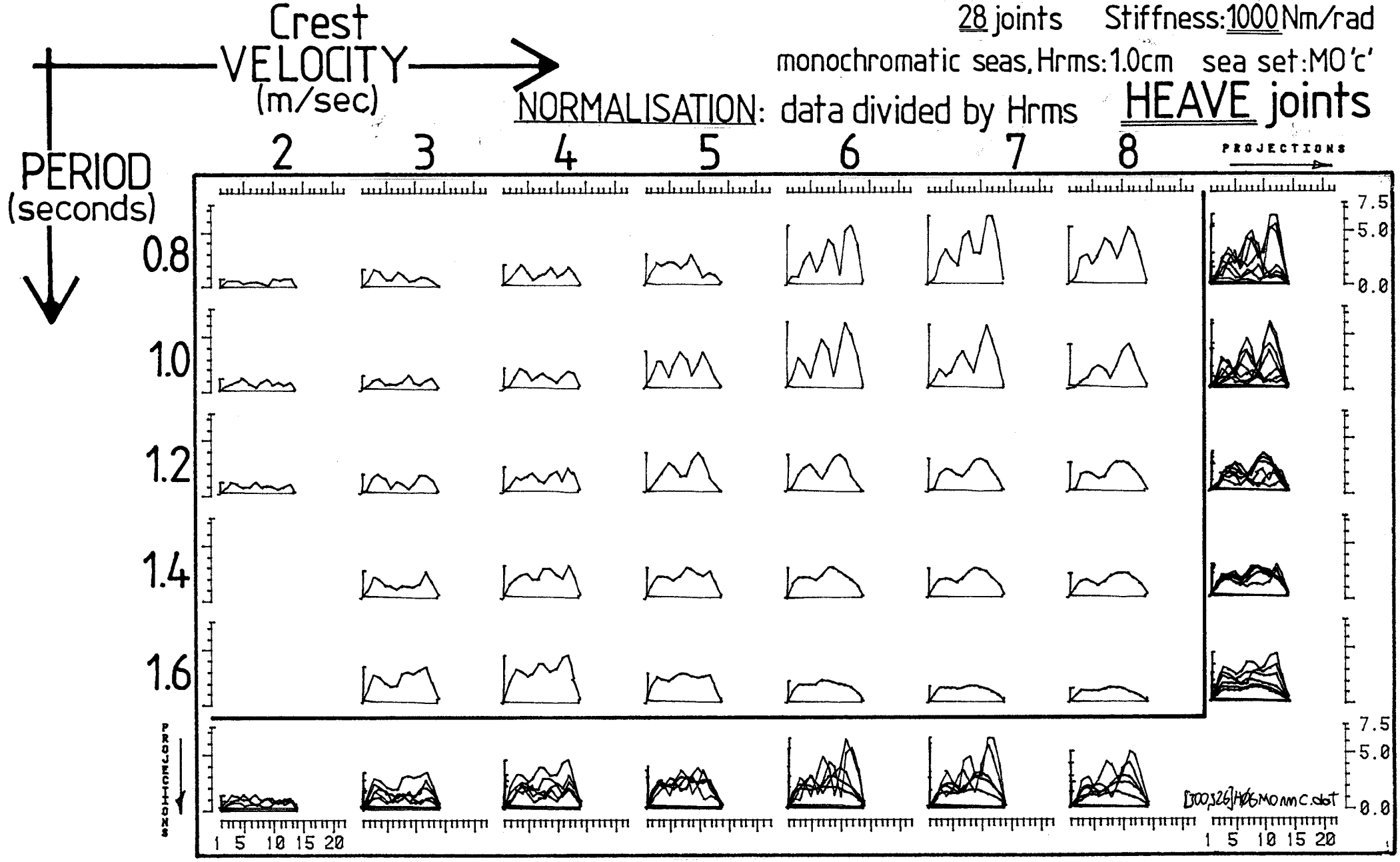

GRAPH 4.108

monochromatic seas

effect on Bending Moments of varying CREST VELOCITY and Energy Period

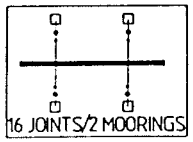

16 joints Stiffness:3500Nm/rad

monochromatic seas, Hrms:1.0cm sea set:MO 'c'

SURGE & HEAVE joints

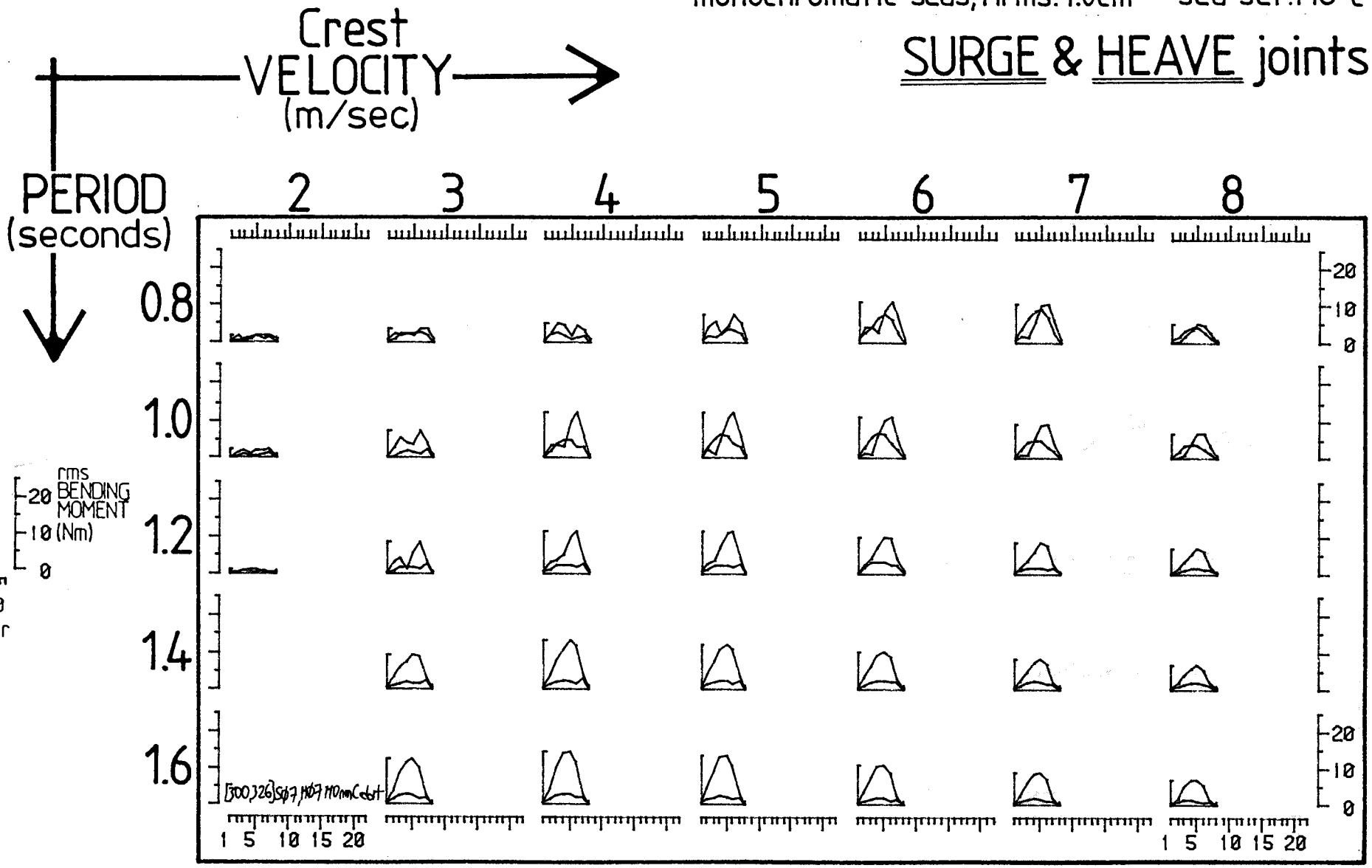

GRAPH 4.109

monochromatic seas

effect on Bending Moments of varying CREST VELOCITY and Energy Period

16 joints Stiffness:3500Nm/rad

monochromatic seas, Hrms:1.0cm sea set:MO 'c'

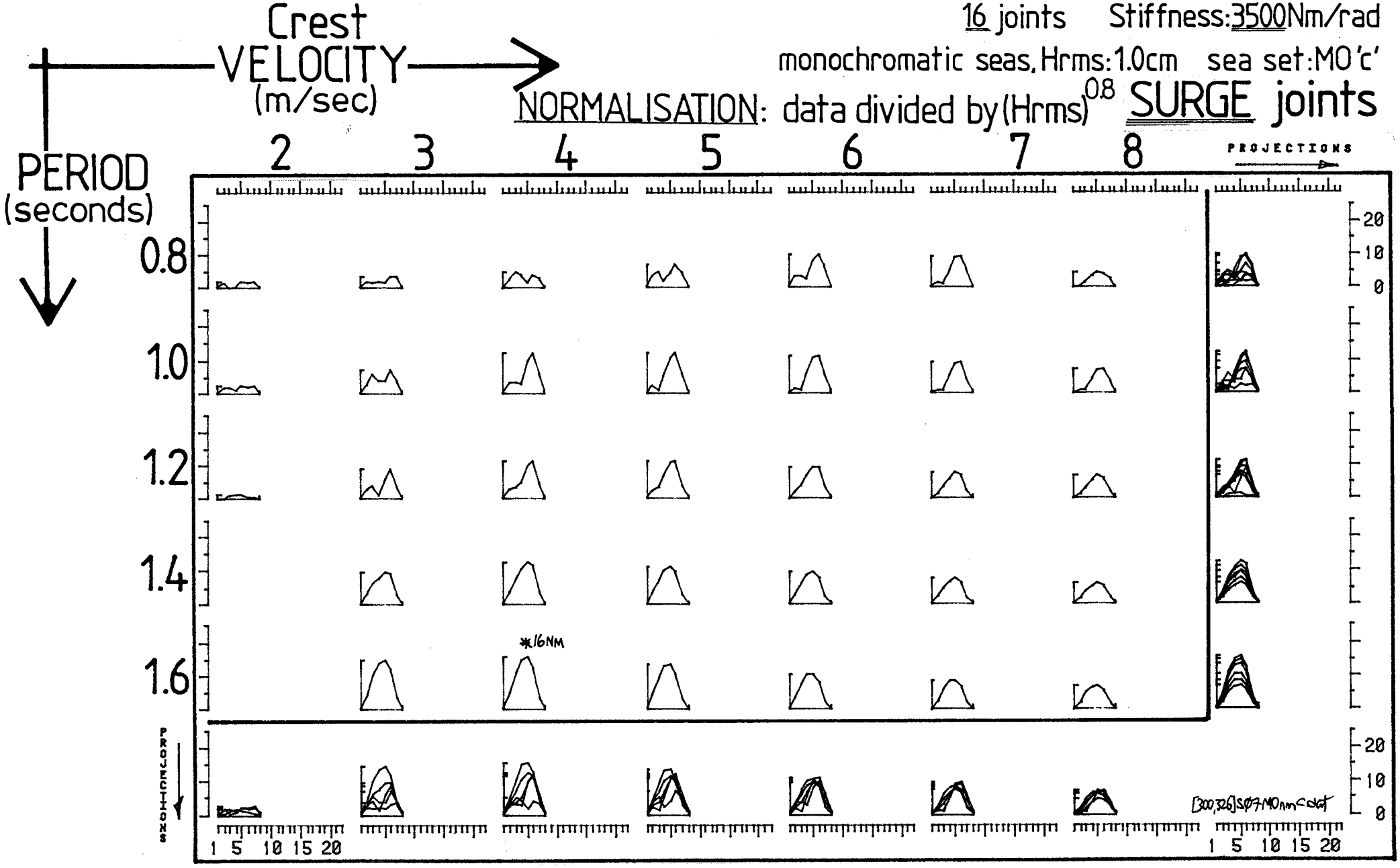

GRAPH 4.110

monochromatic seas

effect on Bending Moments of varying CREST VELOCITY and Energy Period

16 joints Stiffness:3500Nm/rad

monochromatic seas, Hrms:1.0cm sea set:M0 'c'

NORMALISATION: data divided by Hrms

HEAVE joints

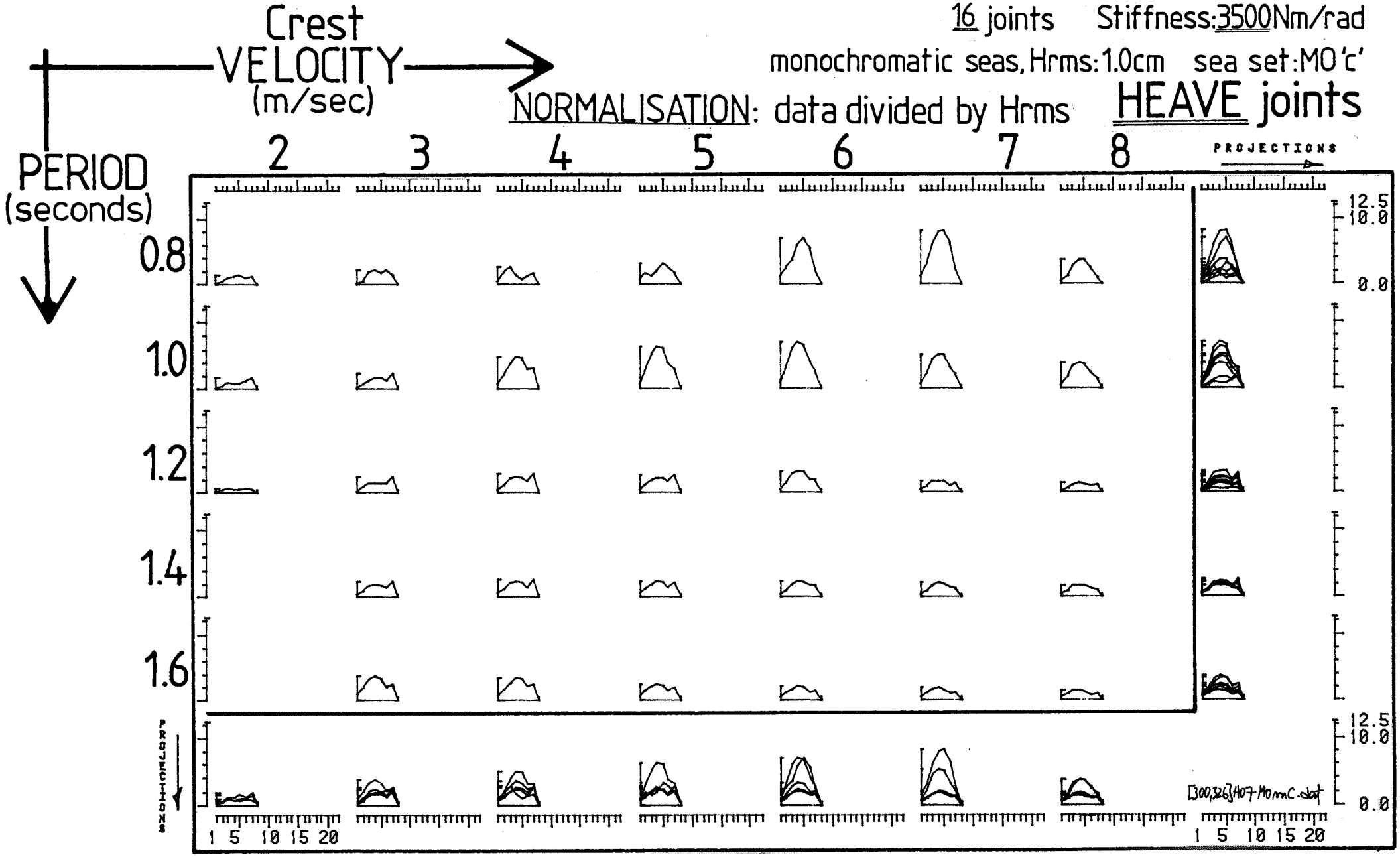

GRAPH 4.111

monochromatic seas

effect on Bending Moments of varying CREST VELOCITY and Energy Period

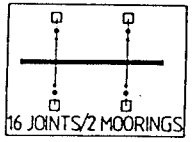

16 joints Stiffness: 1000 Nm/rad

monochromatic seas, Hrms: 1.0cm sea set: MO 'c'

SURGE & HEAVE joints

Crest VELOCITY (m/sec) →

PERIOD (seconds) ↓

2 3 4 5 6 7 8

0.8 1.0 1.2 1.4 1.6

Surge
Heave

15 10 0 rms BENDING MOMENT (Nm)

1 5 10 15 20 JOINT number

GRAPH 4.112

monochromatic seas

effect on Bending Moments of varying CREST VELOCITY and Energy Period

16 joints Stiffness: 1000 Nm/rad

monochromatic seas, Hrms: 1.0cm sea set: MO 'c'

NORMALISATION: data divided by $(Hrms)^{0.8}$ SURGE joints

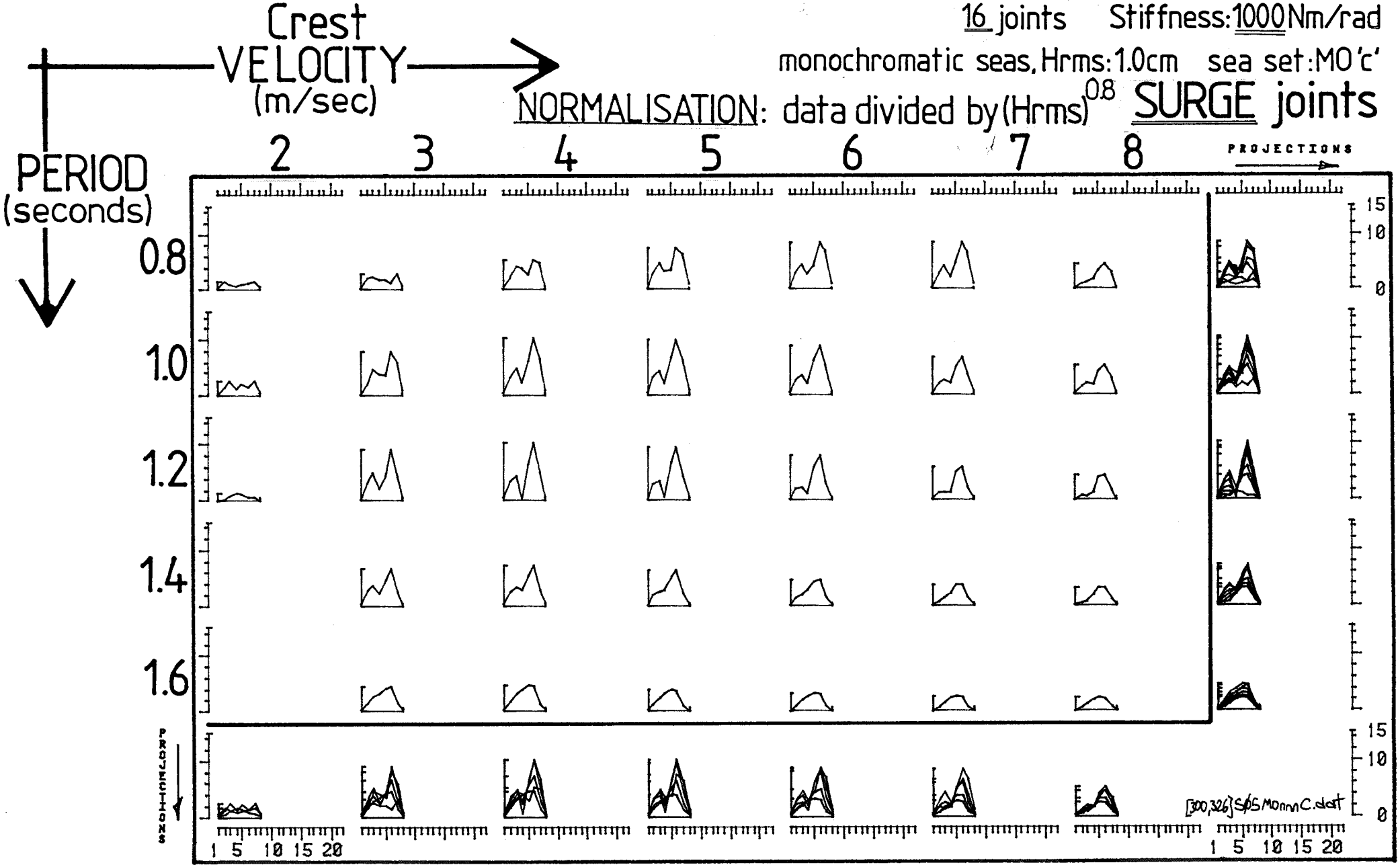

GRAPH 4.113

monochromatic seas

effect on Bending Moments of varying CREST VELOCITY and Energy Period

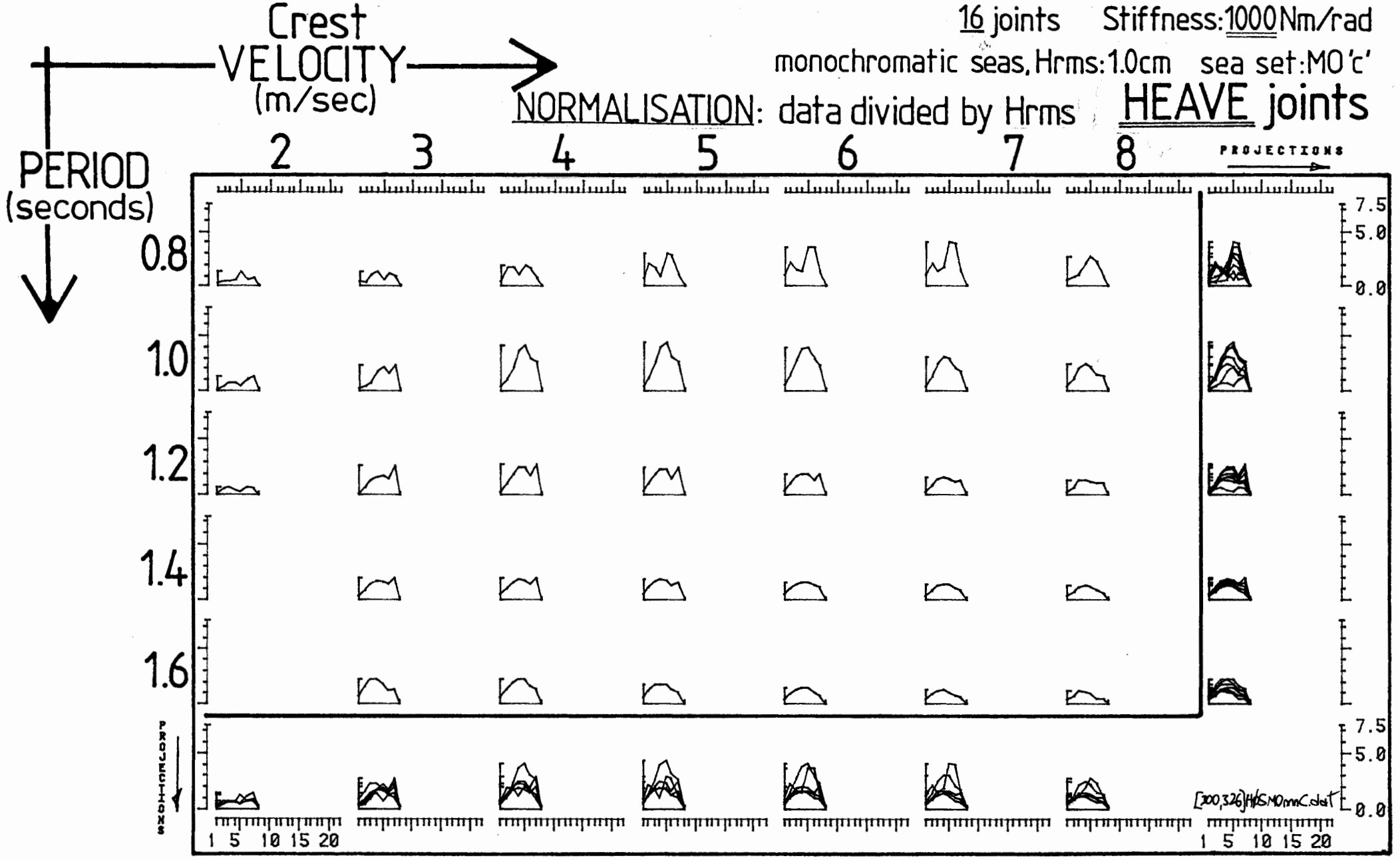

GRAPH 4.114

4.J EFFECT OF LENGTH IN SOUTH UIST SEAS

In this section we are trying to identify the various effects of length changes. Three different lengths, 48, 36 and 22 joints are tested in the South Uist spectra at two different stiffness values. The scale for each separate sea is adjusted to make the maximum moment in the shortest spine equal to unity.

The results of length changes are less obvious than for all the previous variables of stiffness, crest-angle, crest-length, crest-velocity, energy period and wave amplitude.

In some cases increasing the length makes bending moments bigger, in some cases the opposite. In some cases the intermediate length has the largest moments. But even in sea 220 the changes are not violent. Seas 280 and 318 (graph 4.123) show a left-hand peak for a short spine and a right-hand peak for a long one.

effect of LENGTH on Bending Moments

3 different lengths: 22, 36, 48 joints

SURGE joints

Stiffness: 3500Nm/rad

sea set: SU 'a'

S C A L I N G

For each sea the relative values of Bending Moments for the 3 different lengths are correct. They are scaled so that the maximum Bending Moment in the shortest spine is unity.

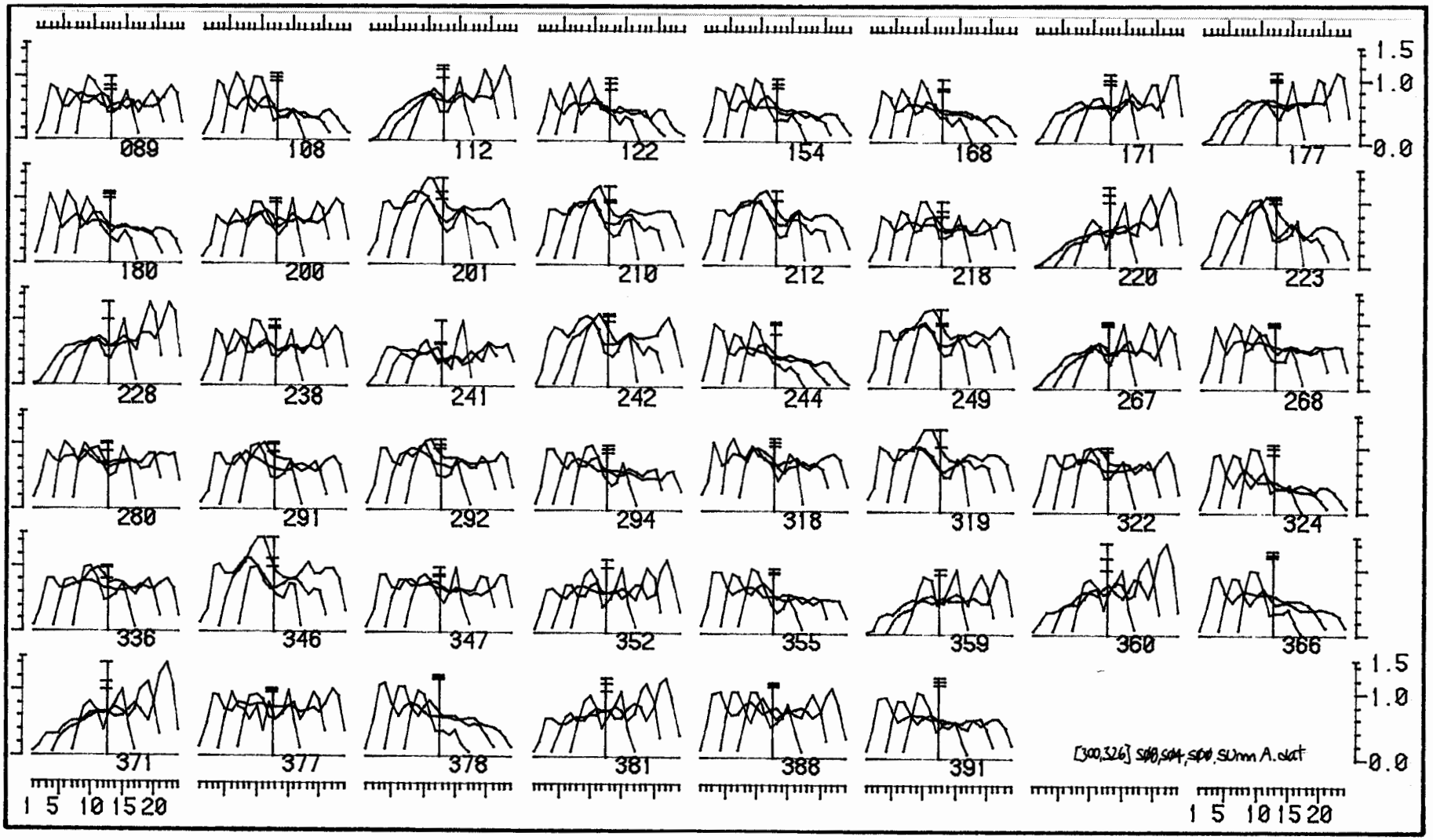

the 46 SPECTRA 'a' set

GRAPH 4.120

effect of LENGTH on Bending Moments

3 different lengths: 22, 36, 48 joints

HEAVE joints

Stiffness: 3500 Nm/rad

sea set: SU 'a'

S C A L I N G

For each sea the relative values of Bending Moments for the 3 different lengths are correct. They are scaled so that the maximum Bending Moment in the shortest spine is unity.

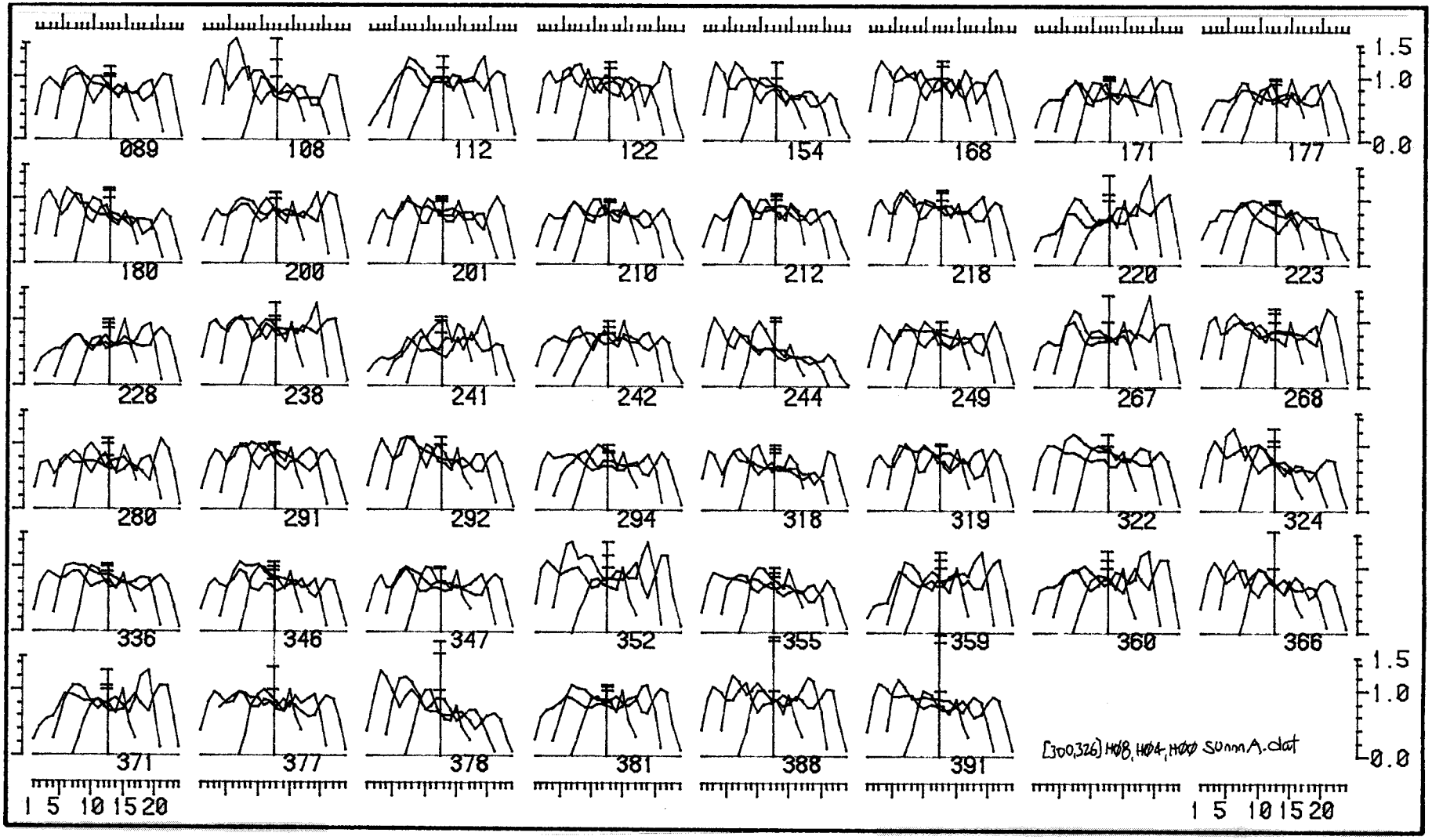

the 46 SPECTRA 'a' set

GRAPH 4.121

effect of LENGTH on Bending Moments

3 different lengths: 22, 36, 48 joints

SURGE joints

Stiffness: 1000 Nm/rad

sea set: SU 'a'

S C A L I N G

For each sea the relative values of Bending Moments for the 3 different lengths are correct. They are scaled so that the maximum Bending Moment in the shortest spine is unity.

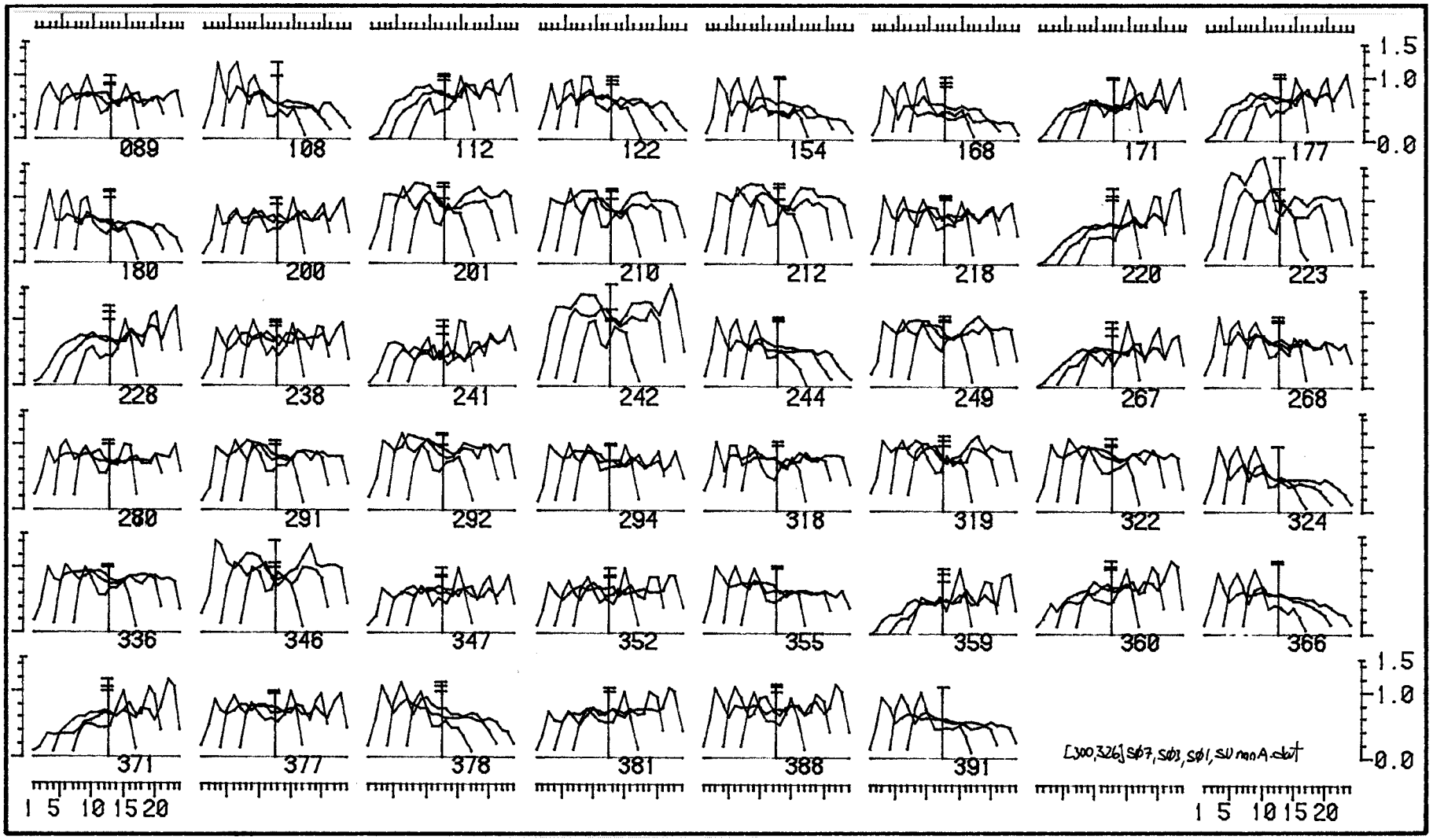

the 46 SPECTRA 'a' set

GRAPH 4.122

effect of LENGTH on Bending Moments

3 different lengths: 22, 36, 48 joints

HEAVE joints

Stiffness: 1000 Nm/rad

sea set: SU 'a'

S C A L I N G

For each sea the relative values of Bending Moments for the 3 different lengths are correct. They are scaled so that the maximum Bending Moment in the shortest spine is unity.

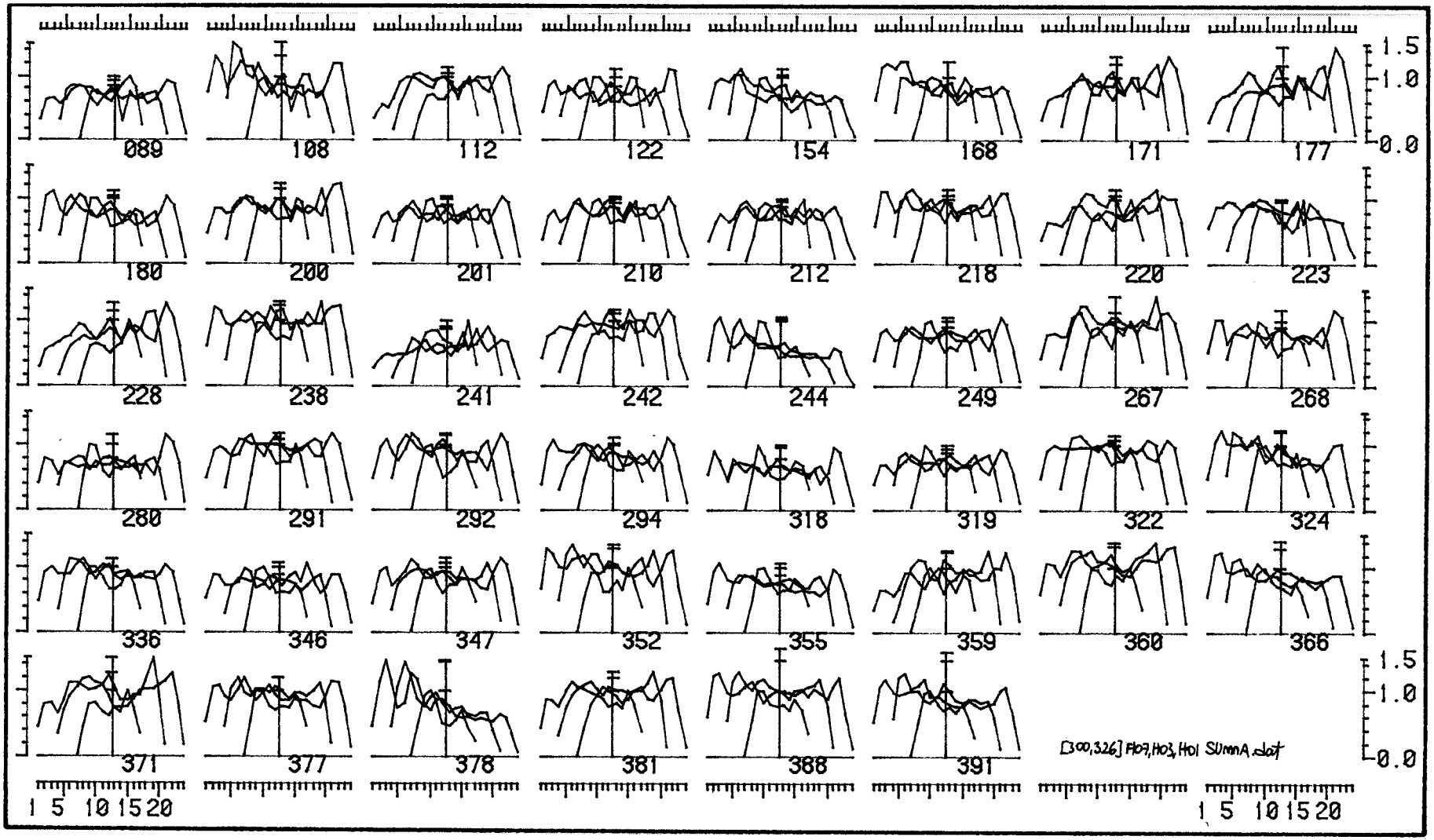

the 46 SPECTRA 'a' set

GRAPH 4.123

(4.J cont)

The difficulty of interpreting the graphs 4.120 to 4.123 led us to try replotting the same data in graphs 4.124 and 4.125. Here we use the shortest spine as a reference and plot South Uist results for other lengths in terms of their ratio to the shortest.

Data are separated into the maximum single highest value, the mean of the entire spine and the mean of the central three. Each sea is shown as a short dash, the root mean square of all the results as a longer one, and the mean of all as the longest dash. As some of seas give identical results within the plotting resolution, they are repeated as sideways histogram blocks.

No clear pattern emerges. We might have thought that increasing length was increasing bending moment but sometimes the 36 joint model has higher values than the 44 joint one. While we see low heave results for both longer lengths in graph 4.124 we find the opposite when stiffness is reduced in graph 4.125. The only certain conclusion is that the length squared and length cubed theories are incorrect for these lengths and stiffness values.

effect of LENGTH on Bending Moments

3 different lengths: 22, 36, 48 joints

South Uist 46 spectra: SU'c'

SURGE — HEAVE

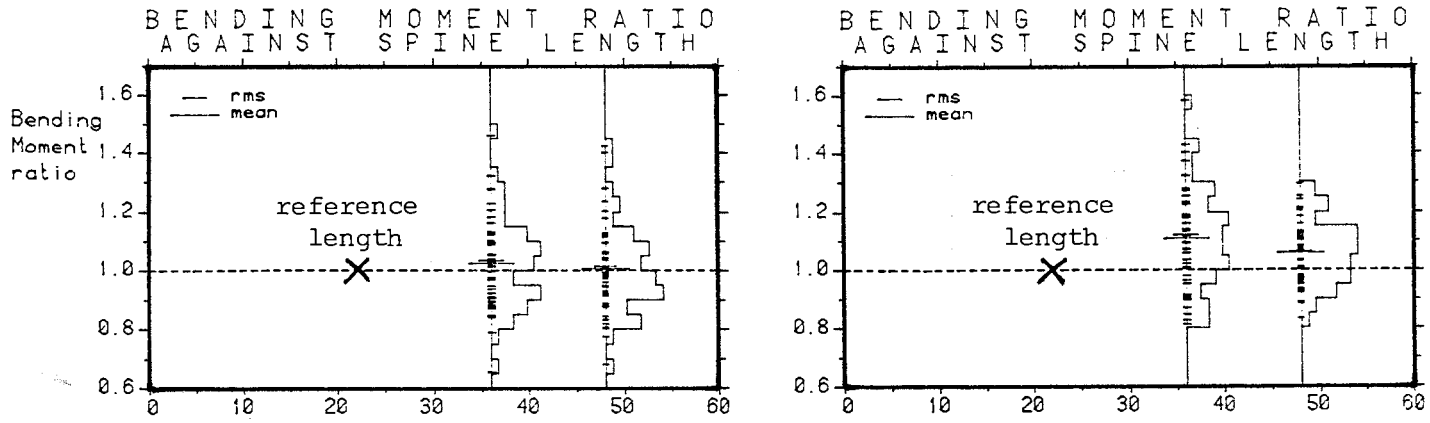

MAXIMUM – single highest value

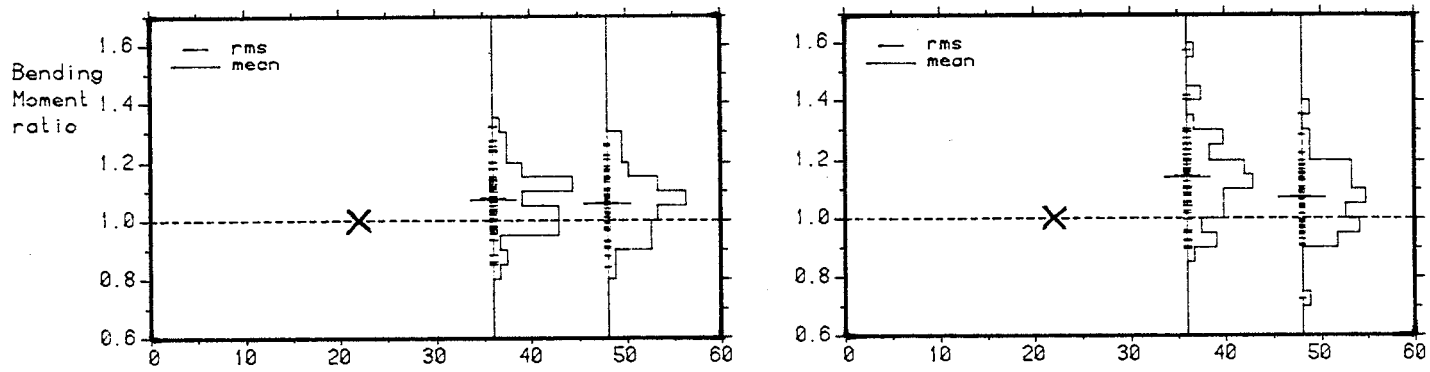

RMS – of ALL joints

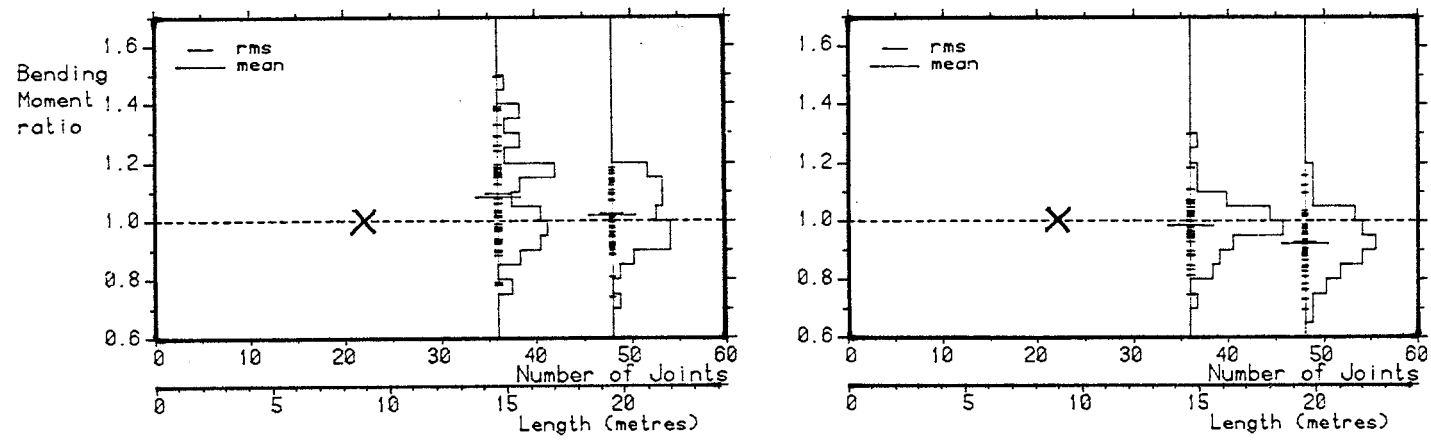

RMS – of MIDDLE 3 joints

D00,226] S,H 40,04 48 SUmm A.dat

the 46 SPECTRA

STIFFNESS 3500 Nm/rad

GRAPH 4.124

effect of LENGTH on Bending Moments

3 different lengths: 22, 36, 48 joints

South Uist 46 spectra : SU'c'

SURGE — HEAVE

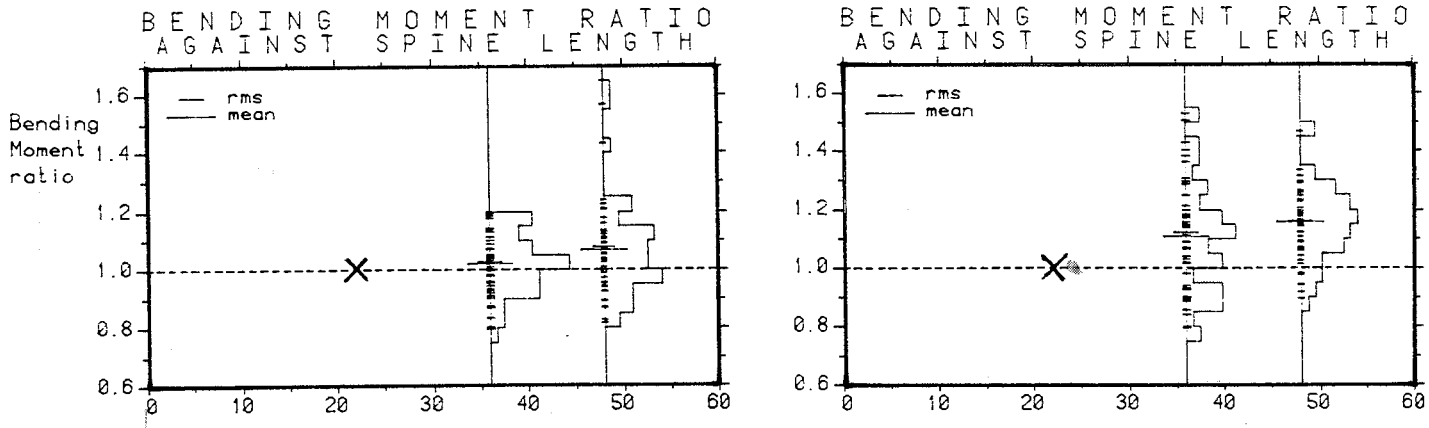

MAXIMUM – single highest value

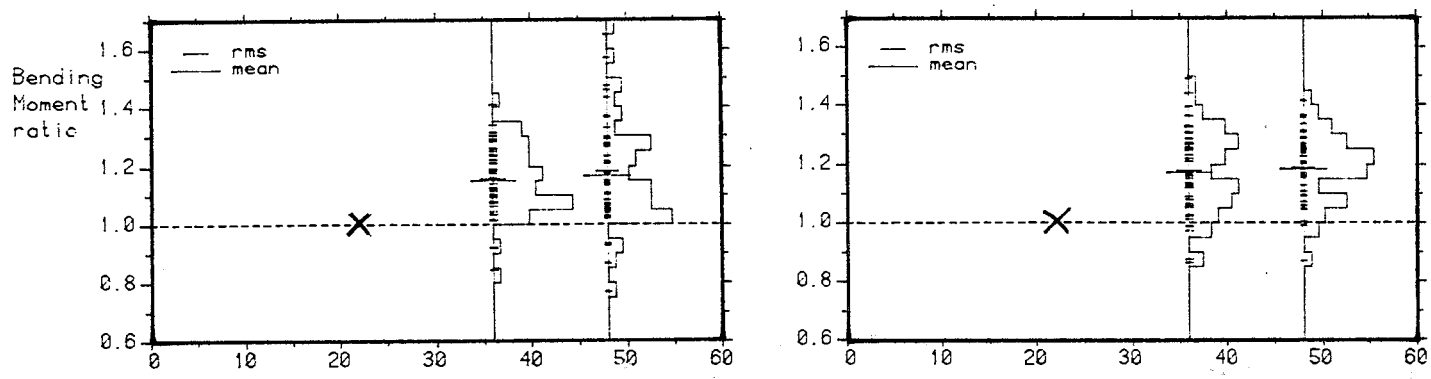

RMS – of ALL joints

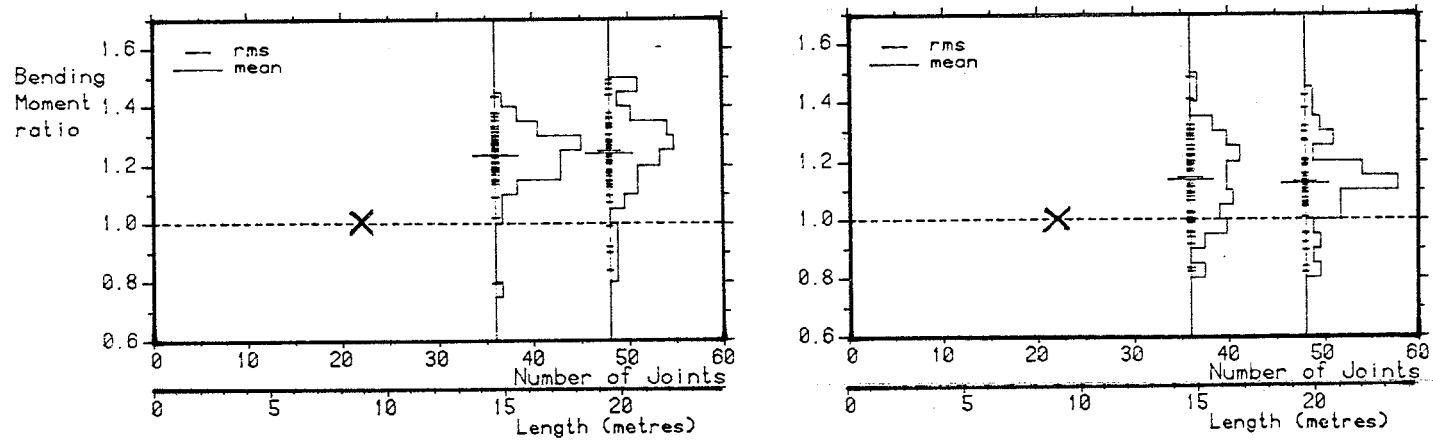

RMS – of MIDDLE 3 joints

CJ00,326 SH #1,#3,#7 SUcmA.dat

the 46 SPECTRA

STIFFNESS 1000 Nm/rad

GRAPH 4.125

4.K EFFECT OF LENGTH IN ANGLED MONOCHROMATIC SEAS

In this section we continue the search for a theory for length-effects. We use monochromatic wavefronts, varying both crest velocity and period for two stiffness values and for three spine lengths. The shortest spine length is plotted more heavily to assist identification. 'Telegraph-poles' are added to mark the maximum values.

Results are a little clearer than for the South Uist seas. For surge at 3500 Nm/rad in 4.130 it looks as though the longer length spine results are pivoted about the maximum of the short one. Only for 8 m/sec and 0.8 seconds is there a dramatic enhancement for all the length of the longer spines. This is accompanied by a great reduction at the bottom of the 8 m/sec column. The overall enhancement effects vanish for the lower stiffness in graph 4.132, which shows pivoting nearly everywhere. In heave on graphs 4.131 and 4.133 the pattern is similar.

Corresponding histograms are given on graphs 4.134 and 4.135. Ratios up to 3.5 are evident but there are also some depressions. In graph 4.134 the central joints are as low as 0.35 of the shortest spine.

effect of LENGTH on Bending Moments

3 different lengths: 16, 28, 44 joints

SCALING
For each sea the relative values of Bending Moments for the 3 different lengths are correct. They are scaled so that the maximum Bending Moment in the shortest spine is unity.

SURGE joints
Stiffness: 3500 Nm/rad
Monochromatic sea set: MO'c'

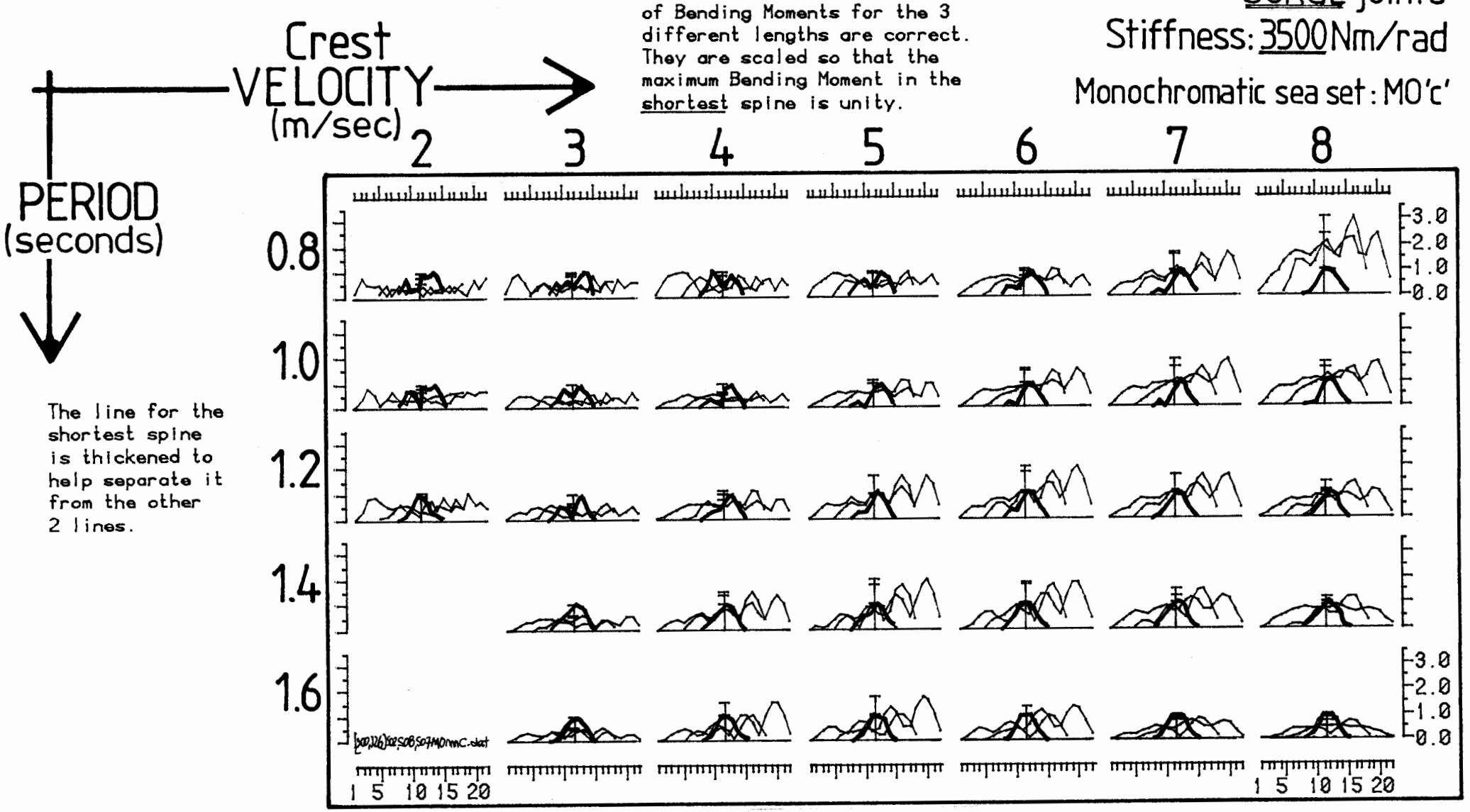

The line for the shortest spine is thickened to help separate it from the other 2 lines.

GRAPH 4.130

effect of LENGTH on Bending Moments

3 different lengths: 16, 28, 44 joints

S C A L I N G

For each sea the relative values of Bending Moments for the 3 different lengths are correct. They are scaled so that the maximum Bending Moment in the shortest spine is unity.

HEAVE joints

Stiffness: 3500 Nm/rad

Monochromatic sea set: M0'c'

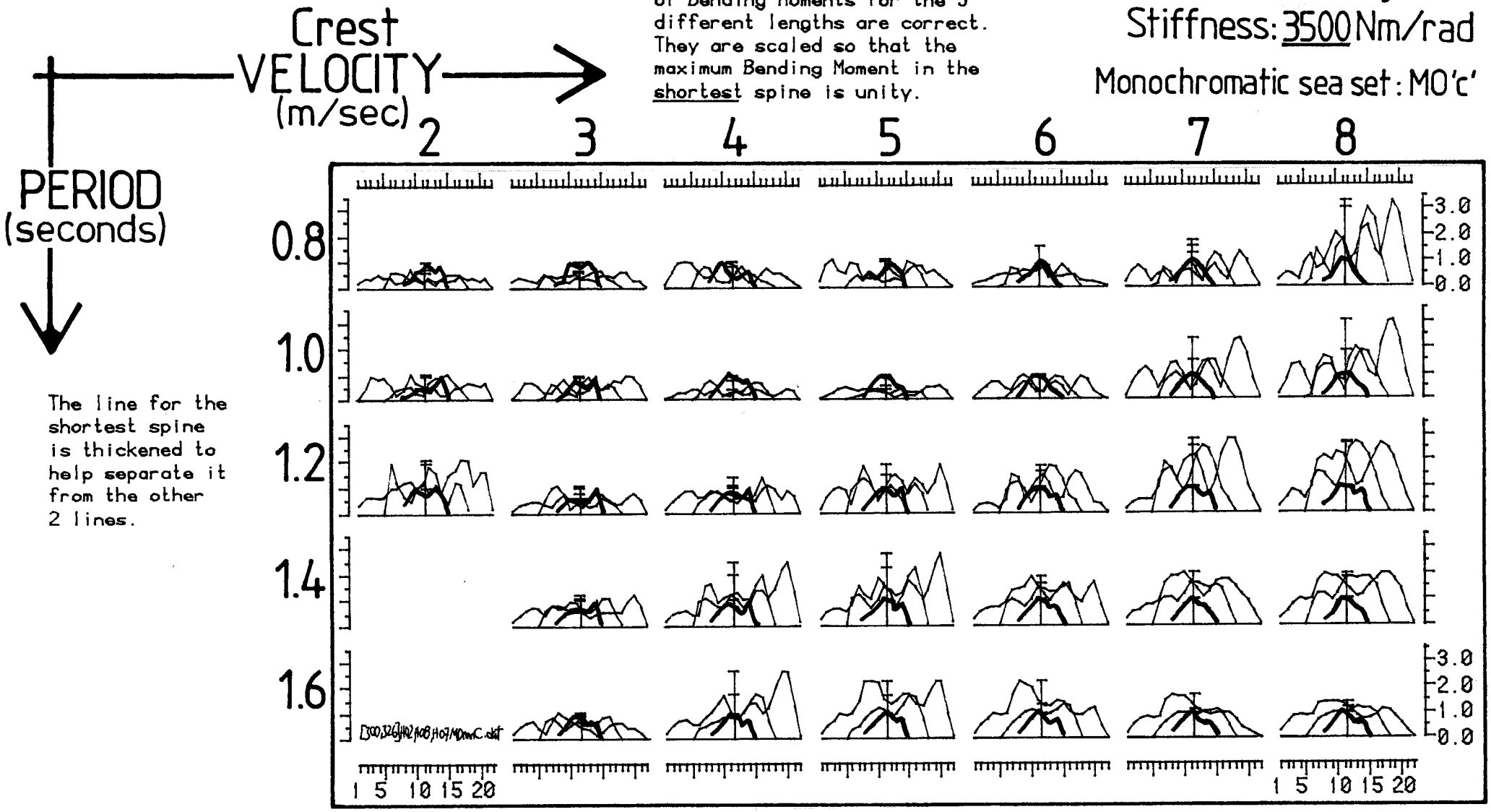

The line for the shortest spine is thickened to help separate it from the other 2 lines.

GRAPH 4.131

effect of LENGTH on Bending Moments

3 different lengths: 16, 28, 44 joints

SCALING
For each sea the relative values of Bending Moments for the 3 different lengths are correct. They are scaled so that the maximum Bending Moment in the shortest spine is unity.

SURGE joints
Stiffness: 1000 Nm/rad
Monochromatic sea set: MO'c'

Crest VELOCITY (m/sec) →
PERIOD (seconds) ↓

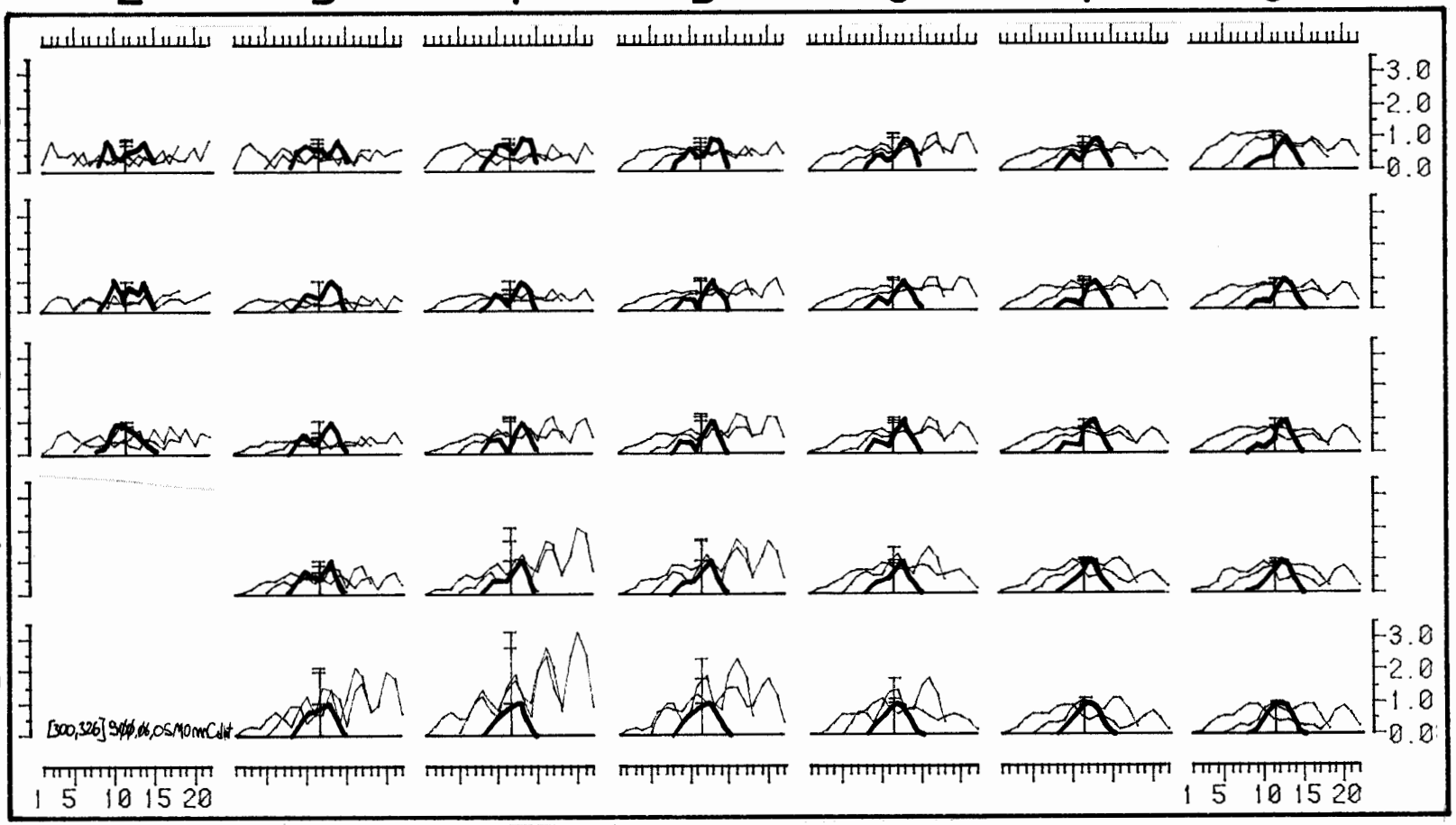

The line for the shortest spine is thickened to help separate it from the other 2 lines.

GRAPH 4.132

effect of LENGTH on Bending Moments

3 different lengths: 16, 28, 44 joints

S C A L I N G

For each sea the relative values of Bending Moments for the 3 different lengths are correct. They are scaled so that the maximum Bending Moment in the shortest spine is unity.

HEAVE joints

Stiffness: 1000 Nm/rad

Monochromatic sea set: M0'c'

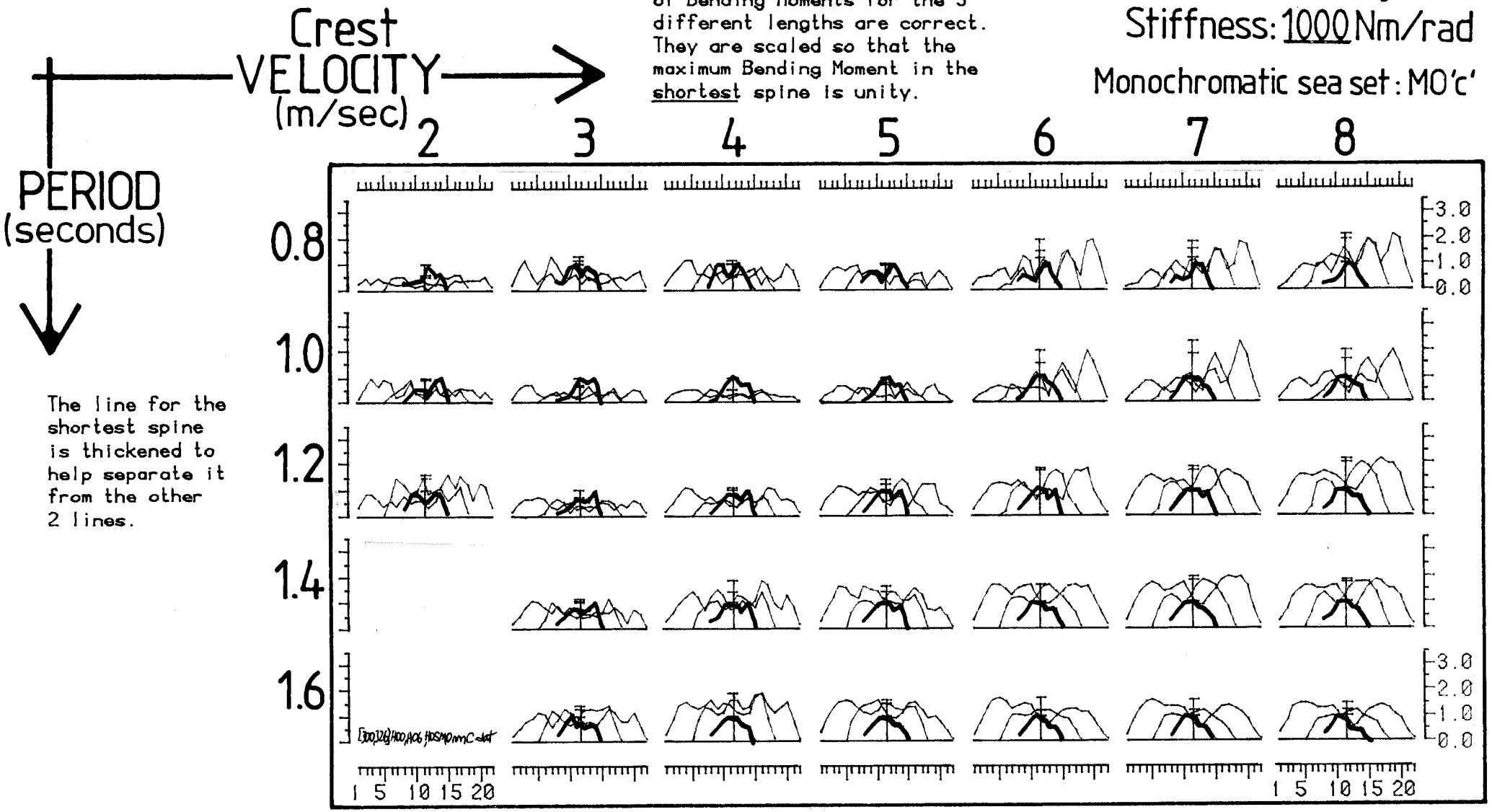

The line for the shortest spine is thickened to help separate it from the other 2 lines.

GRAPH 4.133

effect of LENGTH on Bending Moments

3 different lengths: 16, 28, 44 joints

Monochromatic sea set: MO'c'

SURGE — HEAVE

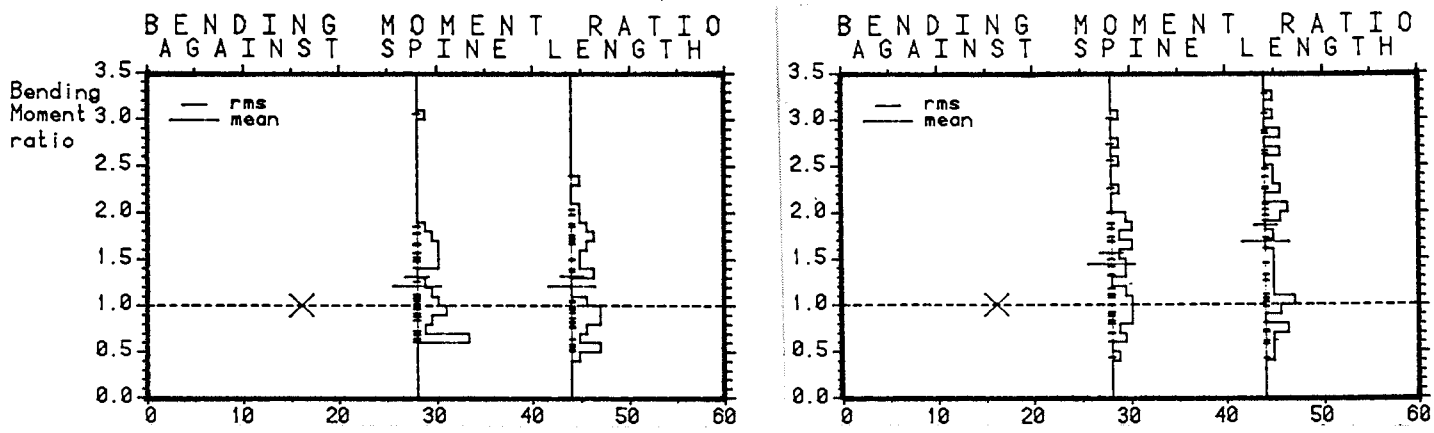

MAXIMUM – single highest value (near end)

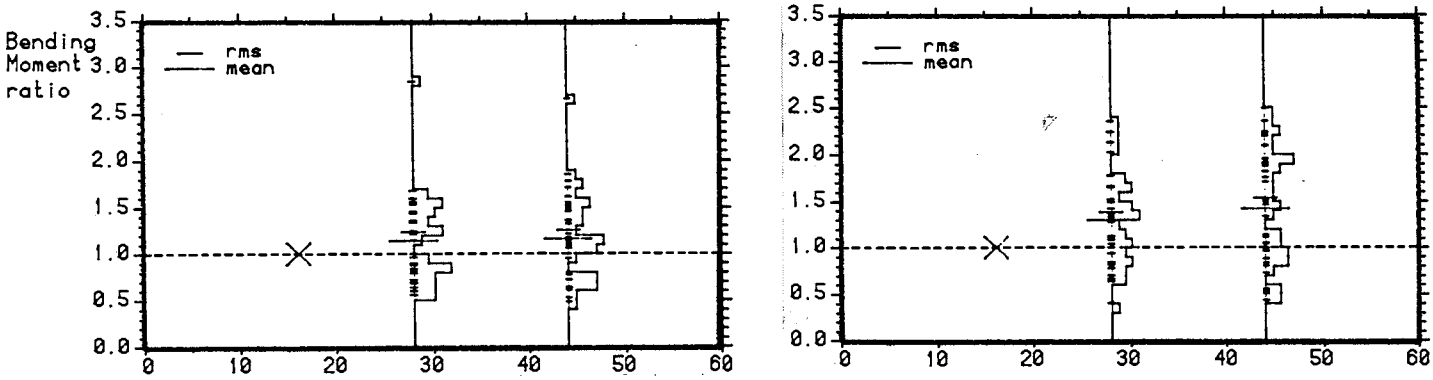

RMS – of ALL joints

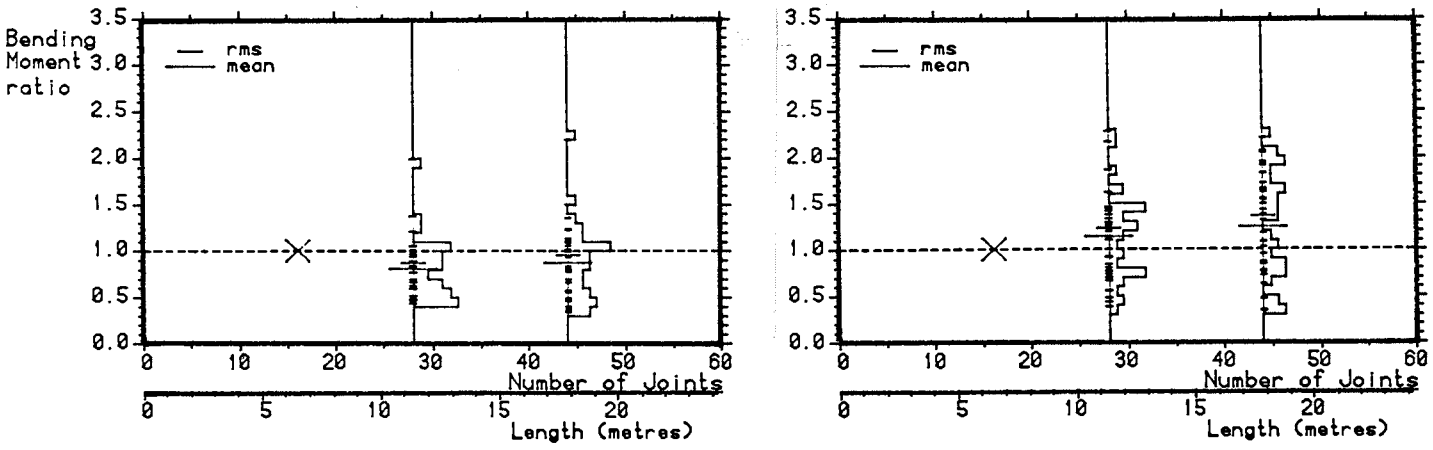

RMS – of MIDDLE 3 joints

[300,326]S,H 02,07,08MOmmC.dat

STIFFNESS 3500 Nm/rad

GRAPH 4.134

effect of LENGTH on Bending Moments

3 different lengths: 16, 28, 44 joints

Monochromatic sea set: MO'c'

SURGE — HEAVE

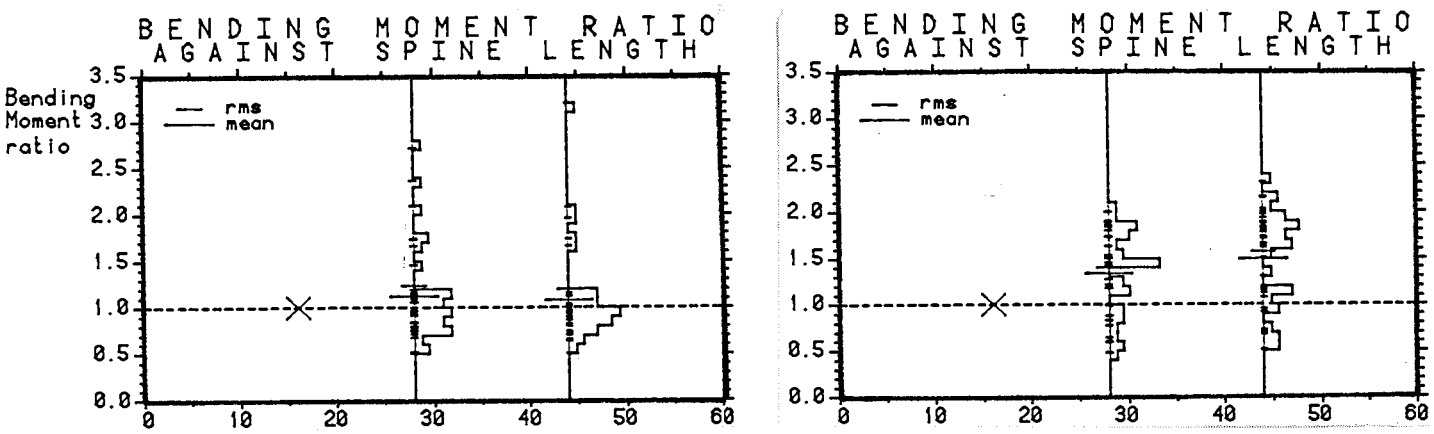

MAXIMUM - single highest value (near end)

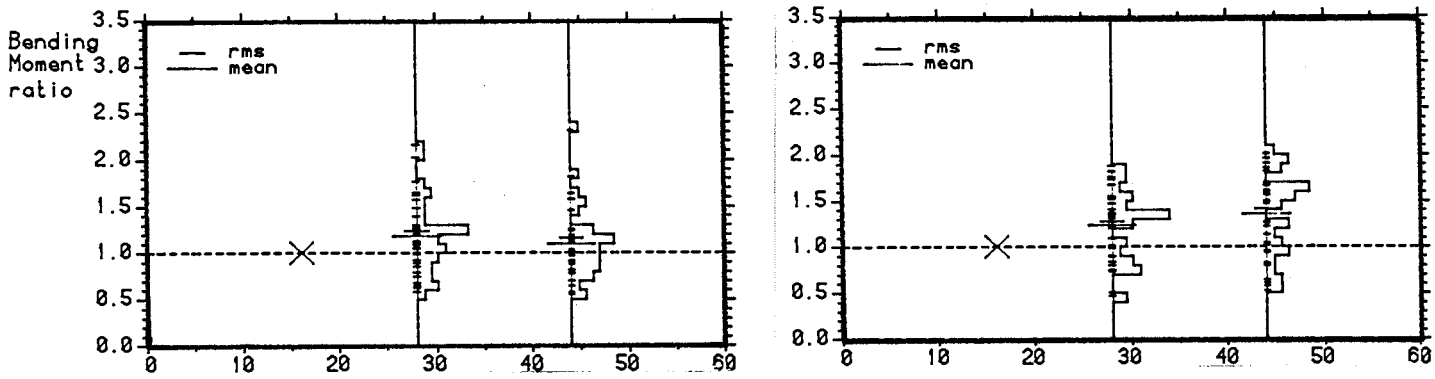

RMS - of ALL joints

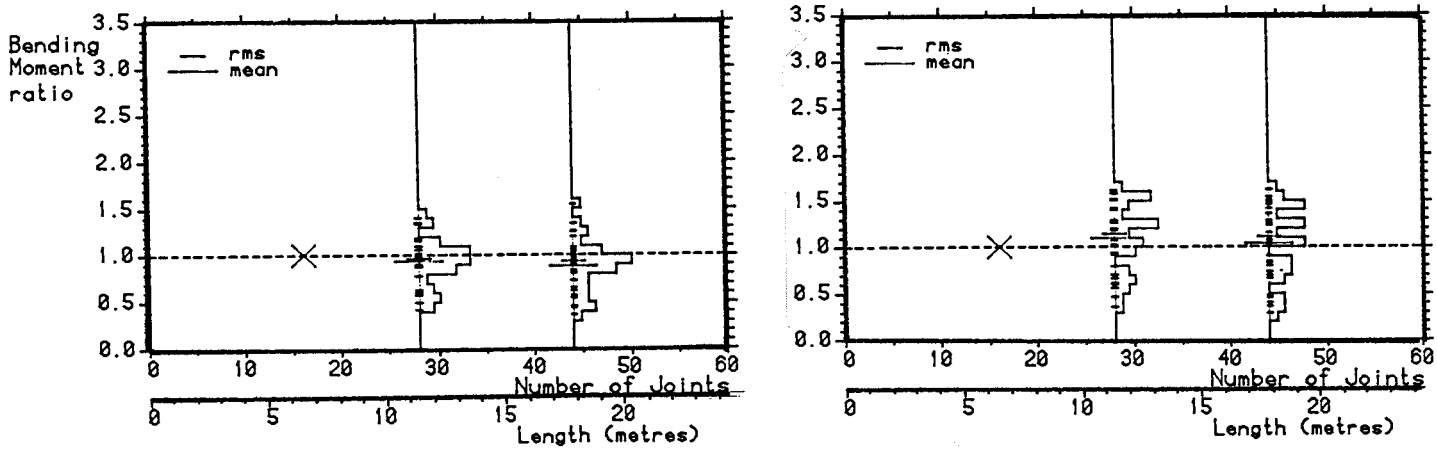

RMS - of MIDDLE 3 joints

[300,326] S,H 00,05,06 MOmmC.dat

STIFFNESS 1000 Nm/rad

GRAPH 4.135

4.L EFFECT OF MOORING MODIFICATIONS

If the safety of an installation depends on the integrity of its moorings there must be stringent rules about inspection. We wanted to find out whether bending moments would be changed by the loss of moorings.

We measured bending moments in the 46 South Uist seas for the normal 5 mooring layout, and then moved the number 2 mooring to a position between numbers 4 and 5, as shown in graph 4.140, for a repeat test. The results for heave and surge before and after the changes are superimposed. In many cases they are within the line thickness of the plotter pen. The biggest difference occurs when lost moorings are at the down-wave end of the spine. Compare, for example, sea numbers 378 and 220. We suffered a multiplex failure for sea numbers 112 and 377.

The data are replotted in graphs 4.141 and 4.142 separately for heave and surge with scale changes to make maximum values all the same. This allows shape comparisons to be made more easily. Surge behaviour looks more repeatable after a mooring change than does heave.

As the first condition itself represented only 25% of the planned mooring density, we can be confident that tolerance to the loss of moorings is very high. While we must repeat the tests when ducks are mounted on the spine it would seem that leaving moorings to fail and replacing them the following summer could well be the best maintenance policy despite its heretical implications.

Bending Moment change with major MOORING MODIFICATION

Comparison with regular arrangement

36joints Stiffness: 1000 Nm/rad
sea set: SU'a'

BEFORE CHANGE

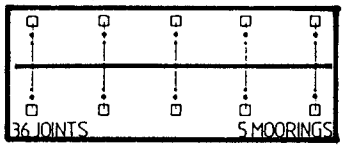

AFTER CHANGE

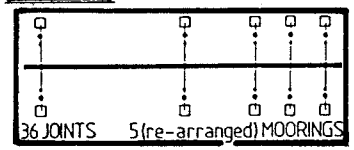

SURGE & HEAVE joints

the 46 SPECTRA 'a' set

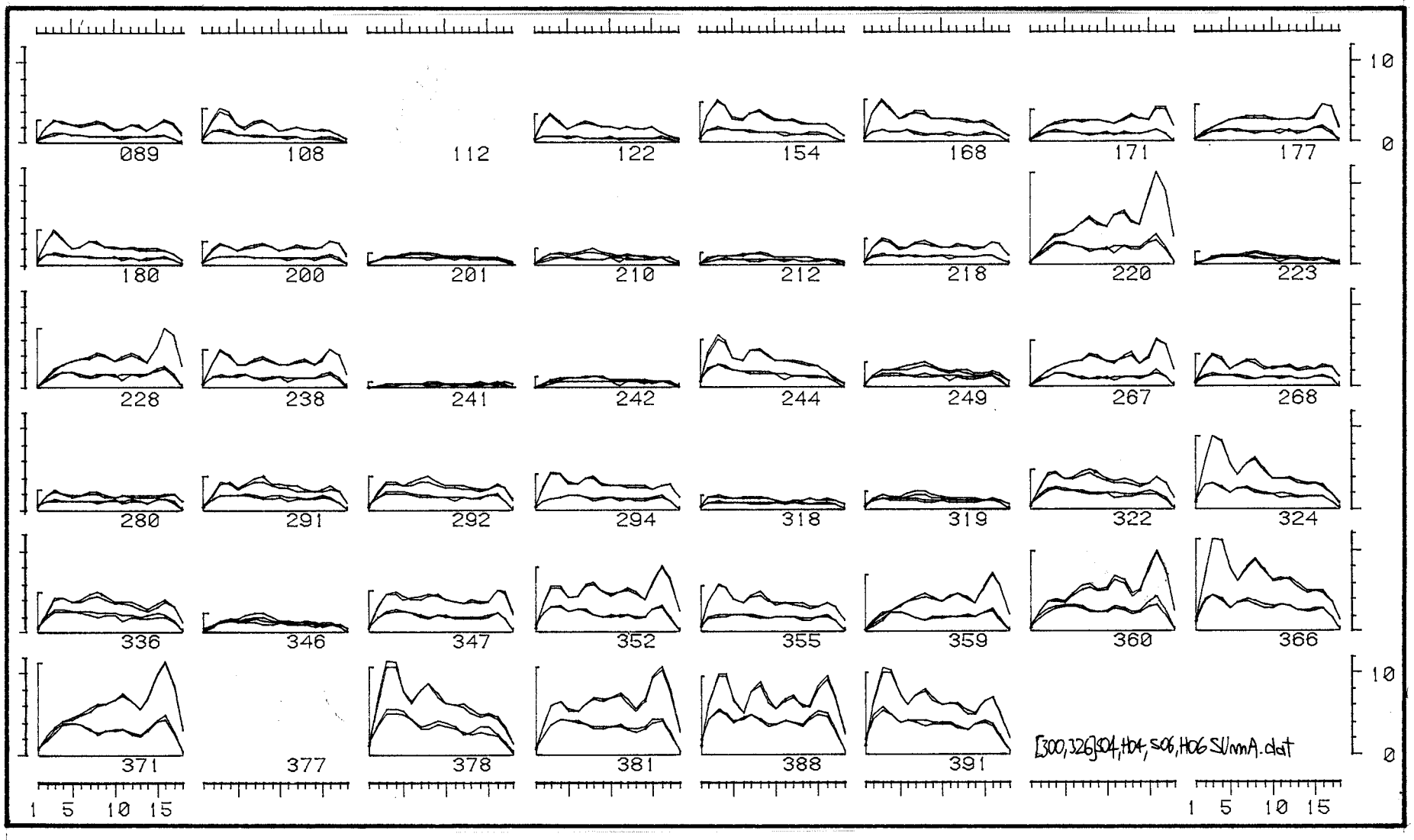

GRAPH 4.140

Bending Moment change with major MOORING MODIFICATION

Comparison with regular arrangement

36joints Stiffness: 1000 Nm/rad
sea set: SU'a'

BEFORE CHANGE

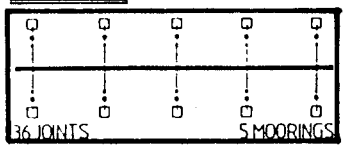

AFTER CHANGE

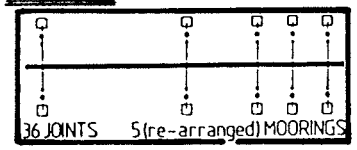

each test self-scaled

SURGE joints

the 46 SPECTRA 'a' set

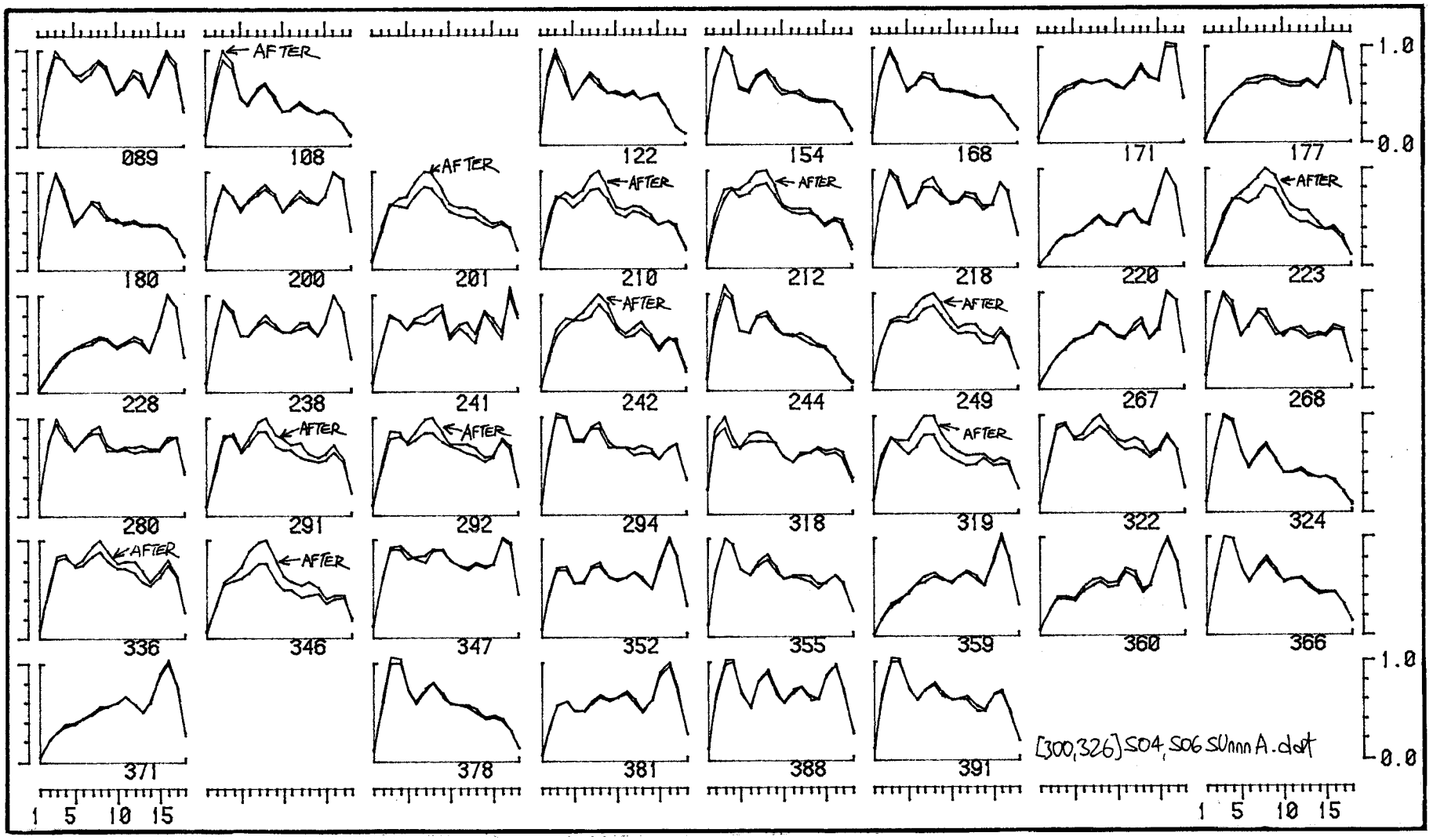

GRAPH 4.141

Bending Moment change with major MOORING MODIFICATION

Comparison with regular arrangement

36joints Stiffness: 1000 Nm/rad
sea set: SU'a'

BEFORE CHANGE

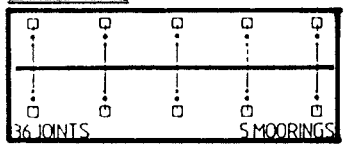

AFTER CHANGE

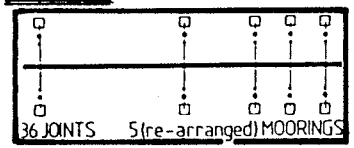

each test self-scaled

HEAVE joints

the 46 SPECTRA 'a' set

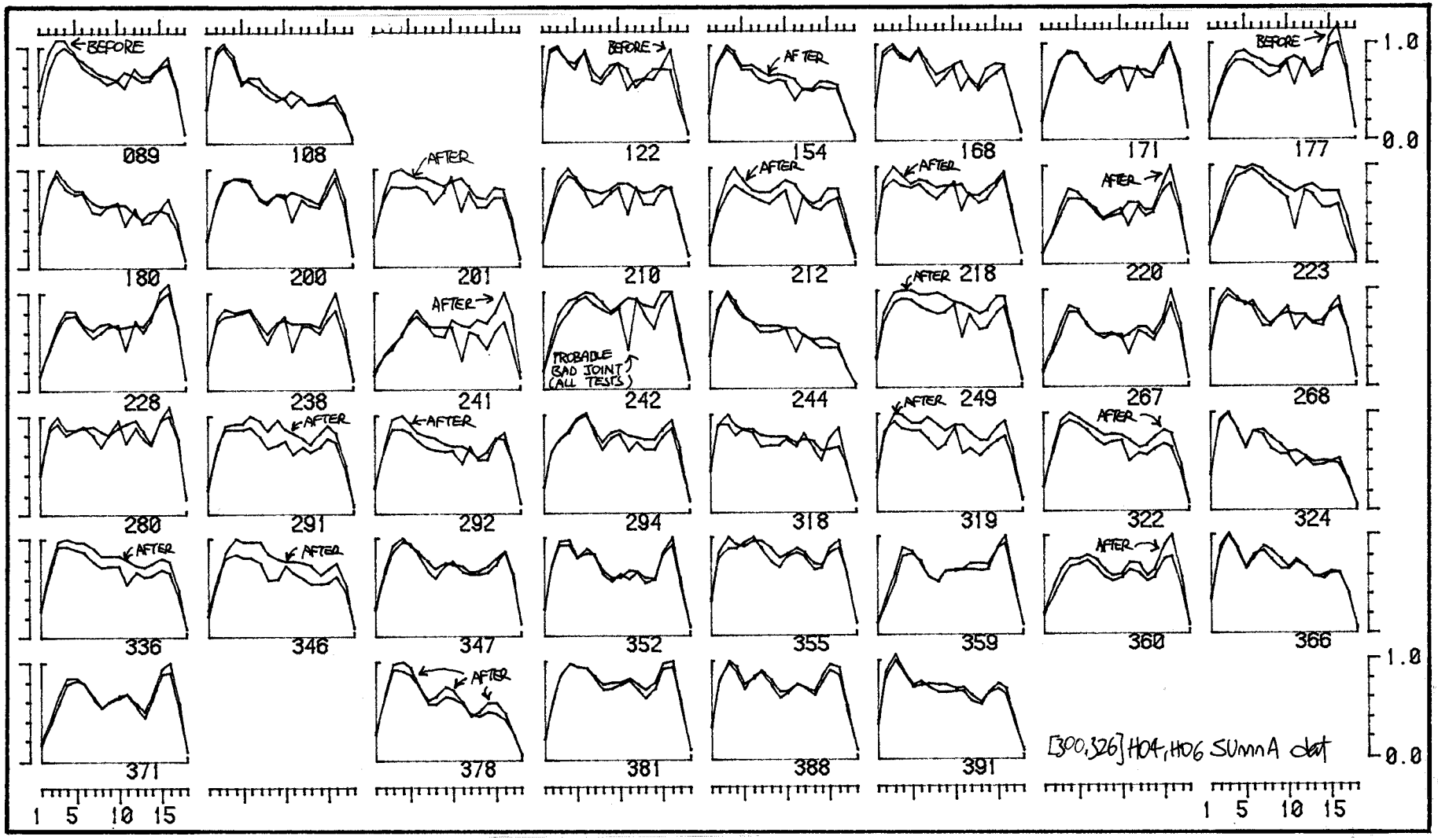

GRAPH 4.142

4.M EFFECT OF BROKEN JOINTS

In graph 4.150 we show the effect of an accidentaly cracked finger clamp. (These were designed to sacrifice themselves before damage to the inside of the spine.) The joint was still able to pass shear forces. Both heave and surge moments are reduced at the break and elevated to either side. The model is behaving like a pair of shorter strings.

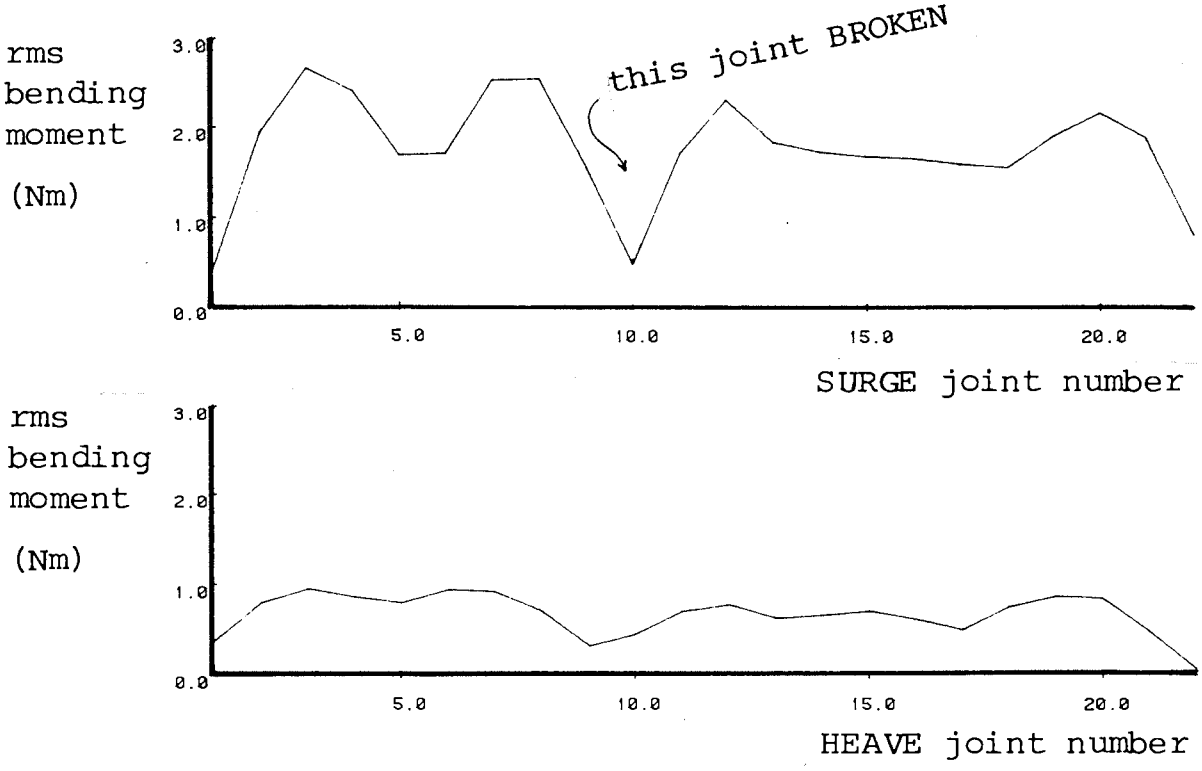

GRAPH 4.150 Effect of a broken surge joint on measured bending moments

5.A CUMULATIVE JOINT ANGLES

We define cumulative joint angle as the total travel of a joint during a given period. It is a useful number to know if you are designing full-scale spine joints for long maintenance-free periods at sea. Values are calculated from the spine tacho-generator velocity signals, by integrating their moduli. They are surprisingly low.

Each test lasted 51.2 seconds. For a scale of 107.7 the degrees-per-test result should be multiplied by the numbers shown below to give values for total angular excursion over longer periods. (Angles remain the same at all scales.)

time	revolutions multiplier
1 hour	18.8×10^{-3}
1 day	0.45
1 year	165.0
25 years	4.1×10^{3}

The data are plotted separately in surge and heave. The spine has 40 joints, and the cumulative angle at each joint is shown as a short bar. The range of values along the spine is clearly shown. In graph 5.1 joint stiffness was varied in four steps from 500 to 5000 Nm/rad. Energy Period and wave amplitude were kept constant. We see that angles rise with the inverse root of stiffness. Heave angles are about half the size of surge angles.

Example

In seas equivalent to our 1 second Pierson-Moskowitz with Hrms = 1.46m and Te = 10.4 seconds, a central surge joint with stiffness equivalent to 1000 Nm/rad would be moving through 50 degrees per test. Although this is a very rough sea (power = 173 kW/m, about three times our power limit) the full scale joint would only be moving at 0.94 revolutions per hour. It is likely that attempts to make more use of the power-generating capacity of joints will produce much larger values of cumulative angle. But we can go a long way in this direction before wear becomes a problem.

Cumulative Angles

1.0sec PM, Mitsuyasu, 40 joints

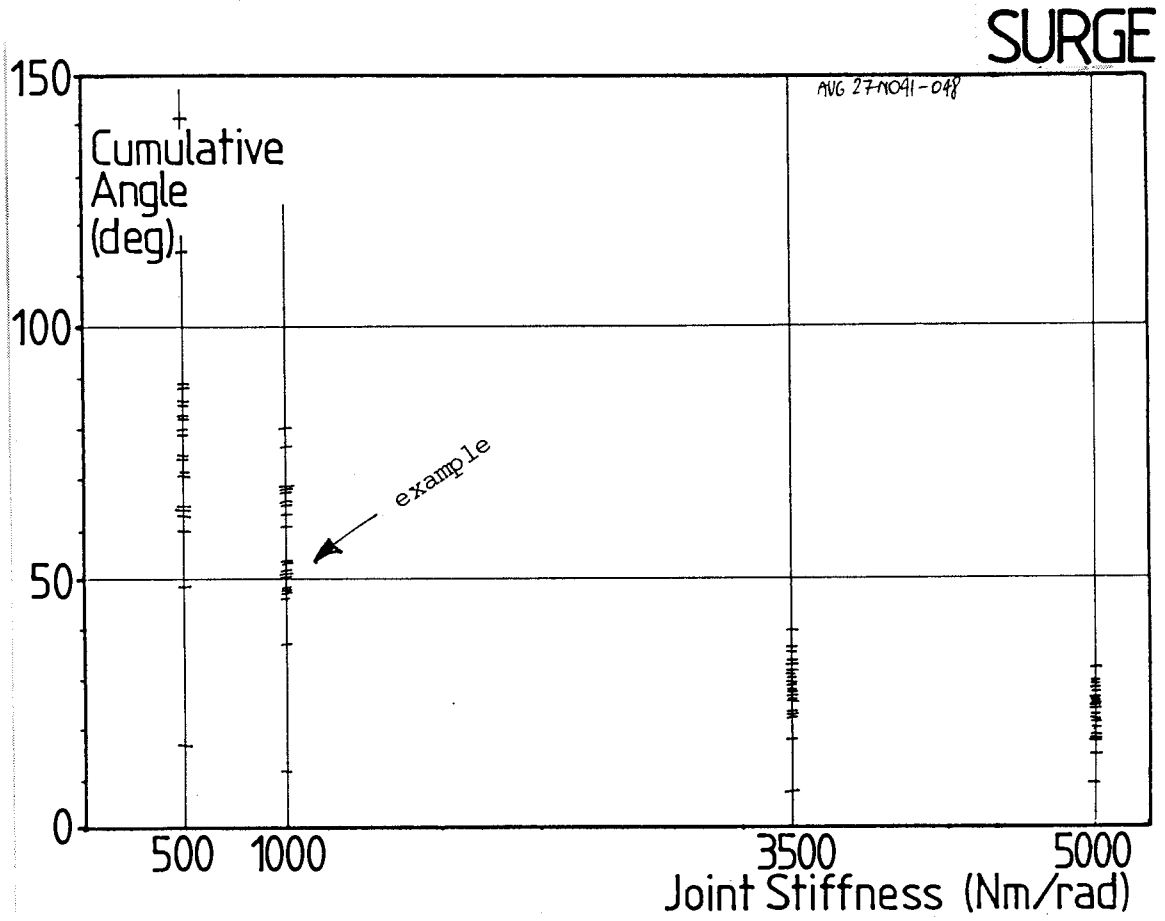

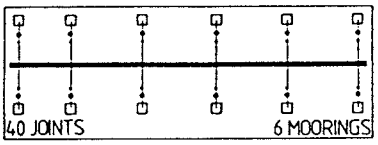

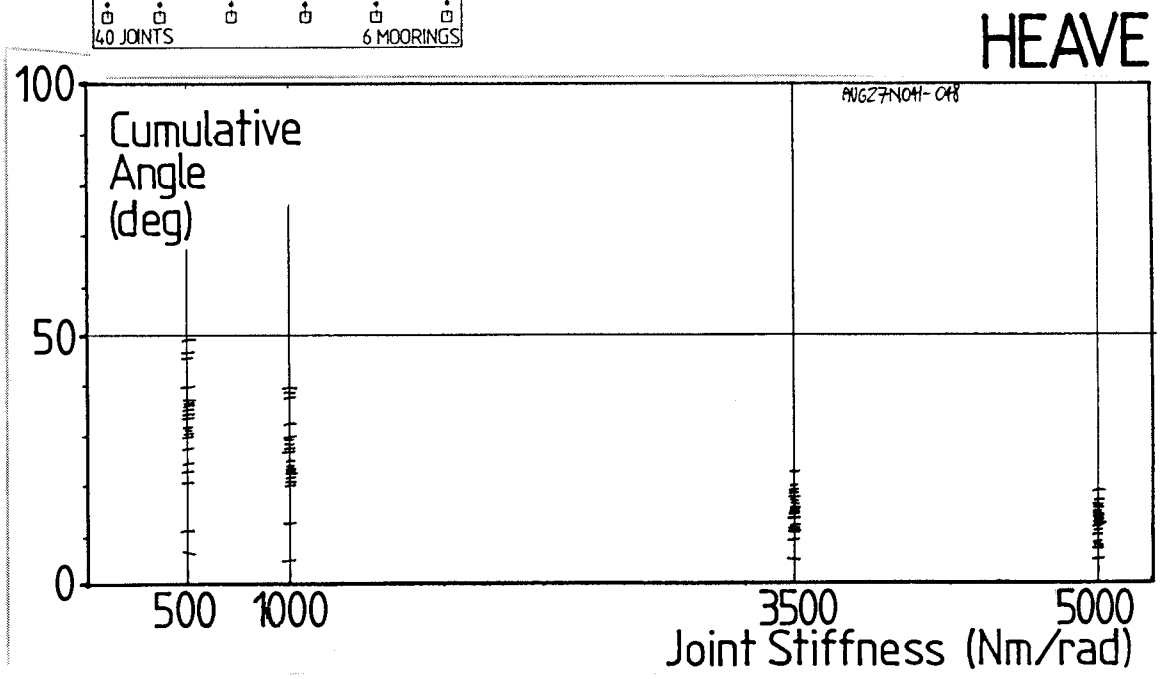

Varying STIFFNESS

GRAPH 5.1

(5.A cont)

In graph 5.2 the sea amplitude multiplier was raised in 5 steps from 0.25 to 2.0. Energy period was kept constant at 1.0 sec. Stiffness was kept constant at 1000 Nm/rad.

We see that surge angles are rising linearly with Hrms except for the biggest ones. The trends for these remind us of the 0.8 power rule (section 4.A). Heave angles rise very slightly faster than the first power of amplitude.

In Graph 5.3 we varied energy period by six steps from 0.7 to 1.5 seconds while wave amplitude and stiffness were kept constant. Both heave and surge angles rise rapidly between 0.7 and 0.9 seconds with another rise from 1.3 to 1.5 seconds. Heave angles are about half the size of corresponding surge ones except at 1.5 seconds where they rise to about two-thirds.

Cumulative Angles

1.0sec PM, Mitsuyasu, 1000Nm/rad, 40 joints

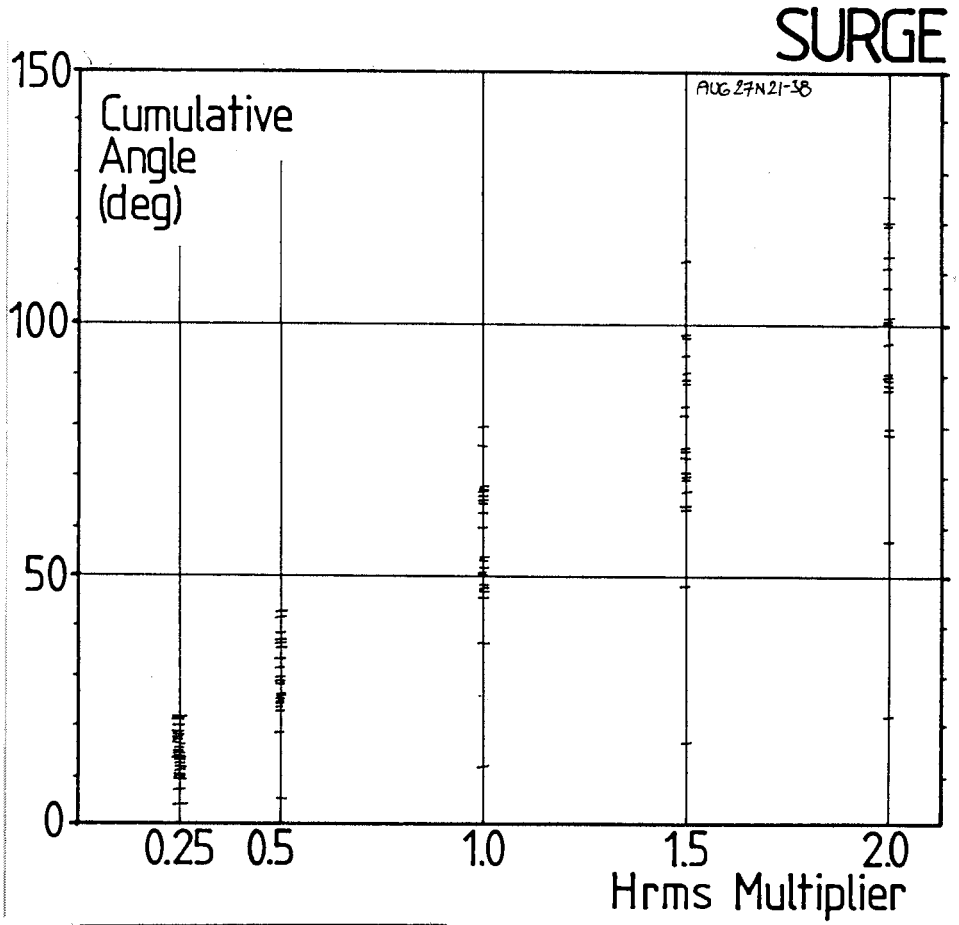

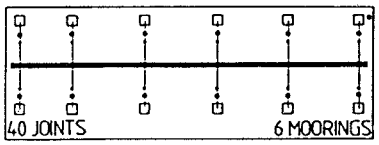

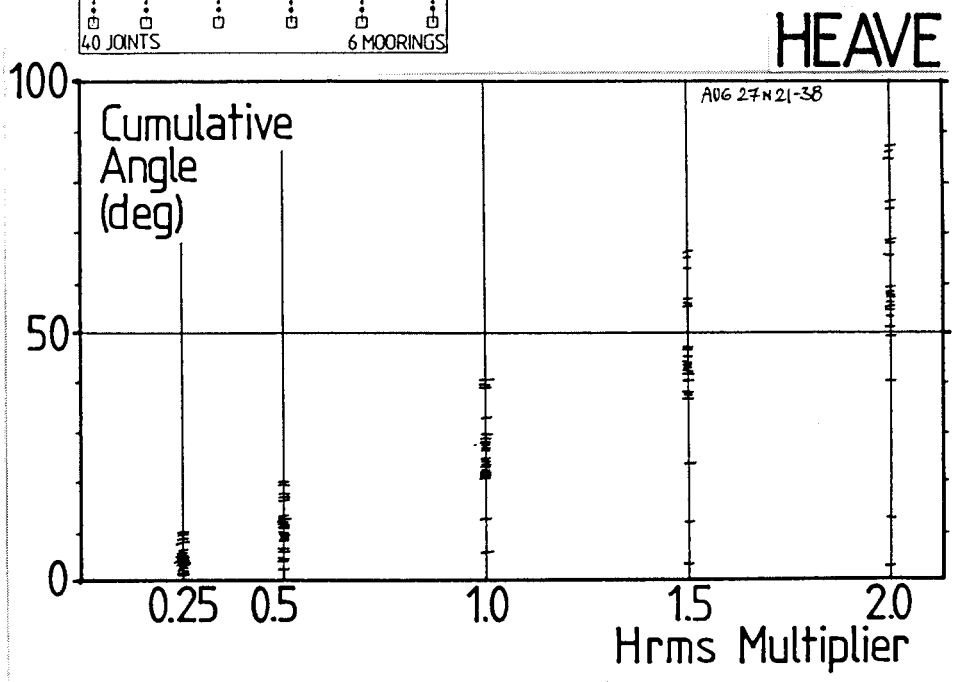

Varying Hrms MULTIPLIER

GRAPH 5.2

Cumulative Angles

PM, Mitsuyasu, 1000Nm/rad, 40 joints

SURGE

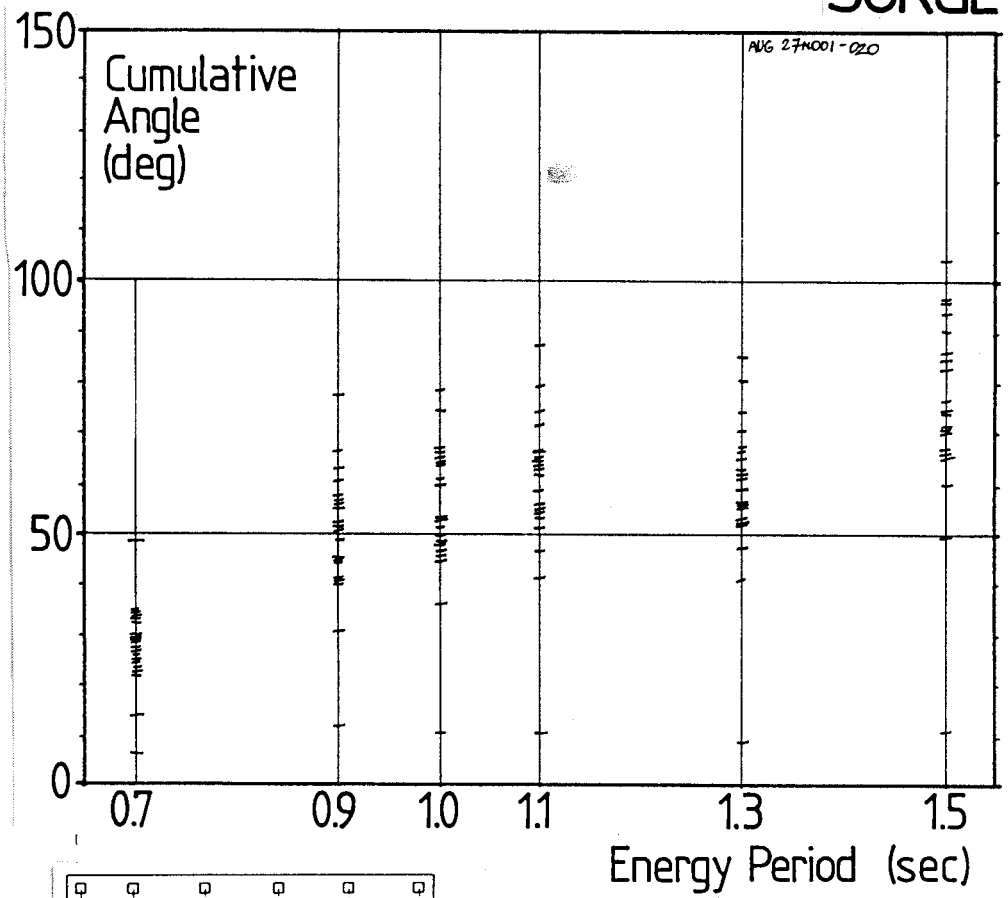

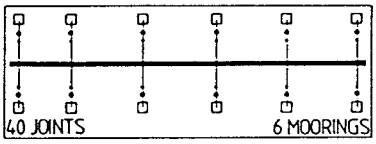

HEAVE

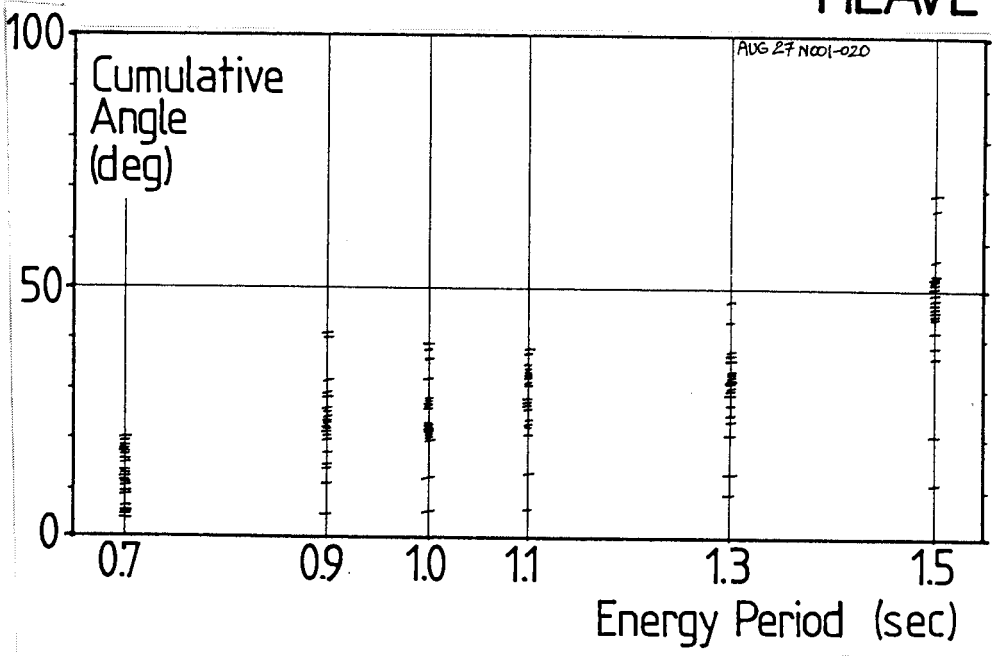

Varying ENERGY PERIOD

GRAPH 5.3

5.B MAXIMUM JOINT ANGLE IN FREAK WAVE

Graph 5.4 shows a time series from a spine surge joint during the passage of an extreme wave. This was the largest angular excursion of all joints.

The sea was a standard Pierson-Moskowitz spectrum with 1.0 second energy period and Mitsuyasu spread. We arranged the starting phases such that crests in each of the 75 component wavefronts would occur at the same place and time. We chose the place to be at the joint which suffered the biggest bending moment in normal 1 second Pierson-Moskowitz seas.

We increased the wavemaker drive voltage to give a well-defined plunging breaker. This command signal had an rms value four times the Pierson-Moskowitz norm.

The resulting wave (used to sink model trawlers during tank demonstrations) is outside the range of our wave gauges. We therefore took a video film of the wave hitting a metre-stick and by use of a single frame playback judged its trough-to-crest height to be 32 cm. At full scale this would be equivalent to 34.5 metres - about the 50 year extreme for Station India and well above anything expected at South Uist.

Joint angle records were identical regardless of whether we were trying to make the spine as compliant or as stiff as possible.

The time-series was produced by taking the integral of the joint angular velocity. The maximum value of 4.01° is just a fraction less than the maximum design angle of the joint, 4.2°, but there is no evidence of clipping in the angle waveform.

We conclude that the ±12° joint angle estimated for the present reference design provides a generous allowance.

Maximum JOINT ANGLE in 'FREAK WAVE'

PM Spectrum, Mitsuyasu Spread, Te=1.0sec

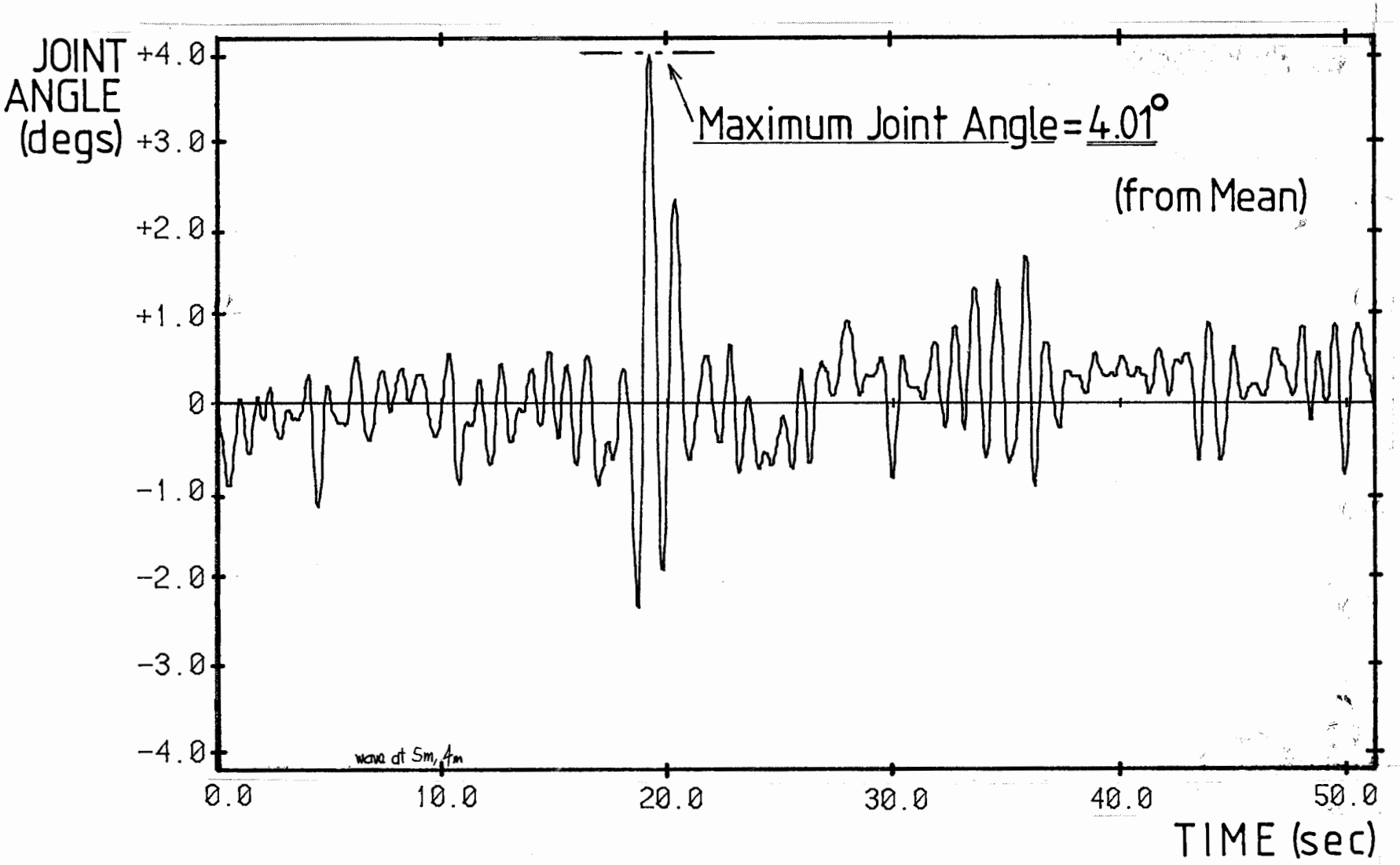

GRAPH 5.4

6.A WAVELENGTHS

Tables 6.1 and 6.2 compare deep water wavelengths with the wavelengths in the narrow and wide tanks, for a number of frequencies and periods.

Graph 6.1 shows the ratio of shallow-water wavelength to deep-water wavelength for both tanks.

The expression for wavelength **L** of small amplitude waves as a function of period is:

$$L = \frac{gT^2}{2\pi} \tanh\left(\frac{2\pi d}{L}\right)$$

and as a function of frequency:

$$L = \frac{g}{2\pi f^2} \tanh\left(\frac{2\pi d}{L}\right)$$

where:
- **g** = gravitational acceleration = 9.81 m/s^2
- **d** = water depth (metres)
- **T** = period (sec)
- **f** = frequency (hertz)

L appears on both sides of the equations, and it is usually found by an iterative process starting by inserting the deep water value on the right.

In both tanks the effect of the tanh correction drops to less than one part in a thousand at 1.3 hertz and above.

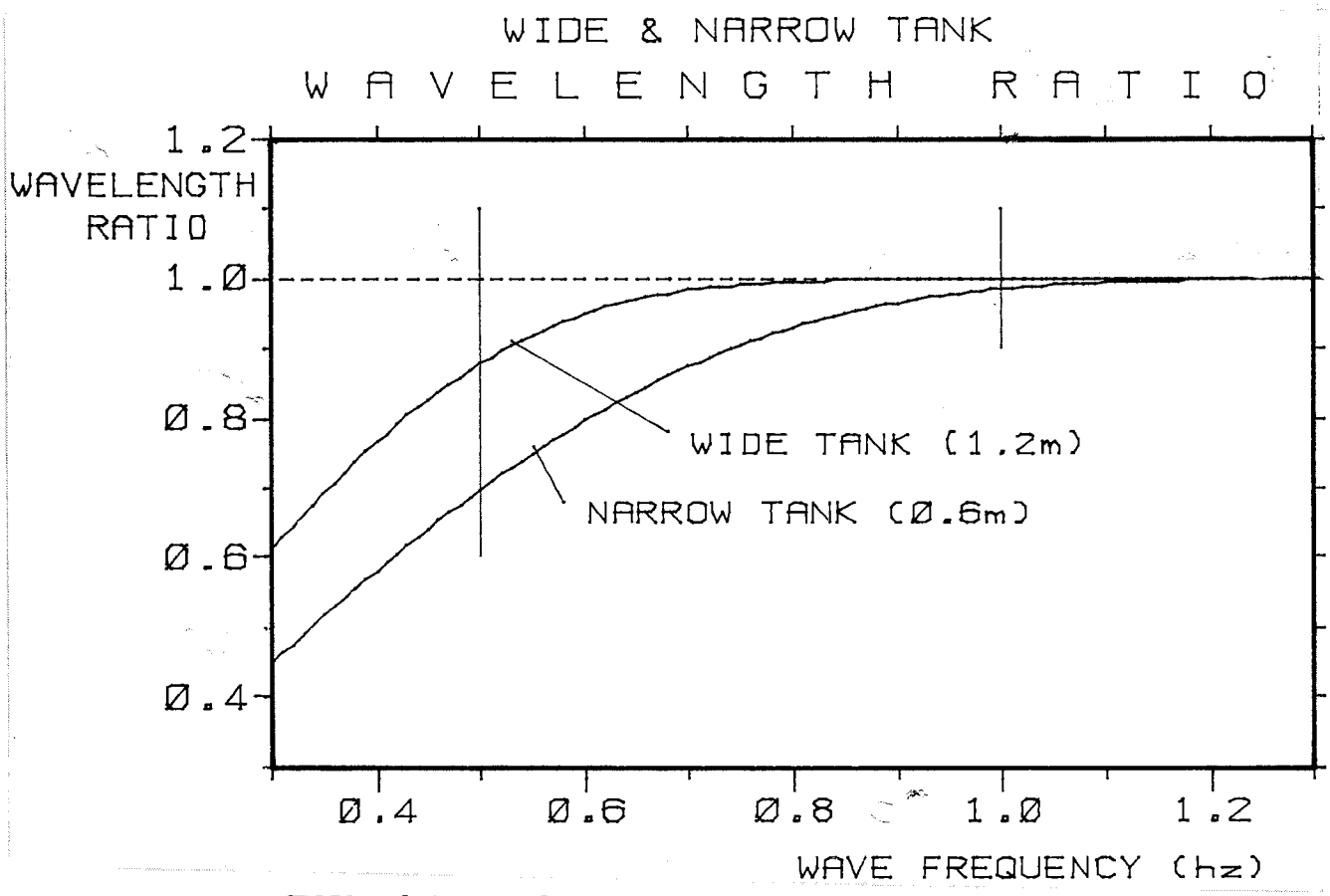

GRAPH 6.1: Wavelength Ratio against Frequency

frequency (hz)	deep water	wide tank (1.2m)	narrow tank (0.6m)
0.5	6.249	5.494	4.363
0.6	4.340	4.122	3.458
0.7	3.188	3.137	2.788
0.8	2.441	2.431	2.271
0.9	1.929	1.927	1.863
1.0	1.562	1.562	1.539
1.1	1.291	1.291	1.284
1.2	1.085	1.085	1.083
1.3	0.924	0.924	0.924
1.4		0.797	
1.5		0.694	
1.6		0.610	
1.7		0.541	
1.8		0.482	
1.9		0.433	
2.0		0.391	
2.1		0.354	
2.2		0.323	
2.3		0.295	
2.4		0.271	
2.5		0.250	

Table 6.1: WAVELENGTHS against FREQUENCY

period (sec)	deep water	wide tank (1.2m)	narrow tank (0.6m)
0.4		0.250	
0.5		0.391	
0.6	0.562	0.562	0.562
0.7	0.766	0.766	0.765
0.8	1.000	1.000	0.999
0.9	1.265	1.265	1.259
1.0	1.562	1.562	1.539
1.1	1.890	1.889	1.830
1.2	2.250	2.244	2.124
1.3	2.640	2.623	2.417
1.4	3.062	3.021	2.706
1.5	3.515	3.430	2.992
1.6	3.999	3.844	3.273
1.7	4.515	4.260	3.550
1.8	5.062	4.675	3.824
1.9	5.640	5.086	4.095
2.0	6.249	5.494	4.363

Table 6.2: WAVELENGTHS against PERIOD

6.B POWER RATIO

This is the ratio of the power of a regular wave in water of finite depth, to the power in a wave of the same height and period travelling in water of infinite depth.

The energy **E**, in a regular wave of unit width, but one wavelength long, can be written as (ref g, p21):

(1) $E = \rho g H_{RMS}^2 L$ where: ρ is water density
g is gravitational acceleration
Hrms is root mean square wave height
L is wavelength

The power density **P** can be calculated by dividing the energy by the time taken for it to cross a line perpendicular to its direction of travel. If the energy travelled at the phase velocity (the visually apparent speed of the troughs and crests) this time interval would be the wave period **T**, but in fact it travels more slowly at the group velocity. Denoting the ratio of group to phase velocities as **n**, power density can be written as:

(2) $P = n \frac{E}{T}$

Combining (1) and (2): $P = \frac{n L \rho g H_{RMS}^2}{T}$

Both the velocity ratio **n**, and the wavelength **L** are functions of water depth:

$n = \frac{1}{2}\left[1 + \frac{4\pi d/L}{\sinh(4\pi d/L)}\right]$ **d** is water depth

$L = \frac{gT^2}{2\pi} \tanh \frac{2\pi d}{L}$ (see section 6.A)

The value of **n** increases from 0.5 in deep water to 1 in very shallow water, while **L** gets shorter as depth decreases. The combined effects of these variations causes the power ratio to vary with wave frequency as shown in Graph 6.2 for the narrow and wide tanks, and Tables 6.3 and 6.4 list values for some selected frequencies and periods. The tank transfer function takes both effects into account but can be replaced by an 'amplitude priority' one for over-topping experiments.

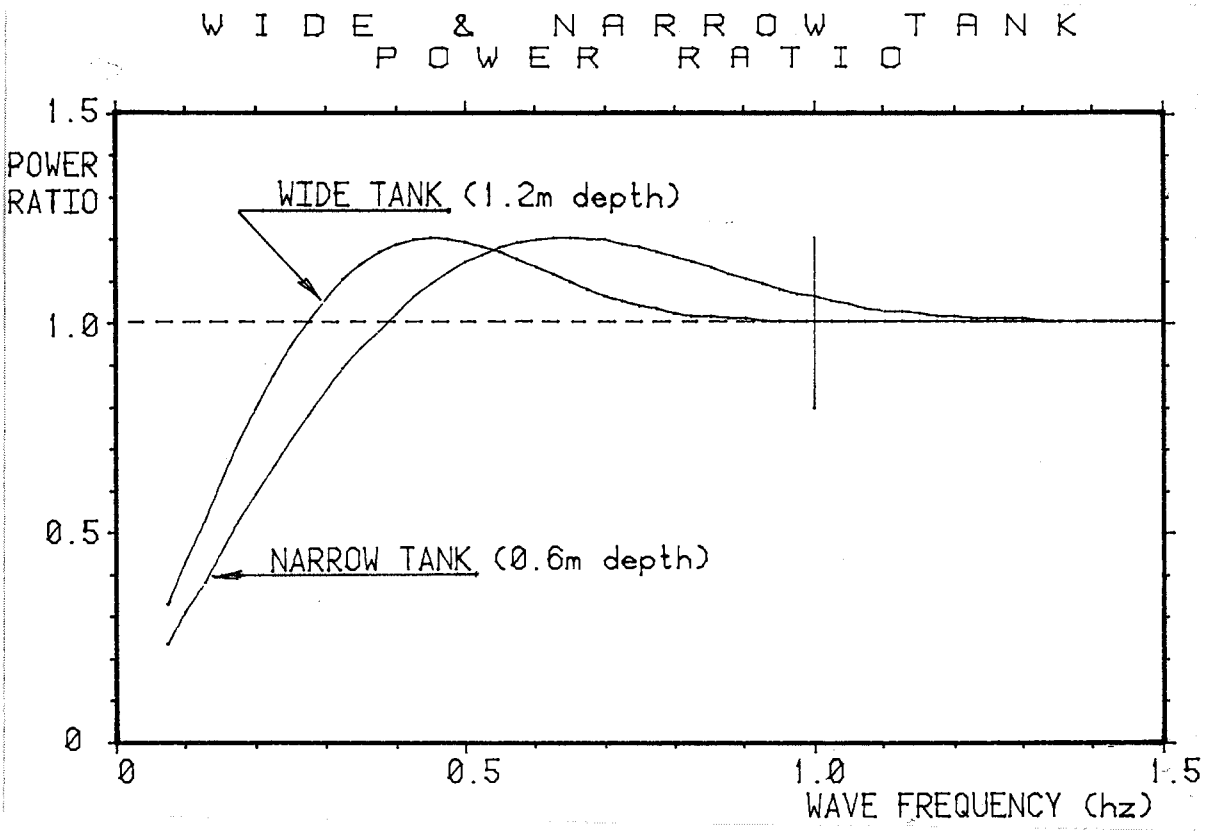

GRAPH 6.2: Power Ratio against Frequency

frequency (hz)	wide tank (1.2m)	narrow tank (0.6m)
0.5	1.191	1.141
0.6	1.129	1.195
0.7	1.061	1.193
0.8	1.021	1.154
0.9	1.005	1.102
1.0	1.001	1.057
1.1	1.000	1.027
1.2	1.000	1.011
1.3	1.000	1.004
1.4	1.000	1.001
1.5	1.000	1.000

Table 6.3: POWER RATIO/FREQUENCY

period (sec)	wide tank (1.2m)	narrow tank (0.6m)
0.5	1.000	1.000
0.6	1.000	1.000
0.7	1.000	1.001
0.8	1.000	1.007
0.9	1.000	1.025
1.0	1.001	1.057
1.1	1.005	1.098
1.2	1.014	1.137
1.3	1.030	1.168
1.4	1.053	1.189
1.5	1.081	1.198
1.6	1.110	1.199
1.7	1.138	1.192
1.8	1.161	1.179
1.9	1.178	1.161
2.0	1.191	1.141

Table 6.4: POWER RATIO/PERIOD

6.C CREST-LENGTHS

For a regular wave, crest-length is the distance between crests along a line parallel to the wavemakers.

Crest-length = **L/sin a**

where **L** is the wavelength $= \frac{gT^2}{2\pi} \tanh\left(\frac{2\pi d}{L}\right)$

a is the angle that the wavefront makes with the wavemakers.

Tables 6.5 and 6.6 list crest-lengths against frequency and period, for a number of wave angles. The values in the 90 degree columns are of course the same as the wavelengths. These tables avoid the need for the unpleasant iterative solution of the TANH equation. They allow for the tank depth of 1.2 metres but do not take larger amplitude effects into account. These become significant for breaking waves. We have not yet thought of a way to incoporate amplitude effects into the tank transfer function.

frequency (hz)	angle (degrees) 5	10	15	20	25	30	35	40	45	50	55	60	65	70	75	80	85	90
0.5	63.05	31.65	21.23	16.07	13.00	10.99	9.58	8.55	7.77	7.17	6.71	6.35	6.06	5.85	5.69	5.58	5.52	5.49
0.6	47.30	23.74	15.93	12.05	9.75	8.24	7.19	6.41	5.83	5.38	5.03	4.76	4.55	4.39	4.27	4.19	4.14	4.12
0.7	36.00	18.07	12.12	9.17	7.42	6.27	5.47	4.88	4.44	4.10	3.83	3.62	3.46	3.34	3.25	3.19	3.15	3.14
0.8	27.90	14.00	9.40	7.11	5.75	4.86	4.24	3.78	3.44	3.17	2.97	2.81	2.68	2.59	2.52	2.47	2.44	2.43
0.9	22.12	11.10	7.45	5.64	4.56	3.86	3.36	3.00	2.73	2.52	2.35	2.23	2.13	2.05	2.00	1.96	1.93	1.93
1.0	17.93	9.00	6.04	4.57	3.70	3.12	2.72	2.43	2.21	2.04	1.91	1.80	1.72	1.66	1.62	1.59	1.57	1.56
1.1	14.82	7.44	4.99	3.78	3.06	2.58	2.25	2.01	1.83	1.69	1.58	1.49	1.42	1.37	1.34	1.31	1.30	1.29
1.2	12.45	6.25	4.19	3.17	2.57	2.17	1.89	1.69	1.53	1.42	1.32	1.25	1.20	1.15	1.12	1.10	1.09	1.08
1.3	10.61	5.32	3.57	2.70	2.19	1.85	1.61	1.44	1.31	1.21	1.13	1.07	1.02	0.98	0.96	0.94	0.93	0.92
1.4	9.15	4.59	3.08	2.33	1.89	1.59	1.39	1.24	1.13	1.04	0.97	0.92	0.88	0.85	0.83	0.81	0.80	0.80
1.5	7.97	4.00	2.68	2.03	1.64	1.39	1.21	1.08	0.98	0.91	0.85	0.80	0.77	0.74	0.72	0.71	0.70	0.69
1.6	7.00	3.52	2.36	1.78	1.44	1.22	1.06	0.95	0.86	0.80	0.75	0.70	0.67	0.65	0.63	0.62	0.61	0.61
1.7	6.20	3.11	2.09	1.58	1.28	1.08	0.94	0.84	0.76	0.71	0.66	0.62	0.60	0.58	0.56	0.55	0.54	0.54
1.8	5.53	2.78	1.86	1.41	1.14	0.96	0.84	0.75	0.68	0.63	0.59	0.56	0.53	0.51	0.50	0.49	0.48	0.48
1.9	4.97	2.49	1.67	1.27	1.02	0.87	0.75	0.67	0.61	0.57	0.53	0.50	0.48	0.46	0.45	0.44	0.43	0.43
2.0	4.48	2.25	1.51	1.14	0.92	0.78	0.68	0.61	0.55	0.51	0.48	0.45	0.43	0.42	0.40	0.40	0.39	0.39
2.1	4.07	2.04	1.37	1.04	0.84	0.71	0.62	0.55	0.50	0.46	0.43	0.41	0.39	0.38	0.37	0.36	0.36	0.35
2.2	3.70	1.86	1.25	0.94	0.76	0.65	0.56	0.50	0.46	0.42	0.39	0.37	0.36	0.34	0.33	0.33	0.32	0.32
2.3	3.39	1.70	1.14	0.86	0.70	0.59	0.51	0.46	0.42	0.39	0.36	0.34	0.33	0.31	0.31	0.30	0.30	0.30
2.4	3.11	1.56	1.05	0.79	0.64	0.54	0.47	0.42	0.38	0.35	0.33	0.31	0.30	0.29	0.28	0.28	0.27	0.27
2.5	2.87	1.44	0.97	0.73	0.59	0.50	0.44	0.39	0.35	0.33	0.31	0.29	0.28	0.27	0.26	0.25	0.25	0.25

for wide tank (depth: 1.2m)

Table 6.5 CREST-LENGTHS (metres) against FREQUENCY

period (sec)	angle (degrees) 5	10	15	20	25	30	35	40	45	50	55	60	65	70	75	80	85	90
0.4	2.87	1.44	0.97	0.73	0.59	0.50	0.44	0.39	0.35	0.33	0.31	0.29	0.28	0.27	0.26	0.25	0.25	0.25
0.5	4.48	2.25	1.51	1.14	0.92	0.78	0.68	0.61	0.55	0.51	0.48	0.45	0.43	0.42	0.40	0.40	0.39	0.39
0.6	6.45	3.24	2.17	1.64	1.33	1.13	0.98	0.88	0.80	0.73	0.69	0.65	0.62	0.60	0.58	0.57	0.56	0.56
0.7	8.78	4.41	2.96	2.24	1.81	1.53	1.33	1.19	1.08	1.00	0.93	0.88	0.84	0.81	0.79	0.78	0.77	0.77
0.8	11.47	5.76	3.86	2.92	2.37	2.00	1.74	1.56	1.41	1.31	1.22	1.15	1.10	1.06	1.04	1.02	1.00	1.00
0.9	14.52	7.29	4.89	3.70	2.99	2.53	2.21	1.97	1.79	1.65	1.54	1.46	1.40	1.35	1.31	1.29	1.27	1.27
1.0	17.93	9.00	6.04	4.57	3.70	3.12	2.72	2.43	2.21	2.04	1.91	1.80	1.72	1.66	1.62	1.59	1.57	1.56
1.1	21.68	10.88	7.30	5.52	4.47	3.78	3.29	2.94	2.67	2.47	2.31	2.18	2.08	2.01	1.96	1.92	1.90	1.89
1.2	25.75	12.93	8.67	6.56	5.31	4.49	3.91	3.49	3.17	2.93	2.74	2.59	2.48	2.39	2.32	2.28	2.25	2.24
1.3	30.11	15.11	10.14	7.67	6.21	5.25	4.57	4.08	3.71	3.43	3.20	3.03	2.89	2.79	2.72	2.66	2.63	2.62
1.4	34.67	17.40	11.67	8.83	7.15	6.04	5.27	4.70	4.27	3.94	3.69	3.49	3.33	3.21	3.13	3.07	3.03	3.02
1.5	39.36	19.75	13.25	10.03	8.12	6.86	5.98	5.34	4.85	4.48	4.19	3.96	3.78	3.65	3.55	3.48	3.44	3.43
1.6	44.12	22.14	14.86	11.24	9.10	7.69	6.70	5.98	5.44	5.02	4.69	4.44	4.24	4.09	3.98	3.90	3.86	3.84
1.7	48.89	24.54	16.46	12.46	10.08	8.52	7.43	6.63	6.03	5.56	5.20	4.92	4.70	4.53	4.41	4.33	4.28	4.26
1.8	53.65	26.93	18.07	13.67	11.06	9.35	8.15	7.27	6.61	6.10	5.71	5.40	5.16	4.98	4.84	4.75	4.69	4.67
1.9	58.37	29.30	19.66	14.87	12.04	10.17	8.87	7.91	7.19	6.64	6.21	5.87	5.61	5.41	5.27	5.17	5.11	5.09
2.0	63.05	31.65	21.23	16.07	13.00	10.99	9.58	8.55	7.77	7.17	6.71	6.35	6.06	5.85	5.69	5.58	5.52	5.49

for wide tank (depth: 1.2m)

Table 6.6 CREST-LENGTHS (metres) against PERIOD

6.D TANK LIMITS

Sea states in the wide tank are composed of up to 75 separate wave fronts. Each is defined by an amplitude, a frequency, an angle, and a starting phase.

The range of useful angles is limited by the pitch of individual wave makers.

Angles are produced by arranging a constant phase difference, ϕ between the command signals to each wavemaker.

$$\phi = \frac{2\pi P \sin a}{L}$$

where **P** is the pitch of the wavemaker
L is the wavelength corrected for shallow water effects
a is the required wavefront angle

Inversely, phase difference ϕ produces angle **a**:

$$a = \sin^{-1}\left(\frac{\phi L}{2\pi P}\right)$$

Phase difference ϕ between wavemaker n and wavemaker n + 1, implies phase difference $\phi' = (2\pi - \phi)$ between wavemaker n and wavemaker n - 1. This may result in a second wave at angle **a'** if the expression in brackets above is less than or equal to 1 when ϕ is replaced by ϕ'.

This is shown in graph 6.3. Lines of constant wave angle are plotted against wave making frequency and phase difference. Normal tank operation corresponds to the 2 truncated triangular areas at top and bottom, where only one wavefront is possible. The area where

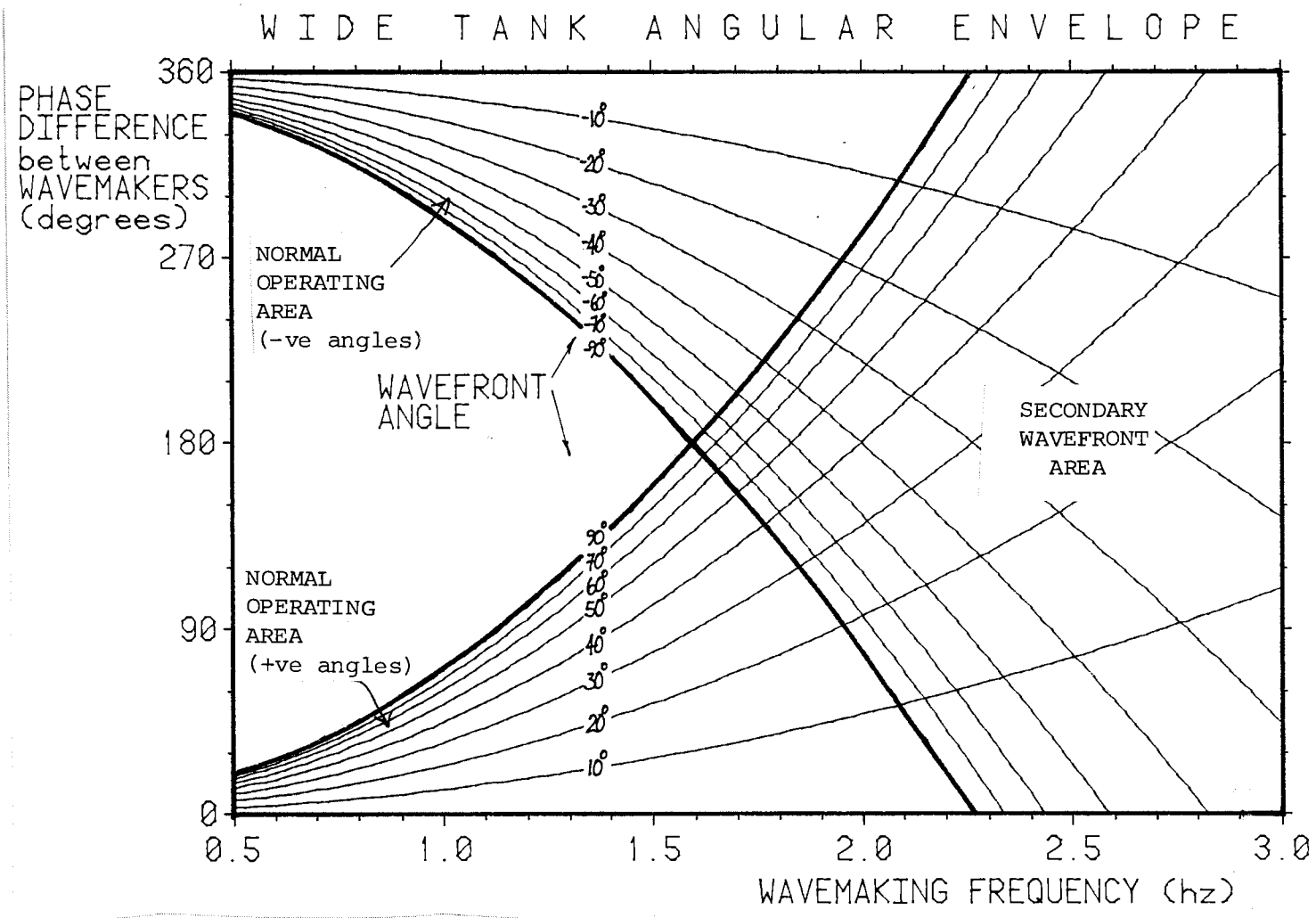

GRAPH 6.3. The wide tank angular envelope.

(6.D cont)

secondary wave fronts will occur is to the right where angle lines intersect. At frequencies above 2.26 hertz, where the wavemaker pitch is equal to or greater than wave length, secondary fronts are inevitable, whatever the angle. Phase differences and frequencies in the white area produce lots of movement at the wavemakers but little in the tank. The waves are trying to go backwards 'into the car-park'.

Phase differences ϕ and ϕ' are of course the same as

$$\phi \pm 2\pi, \quad \phi' \pm 2\pi \; ; \quad \phi \pm 4\pi, \quad \phi' \pm 4\pi \ldots\ldots$$

Fig 6.4 shows the areas where these 'ghosts' will appear in the tank.

Graph 6.5 shows how we could make the tank better or worse by changing the pitch of the wavemakers from the present 12". Very narrow wavemakers present a severe hinge design problem.

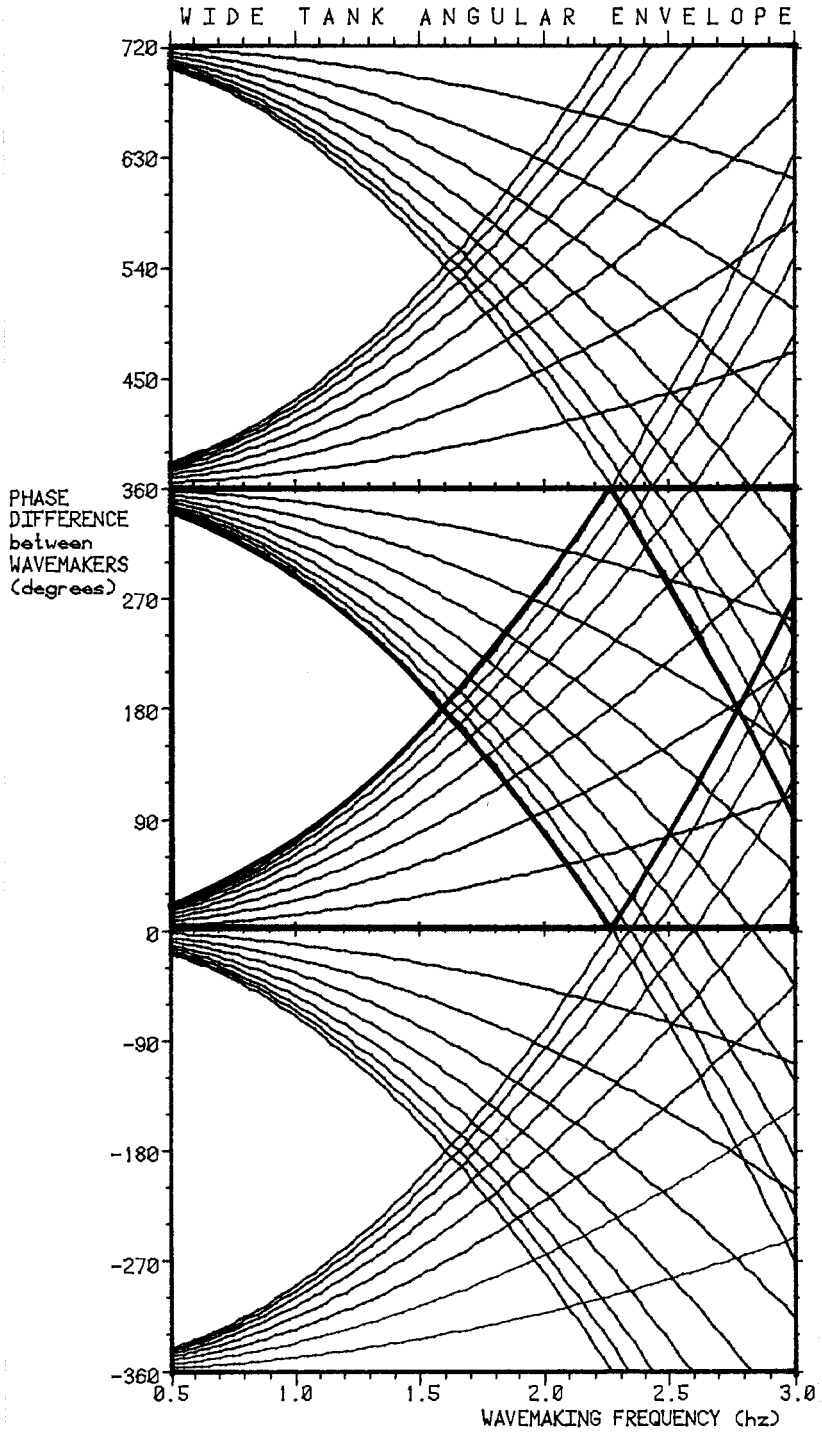

GRAPH 6.4: Wide Tank angular envelope - extended

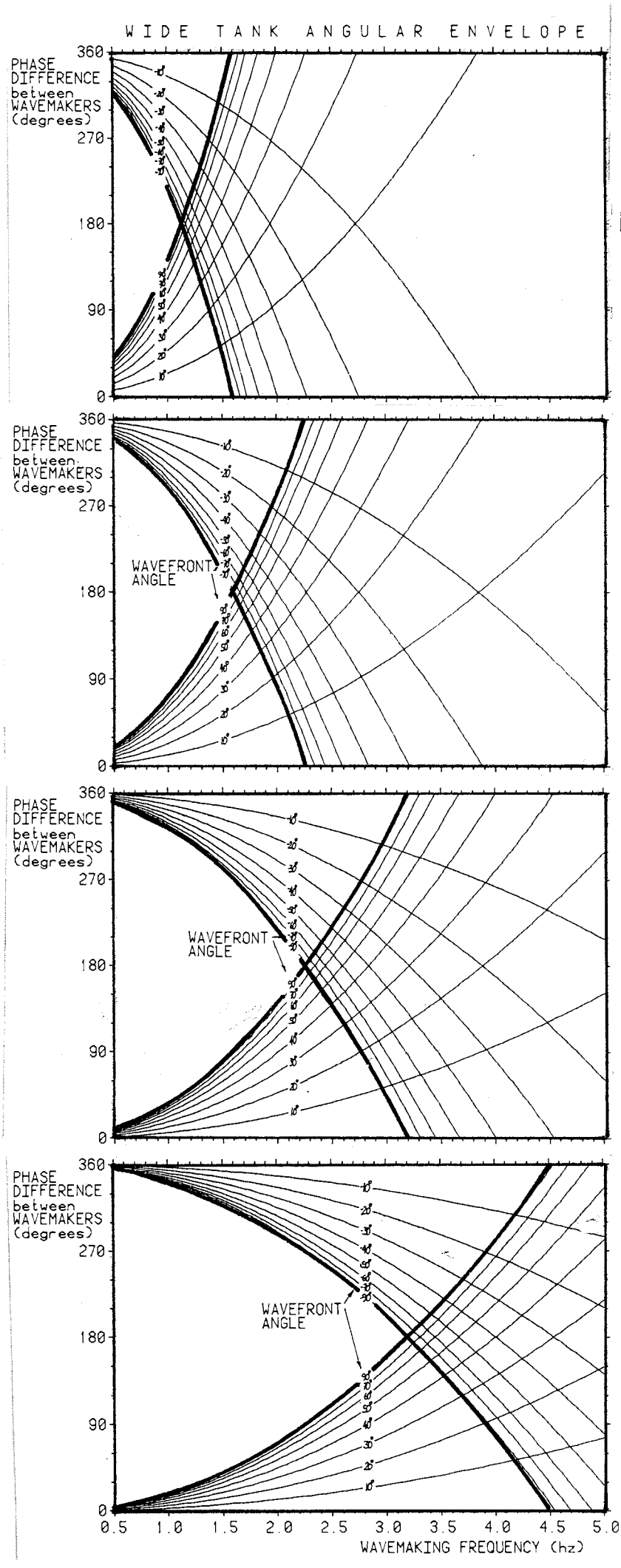

GRAPH 6.5
Angular envelope for 4 different wavemaker pitches

6.E INHERENT JOINT STIFFNESS

The spine model is designed so that bending forces are opposed by a motor driven arm. There are also small torsion springs with stiffness of 15NM/rad at each joint to provide mean reference positions for the joints.

In addition to these known compliances, the mechanical components of the spine units deflect under the action of the transmitted forces, such that the angular deflections of the joints may be a little greater than indicated by the integrated angular velocity signals from the tacho-generators. We measured the combined stiffness characteristics of 5 joints and the results are shown in graph 6.6.

We used a metal-working lathe to provide a rigid reference frame. The active joint was gripped by the chuck, and a conical centre attached to the tail stock provided a shear reaction at the passive end without exerting any additional torque.

With sinusoidal command signals applied, the force feedback circuit drove the joint motor back and forth through whatever angle was required to match and cancel the command torque. As the ends were held rigidly by the lathe, this angular movement was entirely a function of the inherent compliance of the spine components.

We recorded bending moments at the strain gauges and divided them by angular deflections calculated from the integral of the tacho velocity signals. The graph shows these derived stiffnesses plotted against the bending moments.

The curves for all spines are similar. The inherent stiffness increases with applied torque and then flattens out. The most obvious source of the non-linear part of the characteristic is the toothed drive belts. They are made with steel reinforcing bands encased in polyurethane.

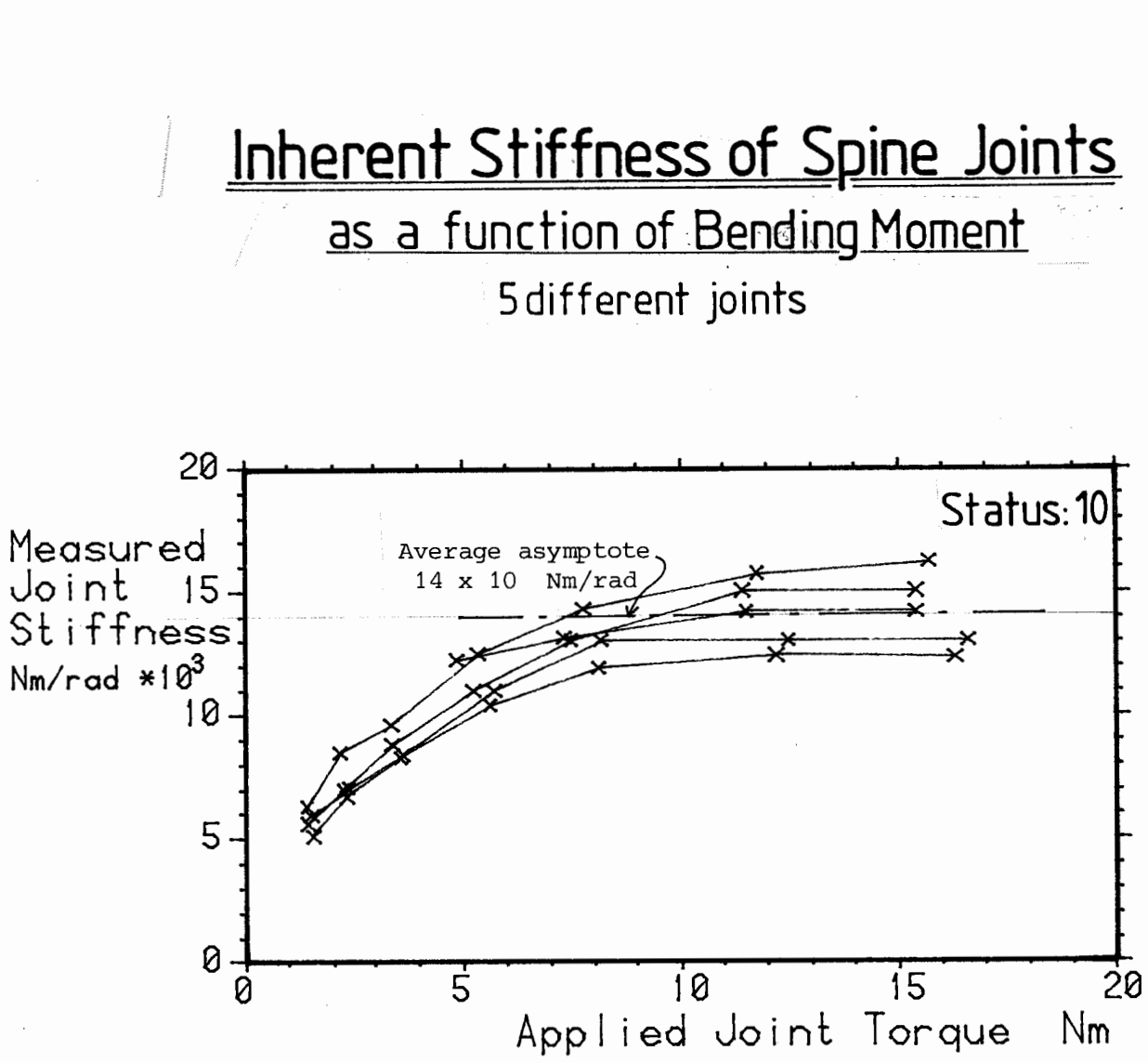

GRAPH 6.6: Joint inherent stiffness against applied torque

Nominal Stiffness	250	500	1000	2000	3500	4000	5000	8000	(Nm/rad)
Net Stiffness	245	485	930	1750	2800	3100	3700	5100	(Nm/rad)
Moment Multiplier	1.00	1.00	1.01	1.08	1.12	1.14	1.17	1.17	

TABLE 6.7 Approximate asymptotic net stiffness of joints and estimated bending moment multipliers, against nominal stiffnesses.

(6.E cont)

The inherent stiffness is in series with the 'electronic' joint stiffness and so the net stiffness is calculated using the reciprocal of the sum of the reciprocals of the separate values.

In practice it is not easy to adjust single rms bending moment values for the effect of inherent stiffness, because it varies throughout the original time series, depending on the instantaneous forces. The actual joint stiffness will always be lower than desired, but the effect will be worse for higher nominal stiffnesses. We were relieved when narrow tank results showed that required stiffness values were going to be at the bottom end of the range.

Table 6.7 shows the effect of adding the average asymptotic value of 14,000 Nm/rad suggested by graph 6.6 to various nominal stiffnesses and lists estimated correction multipliers for bending moments.

6.F TIME SERIES AND HISTOGRAMS

a) Mixed Seas

Most of the data in this report are presented as arrays of root mean square (rms) values, each of these numbers itself being a function of a complete time series.

Using rms values reduces the amount of data that we have to display and store, typically by a factor of 1024. This was necessary before we installed tape handling equipment for bulk data storage. The use of rms values implies the assumption of a shape of the distribution of the measurements. Graphs 6.7 and 6.8 show compressed Bending Moment time series in Surge and Heave for each joint in a spine of 35 joints. Histograms derived from the time series are drawn at the bottom of the pages as sets of vertical lines. A normal distribution curve with a standard deviation equal to the rms value of the time series is plotted over each histogram. A theoretical normal distribution curve is plotted over each histogram, with standard deviation equal to the rms of the time series.

The time series are plotted to a common vertical scale on each page, but the histograms are adjusted so that the highest tooth in each case is the same height, and the areas under the normal curves are made equal to those under the histogram.

The sea used is one of the smallest of the South Uist spectra, so we would expect to see any imperfections in the joint hinge mechanism, particularly in end spines where the bending moments usually fall to their lowest values, and in heave where the values tend to be about half of those in surge.

In fact the quality of fit of the measured histograms to the normal curves is gratifying. Occasional high teeth near the middle of the histograms suggest slackness in the drive belt, with an appreciable delay before the motor can reverse its reaction as the wave-induced forces change polarity. Low teeth in the middle of histograms suggest stiction in the drive so that waves have to work extra hard to get the joints moving.

spine joint TORQUE SIGNALS

Time Series & Histograms

Stiffness: 1000Nm/rad, Status: 10

Sampling: 1024 points at 20Hz = 51.2sec

Time Series

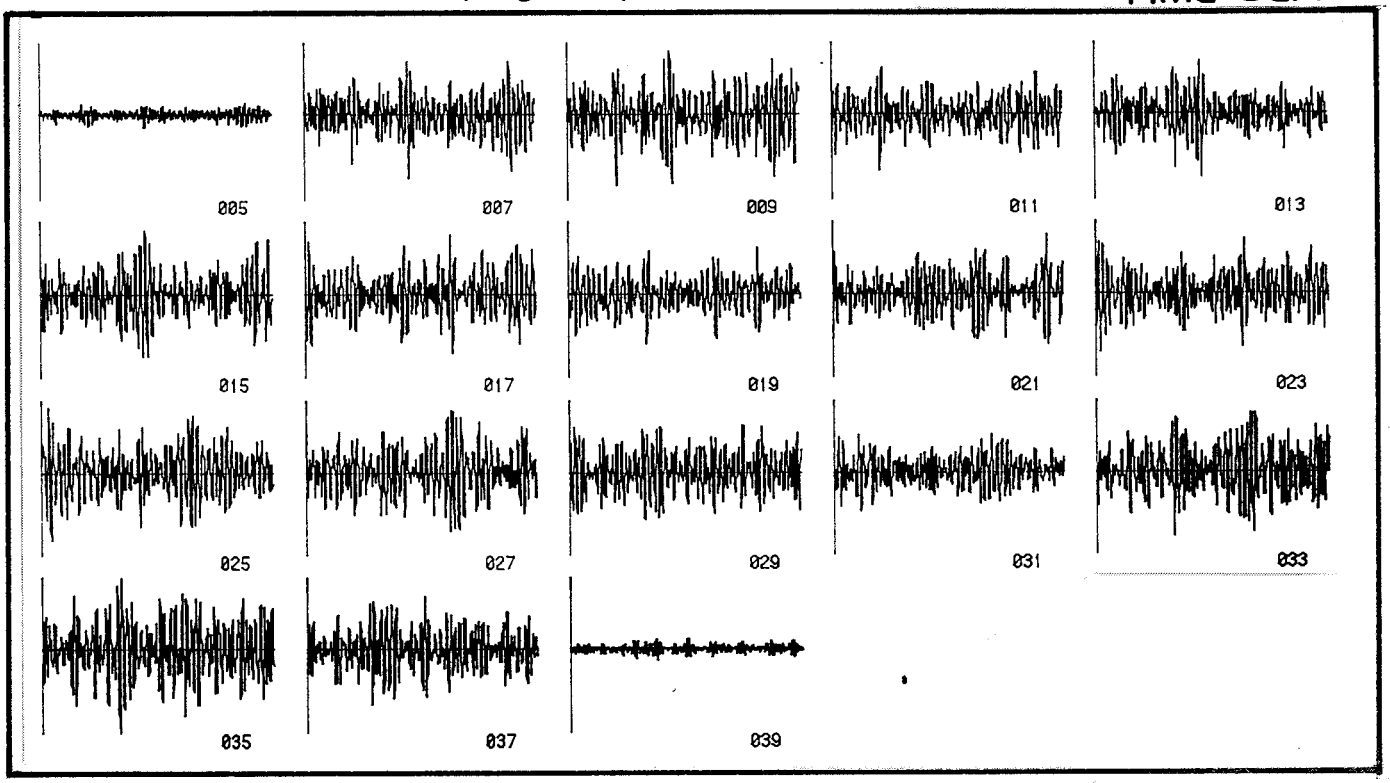

Histograms

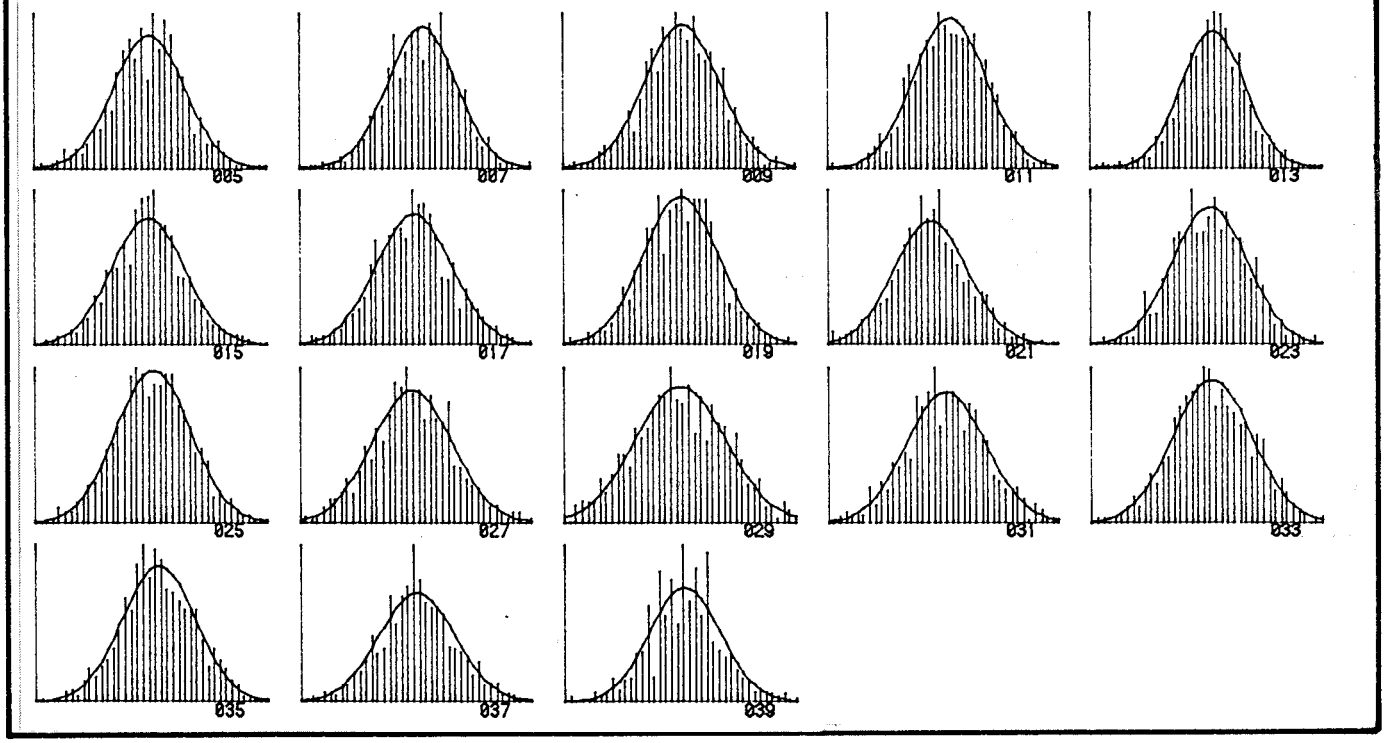

South Uist sea: 089 (small) Hrms=0.38cm

SURGE joints

GRAPH 6.7

spine joint TORQUE SIGNALS

Time Series & Histograms

Stiffness: 1000Nm/rad, Status: 10

Sampling: 1024 points at 20Hz = 51.2sec

Time Series

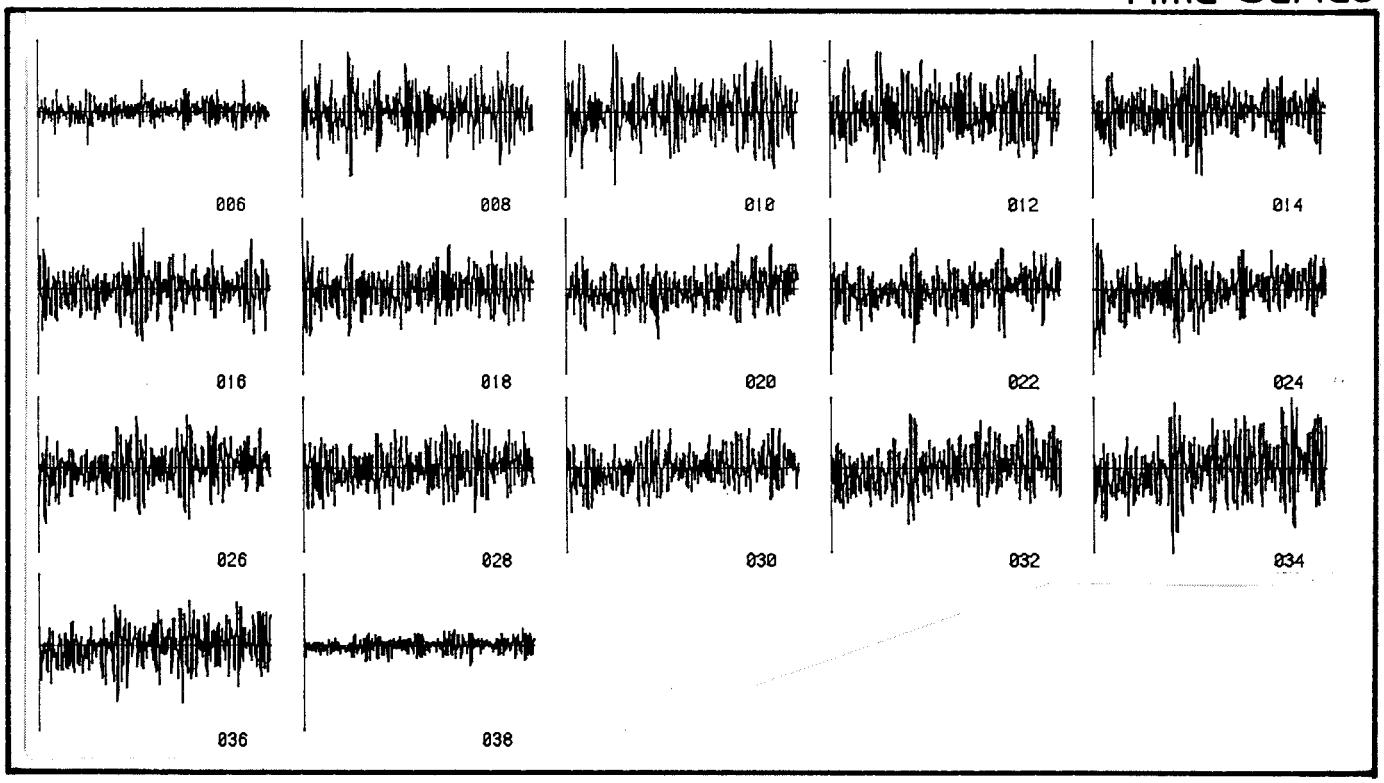

Histograms

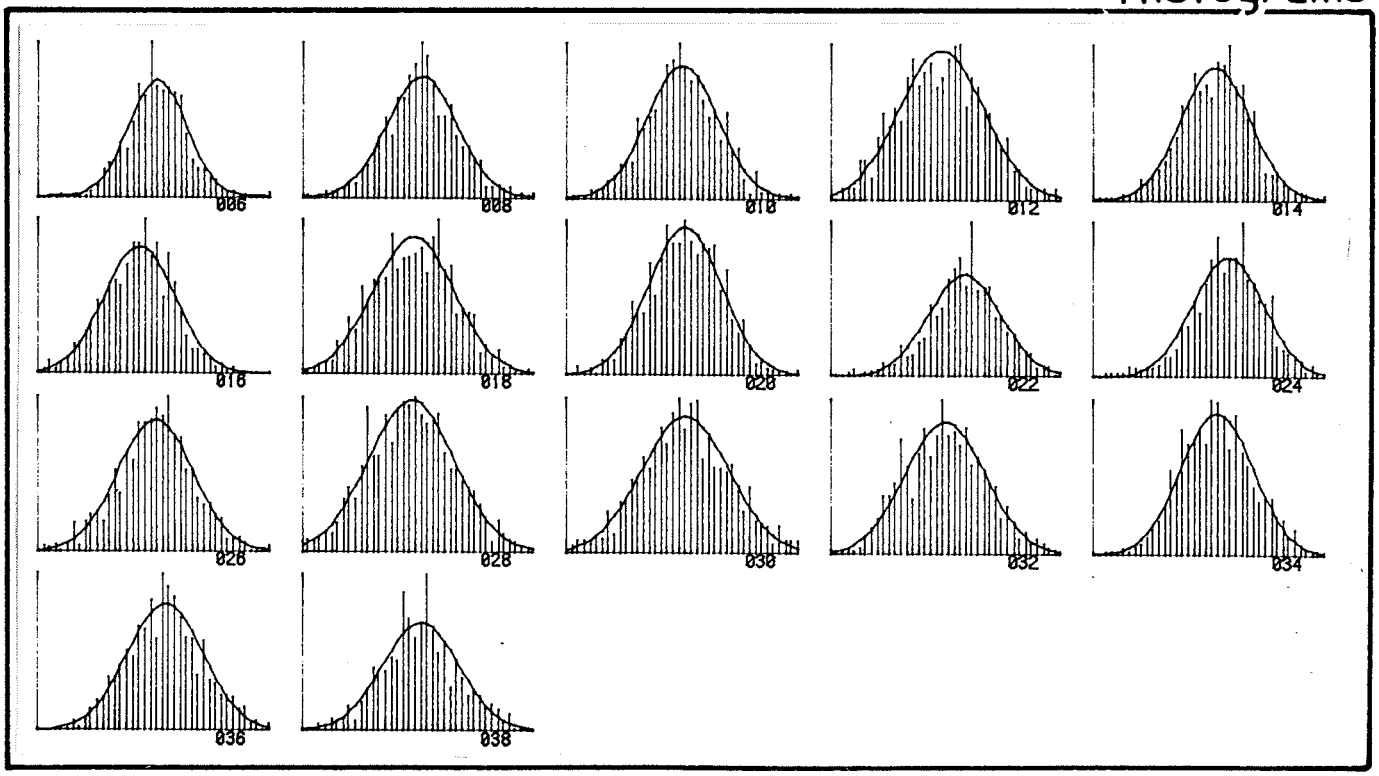

South Uist sea: 089 (small) Hrms=0.38cm

HEAVE joints

(6.F cont)

b) Regular Waves

Graphs 6.9 and 6.10 show time series and histograms for the joints in a regular wave.

The time series on each page are plotted to the same vertical scale, but the histograms are individually scaled according to the highest tooth. The horizontal time-scale is one quarter of that used in the preceding South Uist plots, although, for the monochromatic wave tests shown elsewhere in this report, the test times were the same.

The time series in surge are strikingly symmetrical. With only 256 data samples per plot shown here, the sampling time steps are clearly visible. Most of the peaks are ragged, and the histograms are fairly noisy versions of the U shapes expected with approximately sinusoidal signals. The effect of stiction is particularly visible in the histogram for joint number 039 which had unusually low loading for this sea.

In heave, the striking asymmetry of the time series is reminiscent of our work with cylinders in the narrow tank (see page 15.2 of our 1976 report). Frequency doubling is evident in many of the joints and the 2 least distorted waveforms, 040 and 042, show interesting modulation in their envelopes, suggestive of beating. We know that wave amplitude stability is much better than that.

Before plotting each time series we subtracted the mean value of the time series from each data point to remove the effects of any electrical offsets in the system. At this stage, we are not able to distinguish genuine non-zero bending moment means from such offsets, so the apparent asymmetry of positive and negative peak values should be treated with caution. This caveat applies particularly to the modulus results in section 4.A. However it is difficult to imagine a hydrodynamic mechanism which could induce permanent bending moment offsets in a free floating structure of constant section and weight distribution.

We have now installed economic mass data storage in the wide tank. Magnetic tape is used to record the millions of numbers produced during each experiment and so we can, in future, maintain access to the original time series indefinitely.

spine joint TORQUE SIGNALS

Time Series & Histograms

Stiffness: 1000Nm/rad, Status: 10

Sampling: 256 points at 20Hz = 12.8sec

Time Series

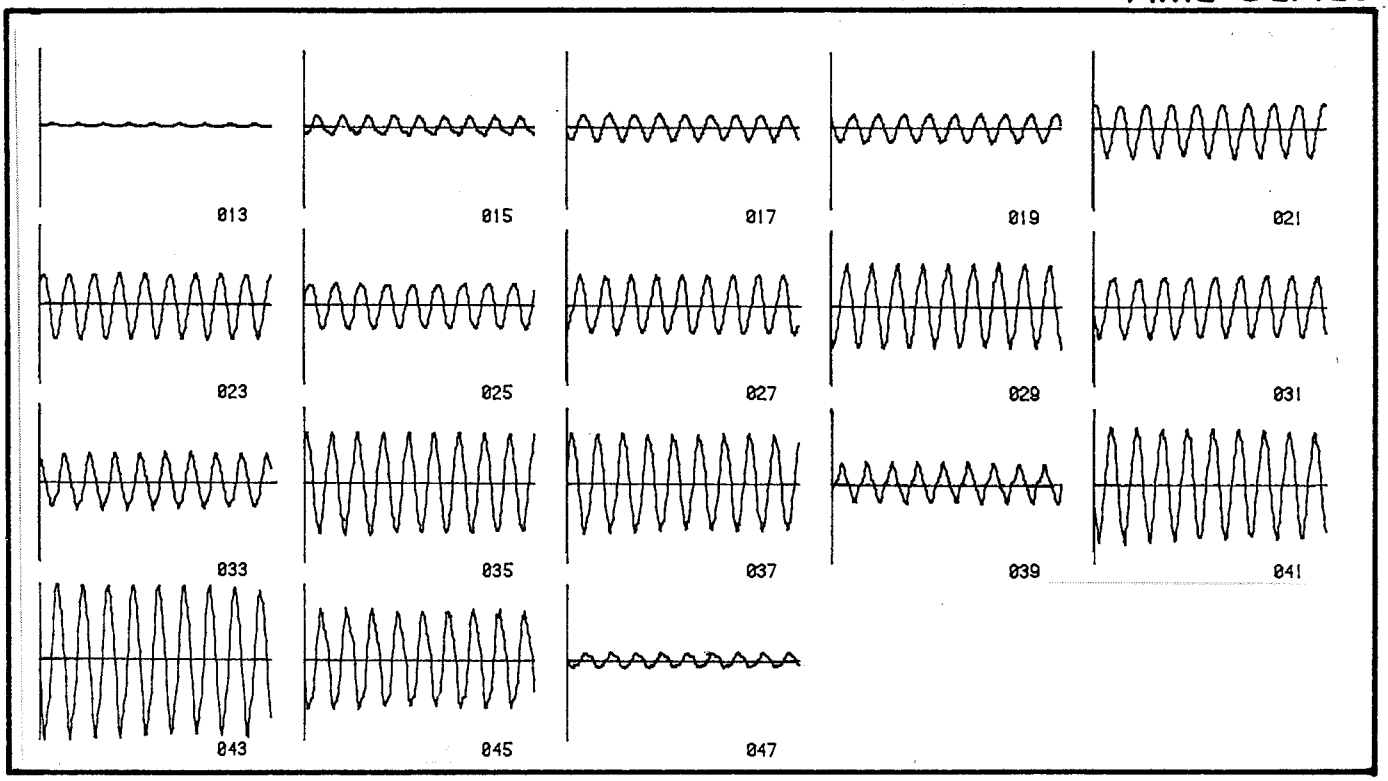

Histograms

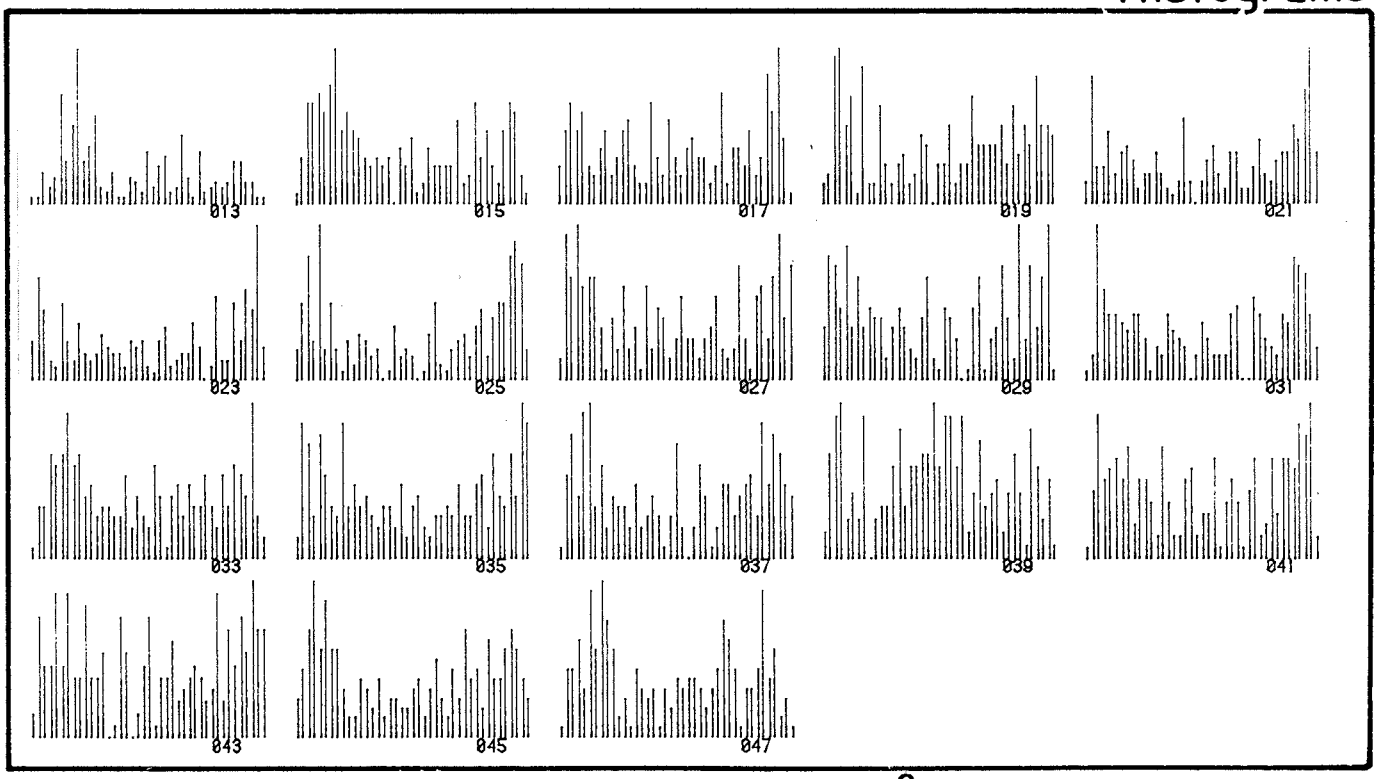

Monochromatic sea: T=1.1sec, Angle=35°, Hrms=1.414cm

SURGE joints

GRAPH 6.9

spine joint TORQUE SIGNALS

Time Series & Histograms

Stiffness: 1000Nm/rad, Status: 10

Sampling: 256 points at 20Hz = 12.8sec

Time Series

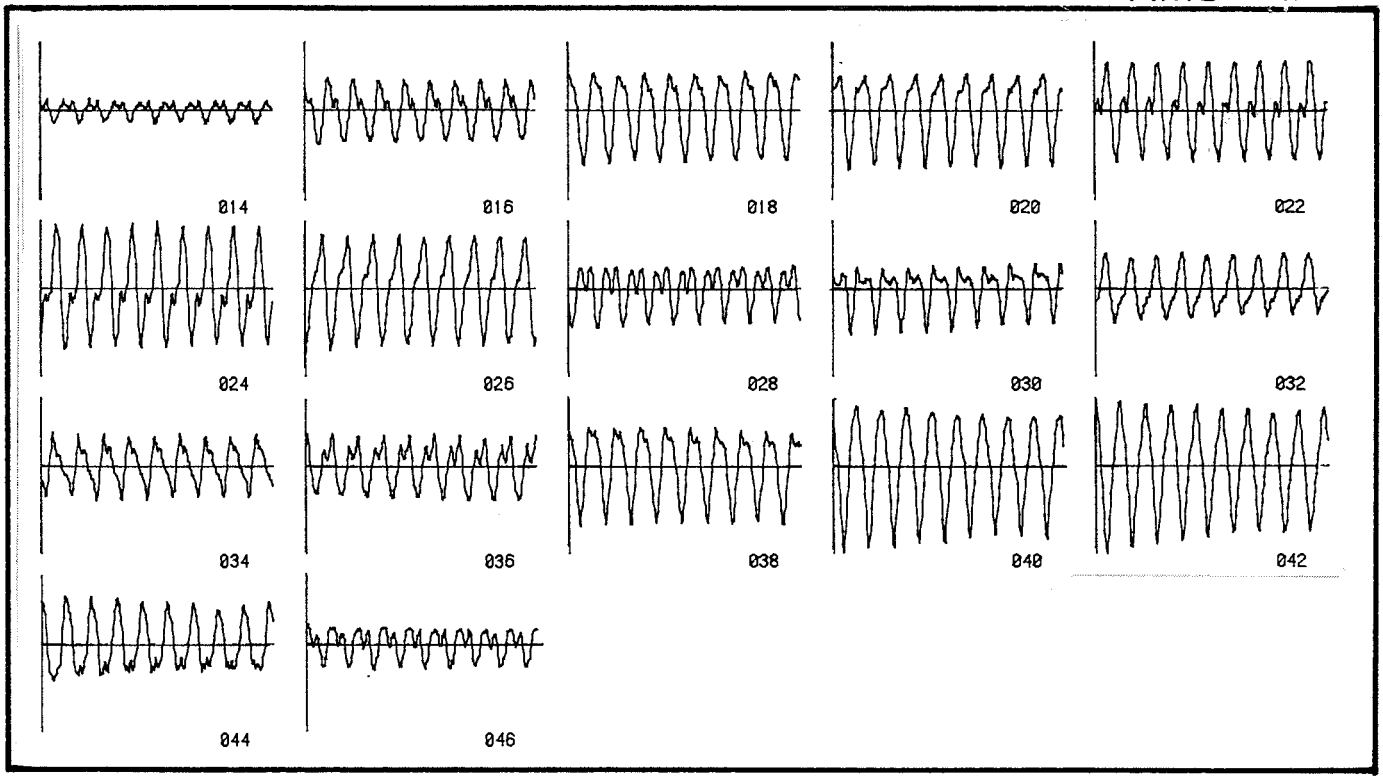

Histograms

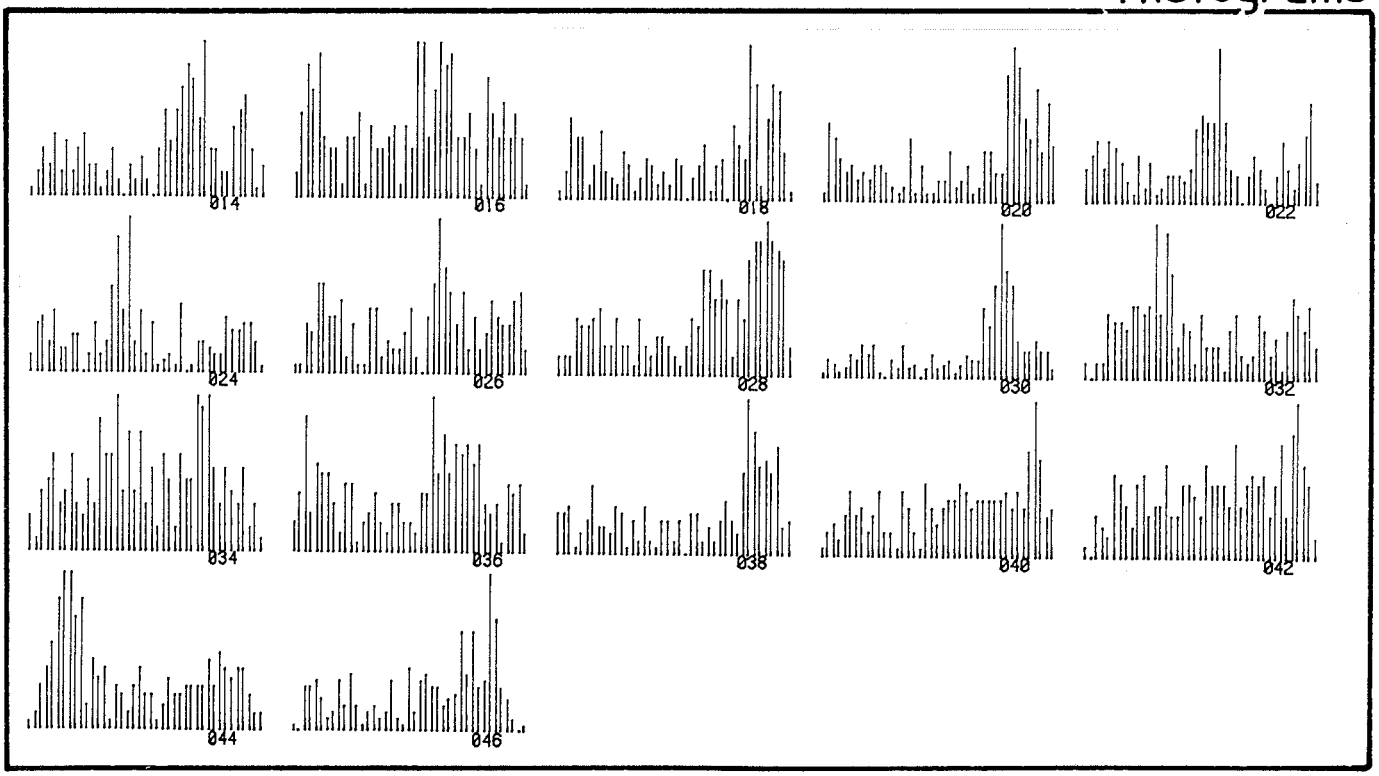

Monochromatic sea: T=1.1sec, Angle=35°, Hrms=1.414cm

HEAVE joints

GRAPH 6.10

6.G THE SOUTH UIST 46 SPECTRA

Introduction

Crabb has given an excellent description of the collection and analysis of wave data from seas off South Uist carried out by the Institute of Oceanographic Sciences (ref a). Wave measurement had started in March 1976 with a waverider buoy operating 8 nautical miles offshore in 15 metres depth, and at 2 other sites in 23 metres depth and 100 metres depth (Mollison ref f).

They produced a group of 399 evenly weighted spectra, collectively representative of a 'standard' Hebridean year, with wave directions synthesised from hindcasts using local and distant wind data.

The individual spectra were expressed as combinations of up to 3 components:

a) Wind sea: the higher frequency part of the spectrum caused by local winds concurrent with the wave record.

b) Swell sea: the low frequency part of the spectrum attributable to earlier and distant wind conditions.

c) Old Wind Sea: a central part of the spectrum caused by local winds which had changed just prior to the wave sampling period.

Graph 6.11, reproduced from ref a, shows a typical measured South Uist spectrum with clearly visible 'wind' and 'swell' components.

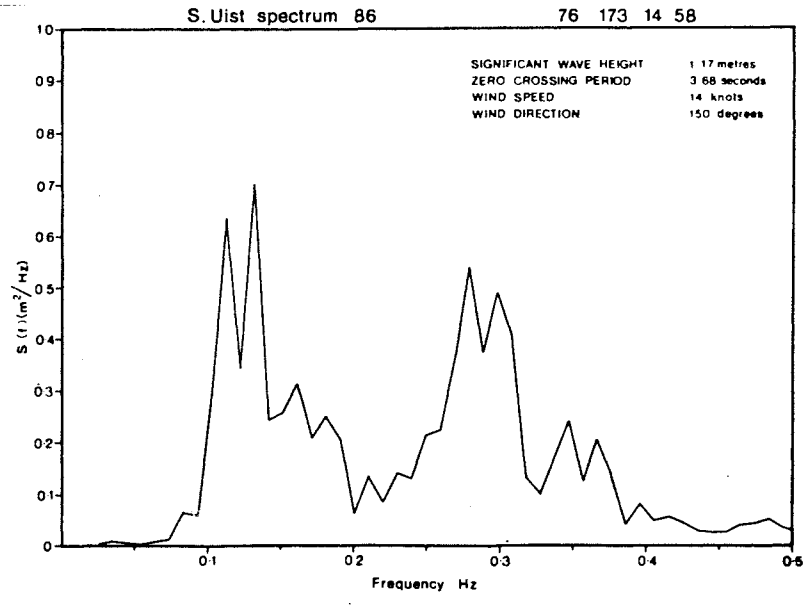

GRAPH 6.11

(6.G cont)

Selection of a Sub-Set

Subsequently, IOS were asked by the Department of Energy's consultants, Rendal, Palmer and Tritton, to select a small subset of about 40 spectra which would collectively reflect the principal characteristics of the 399, but which could conveniently be used in scale model tests (refs k & j).

IOS first sorted the 399 spectra into classes according to 3 parameters (ref i):

a) 'Frequency-Width': the frequency interval within which 80% of the power is contained, (4 classes)

b) 'Direction-Width': the angular interval within which 80% of the power in the frequency width is contained. (4 classes)

c) Energy Period **Te**: (5 classes)

Within each class the 399 spectra were further sorted into groups according to power density.

Even with this grouping process it was found that the number of sea types was too great to be adequately represented by a small sub-set and so 2 separate sub-sets were proposed:

Set 1 - A group of spectra covering as wide a range as possible of frequency width, direction width and energy period but restricted in the range of power and the directions of peak power. 38 spectra were eventually selected for this group and it was suggested that they be used to predict full-scale system behaviour from 2-dimensional model test data.

Set 2 - A group of spectra covering as wide a range as possible of frequency width, direction width, energy period and power, associated with those spectra which contain the bulk of the power arriving at South Uist. 46 spectra were eventually selected for this group, which was intended for use in assessing full-scale output productivity of wave energy devices. Set 2 is the group of South Uist spectra implemented in the wide tank and referred to below and throughout this report.

(6.G cont)

Selection of the 46 Spectra

The classification of the 399 spectra, by frequency-width, direction-width, energy period and power density produced a 4-dimensional histogram, with 107 occupied cells, each of which should ideally have a representative assigned to Set 2. By excluding from representation sea states which did not greatly contribute to the annual energy available a further reduction of numbers was made.

The rules chosen for exclusions were:

a) power density too low (10 kW/m)
b) power density too high (300 kW/m)
c) energy period too low (7.0 sec)
d) energy period too high (12.9 sec)
e) 'unusual' combinations of Energy Period, Power, Spectral Width, Directional Spread and Principal Direction

This reduced the number of spectra to be represented to 267, occupying 46 different cells of the histogram. 76.5% of the total energy in the 399 spectra is accounted for by these cells. (see below for details of 46 spectra weightings.)

The Set 2 spectra were made up by selecting, from each of the 46 occupied cells, a spectrum whose power density was near the average for that cell and whose direcion of peak power was close to either 240 degrees or 270 degrees.

(6.G cont)

Wide Tank Implementation of the 46 Spectra

Our current full-scale designs are based on 14 metre ducks. The wide tank model uses 130mm ducks on 125mm diameter spines, implying a tank scale of 14 metres/130mm, or 107.7.

The IOS spectra are based on wave data collected at 42 metres depth, but we favour operation around the 100 metre contour. The small amount of data collected by IOS at their 100 metre site allowed us to make frequency dependent corrections to the 46 so as to estimate their spectral content at 100 metres. The directional distributions already assigned to the 42 metre set by IOS, are in fact more appropriate to our deep water site. (Mollison, ref f).

The three possible sub-spectra in the sea states were each described by IOS using a Pierson-Moskowitz model (ref b, pp6.8–6.9) with assigned values of Hrms and Te, and a modified 'spectral width parameter' which allowed the range of wavefront frequencies to be compressed or expanded. The spectral width parameter is analogous to our 'compression factor'. Directionality is indicated by a 'principal direction' parameter, and an angular distribution model with exponent if appropriate.

The table below summarises the parameters used:

Component name	Parameters specified for all components	angular distribution model	distribution exponent
Wind sea	Hrms, Energy period	Mitsuyasu	frequency-dependent
Swell sea	Spectral Width	$\cos^{2s}\frac{1}{2}(\theta-\theta_0)$	s varies
Old Wind sea	Principal Direction	$\cos^{2s}\frac{1}{2}(\theta-\theta_0)$	s = 6

Our current wavemaking computer can produce 75 separate wavefronts for each sea state. We make best use of this limited number by arranging that the total energy in the sea is, where possible, evenly divided between them but we must also ensure that the range of frequencies is reasonably covered. We used a simple rule and divided the 75 wavefronts between the 3 sea components in proportion to the product of Hrms and the spectral width parameter for that component.

We ignored several wind sea components with easterly mean directions, as in every such case the energy contributed was 3% or less.

(6.G cont)

Angle Considerations

The 46 spectra contain energy arriving from all compass bearings, but a line of wavemakers has a limited angular range. At frequencies below 1.6 Hz the theoretical angle limit is ±90°, and it rapidly falls off to 0 degrees at 2.26 Hz (see Section 6.D). We can make 90° waves at the wavemakers but they do not find their way into the centre of the tank. The width of tank usefully served by the wavemakers is reduced by the product of the tangent of the wavefront angle and the distance of the model from the wavemakers. We lose this width at both ends of the tank if there are positively and negatively angled wavefronts, so that very long models in mixed seas must be deployed as close to the wavemakers as possible.

We used an angular range of -70° to +70°, and a frequency range of 0.5 to 3.0 Hz in implementing the 46 spectra. With hindsight these limits are clearly too wide. The second set of pox-plots (section 3.B) show the presence of numerous additional 'ghost' wavefronts wherever the specified wavefronts fall outside the tank angular envelope (see section 3.B, and section 6.D). Current tank work, to be reported later, suggests that the 'ghost' wavefronts are at frequencies and angles generally benign to spines, but we propose creating further sets of 46 tank spectra with better limits.

The closest that we can get spine models to the wavemakers is about 2 metres. The ±70° limit suggests that the maximum width of model exposed to all wavefronts would be equal to the width of wavemakers minus 11.0 metres, which works out at 14.0 metres for 82 wavemakers. This is equivalent to 35 of our spine units. In practice, deployment of the models so close to the wavemakers is difficult because of mooring access problems, and we usually work further out into the tank. The monochromatic spine tests in section 4.H suggest that bending moments rise towards the down-wave end so this problem is unlikely to affect the maximum values recorded.

(6.G cont)

Alternative Realisations

Most of the 46 spectra can be reasonably realised with the model lying parallel to the wavemakers, so that their normal represents a compass bearing of 260°, which is thought to be the angle of optimum energy capture for a line of wave energy absorbers. However, 13 of the spectra have important amounts of energy approaching from southerly or northerly directions which fall outside the ±70° limit discussed above. We cannot increase the tank angular window above 140° but we can improve the representation of these spectra by moving the model. We produced a second set of 9 spectra for southerly seas with the model yawed through +40° (clockwise from above), so that the normal to the wavemakers represents a bearing of 220°. A third set of 4 spectra cater for northerly seas with the model yawed through -50° to make the wavemaker normal represent a bearing of 310°. In practice, in this latter case, a mirror image set is used to invert the angles and allow the direction of yaw to be the same as in the second set. These alternative realisations limit the model length to about 22 units.

The 4 sets of South Uist spectra are depicted in the pox-plots and 3-D plots of Section 2.

(6.G cont)

Weightings of the 46 Spectra

The selection of a sub-set of spectra from the original 399 equally weighted South Uist seas results in an unequally weighted set of 46.

Table 6.8 below shows the number of original spectra represented by each of the 46 and, by implication, their relative weightings. (A method suggested by Rendel, Palmer and Tritton for weighting test results to represent performance over the whole year is described in ref j.)

	IOS ref no	relative WEIGHT		IOS ref no	relative WEIGHT		IOS ref no	relative WEIGHT
1	089	4	16	223	5	31	322	4
2	108	4	17	228	3	32	324	3
3	112	3	18	238	6	33	336	3
4	122	4	19	241	4	34	346	4
5	154	8	20	242	4	35	347	2
6	168	7	21	244	15	36	352	2
7	171	19	22	249	3	37	355	2
8	177	6	23	267	4	38	359	11
9	180	6	24	268	2	39	360	3
10	200	9	25	280	7	40	366	3
11	201	21	26	291	5	41	371	5
12	210	20	27	292	7	42	377	5
13	212	3	28	294	3	43	378	2
14	218	9	29	318	6	44	381	2
15	220	4	30	319	8	45	388	3
						46	391	4

Weights total: 267

TABLE 6.8 Weightings for the 46 South Uist Spectra (source: ref i)

6.H CONVERTING BENDING MOMENTS TO ANGLES

Most of the graphs in this report show bending moments. If we assume that the joints are behaving as undamped, linear springs with known stiffness the conversion is obvious. One divides a bending moment result by the stiffness at which it was measured to obtain a value of joint movement in radians.

After the angular measurements in extreme waves showed that joint-angle would be the very least of our problems we decided to defer the presentation of angle data to a later report which will deal with the effects of torque limits and joint damping.

6.J CALIBRATIONS AND ACCURACIES

Wave Height Measurement

Our knowledge of the wave height in the tank depends on two things:

1. Wave gauge calibration.

An array of 16 three-wire conductivity-compensating gauges is arranged about 2 metres in front of the wavemakers. These are calibrated before every experiment. A monthly check was made of their drift, and over the period January to July 1983 the RMS monthly error was 1.43% (Note that an average monthly error would have been less due to cancellation). Most gauges managed to stay within ±1%, but the RMS is pulled up by the occasional rogue.

2. Tank repeatability.

Experiments on long spines are done by measuring the sea in the absence of the model, and relying on repeatability to ensure the model seeing the same waves. (In the narrow tank with regular waves we can separate incident and reflected waves. This is not possible in the wide tank and wave measurements done with the model in the water are always high because of reflection.) Over a test, the wavemaking system gives us an RMS repeatability of better than 2%, while instantaneous wave height can have up to 5% error.

Spine Torque Measurement

Spine torque is measured with a bridge of 4 strain gauges on the torque plate. These are positioned so that all torque is applied through them with the following exceptions:

1. Spine angle-centring torque spring
2. Spine bearing friction

The stiffness of the centring spring is known, at 15 Nm/rad (this is approximately 0.1% of the maximum stiffness obtainable), while the bearing friction of a new spine is less than 1% of the full-scale torque limit.

(6.J cont)

The strain gauge circuit is calibrated using a special calibration rig. We trim every spine to better than 0.5% but the combination of drift and non-linearity increases this error. We believe that most spines have a worst error of less than 2%.

The torque calibration is 10 Nm/volt.

Spine Velocity Measurement

This is done using a tacho-generator on the back of the spine motor. We calibrate it by mounting the spine on a special rig and allowing it to move through a precise angle between end stops: the output of the tacho-generator is accurately integrated, and the output of the integrator compared with the angle it has gone through. We aim at calibrating this to better than 0.25%. However, the 'inherent stiffness' (see graph 6.6) means that if the joint is experiencing a high torque it will underread its velocity. The 'movement multiplier', mentioned in Table 6.7, can be used to generate a correction if necessary.

The velocity calibration is 0.1 rad/sec/volt.

Spine displacement

This is obtained by doing a digital integration of the sampled velocity signal in the Plessey Miproc computer. Its accuracy therefore is no worse than the velocity from which it is derived.

6.K USEFUL EQUATIONS

A Note on Scale

If dynamic similarity exists between model and prototype, we can get full-scale figures from model figures with the right scaling factor. This is best described by some index of scale. These are listed below for various parameters. The second column gives actual multiplication factors for our current wide tank scale of 107.7

PARAMETER	INDEX OF SCALE	FOR FULL SCALE MULTIPLY BY
Bending moments	4	135×10^{6}
Wave height and length	1	107.7
Period	0.5	10.4
Frequency	-0.5	96×10^{-3}
Distances	1	107.7
Linear Velocities	0.5	10.4
Linear accerations	0	1.0
Angles	0	1
Angular velocity	-0.5	96×10^{-3}
Angular acceleration	-1	9.3×10^{-3}
Buoyancy	3	1.25×10^{6}
Inertial forces	3	
Velocity forces	3	
Drift forces	3	
Torque	4	135×10^{6}
Power	3.5	13×10^{6}
Power per unit length	2.5	120×10^{3}
Force per unit length	2	11.6×10^{3}
Torque per unit length	3	1.25×10^{6}
Mass	3	1.25×10^{6}
Inertia per unit length	4	135×10^{6}
Buoyancy spring per unit length	3	1.25×10^{6}
Damping per unit length	3.5	13×10^{6}
Stiffness density	1	107.7
Compliance density	-1	9.3×10^{-3}
Beam stiffness EI	5	14.5×10^{9}

The ratio of wavelength to diameter L/D is the most useful indicator of dynamic similarity. The ratio of wave height to diameter should also be considered. Scale effects should be less of a worry for inertia-dominated wave behaviour than in other fields.

Vibrations

In the following, k is spring stiffness, c a viscous damping constant, ω_n an undamped natural frequency and m, M masses.

Free vibration with viscous damping

For a mass m the undamped natural frequency is

$$\omega_n = \sqrt{(k/m)}$$

the critical damping constant is

$$c_c = 2\sqrt{(km)}$$

the damping ratio is $\zeta = c/c_c$ and the logarithmic decrement is

$$\delta = 2\pi\zeta/\sqrt{(1 - \zeta^2)} \approx 2\pi\zeta$$

Steady-state vibration with viscous damping

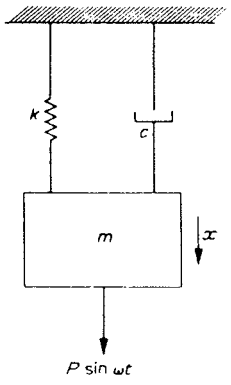

The ratio of peak amplitude X to the steady displacement $X_0 = P/k$ is

$$\frac{X}{X_0} = \frac{1}{[\{1 - (\omega/\omega_n)^2\}^2 + \{2\zeta\omega/\omega_n\}^2]^{1/2}}$$

and the phase angle ϕ is given by

$$\tan\phi = \frac{2\zeta\omega/\omega_n}{1 - (\omega/\omega_n)^2}$$

These relations yield the curves given below.

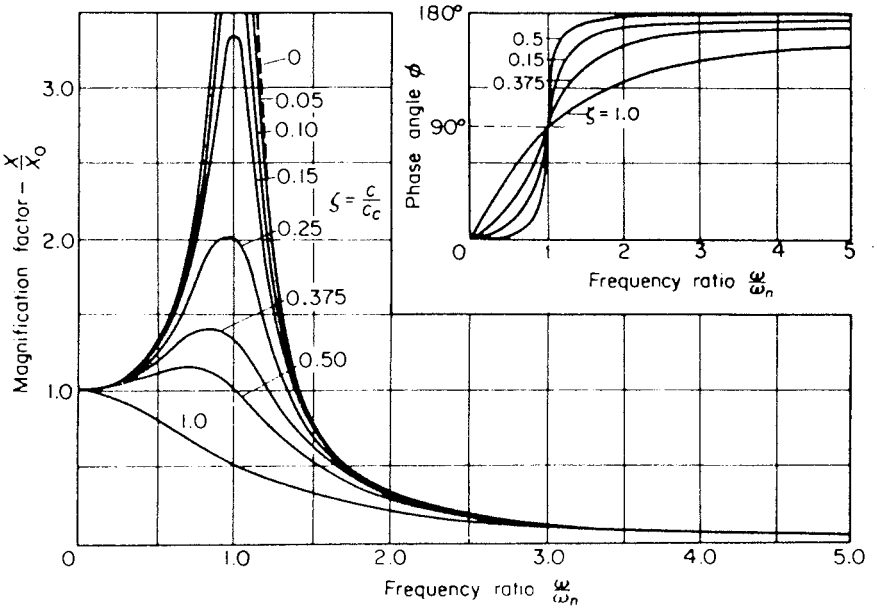

Free beam. ω_{nat} = 1st 22.4, 2nd 61.7, 3rd 121 $\sqrt{\frac{EI}{\gamma L^4}}$

γ = mass / unit length. (inc added mass)

$$H_{RMS} = \frac{H_{sig}}{4} = \frac{H_{\frac{1}{3}}}{4} = \sqrt{M_0}$$

For P.M. norm $H_{RMS} = .0136\, T_e^2$

$T_e = .977\, U_{19.5}$

$$\text{Power} = \frac{\rho g^2}{4\pi} H_{RMS}^2\, T_e$$

For P.M. $= 1.4 \times 10^{-4}\, U_{19.5}^5 = 1.57 \times 10^{-4}\, T_e^5$

$\frac{\rho g^2}{4\pi} = 7.87$ for kW/m.

For deep water phase vel $= \sqrt{\frac{g\lambda}{2\pi}} = \frac{gT}{2\pi} = 2 \times$ group vel

For shallow phase vel $= \sqrt{gd}$ = group vel. $\qquad \frac{d}{\lambda'} \tanh \frac{2\pi z}{\lambda'} = \frac{d}{\lambda}$

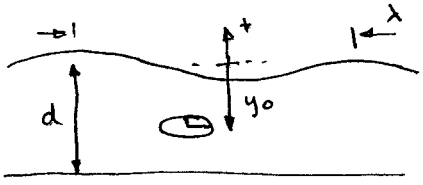

$$x = -\frac{H}{2}\left[\frac{\cosh 2\pi (y_0+d)\lambda}{\sinh \frac{2\pi d}{\lambda}}\right] \sin 2\pi\left[\frac{x_0}{\lambda} - \frac{t}{T}\right]$$

$$y = \frac{H}{2}\left[\frac{\sinh 2\pi (y_0+d)\lambda}{\sinh \frac{2\pi d}{\lambda}}\right] \cos 2\pi\left[\frac{x_0}{\lambda} - \frac{t}{T}\right]$$

Sylvester P152, 278

LBL COSH e^x ↑ 1/x +2÷ RTN

LBL SINH e^x ↑ 1/x −2÷ RTN

$$\text{Pressure} = \rho g\left[y + \frac{H}{2}\cdot\frac{\cosh 2\pi (y+d)/\lambda}{\cosh 2\pi d/\lambda}\right] \cos 2\pi\left[\frac{x_0}{\lambda} - \frac{t}{T}\right]$$

$$\text{Power} = \frac{\rho g H^2 \lambda}{8T} \cdot \frac{1}{2}\left[1 + \frac{4\pi d/\lambda}{\sinh 4\pi d/\lambda}\right] = \frac{\rho g H^2 \lambda}{8T} \cdot \frac{C_{group}}{C_{phase}}$$

Beam flexure velocity $= \frac{2\pi}{\lambda}\sqrt{\frac{EI}{\gamma}}$. Frequency $= \frac{2\pi}{\lambda^2}\sqrt{\frac{EI}{\gamma}}$. for travelling waves

Standing wave: $\cos \frac{2\pi L}{C} \cosh \frac{2\pi L}{C} = 1$.

Universal Beam Equation: $\frac{M}{I} = \frac{\sigma}{y} = \frac{E}{R}$

E concrete $= 40 \times 10^9$ N/M²

steel $= 200 \times 10^9$ N/M²

Floatation

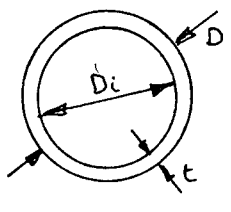

$$\frac{Di}{D} = \sqrt{1 - \frac{1}{\gamma}}$$

γ concrete $= 2.4$

$\therefore \frac{Di}{D} = .76$ max. .8 probable.

Section Moment $I = \frac{\pi\left(D^4 - Di^4\right)}{64} \simeq \frac{\pi D^3 t}{8}$ $\qquad I \simeq .03\, D^4$

$EI_{13.5} = 4 \times 10^{13}$ N m²

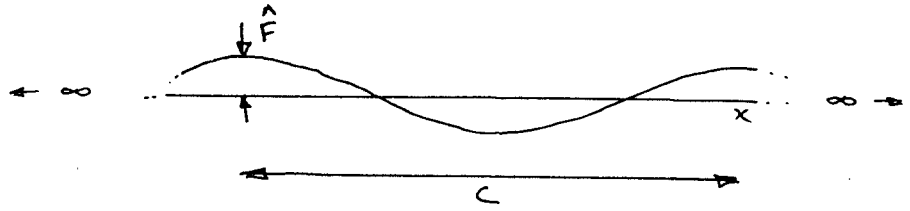

Static force field 'rigid' beam

$\lambda < C < \infty$; $C = 1.7\lambda$?

Local Force density $F = \rho g D H_{Tc} c_f = \hat{F} \cos \frac{2\pi x}{C} = \frac{d\,\text{Shear}}{dx}$

$$\text{Shear} = \frac{C\hat{F}}{2\pi} \sin \frac{2\pi x}{C} + k_1$$

$$M = -\frac{C^2 \hat{F}}{4\pi^2} \cos \frac{2\pi x}{C} + k_1 x + k_2 = EI \frac{d^2 y}{dx^2} = \frac{EI}{R}$$

$$\text{Slope} = \frac{dy}{dx} = -\frac{C^3 \hat{F}}{8\pi^3 EI} \sin \frac{2\pi x}{C} + \frac{k_1 x^2}{2} + k_2 x + k_3$$

$$y = \frac{C^4 \hat{F}}{16\pi^4 EI} \cos \frac{2\pi x}{C} + \frac{C_1 x^3}{6} + \frac{C_2 x^2}{2} + C_3 x + C_4$$

$$\text{Stiffness} = \frac{\hat{F}}{y} = \frac{16\pi^4 EI}{C^4}$$

EI for 13.5 concrete = 4×10^{13} Nm

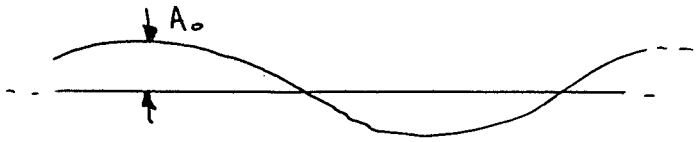

Flexible beam.

Deflection $y = A_0 \cos \frac{2\pi x}{C}$

$$B_{max} = \frac{\omega^2 C^2}{\sqrt{\left(EI C^4 - \gamma \omega^2\right)^2 + \left(Q_H \omega\right)^2}}$$

(Q_H: hyd. damping)

Slope $\frac{dy}{dx} = -\frac{2\pi A_0}{C} \sin \frac{2\pi x}{C}$

Curvature $\frac{d^2 y}{dx^2} = -\frac{4\pi^2 A_0}{C^2} \cos \frac{2\pi x}{C} = \frac{1}{R}$

$$\text{Strain } \epsilon = \frac{\sigma}{E} = \frac{MD}{2IE} = \frac{D}{2R} = \frac{2\pi^2}{C^2} D A$$

Joint angle

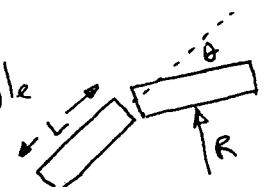

$$\theta = \frac{L}{R} = \frac{LA}{C^2} 4\pi^2 \,, \quad \frac{M}{\theta} = \frac{EI}{L}$$

REFERENCES

a) Crabb, J. A., Synthesis of a Directional Wave Climate, in 'Power from Sea Waves', Count, B. ed., pp 41 - 74, Academic Press, London, 1980.

b) 4th Year Report, Vol 1, Edinburgh Wave Power Project.

c) 4th Year Report, Vol 3, Edinburgh Wave Power Project.

d) Salter, S.H., Absorbing Wave-Makers and Wide Tanks, in Proceedings of the Conference on Directional Wave Spectra Applications, Wiegel, R.L. ed., pp 185 - 202, American Society of Civil Engineers, New York, 1981.

e) Edinburgh SCOPA Laing report, 1979.

f) Mollison, D., Wave Energy Losses in Intermediate Depths, Applied Ocean Research, Vol. 5, No. 4, pp 234 - 237, 1983.

g) Wiegel, R. L., Oceanographic Engineering, Prentice-Hall, New Jersey, 1964.

h) Gilbert, G., Generation of Oblique Waves, H.R.S. Notes No.18, pp 3-4, May 1976.

i) Crabb, J.A., personal communication.

j) Anon, Consultant's Methodology for Establishing Annual Device Productivity Using the 46 Selected Spectra, Rendal, Palmer and Tritton consultants' working paper no 42, 1981, London.

k) Anon, Transformation of the 46 Selected Multidirectional Spectra for Tests of the Devices in the Tank. Rendal, Palmer and Tritton consultants' working paper no. 39, 1981, London.

l) 4th year report, Vol 2, Edinburgh Wave Power Project.

m) Bryden, I. G., Long Floating Cylinders in Three-Dimensional Random Seas, PhD Thesis, University of Edinburgh, 1983.

n) 2nd year report, Edinburgh Wave Power Project.